

# Diagnostic Measurement and Modelling of Electrical Insulation Based on Very Low Frequency High Voltage Excitation

**Author:**

Morsalin, Sayidul

**Publication Date:**

2020

**DOI:**

<https://doi.org/10.26190/unsworks/3945>

**License:**

<https://creativecommons.org/licenses/by-nc-nd/3.0/au/>

Link to license to see what you are allowed to do with this resource.

Downloaded from <http://hdl.handle.net/1959.4/67032> in <https://unsworks.unsw.edu.au> on 2024-03-28

# **Diagnostic Measurement and Modelling of Electrical Insulation Based on Very Low Frequency High Voltage Excitation**

**Sayidul Morsalin**

*Supervisor: Associate Professor Toan Phung*

A thesis in fulfilment of the requirements for the degree of  
Doctor of Philosophy



School of Electrical Engineering and Telecommunications

Faculty of Engineering

The University of New South Wales (UNSW)

January 2020

---

---

**THE UNIVERSITY OF NEW SOUTH WALES**  
**Thesis/Dissertation Sheet**

Surname or Family name: **Morsalin**

First name: **Sayidul**

Other name/s:

Abbreviation for degree as given in the University calendar: **Ph.D.**

School: **Electrical Engineering and Telecommunications**

Faculty: **Engineering**

Title: **Diagnostic Measurement and Modelling of Electrical Insulation Based on Very Low Frequency High Voltage Excitation**

**Abstract 350 words maximum: (PLEASE TYPE)**

Electrical insulation of high voltage (HV) power equipment plays essential roles in sound functioning and reliability of power systems. Examining the insulation condition through various diagnostic testings such as dielectric response (DR) and partial discharge (PD) measurements may be able to reveal the presence of defects and degradations in the insulation. Very low frequency (VLF- 1 Hz or lower) applied voltage has emerged as a promising diagnostic tool as it significantly reduces the required reactive power from the test supply. However, the existing interpretation knowledge at conventional power frequency (PF) 50 Hz cannot be directly applied to understand test results in the VLF range. This is the main motivation of the research which explores the dielectric behaviours and associated physical processes under VLF excitation.

For dielectric response, experimental studies were carried out on short sections of medium voltage service-aged cross-linked polyethylene (XLPE) cables to diagnose the bulk insulation condition, such as the measurement of dissipation factor, polarisation and depolarisation current, frequency domain spectroscopy, activation energy etc. Experimental results show that dielectric behaviours of electric insulation are influenced by several factors including the excitation frequency, voltage amplitude, ambient temperature, dipolar processes (e.g. conduction and polarisation) etc. An empirical physical model describing the loss-factor measurement based on well-known dipolar theories is developed and verified by experimental results.

Different partial discharge processes (e.g. cavity, surface and corona) are also investigated at both VLF (0.1 Hz) and 50 Hz applied voltage. Measurement results are presented with the phase-resolved image and show that discharge characteristics (inception voltage, magnitude and repetition rate) are strongly dependent on the applied frequency. Based on the finite element analysis (FEA) method, a dynamic model to simulate the discharge behaviours in the cavity or on the degraded surface is developed to examine the frequency dependence.

The main contributions of this research include the measurement and modelling of both the dielectric response and partial discharge in electrical insulation. The research findings provide valuable information to understand the diagnostic characteristics at very low frequency excitation.

**Declaration relating to disposition of project thesis/dissertation**

I hereby grant to the University of New South Wales or its agents the right to archive and to make available my thesis or dissertation in whole or in part in the University libraries in all forms of media, now or here after known, subject to the provisions of the Copyright Act 1968. I retain all property rights, such as patent rights. I also retain the right to use in future works (such as articles or books) all or part of this thesis or dissertation.

I also authorise University Microfilms to use the 350 word abstract of my thesis in Dissertation Abstracts International (this is applicable to doctoral theses only).

.....  
Signature

.....  
Witness Signature

.....  
Date

The University recognises that there may be exceptional circumstances requiring restrictions on copying or conditions on use. Requests for restriction for a period of up to 2 years must be made in writing. Requests for a longer period of restriction may be considered in exceptional circumstances and require the approval of the Dean of Graduate Research.

**FOR OFFICE USE ONLY**

Date of completion of requirements for Award:



---

## COPYRIGHT STATEMENT

‘I hereby grant the University of New South Wales or its agents the right to archive and to make available my thesis or dissertation in whole or part in the University libraries in all forms of media, now or here after known, subject to the provisions of the Copyright Act 1968. I retain all proprietary rights, such as patent rights. I also retain the right to use in future works (such as articles or books) all or part of this thesis or dissertation. I also authorise University Microfilms to use the 350 word abstract of my thesis in Dissertation Abstract International. I have either used no substantial portions of copyright material in my thesis or I have obtained permission to use copyright material; where permission has not been granted I have applied/will apply for a partial restriction of the digital copy of my thesis or dissertation.’

Signed .....

Date .....

## AUTHENTICITY STATEMENT

‘I certify that the Library deposit digital copy is a direct equivalent of the final officially approved version of my thesis. No emendation of content has occurred and if there are any minor variations in formatting, they are the result of the conversion to digital format.’

Signed .....

Date.....

---

## ORIGINALITY STATEMENT

‘I hereby declare that this submission is my own work and to the best of my knowledge it contains no materials previously published or written by another person, or substantial proportions of material which have been accepted for the award of any other degree or diploma at UNSW or any other educational institution, except where due acknowledgement is made in the thesis. Any contribution made to the research by others, with whom I have worked at UNSW or elsewhere, is explicitly acknowledged in the thesis. I also declare that the intellectual content of this thesis is the product of my own work, except to the extent that assistance from others in the project’s design and conception or in style, presentation and linguistic expression is acknowledged.’

Signed .....

Date.....

---

## INCLUSION OF PUBLICATIONS STATEMENT

UNSW is supportive of candidates publishing their research results during their candidature as detailed in the UNSW Thesis Examination Procedure.

**Publications can be used in their thesis in lieu of a Chapter if:**

- The candidate contributed greater than 50% of the content in the publication and is the “primary author”, ie. the candidate was responsible primarily for the planning, execution and preparation of the work for publication
- The candidate has approval to include the publication in their thesis in lieu of a Chapter from their supervisor and Postgraduate Coordinator.
- The publication is not subject to any obligations or contractual agreements with a third party that would constrain its inclusion in the thesis

Please indicate whether this thesis contains published material or not:

☐ This thesis contains no publications, either published or submitted for publication *(if this box is checked, you may delete all the material on page 2)*

☒ Some of the work described in this thesis has been published and it has been documented in the relevant Chapters with acknowledgement *(if this box is checked, you may delete all the material on page 2)*

☐ This thesis has publications (either published or submitted for publication) incorporated into it in lieu of a chapter and the details are presented below

### CANDIDATE’S DECLARATION

I declare that:

- I have complied with the UNSW Thesis Examination Procedure
- where I have used a publication in lieu of a Chapter, the listed publication(s) below meet(s) the requirements to be included in the thesis.

Candidate’s Name	Signature	Date (dd/mm/yy)

---

*To my beloved family.....*

*Dedicated to My Wife Monisha.....*

---

# Acknowledgment

The journey to my PhD research has not been smooth, and it is not the results that can be obtained over-night. The total outcome is the results of continuous hardworking, passion, dedication and sacrifice. Without having invaluable support from many people along the way, it would not have been possible to accomplish this research work.

First and foremost, I would like to offer my heartfelt gratitude to my supervisor, Associate Professor Toan Phung, for his constant guidance and enthusiastic support in every single step of this research. His excellent knowledgeable idea and encouragement along with the parenthood supervision helped me to counteract the challenges appeared in my research. I would like to appreciate his valuable comments, suggestions, feedback and constructive discussion over the PhD journey regardless of any time constraints.

I would like to acknowledge all the technical and professional staff at UNSW Electrical Engineering School, especially Mr. Zhenyu Liu who provided endless support to perform experimental work in the High Voltage laboratory and technical suggestions to shape the research.

I am also grateful to Prof. Christian Franck (ETH, Switzerland), A/Prof. Andrea Cavallini (University of Bologna, Italy), Professor Michael G. Danikas (Democritus University of Thrace, Greece), Dr. Jayashri Ravishankar (UNSW) and Dr. Damia Mawad (School of Material Science, UNSW). I want to express my sincere appreciation to Dr. Keith Imrie for his invaluable support in proofreading the majority contents of my thesis.

I would like to acknowledge UNSW Sydney, which honoured me with an international research scholarship to support my education and research during the PhD program. I would also like to acknowledge the IEEE NSW DEIS Section and other scholarship liaisons to present my research work at the national and international levels.

I also thank all my friends in Sydney who shared their memorable times with me. Thanks to Khizir, Ilham, Jakir, Sakib, Amin, and other Bangladeshi students to broaden my cultural perception. To Hana, Majid, Sirojan, Shibo, Animesh and other international friends, I really appreciate your friendship.

Last but not least, no word is sufficient to express my deepest gratitude to my parents, brother Sarwer and sister Mim. Thank you, Ammu (mother) to give me a beautiful life. Thank you, Abbu (father) to offer me continuous support and always being on my side during difficulties. Thank you, brother Sarwer to inspire me always. To my wife Monisha, I earnestly apologise for your uncountable sufferings and sacrifice during the time without me in Bangladesh. I am seeking forgiveness for not having adequate time with you due to the research pressure. Thank you all for staying with me during the study. I love you all!

---

# Abstract

The sound functioning of high voltage (HV) electrical infrastructures (e.g. power cables, transformers, etc.) has paramount importance to the reliable operation of power networks. Particularly, their electrical insulation plays a critical role. The electrical, mechanical and thermal stresses imposed by the power network gradually degrade the insulation condition and may eventually lead to complete breakdown. The regular condition monitoring or diagnostic testing of electrical insulation is important as it can significantly reduce the potential risk of catastrophic damage due to equipment failure while in service.

For examining the insulation conditions, two techniques of diagnostic assessment are the dielectric response (DR) and partial discharge (PD) measurement. The presence of PDs in any HV power equipment/apparatus stands for a sign of defects or degradation in the electrical insulation. A PD produces a short duration current pulse at the localised defect sites such as within an isolated cavity bounded in a solid insulation (known as cavity or void discharge), along the degraded surface (known as surface discharge) or from a sharp protrusion where the electric field is intensified (known as corona discharge). On the other hand, the diagnostic information of the whole insulation condition can be appraised from the DR measurement in either time or frequency domain, popularly known as polarisation and depolarisation current (PDC) method and frequency domain spectroscopy (FDS) respectively.

Generally, DR and PD measurements are performed with an AC supply voltage of power frequency (PF-50/60 Hz) to emulate the normal operating conditions; however, due to the large requirement of reactive power, it is often found unsuitable in on-site testing. As an alternative, condition assessment with very low frequency (VLF - 1 Hz or lower) applied voltage is well recognised test technique for diagnosing electrical insulation. VLF excitation considerably reduces the required reactive power from the test supply. Also, the benefits of lower cost and easier transportation see an increasing trend to deploy VLF testing, especially for field testing of high capacitance loads such as power cables. Because the diagnostic characteristics vary with the supply voltage frequency, the existing interpretation knowledge at 50 Hz may or may not be directly applicable to other test frequencies, particularly in the VLF range. This necessitates investigation of the dielectric behaviours over the VLF to PF test voltage and incorporate the experimental results with the physical modelling.

Therefore, this dissertation provides a diagnostic study of dielectric response and partial discharge measurement by both experimental analysis and analytical modelling, and compares the test results at VLF supply voltage with those at the conventional power frequency. For DR

---

measurement, different short sections of 11-kV service-aged cross-linked polyethylene (XLPE) cables are used as test-objects; this is because power cables insulated with XLPE materials now become a mainstream transmission means for delivering electricity in the cities and urban areas. XLPE is an excellent insulation due to its remarkable physical, chemical and electrical properties. Void discharge is studied using models of artificial voids with different shapes (cylindrical, prism, block) embedded in XLPE. Surface discharge and corona discharge are investigated along an XLPE surface and in a needle-plane electrode geometry, respectively.

Dielectric response study includes dielectric loss or dissipation factor (DDF or  $\tan \delta$ ) measurement, pol/depolarisation current measurement, activation energy measurement, mean relaxation time, frequency domain response, and physical modelling. The DDF results are presented as a function of applied voltage frequency and voltage amplitude and show that the higher  $\tan \delta$  values are observed at VLF as compared to PF excitation. The conduction process is dominant at lower frequencies, while the polarisation process influences the  $\tan$ -delta characteristics at higher frequencies. Moreover, the ionisation process resulted from partial discharge has influential roles for the tip-up of  $\tan$ -delta at 50 Hz.

An equivalent circuit modelling using the Debye model, Cole-Cole (C-C) model and Davidson-Cole (D-C) model is reported to simulate the  $\tan$ -delta characteristics over the 1 mHz to 50 Hz frequency range. It is found that the D-C model supports the experimental results better than the other dipolar theories. With the increasing temperature, due to  $\alpha$ - and  $\beta$ - relaxations, the loss-peak frequency of  $\tan \delta$  tends to be shifted to the higher frequency zone. Increasing temperature also causes the upward transition of the DC conductivity, polarisation and depolarisation current, trapping distributions etc. The activation energy and the mean relaxation time are also estimated using the Arrhenius equation. Determining the number of polarisation branches and establishing the relationship between Debye loss-factor and D-C loss factor are presented and verified with the experimental results. An empirical method is proposed to simulate the recovery voltage response.

Using both measurement and simulation, this research also investigates partial discharge behaviour at VLF as a function of cavity geometry. Measurement results are presented with the phase-resolved PD pattern and show that discharge characteristics (inception voltage, magnitude and repetition rate) are strongly dependent on the applied frequency. Using the finite element analysis (FEA) method, a dynamic model to simulate the discharge behaviour is developed to study the frequency dependence. Comparing with power frequency, lower discharge magnitude and repetition rate are observed at VLF (0.1 Hz). This is attributed to the availability of space charges after a PD event and electron generation rate before a PD occurrence, which are reduced. The numerical simulation includes the free charge (free electrons and positive ions) decay on the cavity wall to model the discharge behaviour and the results matches well with experiments.

---

The differences in PD characteristics along the XLPE surface as a function of applied voltage amplitude at VLF and PF are presented. Measurement results show that the increase of supply voltage results in a larger discharge magnitude at 50 Hz and also, the discharge occurs earlier in the voltage cycle. A two-dimensional physical model is also developed to simulate the surface discharge process.

Corona discharge characteristics are also presented with the phase-resolved discharge patterns for various excitation waveforms (sinusoidal, square and saw-tooth) and voltage levels. Due to the effect of space charges, experimental results show that the discharge magnitude, repetition rate per cycle, power and current are comparatively higher at 0.1 Hz and the square waveform results in a more scattered phase distribution of PD occurrence.

To sum up, this dissertation provides useful information to understand the diagnostic characteristics of solid insulation at very low frequency. This knowledge is essential for diagnosing the health of power apparatus and can form a robust platform for routine or reliability-based maintenance work.



---

# List of publications

## Journal Papers

1. **S. Morsalin**, B. T. Phung, “*Modelling of Dielectric Dissipation Factor Measurement for XLPE Cable Based on Davidson-Cole Model*”, IEEE Transactions on Dielectrics and Electrical Insulation, vol. 26, no. 3, pp. 1018-1026, June 2019.
2. **S. Morsalin**, B. T. Phung, Michael G. Danikas, “*Diagnostic Challenges in Dielectric Loss Assessment and Interpretation: A Review*”, IET Science, Measurement and Technology, vol. 13, no. 6, pp. 767-782, 2019.
3. **S. Morsalin**, B. T. Phung, “*Dielectric Response Measurement of Service-aged XLPE Cable from Very Low to Power Frequency Range*”, IEEE Insulation Magazine, 2019 (Accepted).
4. **S. Morsalin**, B. T. Phung, “*Dielectric Response Study of Service-aged XLPE Cable Based on Polarisation and Depolarisation Current Method*”, IEEE Transaction on Dielectrics and Electrical Insulation, vol. 27, no. 1, pp. 58-66, Feb. 2020.
5. **S. Morsalin**, B. T. Phung, “*Recovery Voltage Response of XLPE Cables Based on Polarisation and Depolarisation Current Measurements*”, IET Generation, Transmission and Distribution, vol. 13, no. 24, pp. 5541–5549, October 2019.
6. **S. Morsalin**, B. T. Phung, A. Cavallini, “*Measurement and Modelling of Partial Discharge Arising from Different Cavity Geometries at Very Low Frequency*”, IEEE Transactions on Dielectrics and Electrical Insulation, 2020 (Accepted).
7. **S. Morsalin**, B.T. Phung, “*Electrical Field Distribution on the Cross-linked Polyethylene Insulation Surface Under Partial Discharge Testing*”, Journal of Polymer Testing, vol. 82, pp. 1-8, 2020.
8. **S. Morsalin**, B. T. Phung, “*A Review of Diagnostic Challenges of Partial Discharge Measurement at Very Low Frequency: Part-I: Detection, Interpretation, Assessment and Modelling*”, (submitting to IET Science, Measurement and Technology).
9. **S. Morsalin**, B. T. Phung, “*A Review of Diagnostic Challenges of Partial Discharge Measurement at Very Low Frequency: Influence of Physical Parameters*”, (submitting to IET Science, Measurement and Technology).

## Book Chapter

10. **Sayidul Morsalin**, Khizir Mahmud, B. T. Phung, Jayashri Ravishankar, “*Grid integration and management of EVs through M2M Communication*”, Smart Grid Management with Electric Vehicle Integration- An ICT Approach, IET, Nov 2019.

## Conference Proceedings

11. **S. Morsalin**, B. T. Phung, Michael G. Danikas, “*Influence of Cavity Geometry on Partial Discharge Measurement at Very Low Frequency*”, Electrical Insulation Conference (EIC), Calgary, AB, Canada, June 2019, pp. 213-216.
12. **S. Morsalin**, A. Sahoo, B. T. Phung, “*Diagnostic Testing of Power Cable Insulation for Reliable Smart Grid Operation*”, 37th IEEE Electrical Insulation Conference (EIC), Calgary, AB, Canada, June 2019, pp. 509-512.

- 
13. **Sayidul Morsalin**, B. T. Phung, Michael G. Danikas, “Influence of Partial Discharge on Dissipation Factor Measurement at Very Low Frequency”, International Conference on Condition Monitoring and Diagnosis (CMD), Perth, Australia, Nov. 2018, pp. 1-5.
  14. **S. Morsalin** and B.T. Phung, “Modelling of Dielectric Dissipation Factor Measurement from Very Low to Power Frequency”, 2<sup>nd</sup> International Conference on Dielectrics (ICD), Budapest, Hungary, July 2018, pp. 1-4.
  15. **S. Morsalin** and B.T. Phung, “Corona Discharge under Non-Sinusoidal Voltage Excitation at Very Low Frequency”, 12th International Conference on the Properties and Applications of Dielectric Materials (ICPADM), Xian, China, May 2018, pp. 653-656.
  16. **S. Morsalin** and B.T. Phung, “A Comparative Study of Dielectric Dissipation Factor Measurement under Very Low and Power Frequencies”, 3rd International Conference on Condition Assessment Techniques in Electrical Systems (CATCON), Rupnagar, India, Nov. 2017, pp. 10-14.
  17. **S. Morsalin** and B.T. Phung, “Comparative Phase-Resolved Analysis of AC Corona Discharges at Very Low (0.1 Hz) and Power Frequencies”, International Conference on High Voltage Engineering and Power Systems (ICHVEPS), Bali, Indonesia, Oct. 2017, pp. 165-169.
  18. H.V.P. Nguyen, B.T. Phung and **S. Morsalin**, “Modelling Partial Discharges in an Insulation Material at Very Low Frequency” International Conference on High Voltage Engineering and Power Systems (ICHVEPS), Bali, Indonesia, Oct. 2017, pp. 451-454.

## Symposium

19. **S. Morsalin**, “Diagnostic Measurement and Modelling of Electrical Insulation Based on Very Low Frequency High Voltage Testing”, 5th Engineering Postgraduate Symposium, University of New South Wales, Australia, Dec. 2019.

---

# Table of Contents

<b>Abstract.....</b>	<b>viii</b>
<b>List of publications.....</b>	<b>xi</b>
<b>List of Figures.....</b>	<b>xix</b>
<b>List of Tables .....</b>	<b>xxiii</b>
<b>List of Abbreviations .....</b>	<b>xxiv</b>
<b>Nomenclatures.....</b>	<b>xxv</b>
<b>Chapter 1 .....</b>	<b>1</b>
1.1 Problem Statement and Background.....	1
1.2 Diagnostic Methods for Condition Assessment.....	3
1.2.1 Motivation of Dielectric Response Measurement.....	3
1.2.2 Motivation of Partial Discharge Measurement .....	5
1.3 Importance of Diagnostic Testing in the Smart Grid .....	6
1.4 Thesis Objectives .....	7
1.5 Original Contributions of the Thesis.....	8
1.6 Thesis Outline .....	10
<b>Chapter 2 .....</b>	<b>12</b>
2.1 Challenges of Dielectric Loss Assessment .....	12
2.1.1 Transportation Challenges .....	12
2.1.2 Various Aspects of Measurement Challenges.....	12
2.1.3 Challenges Related to the Processing .....	14
2.1.4 Diagnostic Standards and Others .....	14
2.2 Various AC High Voltage Testing.....	14
2.3 Different Voltage Sources and Suitability .....	15
2.4 Standards in the Diagnostic Testing.....	17
2.5 Test Voltage Waveforms.....	17
2.5.1 Cos-rectangular Waveform Excitation.....	17
2.5.2 Sinusoidal Waveform Excitation .....	18
2.6 Losses in a Dielectric .....	19
2.7 Dynamic Properties of Dipoles in a Dielectric.....	20
2.7.1 Electronic Polarisation Process.....	20
2.7.2 Ionic Polarisation Process .....	21
2.7.3 Orientation Polarisation Process .....	21
2.7.4 Interfacial Polarisation Process.....	22
2.7.5 Bulk Polarisation Process.....	22
2.7.6 Tunnelling Polarisation Process.....	23
2.8 Various Aspects of Dielectric Response Measurement .....	25
2.8.1 Analytical Expressions of Dielectric Response Function .....	25

---

2.8.2	Time-domain Dielectric Response.....	25
2.8.3	Frequency Domain Dielectric Response Measurement .....	28
2.9	Techniques Followed in HV Measurements .....	29
2.9.1	Schering Bridge for $\tan\delta$ Measurement .....	29
2.9.2	Transformer Ratio Arm Bridge.....	31
2.9.3	Relay-based C- $\tan\delta$ Bridge Circuit .....	32
2.9.4	DSP- based C- $\tan\delta$ Bridge Circuit .....	32
2.10	Modelling of Dielectric Response.....	33
2.10.1	Debye Dipolar Model.....	35
2.10.2	Cole-Cole Dipolar Model.....	35
2.10.3	Davidson-Cole Dipolar Model.....	36
2.10.4	Fuoss-Kirkwood Dipolar Model .....	36
2.10.5	Havriliak-Negami Dipolar Model .....	37
2.11	Some Commercial Diagnostic Instruments.....	37
2.11.1	Baur VLF Diagnostic System .....	37
2.11.2	sebaKMT Diagnostic System.....	37
2.11.3	Pax Diagnostics Instruments .....	37
2.11.4	Tettex Instruments.....	38
2.11.5	HV Diagnostic Instruments.....	38
2.11.6	Omicron Instruments.....	38
2.12	Summary of the Chapter .....	38
<b>Chapter 3</b>	<b>.....</b>	<b>40</b>
3.1	Diagnostic Study and Various Perspectives.....	40
3.2	Discharge Characterised Parameters.....	41
3.3	Standards in Partial Discharge Measurement.....	43
3.4	Modelling Techniques of PD Measurement .....	43
3.4.1	Conventional Three Capacitance Model.....	43
3.4.2	Pedersen's Model.....	45
3.4.3	Niemeyer's Model.....	45
3.4.4	Finite Element Analysis Based Model.....	46
3.4.5	Plasma Analysis Model.....	47
3.5	Partial Discharge Detection Techniques .....	48
3.5.1	Electrical Methods of PD Detection .....	48
3.5.2	Acoustic Methods of PD Detection.....	48
3.5.3	UHF Methods of PD Detection.....	49
3.5.4	Optical Methods of PD Detection .....	50
3.5.5	Chemical Methods of PD Detection .....	50
3.5.6	Hybrid Methods of PD Detection .....	50
3.6	Partial Discharge Analysis Techniques.....	50

---

---

3.6.1	Conventional Statistical Analysis .....	50
3.6.2	Phase-resolved Analysis .....	51
3.6.3	Pulse Sequence Analysis (PSA).....	51
3.6.4	$\Phi$ -q-n Analysis .....	51
3.7	Physical Parameters Affecting PD Activities.....	52
3.7.1	Initial Free Electrons Availability .....	52
3.7.2	Time Constant during a PD Process.....	53
3.7.3	Statistical Time Lag & Formative Time Lag .....	54
3.8	Importance of Filter Bandwidth Setting.....	55
3.9	Instruments for VLF PD Diagnosis.....	56
3.9.1	Omicron Group Commercial System.....	56
3.9.2	HV Diagnostics PD Test System .....	56
3.9.3	PD Test Equipment from Baur.....	56
3.9.4	PD Test Equipment from Megger .....	57
3.9.5	PD Test Equipment from b2HV.....	57
3.9.6	PD System from Power Diagnostix .....	57
3.10	Chapter Conclusion.....	58
<b>Chapter 4</b>	<b>.....</b>	<b>59</b>
4.1	Motivation of the Work.....	59
4.2	Experimental Setup of DDF Measurement .....	60
4.3	Descriptions of All Test Objects .....	62
4.4	Formulation of Dissipation Factor Measurement.....	63
4.5	DDF Measurement as a Function of Applied Voltage .....	65
4.6	Correlation and Differential Tan-Delta Assessment .....	69
4.7	Influence of Partial Discharge to the Dissipation factor .....	70
4.7.1	Relationship between Polarisation and Ionisation Loss .....	70
4.7.2	Test Arrangement for Investigating the Effects of PD.....	71
4.7.3	Partial Discharge Measurement Results.....	71
4.7.4	Dielectric Dissipation Factor Measurement Results .....	73
4.7.5	Interpretations of Measurement Results.....	74
4.8	Chapter Conclusion.....	75
<b>Chapter 5</b>	<b>.....</b>	<b>76</b>
5.1	Previous Relevant Work .....	76
5.2	Principle of Dielectric Modelling.....	77
5.2.1	Application of Extended Debye model for DDF Modelling.....	77
5.2.2	Application of Davidson-Cole Model for DDF Modelling.....	78
5.2.3	Application of Cole-Cole Model for DDF Modelling .....	79
5.2.4	Relation among Different DDF Modelling .....	79
5.2.5	Jonscher Power Law .....	80

---

---

5.2.6	Dielectric Dissipation Factor .....	80
5.3	Experimental Analysis .....	81
5.3.1	Measurement of Polarisation/Depolarisation Current .....	81
5.3.2	DDF Measurement Using Frequency Domain Spectroscopy .....	82
5.3.3	Practical Experimental Setup .....	83
5.4	Computation Process.....	84
5.4.1	Effects of Noise and Filtering .....	84
5.4.2	Elementary Parameters Estimation .....	85
5.4.3	Exponential Fitting.....	86
5.4.4	Debye Parameters Estimations.....	87
5.5	Modelling Results with C-C Model .....	89
5.6	Modelling Results with D-C Model.....	90
5.7	Field Aspects of Measurements .....	93
5.8	Chapter Conclusion.....	94
<b>Chapter 6</b>	<b>.....</b>	<b>95</b>
6.1	XLPE Polymer Geometry and Features .....	95
6.2	Descriptions of Ambient Condition Investigations .....	97
6.3	Frohlich's Analysis .....	98
6.4	Influence of Temperature on $\tan \delta$ Measurements .....	100
6.4.1	Two-Dimensional (2D) Visualisation of $\tan \delta$ Response.....	100
6.4.2	Three-Dimensional (3D) Visualisation of $\tan \delta$ Response.....	102
6.5	Activation Energy and Mean Relaxation Time.....	103
6.6	Influence of Temperature on Pol/depolarisation Current.....	105
6.7	Some Challenges in Frequency Response Measurement .....	107
6.7.1	Edge Effects .....	107
6.7.2	Effects of Termination .....	108
6.7.3	Effects of Voltage Change .....	109
6.8	Necessity of Guarding Arrangement.....	109
6.9	Chapter Conclusion.....	110
<b>Chapter 7</b>	<b>.....</b>	<b>112</b>
7.1	Motivation of Pol/Depolarisation Current Measurement.....	112
7.2	Dipoles Behaviours and Clustering Distribution .....	113
7.3	Descriptions of the Experiment.....	114
7.4	Daniel's Normalisation .....	115
7.5	Number of Polarisation Branches .....	116
7.6	$\tan \delta$ Measurement and Modelling.....	119
7.6.1	Relation between Debye and D-C $\tan \delta$ .....	119
7.6.2	Total $\tan \delta$ and Individual Branch $\tan \delta$ .....	120
7.7	Activation Energy Measurement.....	122

---

---

7.8	Stress Effects and Ambient Conditions.....	123
7.9	Recovery Voltage Response .....	125
7.9.1	Principle of Recovery Voltage Measurements.....	125
7.9.2	Analytical Expression of RVM Measurement .....	127
7.9.3	Computation Process of the RVM Response .....	129
7.10	Chapter Conclusion.....	133
<b>Chapter 8</b>	<b>.....</b>	<b>135</b>
8.1	Physical Process of Cavity or Void Discharge.....	135
8.1.1	Definition of Void or Cavity Discharge.....	135
8.1.2	Physical Mechanism of Discharge Occurrence.....	136
8.2	Motivation of Cavity Discharge Measurement .....	138
8.3	Experimental Descriptions of PD Measurement.....	139
8.3.1	Power Supply and PD measurement system.....	139
8.3.2	Description of Test Samples .....	140
8.3.3	Description of Measurement Procedures .....	141
8.4	Inception Voltage and Field Calculation.....	142
8.5	Phase-Resolved Study of Cavity Discharge.....	144
8.5.1	PRPD of Cylindrical Void Geometry .....	144
8.5.2	PRPD of Prism Void Geometry .....	145
8.5.3	PRPD of Block Void Geometry.....	145
8.5.4	PRPD of Rhombus Prism Void Geometry.....	146
8.6	PD Physical Model.....	146
8.6.1	Model Geometry and Field in 3D View.....	146
8.6.2	Cavity Discharge Occurrence .....	147
8.6.3	Local Cavity Condition During Discharge Process .....	149
8.6.4	Partial Discharge Magnitude Calculation .....	150
8.7	Simulation Process of Cavity Discharge.....	150
8.7.1	Initial Simulation Parameters.....	150
8.7.2	Simulation Flowchart of the Modelling .....	151
8.8	Field before and after a PD Event .....	152
8.9	Comparison between Measurement and Simulation.....	154
8.10	Comparison among Discharge Characteristics .....	156
8.11	Correlate with Real Application.....	158
8.12	Chapter Conclusion.....	159
<b>Chapter 9</b>	<b>.....</b>	<b>160</b>
9.1	Background Study of Surface Discharge .....	160
9.1.1	Motivation of the Work.....	160
9.1.2	Surface Discharge Physical Process.....	161
9.2	Surface Discharge (SD) Measurement.....	161

---

---

9.2.1	Phase Resolved Partial Discharge (PRPD) Study .....	162
9.2.2	Average Discharge Magnitude.....	163
9.2.3	Pulse Repetition Rate per Second (PRPS) .....	164
9.3	Surface Discharge (SD) Simulation Process .....	164
9.3.1	Two-Dimensional (2D) Model Geometry.....	165
9.3.2	Electric Field Distribution along the Surface .....	165
9.3.3	Simulated Discharge Sequence .....	168
9.3.4	Comparison between Measurement and Simulation .....	170
9.4	Chapter Conclusion.....	171
<b>Chapter 10</b>	<b>.....</b>	<b>172</b>
10.1	Motivation of Corona Discharge Measurement .....	172
10.2	Description of Experimental Setup .....	173
10.3	Experimental Measurement .....	174
10.3.1	Inception Field .....	174
10.3.2	Measurement Considerations of Corona Discharge.....	175
10.3.3	Characterised Parameters of Corona Discharge.....	175
10.3.4	Accumulated Charge Comparison between 50 Hz and 0.1 Hz .....	177
10.4	Influence of Excitation Waveform on Corona Discharge .....	178
10.4.1	Sinusoidal Waveform.....	178
10.4.2	Square Waveform .....	179
10.4.3	Sawtooth Waveform .....	181
10.4.4	Explanation of the Phase Distribution.....	182
10.5	Chapter Conclusion.....	183
<b>Chapter 11</b>	<b>.....</b>	<b>184</b>
11.1	Conclusions .....	184
11.2	Future Research Directions .....	187
<b>Appendix A</b>	<b>.....</b>	<b>189</b>
<b>Appendix B</b>	<b>.....</b>	<b>192</b>
<b>References</b>	<b>.....</b>	<b>194</b>



---

# List of Figures

<b>Figure 1.1.</b> Failure of power equipment due to insulation breakdown .....	1
<b>Figure 1.2.</b> Diagnostic testing in smart grid .....	6
<b>Figure 1.3.</b> Overall structure of the thesis .....	8
<b>Figure 2.1.</b> Overall challenge of tan-delta assessment .....	13
<b>Figure 2.2.</b> Generation of the damped oscillating waveform .....	16
<b>Figure 2.3.</b> Generation of the cos-rect waveform .....	18
<b>Figure 2.4.</b> Generation of VLF sinusoidal waveform .....	18
<b>Figure 2.5.</b> Sinusoidal (left) and cos-rect waveforms (right) .....	18
<b>Figure 2.6.</b> Equivalent circuit considering various losses in a dielectric .....	19
<b>Figure 2.7.</b> Schematic view of dipoles and their orientation .....	20
<b>Figure 2.8.</b> Classification of various polarisations .....	21
<b>Figure 2.9.</b> Physical process of polarisation at the molecular level .....	22
<b>Figure 2.10.</b> Physical process of polarisation .....	23
<b>Figure 2.11.</b> Basic DDF circuit of RCM method .....	27
<b>Figure 2.12.</b> Working principle of the RCM method .....	27
<b>Figure 2.13.</b> Schering bridge with different modifications .....	30
<b>Figure 2.14.</b> Two types of transformer ratio arm bridge .....	32
<b>Figure 2.15.</b> Relay-based $c - \tan\delta$ bridge circuit .....	32
<b>Figure 2.16.</b> DSP- based $c - \tan\delta$ bridge circuit .....	33
<b>Figure 2.17.</b> Building up and decaying of polarisation process .....	34
<b>Figure 2.18.</b> Measurement of tan-delta in Debye process .....	35
<b>Figure 2.19.</b> Differences among various commercial instruments .....	39
<b>Figure 3.1.</b> PD Process: (a) Cavity discharge (b) Surface discharge (c) Corona Discharge .....	40
<b>Figure 3.2.</b> Overview of the diagnostic study performed at very low frequency and power frequency ....	41
<b>Figure 3.3.</b> Measurement circuit in which test object is in parallel with the measuring unit .....	42
<b>Figure 3.4.</b> Measurement circuit in which test object is in series with the measuring unit .....	42
<b>Figure 3.5.</b> A schematic diagram of three capacitance model .....	44
<b>Figure 3.6.</b> Basic approaches followed in the modelling of PD measurement .....	48
<b>Figure 3.7.</b> Block diagram of an analogue PD detection system .....	49
<b>Figure 3.8.</b> Block diagram of a digital PD detection system .....	49
<b>Figure 3.9.</b> Graphical representation of various analysis techniques .....	52
<b>Figure 3.10.</b> Frequency spectrum of PD current pulses .....	55
<b>Figure 4.1.</b> Block diagram of DDF measurement circuit .....	60
<b>Figure 4.2.</b> Practical laboratory setup of measurements .....	61
<b>Figure 4.3.</b> Front Panel of waveform generator .....	62
<b>Figure 4.4.</b> Photo of all cable samples for dielectric response measurement .....	63
<b>Figure 4.5.</b> Equivalent model of cable insulation .....	64
<b>Figure 4.6.</b> DDF vs. excitation frequency of cable samples .....	65

<b>Figure 4.7.</b> Voltage dependency (in rms): (a) S-1 (b) S-3 .....	66
<b>Figure 4.8.</b> Equivalent circuit of dielectric and simplified form .....	67
<b>Figure 4.9.</b> Modified circuit for low capacitance test sample.....	68
<b>Figure 4.10.</b> Correlation of DDF between 50 Hz and 0.1 Hz Frequency .....	69
<b>Figure 4.11.</b> Comparison of DTD Values with Frequency .....	70
<b>Figure 4.12.</b> Front panel view of Baur setup .....	71
<b>Figure 4.13.</b> $\phi$ -q-n plot of partial discharge at 50 Hz and 0.1 Hz .....	72
<b>Figure 4.14.</b> Tan-delta measurement at 50 Hz and 0.1 Hz .....	73
<b>Figure 4.15.</b> Box plot of tan-delta values at 50 Hz and 0.1 Hz.....	74
<b>Figure 5.1.</b> Extended Debye circuit (left) and simplified equivalent circuit (right). .....	78
<b>Figure 5.2.</b> Difference between Debye and non-Debye models .....	80
<b>Figure 5.3.</b> Basic circuit for the PDC measurement .....	81
<b>Figure 5.4.</b> Basic circuit for FDS measurement .....	82
<b>Figure 5.5.</b> Practical setup for PDC experiments .....	83
<b>Figure 5.6.</b> Flowchart of working algorithm. *RMSE - root-mean-square error.....	84
<b>Figure 5.7.</b> Pre- and post-filter plot of depolarisation current .....	85
<b>Figure 5.8.</b> Conduction currents of various test samples.....	86
<b>Figure 5.9.</b> Exponential fitting of the measured depolarisation currents .....	87
<b>Figure 5.10.</b> Comparison of DDF values between the experimental and simulation result .....	89
<b>Figure 5.11.</b> Comparison between the experimental and simulation results based on D-C modelling .....	90
<b>Figure 5.12.</b> Influence of D-C and Jonscher (Jos) constant for S-1 .....	92
<b>Figure 5.13.</b> Influence of D-C and Jonscher (Jos) constant for S-P.....	92
<b>Figure 5.14.</b> Comparison of D-C model with other models .....	93
<b>Figure 6.1.</b> The cross-linking process of LDPE with DCP.....	96
<b>Figure 6.2.</b> Relaxation processes in semi-crystalline XLPE material;.....	97
<b>Figure 6.3.</b> Practical laboratory setup for the experiment.....	98
<b>Figure 6.4.</b> Comparison of experimental values with Frolich analysis.....	100
<b>Figure 6.5.</b> 2D view of $\tan \delta$ measurements at different temperatures.....	101
<b>Figure 6.6.</b> 3D view of $\tan \delta$ measurements .....	102
<b>Figure 6.7.</b> Linear fitting of different samples for determining the activation energy.....	104
<b>Figure 6.8.</b> Comparative analysis of dielectric response in the time-domain .....	105
<b>Figure 6.9.</b> Change of conductivity with the increasing temperature .....	106
<b>Figure 6.10.</b> Cross-section of the test sample to explore the impact of leakage current .....	107
<b>Figure 6.11.</b> Edging effects of short length cable section when exposed to 140 V (rms) voltage .....	108
<b>Figure 6.12.</b> Comparison of loss-factor with the guarding arrangement.....	109
<b>Figure 6.13.</b> Difference in tan-delta value at different voltage levels .....	110
<b>Figure 7.1.</b> Clustering model proposed by Dissado-Hill .....	113
<b>Figure 7.2.</b> Dielectric loss measurements of different samples .....	116
<b>Figure 7.3.</b> Fitting curves for various polarisation branches in S-1 .....	118
<b>Figure 7.4.</b> Fitting curves for various polarisation branches in S-3.....	118

<b>Figure 7.5.</b> Analogous circuit of each series branch.....	120
<b>Figure 7.6.</b> Influence of temperature on the resistivity of S-5 .....	122
<b>Figure 7.7.</b> Influence of temperature on the resistivity of S-7 .....	122
<b>Figure 7.8.</b> Activation energy of AC conduction process .....	123
<b>Figure 7.9.</b> Polarisation currents of PSet-1 for different stresses .....	123
<b>Figure 7.10.</b> Depolarisation currents of PSet-1 for different stresses .....	124
<b>Figure 7.11.</b> Influence of temperature on polarisation currents of S-7 .....	124
<b>Figure 7.12.</b> $I_{dep}(t)*t$ vs. $\ln(t)$ curves.....	125
<b>Figure 7.13.</b> RVM measurement and Debye equivalent model.....	126
<b>Figure 7.14.</b> Working principle of the RVM method .....	127
<b>Figure 7.15.</b> Flowchart of the working algorithm in the RVM simulation .....	129
<b>Figure 7.16.</b> Bode plots of the transfer functions for S-1 and S-3.....	131
<b>Figure 7.17.</b> RVM response of the test cable samples.....	132
<b>Figure 8.1.</b> Schematic diagram of a PD event (a) before PD (b) during PD (c) after PD.....	137
<b>Figure 8.2.</b> Physical process of cavity discharge with the impacts of space charges .....	138
<b>Figure 8.3.</b> Schematic diagram of the measurement circuit .....	140
<b>Figure 8.4.</b> Front view and cavity shapes of all test samples.....	141
<b>Figure 8.5.</b> The test-cell and top-view of test samples .....	142
<b>Figure 8.6.</b> PDIV values of all tested samples in the experiment.....	143
<b>Figure 8.7.</b> PRPD patterns of T-1 (a) at 50 Hz, and (b) at 0.1 Hz .....	144
<b>Figure 8.8.</b> PRPD patterns of T-2 (a) at 50 Hz, and (b) at 0.1 Hz .....	145
<b>Figure 8.9.</b> PRPD patterns of T-3 (a) at 50 Hz, and (b) at 0.1 Hz .....	145
<b>Figure 8.10.</b> PRPD patterns of T-4 (a) at 50 Hz, and (b) at 0.1 Hz .....	146
<b>Figure 8.11.</b> Electric field of all test specimens .....	148
<b>Figure 8.12.</b> Flowchart of the cavity discharge simulation.....	152
<b>Figure 8.13.</b> Field plot along the x-axis at 1.10 PDIV level.....	153
<b>Figure 8.14.</b> Field plot before a PD occurrence along the z-axis.....	153
<b>Figure 8.15.</b> Field plot after a PD occurrence along the z-axis .....	153
<b>Figure 8.16.</b> PRPD patterns of T-1 at 50 Hz (a) Measurement (b) Simulation .....	154
<b>Figure 8.17.</b> PRPD patterns of T-1 at 0.1 Hz (a) Measurement (b) Simulation .....	154
<b>Figure 8.18.</b> PRPD patterns of T-2 at 50 Hz (a) Measurement (b) Simulation .....	154
<b>Figure 8.19.</b> PRPD patterns of T-2 at 0.1 Hz (a) Measurement (b) Simulation .....	154
<b>Figure 8.20.</b> PRPD patterns of T-3 at 50 Hz (a) Measurement (b) Simulation .....	155
<b>Figure 8.21.</b> PRPD patterns of T-3 at 0.1 Hz (a) Measurement (b) Simulation .....	155
<b>Figure 8.22.</b> PRPD patterns of T-4 at 50 Hz (a) Measurement (b) Simulation .....	155
<b>Figure 8.23.</b> PRPD patterns of T-4 at 0.1 Hz (a) Measurement (b) Simulation .....	155
<b>Figure 8.24.</b> Measurement (M) and simulation (S) of maximum discharge ( $Q_{max}$ ).....	157
<b>Figure 8.25.</b> Measurement (M) and simulation (S) of average discharge ( $Q_{avg}$ ) .....	157
<b>Figure 8.26.</b> Measurement (M) and simulation (S) of pulse repetition per cycle (prpc) .....	157
<b>Figure 8.27.</b> Electric field distribution at 15 kV; (a) along L2 (b) along L1. ....	159

---

<b>Figure 9.1.</b> Surface discharge occurring in an IEC-B electrode arrangement .....	161
<b>Figure 9.2.</b> Block diagram of the surface discharge measurement circuit.....	162
<b>Figure 9.3.</b> VLF PRPD pattern at (a) $t = 1$ hr. (Left) (b) $t = 6$ hrs. (Right).....	162
<b>Figure 9.4.</b> PF PRPD pattern at (a) $t = 1$ hr. (Left) (b) $t = 6$ hrs. (Right).....	163
<b>Figure 9.5.</b> PRPD pattern at 8 kV voltage (a) 50 Hz (Left) (b) 0.1 Hz (Right) .....	163
<b>Figure 9.6.</b> Average discharge magnitude at VLF and 50 Hz .....	164
<b>Figure 9.7.</b> Pulse repetition rate per second at VLF and 50 Hz .....	164
<b>Figure 9.8.</b> The axis-symmetric two-dimensional view of the model .....	165
<b>Figure 9.9.</b> Simulation of electric field distribution at 50 Hz on the XLPE surface.....	166
<b>Figure 9.10.</b> Simulation of electric field distribution at 0.1 Hz on the XLPE surface .....	167
<b>Figure 9.11.</b> Field distribution along the insulation surface .....	168
<b>Figure 9.12.</b> Simulation of surface electric field at 50 Hz.....	169
<b>Figure 9.13.</b> Simulation of surface electric field at 0.1 Hz .....	169
<b>Figure 9.14.</b> Simulation results of surface discharge at 50 Hz and 0.1 Hz .....	170
<b>Figure 10.1.</b> Laboratory setup of the experiment .....	173
<b>Figure 10.2.</b> Corona discharge characterised parameters .....	176
<b>Figure 10.3.</b> Number of PD events vs. accumulated charge and charge within 10 pC interval.....	178
<b>Figure 10.4.</b> Sinusoidal excitation at 50 Hz: (a) at 1 hour (b) at 6 hour .....	179
<b>Figure 10.5.</b> Sinusoidal excitation at 0.1 Hz: (a) at 1 hour (b) at 6 hour. ....	179
<b>Figure 10.6.</b> Square excitation at 50 Hz: (a) at 1 hour (b) at 6 hour. ....	180
<b>Figure 10.7.</b> Square excitation at 0.1 Hz : (a) at 1 hour (b) at 6 hour.....	180
<b>Figure 10.8.</b> PRPD pattern of 50 Hz excitation: (a) at 1 hour (b) at 6 hour.....	181
<b>Figure 10.9.</b> PRPD pattern of 0.1 Hz excitation: (a) at 1 hour (b) at 6 hour.....	181
<b>Figure 10.10.</b> Phase range where PDs occurred for the three waveforms. ....	183

---

## List of Tables

<b>Table 2.1.</b> Comparative analysis of various voltage sources .....	16
<b>Table 2.2.</b> Brief descriptions of various standards for tan-delta measurement .....	17
<b>Table 2.3.</b> Comparative analysis of various polarisation processes .....	24
<b>Table 2.4.</b> Comparative analysis of various DDF measurement techniques .....	34
<b>Table 3.1.</b> Brief descriptions of various standards for PD measurement .....	43
<b>Table 3.2.</b> Differences among various PD models .....	47
<b>Table 3.3.</b> A comparison among various commercial products .....	57
<b>Table 4.1.</b> Descriptions of cable samples .....	63
<b>Table 4.2.</b> Parameters used in the DDF experiment .....	64
<b>Table 4.3.</b> Characterised parameters for PD .....	73
<b>Table 5.1.</b> Relation among different modelling parameters .....	79
<b>Table 5.2.</b> Elementary parameter estimations .....	86
<b>Table 5.3.</b> Debye parameters estimation for the DDF modelling .....	88
<b>Table 5.4.</b> Assessment Criteria of field aged XLPE cable .....	93
<b>Table 6.1.</b> Analysis of different cable samples .....	98
<b>Table 6.2.</b> Loss peak frequency and values of different samples .....	99
<b>Table 6.3.</b> $f_{max}$ and corresponding $\tan \delta$ values of different samples .....	103
<b>Table 6.4.</b> Activation energy and mean relaxation time .....	104
<b>Table 7.1.</b> Various polarisation processes. ....	114
<b>Table 7.2.</b> Description and analysis of cable samples .....	114
<b>Table 7.3.</b> Dielectric characteristic parameters of different samples .....	116
<b>Table 7.4.</b> Estimation of different performance functions .....	118
<b>Table 7.5.</b> Interpretation of different polarisation processes .....	119
<b>Table 7.6.</b> Relationship among analogous modelling parameters .....	120
<b>Table 7.7.</b> Modelling results of Debye and D-C models .....	121
<b>Table 7.8.</b> Calculated coefficients of the transfer function for S-1 and S-3 .....	131
<b>Table 8.1.</b> Description of all test samples .....	141
<b>Table 8.2.</b> Descriptions of global parameters used in the simulation .....	150
<b>Table 9.1.</b> Descriptions of global parameters used in the simulation .....	166
<b>Table 9.2.</b> Measurement results of all tested samples .....	170
<b>Table 9.3.</b> Simulation results of all tested samples .....	171
<b>Table 10.1.</b> Parameters used in experiment .....	175
<b>Table 10.2.</b> Characterisation under sinusoidal waveform .....	179
<b>Table 10.3.</b> PD characterisation under square waveform .....	180
<b>Table 10.4.</b> PD characterisation under sawtooth waveform .....	182

---

## List of Abbreviations

C-C	Cole-Cole model
Cos-rect	Cosine-rectangular
D-C	Davidson-Cole model
DR	Dielectric response
DS	Dielectric spectroscopy
DDF or DF	Dielectric dissipation factor
DAC	Damped alternating current
DSP	Digital signal processing
FEA	Finite element analysis
F-K	Fuoss-Kirkwood model
FEM	Finite element method
FDS	Frequency domain spectroscopy
FRA	Frequency response analysis
HV	High voltage
H-N	Havriliak-Negami
OWT	Oscillating wave technology
MMF	Magneto-motive force
NHC	Negative half-cycle
PD	Partial discharge
PHC	Positive half-cycle
PDC	Polarisation and depolarisation current
PDIV	Partial discharge inception voltage
PDEV	Partial discharge extinction voltage
PF	Power frequency
RVM	Recovery voltage measurement
RWT	Resonant wave technology
RCM	Recovery charge method
SD	Surface discharge
TDR	Time-domain reflectometry
VLf	Very low frequency
XLPE	Cross-linked polyethylene

---

# Nomenclatures

$\tan\delta$	Dielectric dissipation factor or tan-delta/loss-factor
$p$	Dipole moment
$Q$	Product of charge
$E(t)$	Electric field
$J(t)$	Total current density implicates the
$\tau_i$	Time constant of polarisation process
$\sigma_0$	DC conductivity
$D(t)$	Displacement current
$\varepsilon_0$	Permittivity of vacuum
$\omega$	Applied voltage angular frequency
$\varphi(t)$	Dielectric response function
$N$	Total number of recorded pulses
$\Phi$	Phase of PD occurrence
$I_R$	Leakage current,
$I_C$	Capacitive current
$\delta$	loss angle
$\Delta\omega_w$	Wide-band of PD detector
$\tau_{mat}$	Material time constant
$\tau_{sur}$	Surface time constant
$\tau_{decay}$	Effective charge decay time constant
$Q_{max}$	Maximum discharge
$Q_{avg}$	Average discharge
$C_{eq}$	Lumped capacitance
$\varepsilon'$	Real permittivity
$\varepsilon''$	Imaginary permittivity

---

# Chapter 1.

## Introduction

### 1.1 Problem Statement and Background

For any sustainable electricity infrastructure (e.g. power cables, transformers etc.), reliable functioning is of paramount importance to power utilities and the society as a whole [1]–[3]. In particular, their insulation system plays a critical role in that it must be able to withstand ongoing operating stresses imposed by the electrical network [3]–[5]. Ideally, all dielectrics or insulating materials are perfect and lossless. However, long-term operation will cause ageing, change the physical microstructure or the contents of insulation material and introduce various dielectric losses [5]–[7]. Besides, mechanical and thermal stresses accelerate different chemical processes, alter the chemical composition, and gradually degrade the overall dielectric properties [4], [8]–[10]. To sum up, the deterioration of insulation condition over the operating life is unavoidable and in fact, it is a major concern for the safe and reliable operation of power systems [7], [11]–[13]. In the worst case, the breakdown of electrical insulation in any HV components can lead to catastrophic failure of the whole equipment [9], [10], [14]. Figure 1.1 depicts the percentage of power apparatus for which insulation breakdown plays a major role in the complete failure.

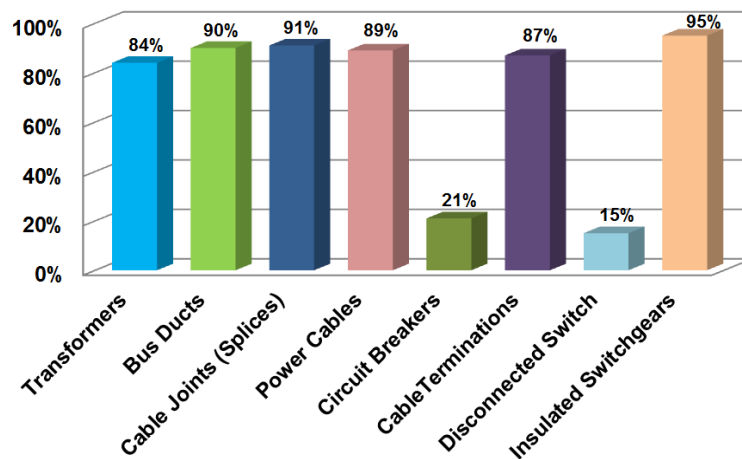


**Figure 1.1.** Failure of power equipment due to insulation breakdown [15], [16]



---

Moreover, the repairs or replacements are often costly and cause large disruption to the supply network, loss of business, and inconvenience to consumers. Therefore, the continuous condition monitoring of electrical insulation or performing diagnostic testing at regular intervals is highly desirable as it can provide critical information about the insulation condition; thus, reducing the risks of unwanted power interruptions and lengthy outage times [1], [17]–[20]. Testing should be done at a voltage level comparable to that when in normal operation to emulate the practical situation [17], [21]–[23]. Conducting any high voltage (HV) testing requires a suitable excitation source, if possible from separate power supplies [22], [24], [25].

Power cables are used in transmission or distribution networks. The polymeric material cross-linked polyethylene (XLPE) is the preferred choice for insulation in extruded MV and HV cables. Cable failures due to ageing and various i-field stresses (electrical, mechanical and thermal stresses) may lead to serious economic strain and consumer dissatisfactions. Power utilities are constantly challenged by the questions of whether to refurbish, repair or completely replace their assets. For obvious reasons, condition assessment of insulation material needs to be performed regularly and reliable diagnostics are critical for cable maintenance [9], [26]–[28]. The simple withstand (go/no-go) test has been widely used but it lacks the ability to provide any diagnostic assessment [10], [29]. However, recent advancements in technology ease the way for online/off-line ‘health condition’ monitoring and help the understanding of how the insulation deteriorates.

As a regular practice, off-line field testing by energising the cable insulation with a high voltage supply is performed to emulate the normal operating condition. This excitation mode can be either DC or AC. In the mid-1980s, DC testing was found unsuitable for testing polymeric insulated cables. The reason is that it can introduce space charge to the cable insulation and cause breakdown when the cable is later put back in service under normal AC stress [8], [30]. This necessitates development of alternative test methods [24], [30].

As an old-fashioned testing system, AC power frequency (50/60 Hz) hi-pot could be an alternative. However, performing on-site or off-line testing of high capacitance loads such as power cables and transformers at 50 Hz requires large reactive power from the test supply. Because of the physically large and bulky size, it is difficult to transport the test system for field testing [24], [31]–[34]. AC resonant wave technology (RWT) with a variable reactor for tuning provides an alternative solution and, when at resonance with test object capacitance, reduces the required power. However, such systems are costly, and their large size/weight makes it difficult to transport to site. Another test system, oscillating wave technology (OWT), generates a short duration attenuated ringing voltage at about 20-500 Hz; however, similar to DC hi-pot testing, it can impose injurious space charge in the polymeric insulation.

---

As an alternative, diagnostic testing with very low frequency excitation (VLF- 1 Hz or lower) was introduced to provide a practical and convenient solution [10], [30], [35], [36]. Since the capacitive reactance of the load (test object insulation) varies in inverse proportion to the test frequency, VLF testing significantly reduces the reactive power required from the supply. Moreover, the advantages of lightweight and easier transportation make this testing system more suitable for field testing. VLF diagnostic testing has come into more attention in recent years [37]–[39].

For condition assessment of HV equipment insulation, dielectric response (DR) and partial discharge (PD) measurements are among the most effective techniques [9], [27], [40]. When a dielectric material is subjected to an applied electric field, the dipoles originating from its primary and side groups movement result in different polarisation processes, which are collectively known as the dielectric response (DR). On the other hand, partial discharge refers to a localised electrical breakdown [41]. In the context of DR and PD measurements, the diagnosis under normal power frequency (50/60 Hz) test voltage has been well explored and documented. However, to date, research findings related to variable frequency excitations are limited [31]–[33], [42]–[45]. The application of VLF excitation has considerably challenged the way and methodology of existing interpretation techniques regarding DR and PD measurements usually found at power frequency [42], [43], [46]. In other words, the diagnostic results at VLF may or may not be comparable with those obtained at the power frequency. Therefore, new methods of data analysis and interpretation are required for the insulation condition assessment over the VLF test voltage range [42]–[48]. This will require performing an in-depth study (experimental, modelling, simulations) at VLF and relating to results at power frequency excitation. This is the main motivation of this research.

## **1.2 Diagnostic Methods for Condition Assessment**

### **1.2.1 Motivation of Dielectric Response Measurement**

Polymeric insulation such as XLPE has an interconnected network of main chains, in which numerous secondary branches are attached. When the material is subjected to an external electrical or thermal field, the dipoles get excited and react in certain ways, hence the term is dielectric response (DR). The dielectric response is mainly contributed by the conduction and polarisation processes of dipolar molecules. The diagnostic information regarding the whole insulation quality can be interpreted by applying a high voltage excitation [4], [49], [50]. For DR measurement, several methods are available either in the time domain or frequency domain. For example, dielectric spectroscopy (DS), frequency response analysis (FRA) and recovery

---

voltage measurement (RVM) have been widely employed in practice to obtain the dielectric response and detect early-stage insulation deterioration [40], [51].

The DS method has a potential to be adopted in the time domain, known as the polarisation and depolarisation current (PDC) method, and in the frequency domain, known as the frequency domain spectroscopy (FDS) method [51]–[53]. In principle, the FDS method operates by sweeping an AC voltage and measuring the corresponding response over a range of frequencies. Generally, a sinusoidal excitation is applied and the phase shift between the applied voltage and the generated current is measured to determine the loss factor. The dielectric dissipation factor (DDF) or tan-delta/loss-factor ( $\tan\delta$ ) measurement is widely used to evaluate the bulk insulation condition [5], [25], [49], [50].

The PDC method monitors the slow polarising effect of a dielectric material in the time domain. In this approach, an electric field is applied for a sufficiently long period to stimulate the charging/polarisation process. After that, the test object is short-circuited, and the resultant response current due to different polarisation processes is measured, known as the depolarisation current. It decays more or less exponentially with time. Diagnosing insulation with the PDC method takes a short time [40], [51], [54]. In general, a higher percentage change of PDC curve reflects the severity of the ageing process and determines the global insulation condition [54].

For  $\tan \delta$  measurement, the traditional way is to excite the test specimen with a sinusoidal voltage of power frequency (50/60 Hz). A high loss factor is indicative of insulation degradation. Nowadays, the advantages of VLF test supply inspires researchers and field engineers to use VLF excitation in the dielectric response measurement, especially for dissipation factor measurement [24], [55].

Previous DR studies [17]–[20] investigate the ageing and deterioration of insulation in transformers and rotating machines. Experimental results obtained from the time domain [40], [51], [54] and frequency domain [51]–[53] measurements provide comprehensive analysis regarding degradation in power cables, transformers, and other high voltage insulation systems. The research in [54] presents the diagnostic testing of XLPE cable by using the PDC method and highlights that ageing can accelerate the growth of water trees and the dielectric loss. Further along, measurement over a wide range of frequencies [53] or at a specific frequency such as VLF or 50 Hz [38] concludes that this loss is influenced by the physical polarisation process, and contributes to a higher DDF value at VLF than at power frequency. However, there is limited research conducted on the modelling of DDF measurement in the very low to power frequency range. Moreover, the simplistic R-C model of  $\tan\delta$  computation, i.e.  $\tan \delta = 1/(\omega RC)$ , is inadequate in answering why its value is not changing proportionally with the change of

---

frequency [38]. Also, the dipolar response under any AC excitation is not the same at each frequency [56]. Therefore, there is still a need to explain the dynamic properties of electrical insulation at different frequency excitations. Hence, the necessity of extensive experimental measurements and interpreting the test results, if possible by a circuit model, are important to help understand the dielectric behaviours.

To date, there is no concise documentation of diagnostic assessment, which provides a dielectric loss interpretation considering aspects such as physical characteristics, testing techniques and dipoles behaviours [1], [10], [56]. To the aim of interpreting dielectric behaviour under an AC excitation, this research provides a comprehensive study of dielectric response measurement and modelling over very low to power frequency range.

### **1.2.2 Motivation of Partial Discharge Measurement**

For condition assessment, partial discharge (PD) measurements have widely been used as an effective diagnostic tool for a long time [8], [10], [24], [57]–[59]. According to the IEC 60270 standard, partial discharge is defined as a short duration current pulse that momentarily bridges only part of the electrical insulation between two electrodes [41]. PDs are usually originated from the areas where the higher electric field is concentrated, such as the sharp points or protrusions of metal electrodes or the defects such as cavities, cracks, contaminations, joints, and deformed surfaces etc. [8]–[10], [14]. The presence of PDs in any HV component indicates a sign of defects and deteriorations in the insulation system. Continuous discharges at a localised site may eventually lead to complete breakdown of the whole insulation system [41], [58], [60]. Statistics show that 85% of power equipment failure at high and medium voltage levels is PD related [15].

PD activities usually take place at a defect site, where the local electric field exceeds the breakdown strength of the insulation material. PDs can be classified into three main categories: internal discharge, surface discharge, and corona discharge [8], [10], [58]. In general, an internal discharge is a streamer type discharge and mainly occurs due to voids (cavities) or defects within the solid insulation. On the other hand, surface discharge along an insulation surface could be initiated by a high tangential field around the wedge gap from the applied voltage. Finally, corona discharge in the gaseous medium is the results of the highly concentrated electric field due to the sharp points, edges, and terminations in the insulation system.

In principle, a PD event depends on the availability of free electrons and the presence of space charges, usually generated after a discharge process. The free electrons, which are responsible for triggering ionisation and the subsequent electron avalanche, can eventually lead to a complete short-duration current in the defect site [33], [34], [61], [62]. The space charge plays prominent roles as depending on the test voltage frequency, it can increase or decrease the

local electric field [21–25]. In other words, the PD process is influenced by the rising/falling time of the applied voltage and different time constants associated with the time-lag characteristics of the free charges (either electrons or ions) before or after a PD event. This dependency implies that PD activity is highly affected by the applied voltage frequency [21–28]. External factors such as environmental conditions (e.g. temperature, pressure moisture, humidity etc.), and excitation waveforms also have some impacts [24–28]. A PD event is associated with various physical processes (e.g. recombination, conduction and decay process of free electrons and space charges), and these physical processes play important roles on discharge characteristics under different frequency excitations. From the diagnostic point of view, this is another motivation of the research which includes in-depth experimental and modelling studies of various discharge sources (e.g. cavity, surface and corona) and their characteristics under very low (0.1 Hz) and power (50 Hz) frequency excitations.

### 1.3 Importance of Diagnostic Testing in the Smart Grid

Figure 1.2 illustrates the concept of smart monitoring of diagnostic testing in smart grids [12]. The traditional electricity grids are evolving into smart grids due to the use of complex control and communications technologies for implementing its operation and monitoring. Various energy sources (e.g. PV, wind) are now integrated to meet up maximum demand. HV apparatus (e.g. power cables, transformer, bushing) are critical components of the grids.

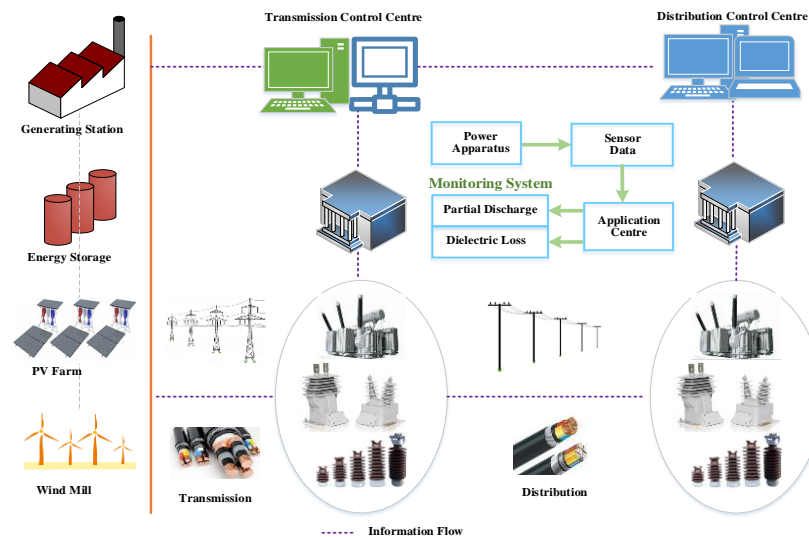


**Figure 1.2.** Diagnostic testing in smart grid

To avoid serious consequences due to insulation breakdown, online condition monitoring (such as PD and DR measurement) is a must which demands for developing various diagnostic tests to be conducted to provide time to time information regarding the insulation condition [1], [5]. This can be done from various control centres located either at distribution or transmission side (Figure 1.2). Moreover, as the smart grid uses advanced communications and control

---

platforms, information regarding the insulation status can easily be transferred to online real-time intelligent monitoring systems.

## 1.4 Thesis Objectives

In diagnostic testing, PD determines localised defect, while the bulk insulation condition can be obtained by DR measurement. The continual exposure of any electrical insulation to high voltage may result in dielectric loss and/or PD which is an earlier sign of insulation deterioration. HV testing with VLF excitation is a promising diagnostic tool [63]. Thus, it is necessary to characterise the DR and PD activities at this frequency range and compare with the power frequency [54], [64], [65].

To achieve these goals, in this research, extensive laboratory experiments are performed over the VLF to PF range to acquire measurement data for the diagnostic study and for the interpretation. Also, numerical simulations are employed to model various physical processes and their dependency on the applied voltage frequency, which is then verified by the experimental results. The key objectives of this thesis are summarised as follows.

- 1) Measure the dielectric loss factor for service-aged XLPE cables over the frequency range from very low (0.1 Hz) to power frequency (50 Hz) as a function of the applied voltage amplitude and explain why the loss-factor does not change linearly with the supply frequency.
- 2) Modelling of the dielectric dissipation factor as a function of applied voltage frequency through a circuit model and compare the simulated values with measurement results. It is also necessary to show the similarities and differences among the simulated results for various dipolar models (e.g. Debye Model, Cole-Cole Model and Davidson-Cole Model).
- 3) Investigate the influence of different polarisation/relaxation processes and the associated dielectric responses when XLPE cables are exposed to different thermal environments. Distribution of the loss factor as a function of test frequency, determination of the loss-peak frequency and effect on the conductivity due to temperature change are also considered.
- 4) Examine the characteristics of the polarisation and depolarisation currents if the insulation material is electrically or thermally excited, and from the test results, determine the number of polarisation processes, trapping effects, activation energy etc.
- 5) Measurement and modelling of partial discharge within a cavity bounded in a solid dielectric material under different conditions such as applied voltage amplitude, frequency and cavity geometry.
- 6) Measurement and modelling of partial discharge along the insulation surface at VLF (0.1 Hz) and power frequency (50 Hz) excitations and determine the key parameters which influence discharge characteristics by comparing the measurement and simulation results.

- 7) Study the influences of applied voltage amplitude and waveshape on corona discharges at VLF (0.1 Hz) and power frequency (50 Hz) excitations.

## 1.5 Original Contributions of the Thesis

In the context of diagnostic testing, it is essential to know how the global and local degradations in the insulation, via DR and PD measurements respectively, are dependent on the applied frequency. Despite advances in detection and analysis techniques, accurate insulation diagnosis at different frequencies is still a challenging and complex matter [9], [27], [28]. The main contributions of this thesis to address this issue are summarised in Figure 1.3 and elaborated as follows.

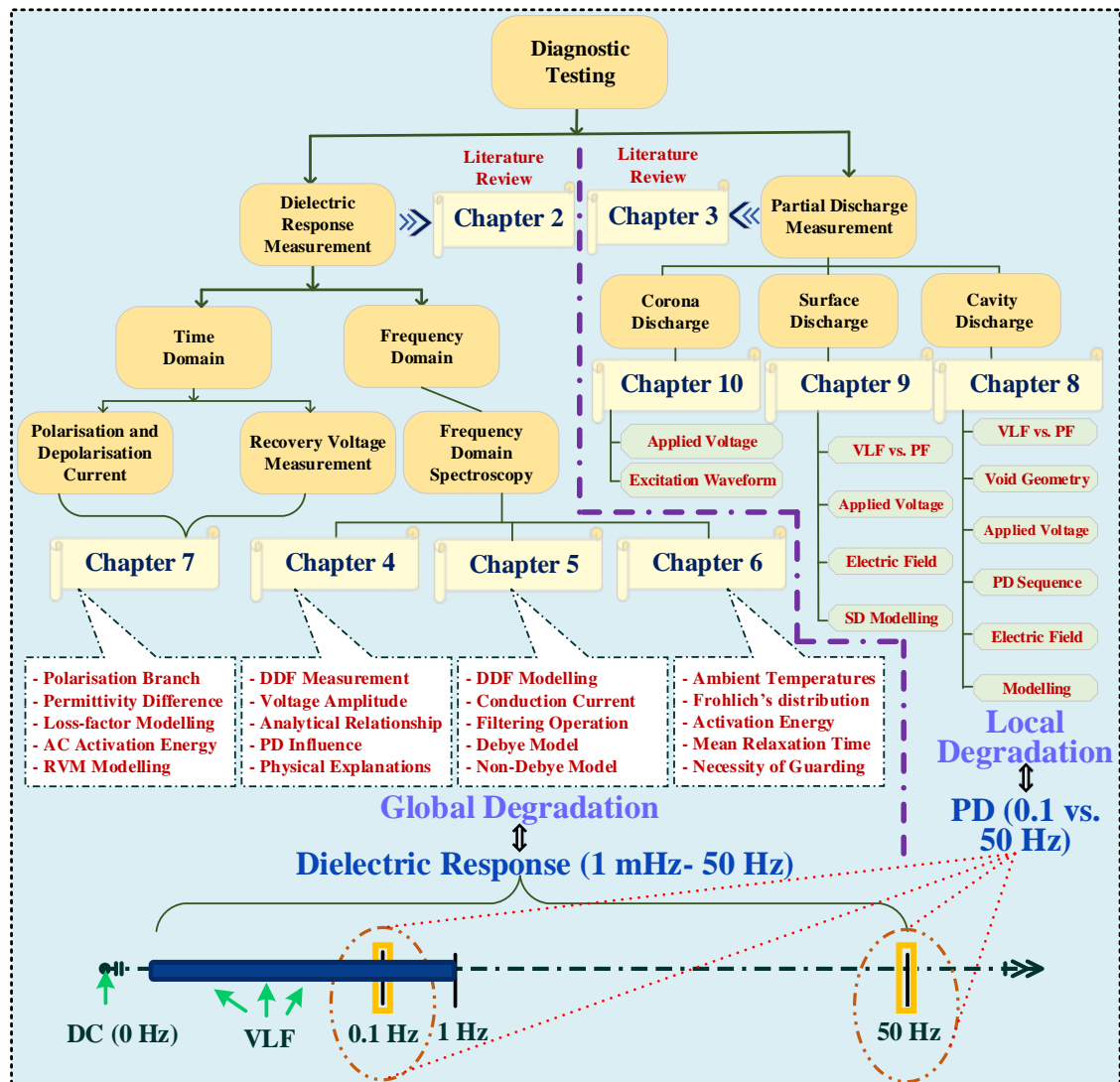


Figure 1.3. Overall structure of the thesis

- 1) Summarises some key aspects of dielectric dissipation factor measurement including challenges, key aspects, standards, dynamic properties of dipoles, various physical processes,



---

assessment techniques, and short descriptions of commercial instruments. Moreover, this thesis provides a general insight of partial discharge measurements, detections, modelling and analyses over the very low to higher frequency range. It also reviews various perspective views of PD diagnostic testing such characteristic parameters, measurement standards, detection techniques, commercial systems including their comparative performance, similarities and differences. This contribution has been reported - articles [2], [8], [9] in the List of Publications.

- 2) The dielectric dissipation factor of serviced-aged XLPE cables from 0.1 Hz to 50 Hz excitation frequencies was measured for various applied voltage amplitudes. An analytical relationship was also developed to estimate the loss factor for low capacitance test specimens (in the pF range). The reasons for higher dissipation factor at the lower frequency were explained by consideration of polarisation and conduction processes. The work has been published - articles [13], [16] in the List of Publications.
- 3) The modelling of the dielectric dissipation factor was performed using various dipolar theories such as Davidson-Cole (D-C) model, Cole-Cole (C-C) model, Debye model and Jonscher conduction law to describe the behaviours of dipoles under AC voltage frequencies. The D-C model-based numerical simulation shows reasonable agreement with experimental results for a wide range of excitation frequencies (1 mHz to 50 Hz). The work has been published - articles [1], [14] in the List of Publications.
- 4) The dielectric dissipation factor of XLPE cables was measured for various ambient temperature conditions and it was found that due to  $\alpha$  and  $\beta$  relaxations, the local loss-peak frequency tends to move to higher frequency zone. From the trends of shifting, the mean activation energy of dipoles and relaxation time were estimated using Arrhenius expression. The study also shows that at room temperature, the dipolar behaviour of XLPE insulation follows Frohlich's distribution and with the transition of temperature, the increasing mobility of the charge carriers results in higher DC conductivity. The influence of cable termination, the impact of voltage amplitude and the necessity of guarding are also explained. The work has been disseminated - article [3] in the List of Publications.
- 5) Based on the polarisation/depolarisation current method, the permittivity difference under DC and high frequency excitation is calculated using Daniel Normalisation. Also, by applying the clustering theorem and various statistical performance functions, the total number of polarisation processes occurring in a dielectric is evaluated, and from there, the basis of recovery voltage measurement is proposed. Moreover, the relationship between the loss factor in the Debye model and D-C model is established. The variation of the activation energy as a function of applied frequency, the influence of electrical stress and ambient conditions on



---

polarisation/depolarisation currents and subsequent trapping effects are also given. The work has been reported - articles [4], [5] in the List of Publications.

- 6) Partial discharge characteristics are investigated for various cavity geometries (cylindrical, block, prism etc.) and voltage amplitudes under VLF and PF excitations. The trends and behaviours are then discussed and explained in terms of physical processes. Finite element analysis (FEA) based numerical simulations are also developed to incorporate with the experimental results. The model accounts for some adjustable parameters such as the charge decay time constant, electron generation rate and void conductivity to simulate the physical processes. The work has been reported - articles [6], [11], [18] in the List of Publications.
- 7) The behaviours of surface partial discharges for XLPE at different applied frequencies are also investigated. The electric field distribution before and after a PD event and its effects on subsequent discharges are evaluated by numerical simulation using finite element method (FEM) software. The work has been published - articles [7], [12] in the List of Publications.
- 8) Corona discharge characteristics as a function of applied voltage amplitude and waveform under VLF and PF excitations are investigated. Measurement results show that the space charges generated after the discharges have a significant influence on the local electric field. As a result, the dependency of discharge characteristics to the supply frequency is not similar under the same stress conditions. The work has been published - articles [15], [17] in the List of Publications.

## 1.6 Thesis Outline

The dissertation comprises 11 chapters. It starts with an overview of the thesis in the Introduction chapter, including the background and motivation of the research, research objectives and research contributions.

Chapter 2 provides a comprehensive literature review of dielectric response measurement such as diagnostic challenges, principle of analysis, existing research trends, research methodologies, test techniques, standards, and so on. It identifies the novelty of the research area and the significance of the problem that needs to be addressed. It describes various physical processes such as dynamic properties of dipoles, polarisation and depolarisation mechanisms, dielectric loss, conduction current and test principles which have significant roles to the dielectric response.

Chapter 3 provides an in-depth literature review of diagnostic challenges related to partial discharge measurement, including discharge sources, physical mechanisms, characterising parameters, modelling techniques, detection systems. Moreover, it includes detailed descriptions

---

of modelling the partial discharge, physical parameters that affect the discharge activities, and various analysis methods to describe PD events.

Chapter 4 describes the measurement of dielectric dissipation factor as a function of applied voltage and provides detailed explanations of physical phenomena associated with the dielectric response. Moreover, the influence of partial discharge on the loss factor at VLF and PF excitation is discussed.

Chapter 5 presents the modelling of dielectric dissipation factor measurement over the very low frequency (1 mHz) to power frequency (50 Hz) range using the Debye model, Cole-Cole model, Davidson-Cole model. The main steps of modelling include filtering of the pol/depolarisation current, exponential fitting, DC conductivity and primary capacitance measurement, Debye parameter estimation etc.

Chapter 6 starts with reviewing the molecular structure of XLPE and various relaxation processes when it is thermally exposed. It shows that with increasing temperature, the loss peak frequency of XLPE moves to the higher frequency zone. Measurement of the mean relaxation time, activation energy, DC conductivity and the necessity of the guarding arrangement are also presented in this chapter.

Chapter 7 presents a detailed study of dielectric response measurement based on the polarization/depolarisation current method. This includes Daniel's normalisation for permittivity difference assessment, establishing the relationship between the loss factor in the Debye model and D-C model, the total number of polarisation process, trapping distribution etc.

Chapter 8 compares the measurement and simulation results to investigate the effects of cavity geometry, test voltage amplitude and frequency on partial discharge occurrence. This comparison identifies the critical parameters which affect the discharge characteristics and the resultant differences at different applied voltage frequencies.

Chapter 9 presents the measurement and simulation result of surface discharge at both VLF and PF. The electric field distributions before, after and during a PD event are also discussed in detail.

Chapter 10 shows the experimental studies of corona discharge under various stress conditions of applied frequency, excitation voltage amplitude and waveform. It highlights the limitations of previous studies and identifies some research gaps. Measurement results at VLF and PF test voltage and their differences due to space charges are also explained in this chapter.

Finally, the conclusion of the research is reported in Chapter 11, summarising the key findings. It also identifies possible directions to extend this work for future research.

---

## Chapter 2.

# Literature Review: Dielectric Response Measurement and Diagnostic Aspects

The regular monitoring and assessment of electrical insulation has paramount importance in power systems. One of the potential tools for insulation diagnosis is the dielectric response measurement. Tan-delta ( $\tan\delta$ ) or loss-factor measurement is a well-known approach to quantify dielectric response. This chapter elucidates a comprehensive review of  $\tan\delta$  measurement. Firstly, a detailed review and explanation of multiple challenges associated with dielectric loss measurement are presented. Various types of dielectric loss, their contribution to tan-delta, measurement techniques, and their comparisons are also discussed. The chapter further reviews the analogy of different physical dipolar theories and modelling. Lastly, a brief survey of commercially available measurement instruments is provided. The work in this chapter has been published in [2] as shown in the List of Publications.

## 2.1 Challenges of Dielectric Loss Assessment

The main challenges regarding the tan-delta assessment of electrical insulation are illustrated in Figure 2.1. These can be summarised as four broad categories: transportation, testing or measurement, processing the results, standards and others [1], [38], [54], [56], [66].

### 2.1.1 Transportation Challenges

One of the main challenges in field testing is the weight and size of the measurement device [67], [68]. Often, it is bulky in size, which offers less flexibility in transportation. For obvious reasons, desirable features for the end users include being light-weight and compact in design so to reduce the cost in transport, handling and storage of the test equipment.

### 2.1.2 Various Aspects of Measurement Challenges

The main challenge in tan-delta assessment is the dielectric loss testing or measurement. The measurement step includes:

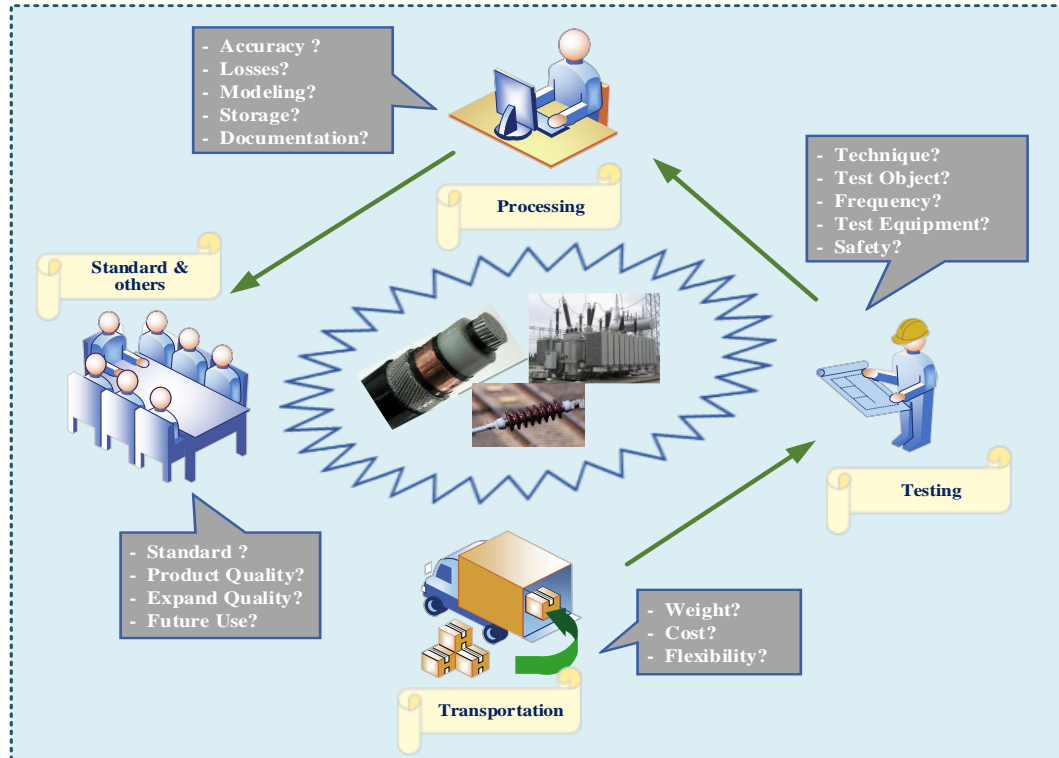


**Figure 2.1.** Overall challenge of tan-delta assessment

**Multi-functional:** The term multi-functional comprises measurement techniques, test objects, test duration and the excitation level at which the measurement can be carried out. Moreover, the testing can be performed at various stages of the insulation such as before installation, during operation or after the occurrence of any fault [29], [40], [51], [67], [68]. The measurement can be applied to different assets such as power cable, power transformer, current transformer, voltage transformer, circuit breaker etc. Different parts of the test objects including insulation, core, winding, and bushing are also required to be considered in the testing.

**Test Frequency:** Testing at different frequencies provides more detailed diagnostic information about the insulation quality of a test object. As an AC excitation, the most common choices are testing at power frequency, very-low-frequency (VLF) and damped AC excitation (DAC) [35], [37]. The measurement can be performed by using different waveforms such as sinusoidal, cosine-rectangular and bipolar pulse. A variable test frequency facilitates the development of standard and diagnostic behaviour of any insulation.

**Safety:** Before starting any HV measurement, safety needs to be taken into account [68]–[70]. The procedures include checking the grounding connection, detecting overload, controlling emergency trip button, discharging the circuit, isolating the multiple outputs, employing safety switches, key lock and grounding box.

**Test Equipment:** Various test equipment provide different measuring techniques and excitation frequencies. Based on the power supply, test object capacitance and portability, the method of

---

employing any HV measuring instrument for dielectric loss can vary from material to material [51], [56]. After measurements, having post-processing availability of results from the instrument calls for another requirement. Delivering reliable and repeatable results from the measuring system is also important. Therefore, selecting the right measuring device is one of the challenges in dielectric loss measurement [71].

### 2.1.3 Challenges Related to the Processing

After the measurement, some following steps are required to analyse and post-process the experimental results.

**Accuracy:** After accomplishment of any measurement, the accuracy of the output results is the primary concern. The accuracy can be determined by a well-recognised equivalent circuit diagram, which is embedded with some mathematical algorithm [71], [72]. The measurement systems should be capable of showing all circuit parameters through software operation. Afterwards, the accuracy can be calculated based on measured parameters, variable load values and other operating conditions.

**Losses and Modelling:** Long-term operation of any HV apparatus can induce different dielectric losses, such as conduction, polarisation, or ionisation loss in dielectrics [38], [56]. The occurrence of losses and associated physical phenomena should also be investigated. For tan-delta modelling, it is a significant challenge to explain all the losses.

**Documentation:** User-friendly software for documentation is another basic requirement. The measuring device needs to be efficient at generating an automated report for post-processing and analysing the results [73]. Furthermore, the implemented software should customise the reports, complying with customer preferences.

### 2.1.4 Diagnostic Standards and Others

Apart from the requirement of high signal and measurement accuracy, the testing procedures and analysis of the experimental results should follow some IEEE or IEC standards to determine whether the test object is faulty or not [10], [29], [70]. The manufacturer should ensure the premium design and quality of their product, so that it can have a longer lifetime and accurately measure diagnostic properties in rough environments. The expandable ability includes carrying out further applications by adding additional hardware accessories, upgrading the software etc [8], [72].

## 2.2 Various AC High Voltage Testing

Considering technical and application aspects, several forms of insulation testing can explicitly be categorised to facilitate better guidelines. From the application point of view, three types of testing are conducted over the operating life of any high voltage insulation [29]:

- 
1. **Installation Test:** a field test which is usually conducted after the installation of a new component or equipment.
  2. **Acceptance Test:** a field test which is made after installation but before the equipment is connected online to perform the normal operation.
  3. **Maintenance Test:** a field test conducted during the operating life of a high voltage apparatus in service.

On the other hand, from the technical point of view, all these tests can be divided into five different categories:

1. **Diagnostic test:** It is usually performed during the operating life to extract the diagnostic features of any insulation system. The features can be used as a potential tool to assess the overall condition of the insulation and, in some cases, to locate a vulnerable and degraded region in the tested insulation [2].
2. **Non-monitored Withstand Test:** This type of test is deployed by an exciting voltage with predetermined magnitude for a specified period. The test object is regarded as a good insulator if it survives after the test [74].
3. **Monitored Withstand Test:** The only difference of this test from the non-monitored test is to observe the dielectric properties during the test period. Depending on the condition of the insulation, the test duration may be extended or curtailed [74].
4. **Offline Test:** For diagnostic analysis, an offline test is always a preferred one. Technically, this means disconnecting the test object from the servicing power supply and exciting the material with an external high voltage supply [38], [51].
5. **Online Test:** This implies the observation of diagnostic parameters when the test-object is connected in service and energised by the regular supply source of 50/60 Hz [22].

## 2.3 Different Voltage Sources and Suitability

From classical circuit theory, the capacitive reactance of any dielectric varies inversely proportional to the excitation frequency. Comparing with power frequency, VLF testing takes a longer time to charge up any capacitor during the first quarter of an AC cycle. Generally, VLF implies employing measurements at 1.0 Hz or lower; however, the choice of 0.1 Hz is widely adapted for VLF testing in practice. Advancements in power electronics enabled robust VLF hardware design, and VLF diagnostic testing is nowadays considered as a promising tool for regular monitoring of insulation systems.

Damped AC (DAC) voltage works on the principle of generating a natural frequency from the test specimen's capacitance. Following the sinusoidal excitation, the decay

characteristics of the damped oscillatory response can readily be used to interpret the dielectric loss and corresponding loss factor [35], [75]. The basic circuit to generate DAC excitation is shown in Figure 2.2. For DAC signal generation, the AC sinusoidal voltage is firstly rectified and then passed through an RLC circuit to generate the natural frequency. The frequency of DAC signal is precisely controlled by switching operations.

Table 2.1 provides a comparison of test voltage sources, including online and offline AC, VLF AC and DAC testing and lists their advantages, operation, suitability, application, additional requirement etc.

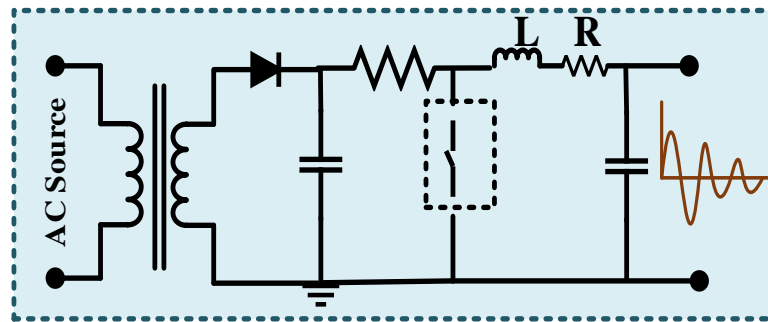


**Figure 2.2.** Generation of the damped oscillating waveform

**Table 2.1.** Comparative analysis of various voltage sources

Voltage Sources	Online AC	Offline AC	VLF AC	DAC
Testing Frequency [29], [35]	50/60 Hz	20-300 Hz	0.1 Hz or Lower	20 – 500 Hz
External Voltage Sources [76]	No	Yes	Yes	Yes
Similarity with the Operating Voltage Waveform	Yes	Yes	Yes	No
Integrate with other diagnostic testing [77]	No	Yes	Yes	Moderate
Test with Variable Voltage Level	Unsuitable	Suitable	Suitable	Moderate
Test Equipment Connectivity with System	Yes	No	No	No
Portability [35]	Unsuitable	Unsuitable	Suitable	Suitable
Size [37], [78]	-	Unsuitable	Suitable	Moderate
Defect Growth Rate [35], [78], [79]	Moderate	Moderate	Suitable	Moderate
Scale of Equipment [67], [76]	Unsuitable	Unsuitable	Suitable	Moderate
Soundness and Visibility [67], [80], [81]	Moderate	Moderate	Suitable	Unsuitable
Long Cable Test [5], [80]	Yes	Yes	Yes	No
Applicability to various failure modes [80], [82]	Moderate	Suitable	Moderate	Moderate
Similarity of results with power frequency [3], [38], [83]	Yes	Yes	No	No
Shorter Duration [35], [36], [78]	Moderate	Moderate	Unsuitable	Suitable
Additional capacitance for low capacitance sample [35], [38], [78]	No	No	Moderate	Yes

---

## 2.4 Standards in the Diagnostic Testing

Various standards are available for test specimens, test techniques, applied voltage, excitation frequency and grounding requirements. Most of the standards are provided by IEEE, IEC and ANSI/NETA etc. A summary of various standards for HV diagnostics is presented in Table 2.2. During any HV measurements, safety is always of the utmost importance and some relevant safety standards are also listed in Table 2.2.

**Table 2.2.** Brief descriptions of various standards for tan-delta measurement

Standard	Descriptions
IEC 60060 (1-3)	Various high voltage testing techniques, definitions, measuring systems and requirements for on-site tests [8]
IEC 60885 (1-3)	Various electrical testing methods (e.g. partial discharge measurement) for extruded power cables [8].
IEC 60270	High voltage testing technique for partial discharge: definitions, requirements and measurements [41]
IEC 61230	Power equipment grounding, earthing or short-circuiting
IEEE Std 4	Various standardised techniques for high voltage insulation testing [10]
IEEE Std 48	Testing procedures and fundamental requirements of AC cable terminations
IEEE Std 400	Guidelines of field testing and evaluating the insulation of AC shielded power cables [29]
IEEE Std 510	Safety recommendations for any high voltage testing [70]
IEEE Std 1617	Guidelines for detecting, mitigating and monitoring natural corrosion in medium-voltage underground cables
IEEE Std 433	AC insulation testing of rotating machines with high voltage excitation at very low frequency
IEEE Std 400.2	Guidelines of field testing and evaluating the insulation of AC shielded power cables using (VLF) [55]
IEEE Std 400.3	Guidelines of field testing for partial discharge testing in shielded power cable systems [68]
IEEE P400.4	Guidelines of field testing in shielded power cable systems using Damped Alternating Current Voltage (DAC)
ANSI/NETA	Standardised specifications for maintenance and acceptance test for electrical power equipment and systems
NFPA 70E	Standardised working procedures and requirements for electrical safety in the workplace [69]
ASTM D 150	Standardised testing techniques for measuring ac loss and permittivity of solid insulating materials

## 2.5 Test Voltage Waveforms

When considering the test voltage waveform, the two wave-shapes, sinusoidal and cosine-rectangular, are commonly adopted in industry [29], [68].

### 2.5.1 Cos-rectangular Waveform Excitation

In the early days, the generation of the cosine-rectangular (cos-rect) waveform was achieved by an arrangement of a DC source, a high-value capacitor, and an inductance controlled externally by a rotor switch [84], [85]. The extensive developments of power electronics nowadays replace this manually controlled switch by an automated thyristor, which results in a lighter, cheaper and more convenient test system. During polarity reversal of the waveform, the technology offers the recycling of power [85]. Furthermore, its resonance-based circuitry can reduce power consumption and increase load capacity at the output terminal.

It is intentional in the design that the polarity reversal of cos-rect takes a cosine in shape and contains a frequency close to 50 Hz. Because of the rectangular shape, it also possesses the



advantage of measuring the leakage current [85]. Figure 2.3 shows a block diagram for VLF cos-rect waveform generation.

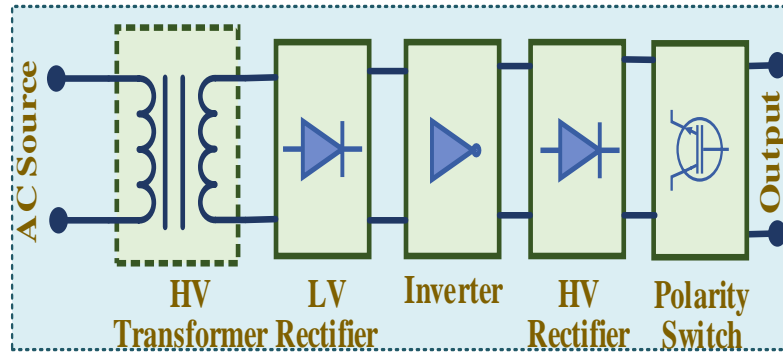


**Figure 2.3.** Generation of the cos-rect waveform

## 2.5.2 Sinusoidal Waveform Excitation

Similar to the cos-rect waveform, the evolution of modern power electronics assists considerably in realising a VLF power supply with higher testing capacity, lightweight and portability [24], [84]. The working principle is based on the AC-DC-AC converter, as illustrated in Figure 2.4.

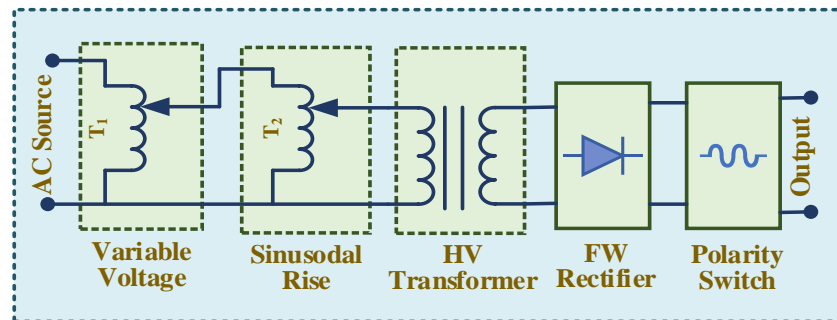


**Figure 2.4.** Generation of VLF sinusoidal waveform

The system cannot reuse the recycled energy stored in the capacitor which is dissipated as heat during discharging. Because of higher dissipation energy, the capacitive load in the sinusoidal system is comparatively lower than for the cos-rect waveform [84]. The difference between the cos-rect and sinusoidal waveform is illustrated in Figure 2.5.

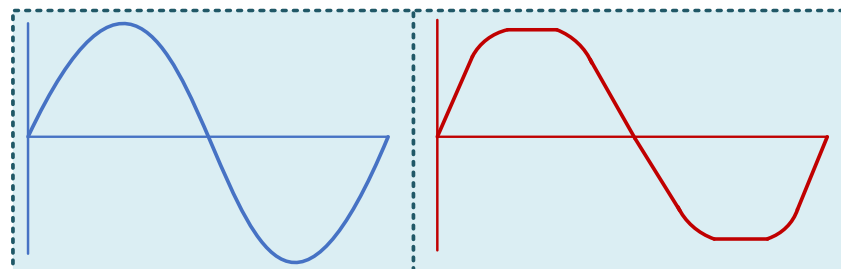


**Figure 2.5.** Sinusoidal (left) and cos-rect waveforms (right)

## 2.6 Losses in a Dielectric

Over-stressing of electrical insulation with an alternating voltage may damage the equipment [58], [71]. For this reason, diagnostic testing is essential to enable early detection of any incipient faults. Therefore, to facilitate a better understanding, it is worthwhile to interpret various types of losses which reflect the insulation quality. The dominant losses are represented by an equivalent circuit model of Figure 2.6.

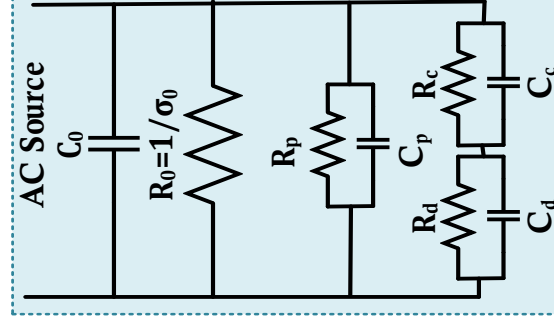


**Figure 2.6.** Equivalent circuit considering various losses in a dielectric

The rationale for this modelling is as follows:

- No insulator is perfect, all have an ohmic loss. This conduction loss is modelled by a resistor  $R_0$  in parallel with the prime capacitance  $C_0$  [10], [58].
- The orientation of dipoles and trapped charge at the boundary or irregular formation of material causes a polarisation loss. Apart from the conduction loss, the polarisation loss results in a displacement current. Therefore, this loss can be modelled by a parallel combination of resistance  $R_p$  and capacitor  $C_p$  and for illustration, only one such set is shown in Figure 4.8. More similar branches might be required to account for different polarisation phenomena in the dielectric [20], [58].
- After exceeding a certain inception voltage, the presence of voids or cracks inside a material ignites partial discharges. Due to a discharge, a short-duration conductive channel forms across the spark gap. After discharge compensating the voltage drop across the void gap, some charges are immediately transferred from the bulk insulation to the cavity [58], [77], [79]. This physical process can be modelled by a series arrangement of two parallel blocks. One block, formed by channel resistance  $R_d$  and void capacitance  $C_d$ , represents the discharging process while another block for the charging process consists of a resistance  $R_c$  and capacitance  $C_e$ .

The total dielectric loss is the sum of the effects of all three described loss mechanisms. Hence,

$$P_{tot} = P_{cond} + P_{pol} + P_{ion} \quad (2.1)$$

## 2.7 Dynamic Properties of Dipoles in a Dielectric

In recent years, the increase of commercially available test equipment and improvement in understanding of associated physical phenomena influence researchers and engineers to apply the polarisation-based technique in DDF measurements. This continuous rise of interest indeed facilitates interpreting the measurement in either the time or frequency domain [19], [20], [23], [54]. The dielectric phenomena observed under exposure to an electric field are described by the polarisability of the material and are well reported in the literature [56], [86], [87].

As soon as an external voltage is applied, the resultant electric field causes the excitation of various dipoles in the dielectric. Here, a dipole consists of a pair of equal and oppositely charged particles. A dipole can be characterised by its dipole moment, i.e. the product of charge ( $Q$ ) and separating distance ( $d$ ):

$$p = Q d \quad (2.2)$$

On the macroscopic scale, a schematic representation of various charges and their orientations is illustrated in Figure 2.7. Ignoring the permanent dipoles at macroscopic levels, the excited dipoles contribute to three types of polarisation. In general, these can be classified as electronic, atomic and orientation polarisation.

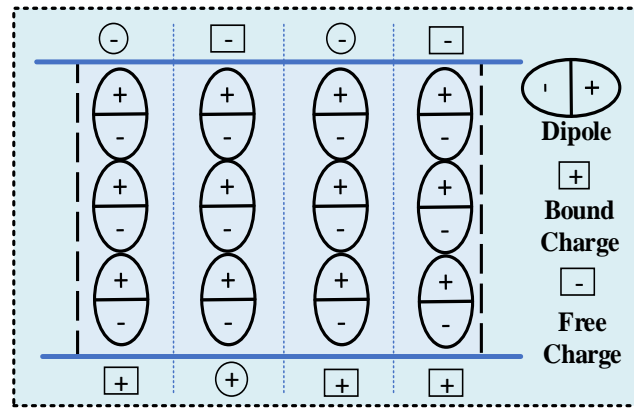


**Figure 2.7.** Schematic view of dipoles and their orientation

Moreover, based on the concentration of bulk insulation, their surface interaction, and the density of metal ions, the polarising material is subject to three main types of process. These are bulk insulation polarisation, interfacial polarisation and tunnelling polarisation [56], [86]–[89]. The classification is illustrated in Figure 2.8.

### 2.7.1 Electronic Polarisation Process

From classical physics, the nucleus of an atom electrically consists of positively charged protons and neutrally charged neutrons, while negative electrons revolve around the centre in fixed orbits. Under the actions of some external field, the electron cloud will be displaced and result in a dipole moment in the atom.

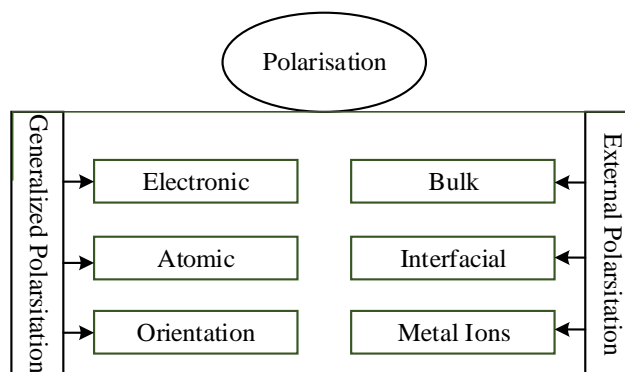


**Figure 2.8.** Classification of various polarisations

The distorted atom with respect to the nucleus is said to be electronically polarised and can be approximated by assuming that all the charged particles have a uniform distribution inside a spherical volume of constant radius. The magnitude of the induced moment varies proportionally with the field strength and is zero value in the absence of the field. This is because, after moving away the field, the charged clouds return to the previous equilibrium positions and the rest state is eventually restored. In short, the polarisation process is very likely to be spontaneous and fast [86], [90]–[92].

### 2.7.2 Ionic Polarisation Process

Considering frequency dependency, ionic polarisation is substantially analogous to electronic polarisation. In this process, after exposure to an electric field, two oppositely charged ions in a molecule or dielectric gain a relative displacement to each other and form an ionic dipole. Under the condition of an absent field, likewise, the observed restoring forces pull them back to the former equilibrium state. Meanwhile, the ionic displacement follows harmonic oscillations in the infrared region of the electromagnetic spectrum ( $10^{14}$  rad/s) [86], [91], [92].

### 2.7.3 Orientation Polarisation Process

The third significant contribution to polarisation is referred to as orientation polarisation. First of all, the physical process can be interpreted as to realise an ionic molecule having a slightly higher electro-positivity in one atom than in another. This molecular behaviour evidently contributes to the formation of permanent dipoles even in the absence of an applied electric field. Thus, the moment of the dipole can be described by the product of charge transferred from one atom to another and the inter-nuclei distance [91]–[93]. For a polyatomic molecule with different permanent moments from the several bonds, the resultant moment of the whole is obtained by the vector sum of the associated individual moments. A polarised molecule with symmetrical atomic arrangement results in a null moment. Conversely, because of the lack of permanent dipoles, the same null moment can be observed in molecules consisting

of similar atoms. By definition, the process of orientation polarisation is present if the application of a strong electric field stimulates all the dipoles in a molecule/dielectric to orient along the direction of the field. In summary, the frequency dependence of orientation polarisation from the engineering point of view is regarded as the dipolar relaxation in dielectrics [91], [93].

The string diagram depicted in Figure 2.9 provides a comparison to help understand various polarisation phenomena. Here, both positive and negative ions are represented by circles and contribute to a relative shifting of the associated electron cloud or nuclei with respect to their initial positions.

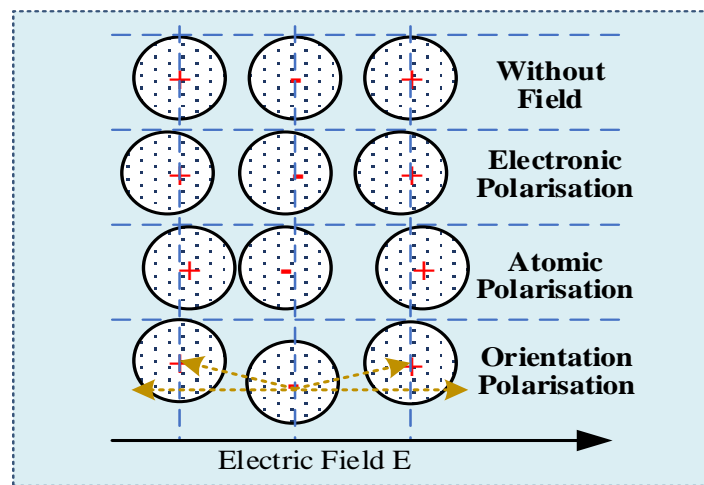


**Figure 2.9.** Physical process of polarisation at the molecular level

### 2.7.4 Interfacial Polarisation Process

Interfacial polarisation is effective in inhomogeneous dielectrics and mainly occurs when associated boundaries are composed of multi-dielectrics with different conductivities. In fact, this polarisation activity contributes to the anomaly in the low-frequency zone of the spectrum, typically dominant in the frequency range of 0.1 Hz-10 kHz, popularly known as Maxwell-Wagner effect [20], [94], [95]. The attributed fact may be due to the accumulation of space charges at the interfacial zone of boundaries. Instead of relying on the single material, the accumulated charge influences the dependency of the total conductivity and dielectric constant on the mixture of their properties [95].

### 2.7.5 Bulk Polarisation Process

Bulk polarisation is generally caused by hopping of charge carriers and implicitly occurs in amorphous and nonconductive insulating material. Based on the hopping mechanism, this polarisation process contributes significantly to the conduction current. The asymmetric geometrical arrangement and strong molecular randomness in bulk insulation play important

roles in yielding various localised sites [56], [96]. Readily traversable, these localised sites impede charge particles to conduct through the surrounding high potential walls. Therefore, hopping regions extend throughout the material and form an interconnected network that allows various intermediate energy levels in the forbidden gap. Easily accessible, these local levels enable electrons to jump from one trapping site to another. However, if the travelling distance between two consecutive sites is shorter, or the time spent at a localised site is longer than the time for the vibration frequency, then it is possible to observe the process of dipolar relaxation in the dielectrics [91].

### 2.7.6 Tunnelling Polarisation Process

The final form of polarisation, due to the tunnelling effect, can be attributed to the electrode/polymer interface. Even with little/no field, this effect can be realised as the tunnelling of charge carriers from the electrode's interface into unoccupied traps of lower energy. This is because voltage polarity reversal results in the inversion of space charges and thus causes travelling of delocalised charges across the channel [97]–[99].

Table 2.3 presents a comparative analysis of various polarisation phenomena. Figure 2.10 depicts the graphical representation of various polarisations and their contribution to the dielectric losses across multiple frequency zones. As can be observed, electronic, ionic, orientation and interfacial polarisations are significant at the visible, infrared, radio and lower frequency zones, respectively.

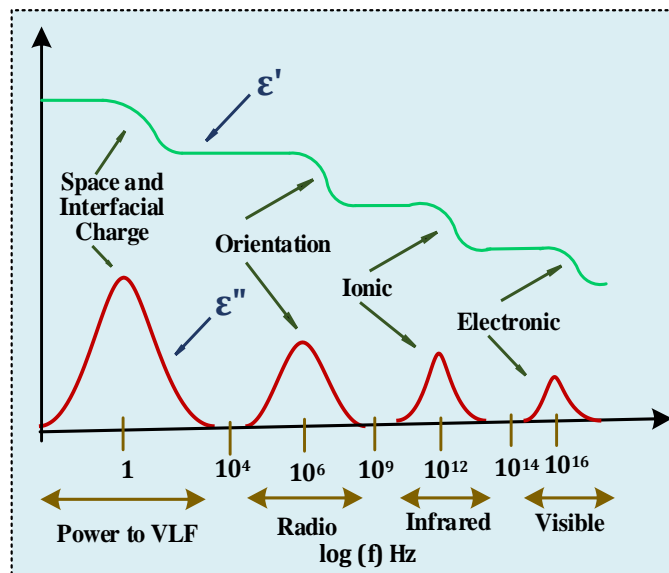


**Figure 2.10.** Physical process of polarisation

**Table 2.3.** Comparative analysis of various polarisation processes

<b>Type/Property</b>	<b>Electronic</b>	<b>Ionic</b>	<b>Orientation</b>	<b>Interfacial</b>	<b>Bulk</b>	<b>Tunnelling</b>
<b>Formation</b> [97]	Inside atom	Inside molecule	Inside lattice	Lattice boundary	Localised sites of lattice	Boundary to unoccupied traps
<b>Mechanism</b> [86], [92]	Relative shifting of electron clouds	Relative shifting of ions each to other	Orientation of permanent dipoles	Accumulation of space charge	Hopping of charges	Tunnelling of charges
<b>Main Reasons</b> [56]	Electric field	Electric field	Permanent dipole and field	Inhomogeneous dielectric and field	Irregular geometry and field	De-localised charge and field
<b>Temperature dependency</b> [56], [92]	Independent	Independent	Inversely proportional	Linearly proportional	Thermally activated	Independent
<b>Charge</b> [56]	Bound charge	Bound charge	Bound charge	Free Charge	Free Charge	Free Charge
<b>Null value</b> [86]	Absence of high frequency excitation	Singular atoms or molecules having similar atoms	Without permanent dipoles	Homogeneous material	Regular shape	Absence of traps
<b>Frequency range</b> [100], [101]	Optical region	Infrared region	Radio frequency region	0.1Hz-10 kHz	0.001Hz-100 kHz	Microwave zone
<b>Electrode dependency</b> [102]	Strongly dependent	Strongly dependent	Independent	Dependent	Independent	Strongly dependent

---

## 2.8 Various Aspects of Dielectric Response Measurement

As discussed earlier, DR technique can broadly be categorised as a time-domain measurement or a frequency-domain measurement. With this method, dielectric properties are not only determined at the service frequencies but also the loss factor or resistance is measured at non-service conditions (e.g. very-low-frequency) [40], [51], [103]. The applied excitation can be either a DC or a periodic form of variable frequency and depends extensively on the test period.

### 2.8.1 Analytical Expressions of Dielectric Response Function

Under the influence of an electric field  $E(t)$ , the total current density  $J(t)$  through a dielectric can be written as the sum of a conduction current and a displacement current  $D(t)$ .

$$J(t) = \sigma_0 E(t) + \frac{\partial D(t)}{\partial t} \quad (2.3)$$

where  $\sigma_0$  represents the DC conductivity of the material. Ignoring the current due to any internal discharge, the electric displacement produced by the electric field and the polarisation effect is shown as:

$$D(t) = \varepsilon_0 \varepsilon_\infty E(t) + \Delta P(t) \quad (2.4)$$

where  $\varepsilon_0$  and  $\varepsilon_\infty$  denote the permittivity of vacuum and the relative permittivity at power frequency respectively. The term  $\Delta P(t)$  implies slow polarisation and conveys crucial information about the dielectric response function  $\varphi(t)$ . This response function correlates with the field excitation and contains memory information; hence, determines the dielectric properties of the material [103]–[105].

$$\Delta P(t) = \varepsilon_0 \int_0^t \varphi(t - \tau) E(\tau) d\tau \quad (2.5)$$

Combining (2.3), (2.4) and (2.5), the final expression of dielectric current can be rewritten as

$$J(t) = \sigma_0 E(t) + \varepsilon_0 \varepsilon_\infty \frac{dE(t)}{dt} + \varepsilon_0 \frac{d}{dt} \int_0^t \varphi(t - \tau) E(\tau) d\tau \quad (2.6)$$

### 2.8.2 Time-domain Dielectric Response

Time domain measurement is performed by applying a DC or AC voltage at a fixed frequency [54], [104]–[106] and then measuring the response as a function of application time. The most popular methods are the polarisation/depolarisation current (PDC) measurement and recovery-voltage measurement (RVM) [20]. Additionally, based on the same principle, the



---

time-domain reflectometry (TDR) method is employed in various commercial systems to locate the cable faults in operation [107].

### 2.8.2.1 Polarisation/Depolarisation Current Method

The polarisation/depolarisation current (PDC) method has proven to be a useful tool for diagnosing the ageing of polymer or oil-paper insulated systems. Details of the circuit setup are described in Section 5.3.1. In the method, the dielectric material is excited by a DC voltage, and the resultant charging or polarisation current is measured. When the excitation is removed, a depolarisation current occurs and can be measured using a highly-sensitive electrometer [54], [80], [88].

For a geometrical capacitance  $C_0$  and field strength  $E(t)$  due to the external voltage  $U(t)$ , the current through a homogeneous dielectric can be written as follows

$$i(t) = C_0 \left[ \frac{\sigma_0}{\varepsilon_0} U(t) + \varepsilon_\infty \frac{dU(t)}{dt} + \frac{d}{dt} \int_0^t \varphi(t-\tau) U(\tau) d\tau \right] \quad (2.7)$$

For a constant DC supply of voltage  $U_0$ , the polarisation or charging current  $i_p(t)$  can be simplified as:

$$i_p(t) = C_0 U_0 \left[ \frac{\sigma_0}{\varepsilon_0} + \varepsilon_\infty \delta(t) + \varphi(t) \right] \quad (2.8)$$

Here,  $\varphi(t)$  denotes the response function. It is of interest to find the response function, especially its shape. The general form of the dielectric response can be obtained from various field experiences. For an oil/paper insulation system [3], [25]:

$$\varphi(t) = \frac{A}{\left(\frac{t}{T_0}\right)^x + \left(\frac{t}{T_0}\right)^y}; \quad 0 < x < y \text{ and } T_0 > 0 \quad (2.9)$$

and for a finite time constant  $\tau$ , the  $\varphi(t)$  of polymeric insulation system is [54]:

$$\varphi(t) = A e^{-\frac{t}{\tau}}; \quad (2.10)$$

After measuring the pol/depolarisation current, all the unknown parameters of the equations can be obtained mathematically using a nonlinear fitting process [108], [109].

### 2.8.2.2 Recovery Voltage Method (RVM)

Another time domain-based approach is the recovery voltage method (RVM). The measurement system was introduced by Boening in 1938 [8], [10]. Compared to the PDC method, the test object is subjected to a DC stress for a longer time. Instead of measuring the

PDC current, the analysis is based on measuring the return voltage. This is because, after removing the excitation, free charges from the polarised bounded charge are generated, which appears as a return voltage in the system [8], [10], [110]. Details of the measurement circuit are described in Section 7.9.1.

### 2.8.2.3 Recovery Charge Method (RCM)

Another technique based on the relaxation current is the recovery charge method (RCM), as represented by the schematic diagram in Figure 2.11. In principle, the circuit adopts a slight modification of the two systems mentioned before [10], [71]. It integrates the depolarisation current. A schematic diagram of the automatic switching operation and signalling is depicted in Figure 2.12. Like the other systems, the operating principles are self-explanatory.

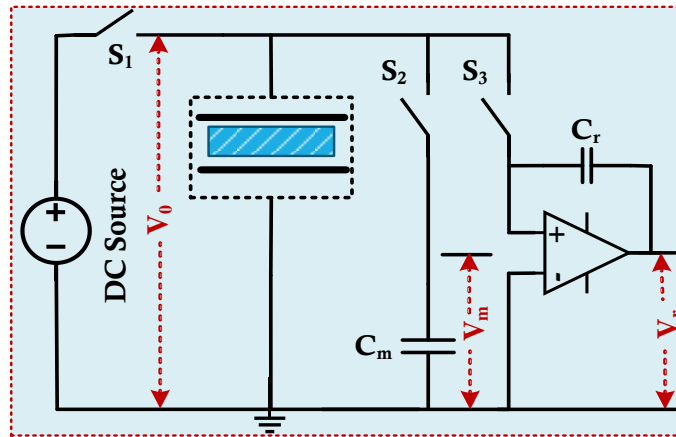


Figure 2.11. Basic DDF circuit of RCM method

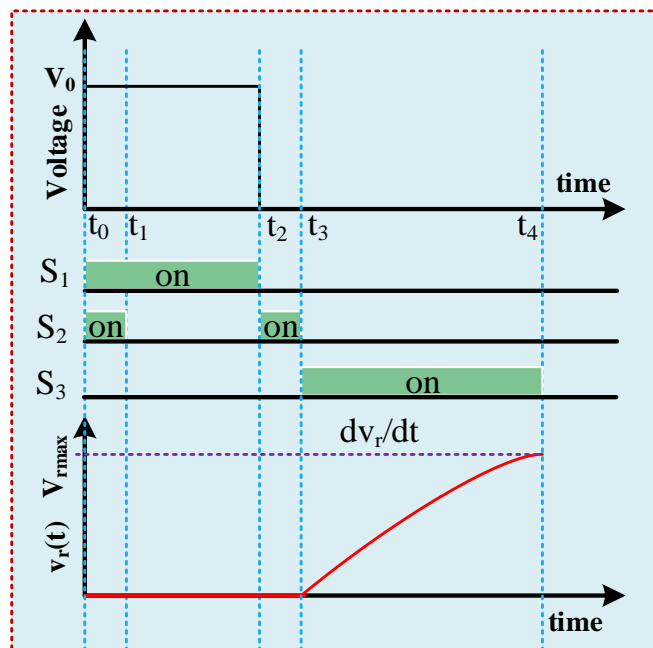


Figure 2.12. Working principle of the RCM method

---

The operation of RCM circuit is controlled by switch  $S_1$ ,  $S_2$  and  $S_3$ . When  $S_1$  is closed, a DC voltage  $V_0$  stresses the insulation and polarised bound charges are generated. The amount of charge is calculated using an integrator by closing switch  $S_3$ . For polymeric insulation, the RCM method always satisfies the condition  $C_m \geq C_0$ . Under this condition, the stored charge across the primary capacitor  $C_0$  of the test object is almost entirely transferred to the measuring capacitance  $C_m$  of known capacitance. Therefore, this primary capacitance can be written as:

$$C_0 \approx C_m \frac{V_m}{V_0} \quad (2.11)$$

Furthermore, the recovery charge  $q_r(t)$  can simply be obtained from the integrator output voltage  $v_r(t)$  and expressed as:

$$q_r(t) \approx C_r v_r(t) \quad (2.12)$$

### 2.8.3 Frequency Domain Dielectric Response Measurement

Frequency domain spectroscopy (FDS) is an approach to study the dielectric response of materials in the frequency domain. The detailed descriptions of the FDS method, including schematic diagram and operation principle, are discussed in Section 5.3.2. In this technique, the dielectric properties due to the physical process of polarisation are assessed and quantified over a wide range of frequencies [19], [20], [40]. The dielectric properties considered include several frequency-dependent parameters such as the electrical conductivity, capacitance, impedance, loss factor [25], [39], [51].

The relative complex permittivity and susceptibility ( $\chi$ ) of an isotropic and uniform material are given by:

$$\underline{\varepsilon}_r(j\omega) = \underline{\varepsilon}'_r(\omega) - j \underline{\varepsilon}''_r(\omega) \quad \text{and} \quad \underline{\chi}(j\omega) = \underline{\chi}'(\omega) - j \underline{\chi}''(\omega)$$

Here,  $\chi'$  and  $\chi''$  are the real and imaginary susceptibility. The current can be expressed as:

$$J(j\omega) = j\omega \varepsilon_0 \left[ 1 + \underline{\chi}'(\omega) - j \left( \underline{\chi}''(\omega) + \frac{\sigma_0}{\omega \varepsilon_0} \right) \right] E(\omega) \quad (2.13)$$

The complex permittivity  $\varepsilon(\omega)$  can be resolved as a real part:

$$\underline{\varepsilon}'(\omega) = \Re[\underline{\varepsilon}(\omega)] = 1 + \underline{\chi}'(\omega) \quad (2.14)$$

and an imaginary part ':

$$\underline{\varepsilon}''(\omega) = \Im[\underline{\varepsilon}(\omega)] = \underline{\chi}''(\omega) + \frac{\sigma_0}{\omega \varepsilon_0} \quad (2.15)$$

---

Therefore, the fundamental basis of dissipation factor measurement in the FDS method can be written as [58], [71]:

$$\tan \delta = \frac{\underline{\varepsilon}''(\omega)}{\underline{\varepsilon}'(\omega)} = \frac{\underline{\chi}''(\omega) + \frac{\sigma_0}{\omega \varepsilon_0}}{1 + \underline{\chi}'(\omega)} \quad (2.16)$$

## 2.9 Techniques Followed in HV Measurements

Various approaches for measuring dielectric properties in the field or non-field aspects are depicted in Figure 2.13 to Figure 2.16. Most of the procedures are based on general test principles and comply with various standards well reported in IEEE 400, IEEE 413 etc. [49], [81].

### 2.9.1 Schering Bridge for $\tan \delta$ Measurement

A traditional method for measuring the loss factor is the Schering bridge and illustrated in Figure 2.13a. The bridge was first developed for diagnostic assessment in HV engineering by H. Schering in 1920 [8], [10]. It is often applied with high precision to low-capacitance samples such as cable, cable joints, liquid insulation and so on [111], [112].

As depicted in the figure, the bridge is composed of two branches: a reference branch and a measuring branch. In the measuring branch, a high voltage arm, the test object ( $Z_I$  - represented by a capacitance  $C_I$  and a hypothetical resistance  $R_I$ ), is connected in series with a low voltage arm ( $Z_4$ ) of a variable resistor  $R_4$ . The reference branch is formed by a standard capacitor  $C_2$  and a parallel combination of a tunable capacitor  $C_3$  and resistor  $R_3$ . A gas-filled standard capacitor (negligible loss) is used in the high voltage arm ( $Z_2$ ) whilst a parallel combination completes the low voltage ( $Z_3$ ) arm.

In principle, the bridge compares the loss angle  $\delta$  of the test object with the standard capacitor  $C_2$  and measures both the capacitance and DDF of the specimen. Considering the dielectric loss, the current flowing through the  $Z_I$  arm lags slightly less than  $90^\circ$  and causes a minimal voltage drop across the variable resistor  $R_4$  [113]. Under balanced condition:

$$\frac{Z_1}{Z_2} = \frac{Z_4}{Z_3} \text{ and } \tan \delta = \omega R_3 C_3 \quad (2.17)$$

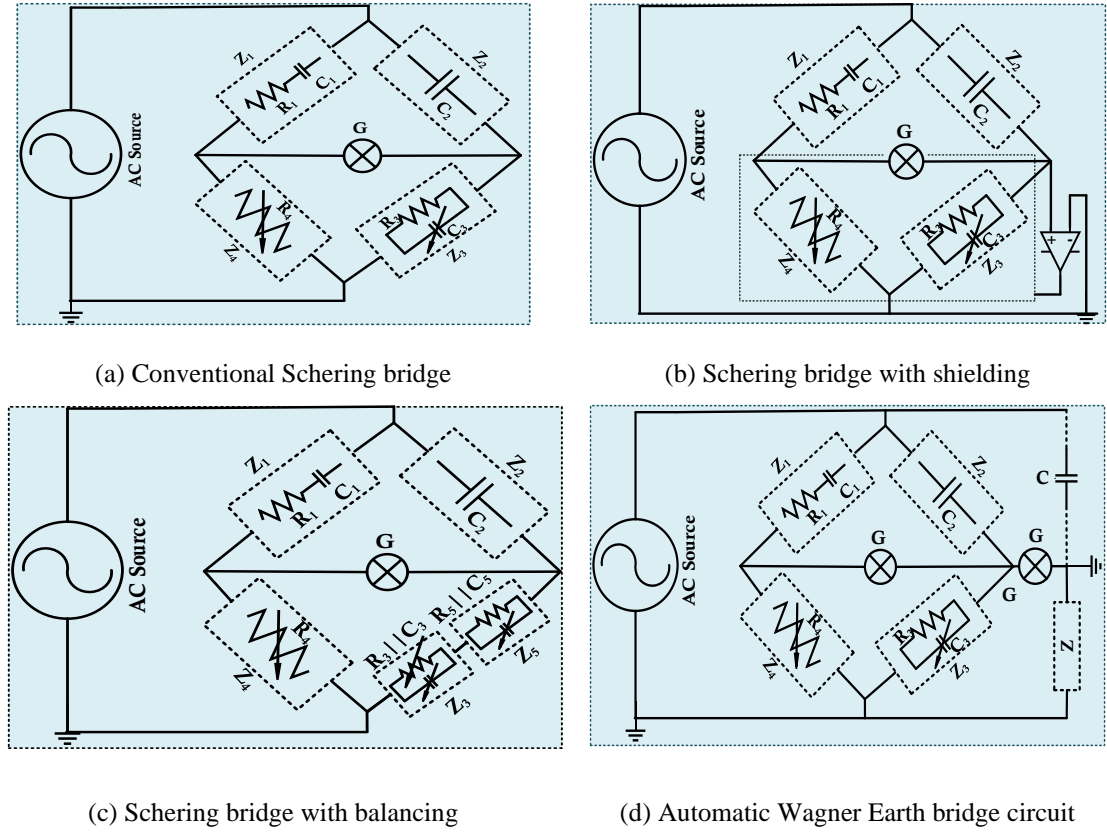


**Figure 2.13.** Schering bridge with different modifications

### 2.9.1.1 Effect of Stray Capacitance

While measuring the dielectric loss, an experimental error can arise due to stray capacitances between the ground and bridge junctions [114], [115]. The adverse effect of this can be neutralised by introducing shielding/screening into the measurement system. However, the use of shielding will involve some critical and rigorous analytical manipulation in calculating the loss factor [113], [115]. The problem, as suggested by Wagner, is overcome by the arrangement shown in Figure 2.13b and Figure 2.13c. In this arrangement, an additional arm  $Z$  together with stray capacitance  $C$  forms a six-arm bridge, which necessitates the double-balancing in the modified circuit. In the balanced condition, the detector terminals are at ground potential and both capacitance  $C$  and impedance  $Z$  are unlikely to influence this balance. However, the implemented additional impedance results in unwanted phase shifts in the low voltage arm of the measurement circuit. Therefore, the method is rarely used in diagnostic assessment [116], [117].

### 2.9.1.2 Automatic Wagner Earth

To counteract the uncontrollable phase errors, it is desirable to adjust the potential of some screen electrodes automatically by employing a block of high input and low output impedance. This can be achieved by using a potential guard regulator or an operational

---

amplifier. The simplified circuit presented in Figure 2.13d acts as an artificial ground at any instant and shifts the screened potential to the balanced level. The arrangement is popularly known as the Automatic Wagner Earth bridge circuit [8], [118].

## 2.9.2 Transformer Ratio Arm Bridge

There are several drawbacks experienced in the four-arm bridge circuits such as the influence of ageing and temperature on the circuit parameters, the impacts of skin effect and residual inductance on the high resistive arms, shielding difficulties for long arms and so on [119]–[123]. These limitations had led to a search for alternative circuits based on transformer coupling or turns-ratio [10]. An improved version of the circuit was introduced in the late 1930s by Glynne, in which, voltages/currents across the standard capacitor and test object are compared with two uniformly distributed coils with different turns ratios, and forcing the circuit to reach the zero-flux conditions quickly [121]. Thus, there are two types of bridge circuit based on this principle as follows.

### 2.9.2.1 Transformer Voltage Ratio Arm Bridge

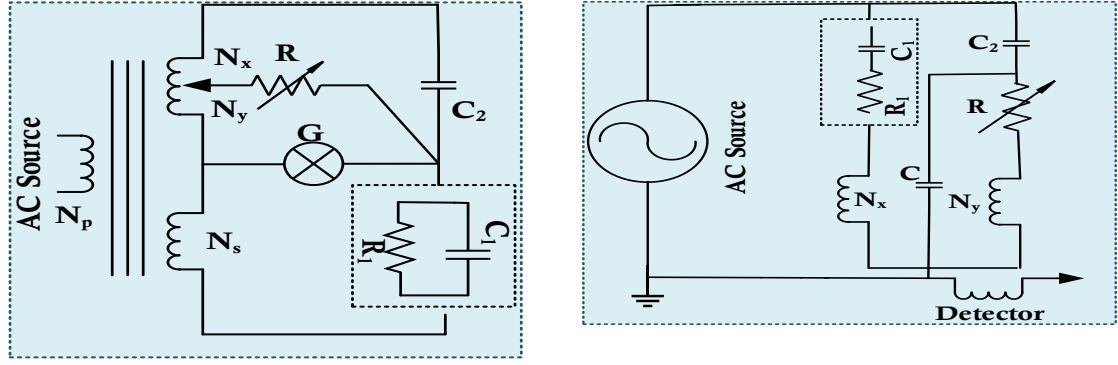
The circuit, illustrated in Figure 2.14a, can precisely measure the dielectric loss for low capacitance samples in low voltage high-frequency conditions. However, the system is limited to materials of high permeability; otherwise, sensitivity errors can occur and adversely affect its performance [119], [123]. Under balanced condition:

$$C_1 = C_2 \frac{N_x}{N_s}, R_1 = R \frac{N_s}{N_y} \text{ and } \tan \delta = \frac{1}{\omega R_1 C_1} \quad (2.18)$$

### 2.9.2.2 Transformer Current Ratio Arm Bridge

The schematic diagram is presented in Figure 2.14b. The arrangement includes a highly precise current comparator, in which all the windings are carefully shielded to eliminate the effect of stray capacitances and mechanical vibrations. Considering low-loss and leakage-free environment, under the balanced conditions, the magneto-motive forces (mmf) developed across the windings cancel each other out [119], [120], [122]. Furthermore, stray capacitances are unlikely to contribute to the balanced expression. This feature permits long leads to the bridge circuit in spite of using a Wagner earth in diagnostic measurements [10], [72]. Under equilibrium condition (null voltage induced in the detector coil):

$$C_1 = C_2 \frac{N_y}{N_x} \text{ and } \tan \delta = \omega R (C_1 + C_2) \quad (2.19)$$



(a) Transformer voltage ratio arm bridge

(b) Transformer current ratio arm bridge

**Figure 2.14.** Two types of transformer ratio arm bridge

### 2.9.3 Relay-based C- $\tan\delta$ Bridge Circuit

The circuit, as depicted in Figure 2.15, was proposed by Osvath and Windmer in 1986, where the fine balancing is realised by employing some relays and associated electronic circuits [8], [10]. The control operation can be carried out by a microcontroller. The current through the test object is compensated by the current flowing from the standard capacitor, and the differential current through the transformer is carefully controlled by the microcontroller. The mmf observed in the primary coil results in inducing a residual flux in the secondary coil. The auxiliary coils compensate for the core flux in the differential transformer and enable the bridge to reach the balanced situation [114], [124].

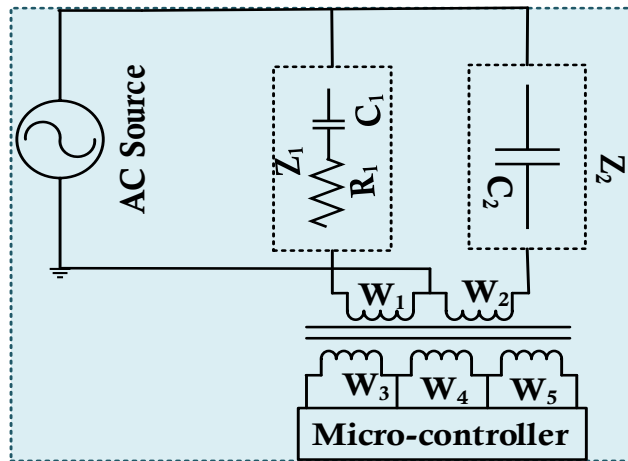


**Figure 2.15.** Relay-based c-  $\tan\delta$  bridge circuit

### 2.9.4 DSP- based C- $\tan\delta$ Bridge Circuit

With the advancement of digital signal processing (DSP), computer-based digital methods provide a better way to replace the conventional relay-based c-  $\tan\delta$  system. Strehl and Engelmann in 2003 proposed a DSP-based solution as illustrated in Figure 2.16 [10], [76].

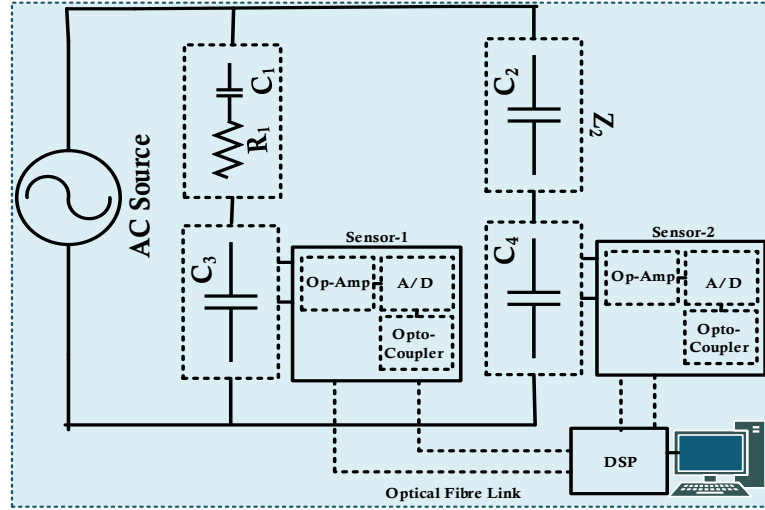


**Figure 2.16.** DSP- based c- tan $\delta$  bridge circuit

Unlike the traditional system, it eliminates the requirement of balancing and compensation. The circuit is composed of two capacitive dividers in which, the reference branch comprises a series connection of an HV standard capacitor  $C_2$  and a low voltage capacitor  $C_4$ . The measuring branch contains the testing object in series with a measuring capacitor  $C_3$ . Instead of measuring voltage magnitudes, two sensors are employed in measuring the voltage vectors from the corresponding branches. Inside the sensor block, the captured signal is digitised, converted to an optical signal, and finally sent to the computer via optical-fibre link for further processing. Here, the data are calculated by discrete Fourier transform, displayed and later stored in real time [8], [10].

A comparative analysis of various measurement systems is summarised in Table 2.4.

## 2.10 Modelling of Dielectric Response

Due to physical relaxation processes, the field-oriented dipoles inside the material have a random distribution of their alignment [125]–[128]. As illustrated in Figure 2.17, when a dielectric is subjected to a long period under an electrical stress, the polarisation builds up from a null value (a non-zero value is observed if there are permanent dipoles) and exponentially reaches its final value ( $P_\infty$ ) [126]. Similarly, after switching off the stress, the dipoles begin to decay and take a significant time for the relaxation. The development of polarisation can be expressed in mathematical form as

$$P(t) = P_\infty (1 - e^{-t/\tau}) \quad (2.20)$$

where  $\tau$  denotes the relaxation constant. Ignoring the atomic polarisation, the total polarisation can be summed as an electronic polarisation and various polarising processes ( $P_0$ ) [127], [128].



**Table 2.4.** Comparative analysis of various DDF measurement techniques

Type/Property	Schering Bridge	Transformer voltage ratio arm bridge	Transformer current ratio arm bridge	Relay based c- tanδ bridge	DSP based c- tanδ bridge
<b>Arms effectively used in measurement</b>	Four arms [111]	Two arms [122]	Two arms [120]	Two arms	Two arms
<b>Dielectric loss measurement</b>	Medium (> 100 pF) to higher capacitances	Typically, 100 pF to 100 μF	Typically 100 pF to 100 μF [122]	Typically, below 1 pF ~ 250 μF	All kinds of capacitances [10]
<b>Operation</b>	Non-automated	Non-automated	Non-automated	Automated	Automated
<b>Circuit elements</b>	Analogue electronic circuit [111]	Analogue	Analogue	Analogue and digital [10]	Digital
<b>Voltage application</b>	Medium to high	Lowest	High [115], [119]	Low to high	Low to high
<b>Frequency Application</b>	High frequency; 0.05 ~10 kHz [10]	High frequency; 0.1 ~100 kHz	Medium frequency; 50 Hz ~1 kHz [119]	Low to medium frequency; 0.01~ 500 Hz.	Low to medium frequency; typically 0.01~ 500 Hz [8]
<b>Accuracy for small capacitance</b>	Lower	Average [121]	Average	Higher	Highest
<b>Maximum voltage level and maximum current</b>	0~10 kV 100 mA [10]	0 ~ 25 kV 1~250 mA [8]	0 ~ 25 kV 1~250 mA [124]	> 10 kV mA to μA range	> 10 kV mA to μA range
<b>Uncertainty</b>	10 <sup>-4</sup>	< 10 <sup>-5</sup>	< 10 <sup>-5</sup> [112], [121]	< 10 <sup>-6</sup>	< 10 <sup>-6</sup>
<b>Stray Capacitance formation</b>	Yes, automatic guard/ shielding is used [115]	Yes, but lacks the shielding	Shielded against stray capacitances	Non-applicable	Non-applicable
<b>Error types</b>	Load error [118]	Ratio error and load error	Ratio error and load error [58]	Error greater than DSP-based system	Minimal error [10]
<b>Sensitivity</b>	Lower [114]	Comparatively higher than Schering bridge	Lower than voltage ratio arm bridge	Higher than a transformer bridge	Highest [8]
<b>Further processing of data</b>	Non-applicable [10]	Non-applicable	Non-applicable	Real time possible	Real time possible

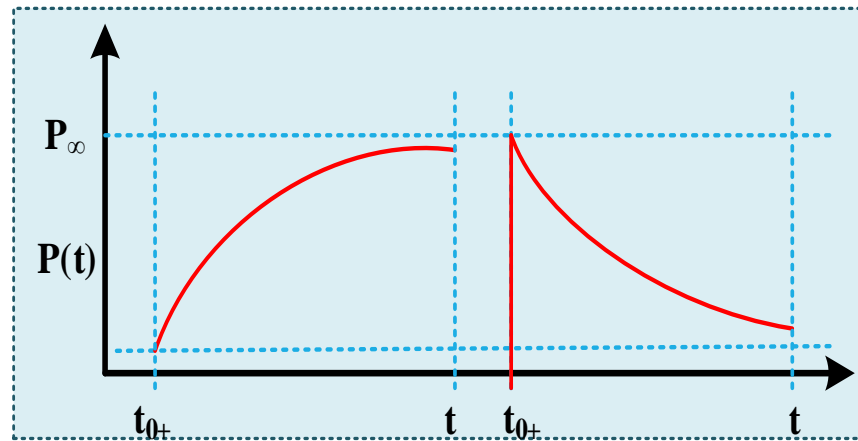


**Figure 2.17.** Building up and decaying of polarisation process

Therefore, the total polarisation at any instant can be written as

$$P_{tot}(t) = P_0(t) + P_e \quad (2.21)$$

For an alternating voltage  $E = E_m e^{j\omega t}$  the total polarisation of equation (2.21) can be described as:

$$P_{tot}(t) = \epsilon_0 \left[ \epsilon_\infty - 1 + \frac{\epsilon_s - \epsilon_\infty}{1 + j\omega\tau} \right] E_m e^{j\omega t} \quad (2.22)$$

Here,  $\epsilon_s, \epsilon_\infty$  denote the dielectric constant at DC voltage and alternating voltage at optical (infinite) frequency.

### 2.10.1 Debye Dipolar Model

The relationship between the real and imaginary permittivity of any dielectric material can be derived from (2.22) and can be described as:

$$\underline{\epsilon} = \epsilon' - j\epsilon'' = \epsilon_\infty + \frac{\epsilon_s - \epsilon_\infty}{1 + j\omega\tau} \quad (2.23)$$

The expression is popularly known as the Debye model, which is extensively applied to explain the behaviour of dielectrics at various frequencies [89], [128]. Now, separating the real and imaginary parts, the following expressions can readily be obtained as:

$$\epsilon' = \epsilon_\infty + \frac{\epsilon_s - \epsilon_\infty}{1 + (\omega\tau)^2} \quad (2.24)$$

$$\epsilon'' = (\epsilon_s - \epsilon_\infty) \frac{\omega\tau}{1 + (\omega\tau)^2} \quad (2.25)$$

A summary of the Debye process is illustrated in Figure 2.18.

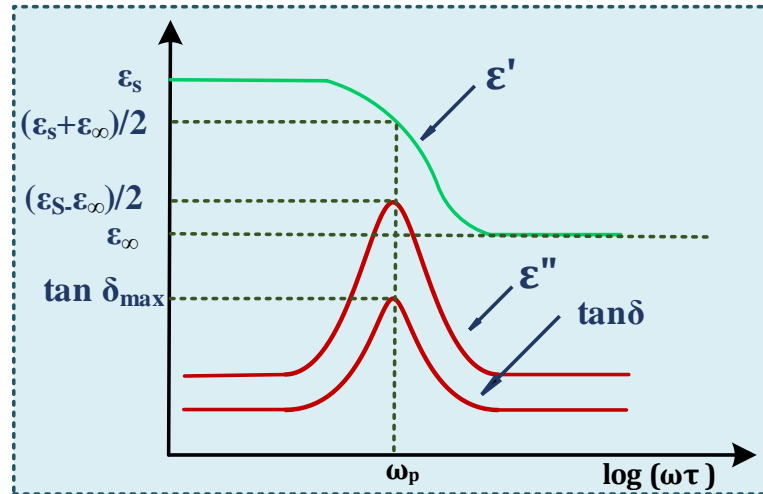


**Figure 2.18.** Measurement of tan-delta in Debye process

### 2.10.2 Cole-Cole Dipolar Model

Ideally, all dielectrics are supposed to follow the Debye model. However, very few dielectrics in practice completely agree with this relaxation process. The reason is the simplistic

---

assumptions of the Debye theory. In principle, the Debye process considers spherical molecules for any geometrical configuration, which gives a negligible field response on their axis of rotation. Instead of a uniform formation, a real dielectric has various molecular shapes, mostly spheroidal or linear in their long-chained polymeric arrangement. Based on the rotation of the main axis, the irregular shapes are very likely to yield different responses. Thus, it is obvious for a dielectric that the dissimilar interactions of molecules to an alternating field result in a discrepancy among their relaxation times, hence, a non-uniform dispersion over a wide range of frequencies [126], [129].

Considering these physical processes, the Cole-Cole (C-C) model makes a small adjustment to the Debye expression. In this method, a polarising constant ( $N$ ) is introduced within the modelling and contributes appreciably to the relaxation process [64], [93]. The general form of the Cole-Cole expression is given by:

$$\underline{\epsilon} = \epsilon_{\infty} + \frac{\epsilon_s - \epsilon_{\infty}}{1 + (j\omega\tau)^{1-N}}; \quad 0 \leq N \leq 1 \quad (2.26)$$

The C-C model suggests a higher value of  $N$  will imply a greater distribution of relaxation times. Comparing with the Debye process, increasing  $N$  also makes a broader loss factor curve.

### 2.10.3 Davidson-Cole Dipolar Model

The empirical model suggested by Davidson-Cole (D-C) can be presented as:

$$\underline{\epsilon} = \epsilon_{\infty} + \frac{\epsilon_s - \epsilon_{\infty}}{(1 + j\omega\tau)^{\beta}}; \quad 0 \leq \beta \leq 1 \quad (2.27)$$

The implications of the  $\beta$  parameter introduced in D-C modelling are significant. The hypothesis proposed in the D-C modelling specifically aims to explain the spatial and temporal fluctuations occurring in the dipoles [97], [125], [130]. In the presence of an electric field, some turbulence happens at the molecular level which creates non-uniform oscillatory rotation in the dipolar motion. As a result, some dipoles oscillate with a higher amplitude, while some with lower, which contributes to the D-C expression in dipolar modelling [131], [132].

### 2.10.4 Fuoss-Kirkwood Dipolar Model

The Fuoss-Kirkwood (F-K) theory can be applied to a dielectric, only if it shows the Cole-Cole relaxation process. However, the value of characterised parameters may differ from one to another. The distribution of the relaxation time in the F-K model is independent of the external temperature [127]. This feature at higher temperatures can principally be applied to

---

derive the distribution function for long-chained polymers. The F-K model is mathematically expressed as:

$$\varepsilon'' = (\varepsilon_s - \varepsilon_\infty)^\delta \frac{(\omega\tau)^\delta}{1 + (\omega\tau)^{2\delta}}; \quad 0 \leq \delta \leq 1 \quad (2.28)$$

### 2.10.5 Havriliak-Negami Dipolar Model

To interpret the physical process for complicated molecular structures, Havriliak-Negami (H-N) proposed a generalised model for complex dielectrics [109]. The H-N model is fundamentally reproduced from the Cole-Cole and Davidson-Cole models, and represented by:

$$\frac{\varepsilon^* - \varepsilon_\infty}{\varepsilon_s - \varepsilon_\infty} = \left[ 1 + (j\omega\tau)^{1-N} \right]^{-\beta} \quad (2.29)$$

where the  $\alpha$ -parameter describes the chain connectivity, and the  $\beta$ - parameter indicates the local density of the polymeric insulation.

## 2.11 Some Commercial Diagnostic Instruments

### 2.11.1 Baur VLF Diagnostic System

The Baur diagnostic system covers all the main requirements in testing medium-voltage cables at very low frequency. Using true-sinus voltage technology invented in 1995, the system offers flexibility to generate excitation voltages with frequency range 0.1-0.01 Hz. Besides the primary measurement requirements, it includes cable status evaluation by following some well-accepted standards, mainly for the installation and maintenance purpose [133].

### 2.11.2 seBaKMT Diagnostic System

seBaKMT has developed the CDS (cable diagnostic system) and tan-delta test instruments for condition assessment of three-phase cable insulation. Technically, the CDS system combines the popular Isothermal Relaxation Current (IRC) and Return Voltage Method (RVM) methods for analysis. The test instrument can conduct measurements for cosine-square wave and is mainly useful for the detection of various ageing effects such as humidity and water treeing in polymeric insulation [84], [134].

### 2.11.3 Pax Diagnostics Instruments

Pax Diagnostics has manufactured the IDAX-206 VAX-230 instrument, which is integrated with the high voltage supply IDA 200 for insulation assessment. The power supply is developed by General Electric (GE). Based on the capacitance and associated dielectric loss of a sample, the system works at a wide range of frequencies from 0.1  $\mu$ Hz- 1 kHz [135].

---

#### **2.11.4 Tettex Instruments**

Haefely Hipotronics has introduced three dielectric loss analysing systems for measurement of the very-low dissipation factor of HV apparatus. These are the Tettex 2820, Tettex Midas 2880 and 2881, and Tettex Midas 2883. All these models measure the loss factor of rotating machines, transformers, bushing and circuit breakers at the power frequency of 50/60 Hz [136].

#### **2.11.5 HV Diagnostic Instruments**

HV Diagnostics has developed two integrated diagnostic systems, HVA28 TD and HVA45TD, which offer both very low frequency power supply and tan-delta measuring system to evaluate the condition of medium-voltage and extra-high voltage power cables. Apart from this, some stand-alone loss-factor assessment tools such as TD 30, TD 60 and TD 90 are also available. All test instruments evaluate the loss for frequencies 0.02-0.1 Hz, particularly effective when moisture, tracking or water-tree degradation are present in cable insulation [137].

#### **2.11.6 Omicron Instruments**

There are several products, such as CPC 80/100 with CP TD1, MI 600, and Dirana developed by Omicron Electronics. Principally, CPC 80/100 is a multi-functional test instrument equipped with CP TD1 for dissipation factor assessment. Various electrical tests on machine insulation, power transformers, instrument transformers, and grounding systems can be performed with this universal system. It can sweep frequency from 15 Hz to 400 Hz. Another highly-precise analysis system is the MI 600, which includes the sweeping frequency from 5 Hz to 50 kHz. The Dirana system is commonly used as a frequency-response analyser for low-voltage application [138], [139].

Figure 2.19 shows a summary of the discussed commercial diagnostic instruments for XLPE and PILC power cables. Based on their operating principle, these are categorised into four major classes. Different manufacturers use different automated techniques for loss-factor assessment. Depending on the available power supply, some instruments show the tan-delta value at very low frequency or the power frequency, or some make a frequency sweep over a wide range of frequencies at low voltage. All the systems developed for diagnostic measurement work in an off-line condition of the power supply.

### **2.12 Summary of the Chapter**

As a potential tool of diagnostic assessment, both experimental and physical aspects of  $\tan\delta$  measurement have been extensively presented in this chapter. To facilitate overall

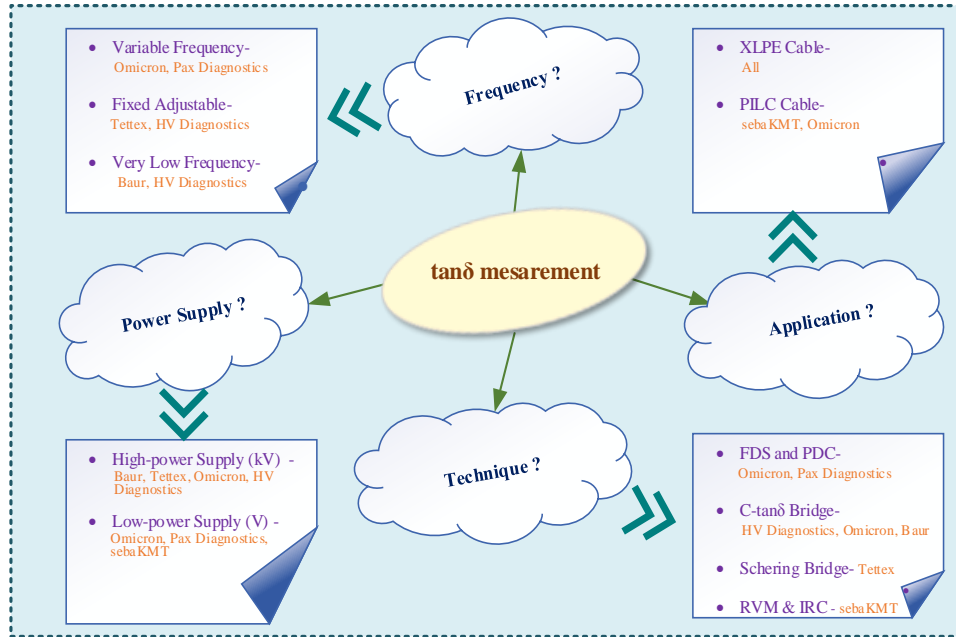


**Figure 2.19.** Differences among various commercial instruments

visualisation, the measurement and explanation have covered a wide range of frequencies. The key points are summarised as follows:

- It provides the applicability of various high voltage AC techniques, different voltage sources: online/offline power frequency, VLF and DAC and their suitability, generation of the excitation waveform and conformity to various standards.
- It highlights dielectric response interpretation challenges including various types of dielectric loss and their contribution to tan-delta measurement, equivalent circuits and dynamic properties of dielectrics, especially polarisation loss, and detailed explanations.
- It reviews key challenges associated with selecting a test object, test techniques, a test instrument and excitation frequency, processing the experimental results, and the problems associated with transportation.
- It presents the principle of dielectric response measurement techniques in the time domain and frequency domain, commercially available techniques followed in HV engineering and their comparison.
- It provides applicability of various analytical modelling methodologies to explain dielectric phenomena and a short survey of instruments that are available commercially to measure the dielectric loss.

---

## Chapter 3.

# Partial Discharge Measurement and Diagnostic Aspects

This chapter provides a comprehensive review of partial discharge measurement, detection, modelling and analysis over the very low to power frequency range.

### 3.1 Diagnostic Study and Various Perspectives

PD is a stochastic process. It varies with the environmental conditions (e.g. temperature, pressure moisture, humidity etc.), the supply voltage frequency, voltage level and waveform [34], [47], [48], [61], [62], [140]–[142]. It can be generalised into three main categories, as illustrated in Figure 3.1: cavity or void discharge, surface discharge, and corona discharge [8], [10], [58].

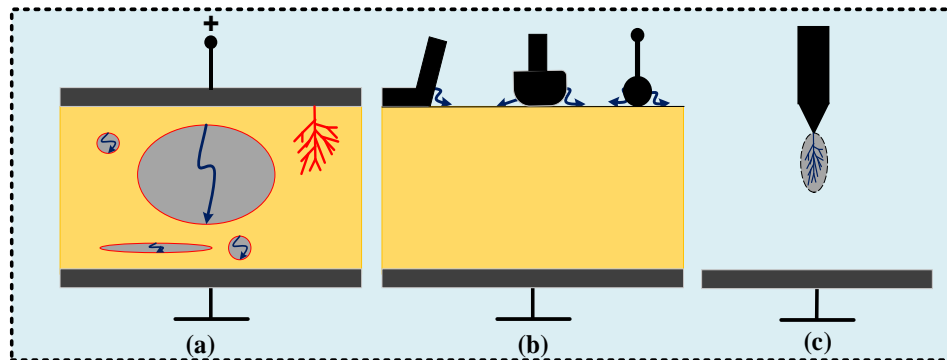


**Figure 3.1.** PD Process: (a) Cavity discharge (b) Surface discharge (c) Corona Discharge

Internal discharge occurring in the void or defect within a solid insulation is known as cavity discharge. Surface discharge is a streamer type discharge which is usually initiated by the high tangential electric field along the insulation surface. Corona discharge refers to partial breakdowns in the gaseous medium due to the high electric field around sharp points, edges and terminations of an insulation system. The spider diagram as shown in Figure 3.2 encapsulates the various perspectives on PD diagnostics.

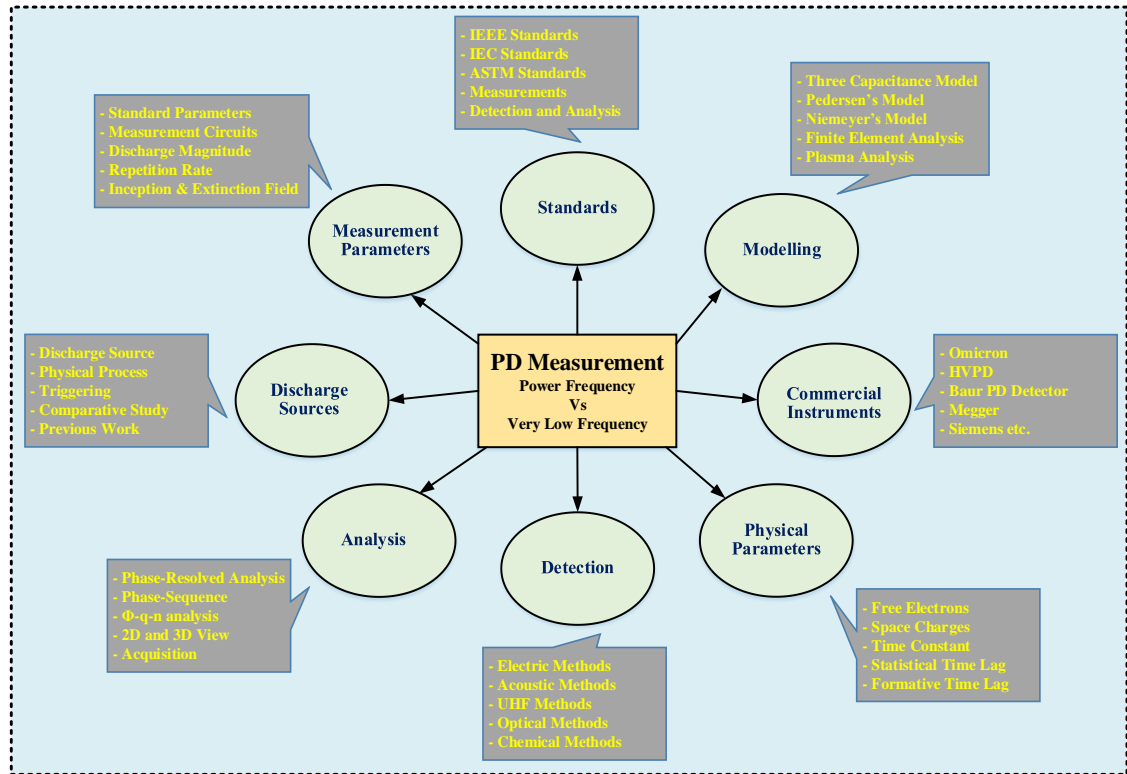


**Figure 3.2.** Overview of the diagnostic study performed at very low frequency and power frequency

### 3.2 Discharge Characterised Parameters

There are several standard parameters which are used for quantifying the discharge activities in the PD measurement. As recommended by IEC 60270 standard, these parameters are defined as follows [41].

- a) **PD Pulse:** A short duration voltage or current pulse (typically in the range of some micro-to-nano seconds) that results from a discharge occurring within a test object under measurement.
- b) **Apparent Charge:** The charge of a PD current pulse appeared at the terminals of a test object during the occurrence of a PD pulse itself. The apparent charge is generally measured in terms of pC and quantified by a specified test setup.
- c) **Real or Actual Charge:** The amount of charge which is locally involved during a PD event at the defect site. It is not possible to measure the real charge directly.
- d) **Repetition Rate:** The ratio of the total number of recorded pulses ( $N$ ) within a specified time and the duration of that time ( $T_{rec}$ ) and is generally denoted by PRPS (pulse repetition per second).
- e) **Repetition Frequency:** or PRPC (pulse repetition per cycle) which means the total number of recorded pulses ( $N$ ) per AC cycle of the applied voltage.



**f) Average Discharge Current,  $I_{dis}$ :** can be derived from the sum of individual apparent charge's absolute magnitude for a given recording period ( $T_{rec}$ ) and expressed as:

$$I_{dis} = \frac{1}{T_{rec}} \sum_{i=1}^n |q_i| = \frac{1}{T_{rec}} (|q_1| + |q_2| + \dots + |q_n|) \quad (3.1)$$

where,  $q_1, q_2, q_3, \dots, q_n$  are the magnitude of individual apparent charge.

**g) Discharge Power,  $P_{dis}$ :** The average power measured from the terminals of the test object due to the apparent charge occurring at different instantaneous test voltages ( $v_i$ ) of an AC cycle and is given by:

$$P_{dis} = \frac{1}{T_{rec}} \sum_{i=1}^n q_i v_i = \frac{1}{T_{rec}} (q_1 v_1 + q_2 v_2 + \dots + q_n v_n) \quad (3.2)$$

**h) Quadratic Rate (QR),  $D$ :** The sum of the squares of the individual apparent charge during a given recording period, generally expressed in  $C^2/s$  and is given by:

$$D = \frac{1}{T_{rec}} \sum_{i=1}^n q_i^2 = \frac{1}{T_{rec}} (q_1^2 + q_2^2 + \dots + q_n^2) \quad (3.3)$$

**i) Partial Discharge Inception Voltage (PDIV):** the lowest applied voltage level at which repetitive PD was first observed in the test circuit. However, due to the background noise in practice, PDIV is taken as the lowest test voltage level at which PDs exceeding the noise floor are first observed.

**j) Partial Discharge Extinction Voltage (PDEV):** the voltage level at which repetitive PD activities are not noticeably observed, if the test voltage is slowly reduced from its maximum to a lower value.

**k) Test Circuit:** The recommended basic circuits for PD measurement are shown in Figure 3.3 and Figure 3.4 respectively. These test circuits are used in conjunction with the analogue or digital detection systems to measure the discharge.

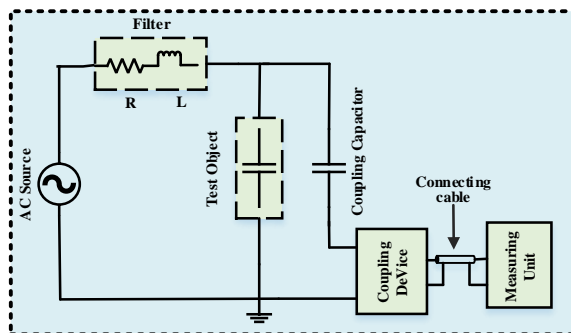


**Figure 3.3.** Measurement circuit in which test object is in parallel with the measuring unit [41]

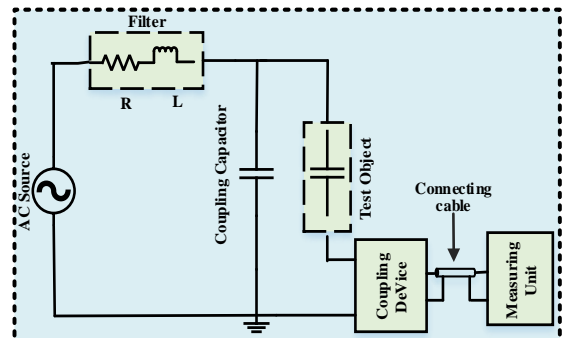


**Figure 3.4.** Measurement circuit in which test object is in series with the measuring unit [41]

### 3.3 Standards in Partial Discharge Measurement

A list of standards followed in the PD study of solid insulation is shown in Table 3.1. The majority of these primarily focus on the measurement carried out at the power frequency; nevertheless, the definitions, terminology, basic circuits and procedures may also be applicable to other test frequencies.

**Table 3.1.** Brief descriptions of various standards for PD measurement

<i>Standard</i>	<i>Descriptions</i>
<b>IEC 60060 (1-3)</b>	Terminology, definitions, basic circuits, techniques and necessary requirements for various HV on-site tests [8]
<b>IEC 60270</b>	A brief overview including definitions, requirements, detections and measurements of PD testing [41]
<b>IEC 60885 (1-3)</b>	Electrical measurements of partial discharges for extruded power cables
<b>IEC 62478</b>	Measurements and detections of partial discharge by acoustic and electromagnetic methods
<b>IEC 61230</b>	Earthing, grounding or short-circuiting of power apparatus
<b>IEEE Std 400</b>	Guidelines for the field testing and evaluating of electrical insulation in the extruded power cables [29]
<b>IEEE Std 400.3</b>	A brief overview of PD measurements for shielded power cable systems in a field environment [68]
<b>IEEE Std 510</b>	Safety procedures and recommendations for any high voltage testing [70]
<b>ASTM D1868</b>	Standardised test methods and procedures for the detection and measurement of corona discharge
<b>ASTM D2275</b>	Evaluating the impacts of corona discharge on the surface of solid electrical insulation
<b>IEEE 1434</b>	Guidelines for the measurement of partial discharge in AC electric machine systems
<b>NFPA 70E</b>	An overview of standard procedures and requirements for maintaining electrical safety in the workplace [69]
<b>IEEE Std 48</b>	Test methods, basic requirements and procedures for diagnosing the AC cable terminations
<b>IEEE Std 433</b>	AC testing of rotating machine insulation at very low frequency in the field environment

### 3.4 Modelling Techniques of PD Measurement

The modelling approach aims to reproduce the measurement results. In this section, the computational model of partial discharge measurement to explain the physical behaviours is briefly discussed. It is interesting to note that most of the modelling in the literature consider the electrical discharge originated from voids encapsulated in the solid insulation [44], [45], [143]. For streamer-type discharges, it is challenging to simulate this physical phenomenon in the computational process [143], [144].

#### 3.4.1 Conventional Three Capacitance Model

A conventional approach of PD modelling is the three-capacitor circuit model, well-known as the ‘abc’ model, represented by three capacitances analogous to a cavity bounded in a solid dielectric [145]–[147], as shown in Figure 3.5 (left side). Here  $C_a$  is the capacitance of the material;  $C_{b1}$  and  $C_{b2}$  represent the capacitance of that region which is in series with the cavity and  $C_c$  denotes the cavity capacitance. The simplified equivalent ‘abc’ circuit derived from the void geometry is illustrated in the right side of Figure 3.5.

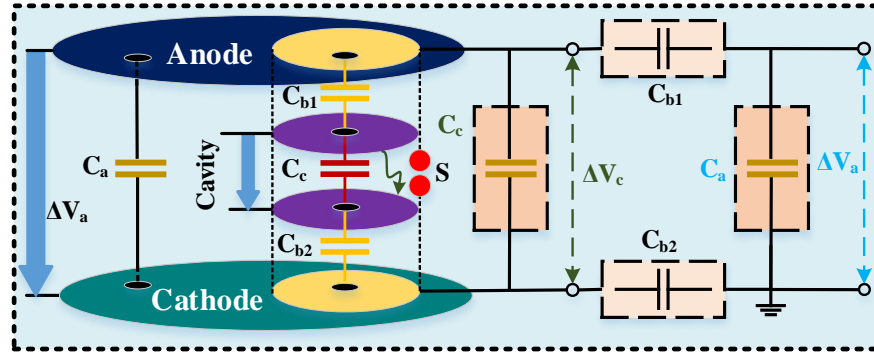


**Figure 3.5.** A schematic diagram of three capacitance model

Primarily, a discharge event is assumed to be ignited if the voltage across the cavity ( $V_c$ ) exceeds the inception voltage (PDIV) and will cease if the cavity voltage is less than the extinction value. During a PD event, the void is short-circuited and allows a fast transient current to flow in the external circuit depending on the voltage difference between the applied voltage and the voltage across the cavity-free region. In other words, during a PD process, the voltage drop across the cavity prompts a transient current which forms the basis of evaluating PD current pulse and the associated apparent charge as a function of the measurement time.

**Analysis:** The real discharge (or internal discharge)  $q_r$  is physically calculated by the time integral of the momentary cavity current flowing through the test object.

For the condition ( $C_b \ll C_c \ll C_a$ ), the magnitude of  $q_r$  can be computed as

$$q_r \approx \Delta V_c (C_b + C_c) \quad (3.4)$$

On the other hand, the apparent discharge (or external discharge)  $q_a$  is determined by integrating the transient current flowing through the series connected capacitors  $C_a$  and  $C_b$  over the measurement period and given by

$$q_a = C_a \Delta V_a = C_b \Delta V_c \quad (3.5)$$

From equation (3.4) and (3.5)

$$q_a = \frac{C_b}{C_b + C_c} q_r \approx \frac{C_b}{C_c} q_r \quad (3.6)$$

From equation (3.6), it can be clearly seen that the apparent charge detected at the test object terminal is much less than the actual physical discharge occurring inside the cavity.

In the context of modelling PD activities in the solid insulation, it should be noted that the three capacitance equivalent circuit is the first attempt to represent the physical mechanism in a discharge event and is very simple and deterministic to realise. However, it was discredited [145], [148]. The model is inadequate in describing the impacts of surface charge deposition on the cavity wall, and assumed the cavity surface is equipotential [148], [149]. Besides, the

---

stochastic discharge behaviour is very complex, and the triggering process cannot be correlated with the change of capacitance due to the induced charge [145], [148]–[150].

### 3.4.2 Pedersen's Model

Pederson introduced an induced charge concept model which is based on the dipole behaviours associated with the physical mechanisms of PDs occurring inside the void or on the insulation surface [151]–[153]. The induced charge can be calculated by the deposited charge difference at the boundary electrode before and after a discharge event. Also, the induced space charges (either positive or negative ions), usually generated after a PD event, result in dipole orientations and reduce the local electric field. At some stage, the reduced electric field completely ceases the discharge avalanche within the void environment.

The induced charge  $q_{ind}$  on the boundary electrodes can be mathematically expressed as:

$$q_{ind} = -\vec{\mu} \cdot \nabla \vec{\psi} = -\left( \int_s \hat{n} \sigma_s dS \right) \cdot \nabla \vec{\psi} \quad (3.7)$$

where,  $\vec{\mu}$  is the induced dipole moments, dependent on the surface integral of deposited space charges ( $\sigma_s$ ) and normalised vector  $\hat{n}$ .  $\nabla \vec{\psi}$  represents the Laplacian vector of voltage due to induced charge [148], [151], [154].

Prior to any discharge, let's assume the charge and the potential at the boundary electrodes are  $Q$  and  $V$  respectively. After a PD occurrence, the appeared charge is increased by  $\Delta Q$  (usually supplied by external circuit); whereas the potential will be dropped by  $\Delta V$ . For an insulated bounded cavity, the induced or apparent charge at any electrode within a capacitive insulation system ( $C$ ) can be written as:

$$q_{ind} = q_a = C \Delta V + \Delta Q \approx C \Delta V \quad (3.8)$$

As can be seen, the  $\Delta Q$  term can be ignored if the impedance of the insulation circuit is much larger. However, this assumption was questioned by Z. Achillides *et al.* and the approximation based on the dipole model is not always appropriate [150], [155].

### 3.4.3 Niemeyer's Model

Niemeyer's work can be considered as the base of the majority literature performed on PD modelling [143]. In this model, the two boundary conditions which are prerequisites for a discharge event are continuously checked at each time step of the numerical simulation. A detailed description of a mathematical model including initial electron generation rate, streamer development and the computation of PD magnitudes is given in [143], [156]. For void discharge, the local cavity field can be obtained by solving the Poisson's equation, and a field

---

enhancement factor is introduced to estimate the elevated field due to the applied voltage and the deposited space charge on the cavity surface. The initial generation rate of free electrons which is responsible for triggering a PD process is closely related to the surface emission and volume ionisation, and determined from the differential equations associated with the physical parameters of the insulation material [156], [157].

The real discharge magnitude is calculated by the product of the momentary voltage drop across the cavity due to a PD event and the cavity capacitance, whilst the apparent charge is computed from the induced charge at the boundary electrode, which depends on several factors such as void location, orientation, geometry, inside gas pressure [156]–[158]. The inception condition of a PD process is deterministic and at each time step, it is compared with the local cavity field. Niemeyer’s model was successful in validating a range of experimental results such as PDs within an air-filled spherical void in epoxy resin and PDs due to an electrode protrusion in SF<sub>6</sub> [143], [156], [157]. However, there are some concerns about the proposed model due to its many primary assumptions; also, it relies on some unquantified free parameters that have to be adjusted in order to match the experimental results [33], [44], [45], [148].

### 3.4.4 Finite Element Analysis Based Model

Advances in computational process allow employing finite element analysis (FEA) software to model the dynamic characteristics of partial discharge within a cavity [44], [45], [63], [159]–[164]. In FEA, the electric field in any test specimen is found by solving Poisson’s equation numerically [8], [58] and given by:

$$\nabla^2 V(x, t) = \frac{\rho(x, t)}{\varepsilon(x)} \quad (3.9)$$

$$E(x, t) = -\nabla V(x, t) \quad (3.10)$$

An inhomogeneous field is likely to be observed inside a small void. An advantage of FEA is that, during a PD event, the surface charge density along the cavity wall can be determined by solving the charge density continuity equation [63], [162]–[165]. In spite of relying on some approximations in other analyses, another advantage of the FEA method is that this model calculates the apparent charge directly from the observed PDs [154], [158]. The time integral of the induced current at the boundary electrode, typically the ground electrode, provides the apparent charge magnitude. However, the PD inception level and electron emission rate are usually controlled by the electric field at a point within the cavity, typically chosen at the void centre [44], [45], [63], [165], [166]. The residual field is often regarded as the PD extinction field which may cause confusion because the parameter is defined in IEC 60270 Standard, implying the minimum voltage at which repetitive PDs stop [41].

In order to fit the experimental data, FEA models adjust the electron generation rate from the volume ionisation, which is also a drawback [143]. The FEA based PD modelling has been successfully applied to describe the PD characteristics for a wide variety of conditions such as different cavity geometries, temperature effects, cavity location, size, and the applied electric stress under variable frequency excitations [63], [164]–[168]. However, literature coverage on the decay mechanism of surface charge via the recombination with the opposite charge or the drifting along the cavity surface at very low frequency excitation voltage is limited [168], [169].

### 3.4.5 Plasma Analysis Model

The plasma dynamics of ionisation has also been considered to model partial discharge in gases, especially for the corona discharge. The drift-diffusion equation in describing the dynamics of free electrons and space ions (either positive or negative) is numerically solved in each time step of the simulation [170], [171]. The plasma analysis has been extensively employed to model the discharges from a needle-plane electrode arrangement with and without a barrier [170]–[172]. However, the majority of these investigations provide limited insight into measuring the PD magnitude and repetition rate. Some were carried out under different circumstances, especially in examining the discharge behaviours at kHz frequencies; whereas, the diagnostic interest lies in the very low to power frequency range [167], [171], [172]. Some work include plasma model in order to model the PD activities in an air gap between electrodes covered by dielectric materials [173], [174].

A summary of various modelling concepts is given in Table 3.2. Also, the differences in the fundamental approach are illustrated in Figure 3.6.

**Table 3.2.** Differences among various PD models

Model	Principle	Applicable Medium	Discharge Source
<b>Three Capacitance</b> [145]–[148]	Analogue Circuit	Solid	Cavity
<b>Pederson</b> [151]– [153]	Induced Charge	Mostly Solid	Cavity and Surface
<b>Niemeyer</b> [156]– [158]	Boundary Conditions and Differential Equations	Solid and Liquid	Cavity
<b>FEM</b> [63], [164]– [168]	Poisson Field, Charge Continuity Equation	Solid, Liquid and Gas	Cavity, Surface and Corona
<b>Plasma</b> [170]–[172]	Plasma Dynamics and Chemical Reaction	Gas	Corona

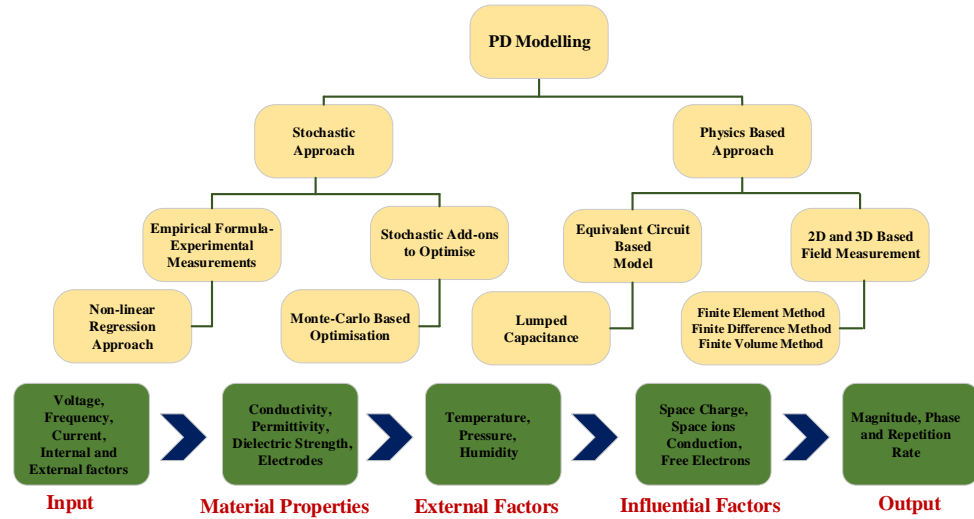


**Figure 3.6.** Basic approaches followed in the modelling of PD measurement [148], [177]–[179]

## 3.5 Partial Discharge Detection Techniques

This section discusses detection techniques for recognising partial discharges in various physical forms. The detection system can be either analogue or digital as illustrated with the block diagrams in Figure 3.7 and Figure 3.8. The detection techniques include electrical methods, acoustic methods, UHF methods, hybrid methods etc. [175], [176].

### 3.5.1 Electrical Methods of PD Detection

The electrical methods include the measurement of PD amplitude, repetition rate, pulse sequence, inception voltage, and extinction voltage of the test specimen [176], [178]. The earlier detection techniques employ some analogue instruments to capture PD signals and measure these quantities by displaying on the oscilloscope. In the late 1990s, the advancement of computerised signal processing techniques allows employing wide varieties of fast response digital circuit for discharge pulse measurement. The conventional detectors work in the range from 10 kHz to 1 MHz, while nowadays the ultra-wideband (UWB) detector has gained some popularity [72]. At present, the majority of PD detection systems follows the IEC 60270 Standard at which PDs are detected and measured in pC using narrowband or wideband detectors [19, 73].

### 3.5.2 Acoustic Methods of PD Detection

In the vicinity of the discharge source, the rise of temperature due to PD currents results in generating pressure waves which can be qualitatively captured through acoustic methods [182]–[184]. During the propagation of the pressure waves from the source to the measuring sensor, the reflection, absorption, attenuation, refraction, and transmission process influence the acoustic signal measured by the sensor [176], [184].

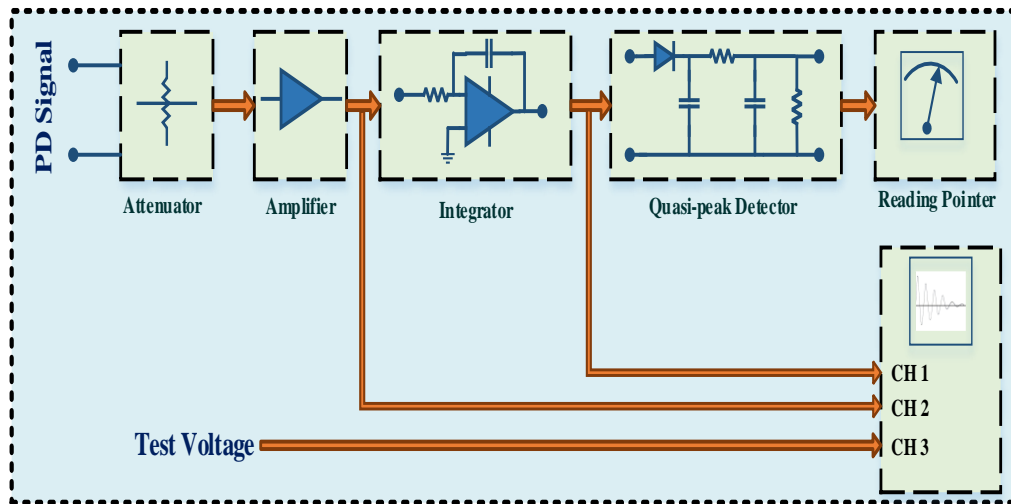


**Figure 3.7.** Block diagram of an analogue PD detection system

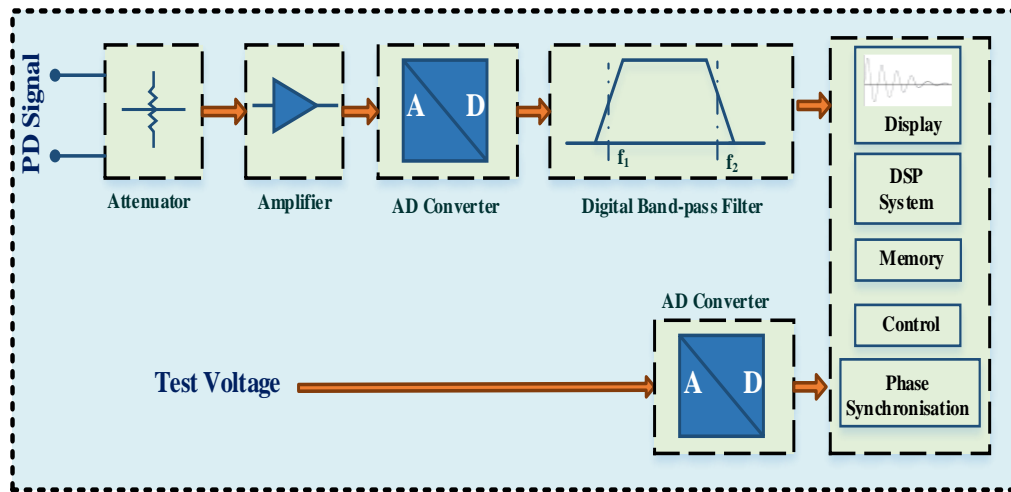


**Figure 3.8.** Block diagram of a digital PD detection system

The technique is useful in diagnosing the multi-material and complex insulation systems. However, the acoustic sensor's sensitivity can vary significantly [175], [176]. A typical acoustic monitoring system consists of piezoelectric sensors, pre-amplifiers, filters, data acquisition and processing units. The sensors can be narrowband, capturing signals in a small frequency range (20 kHz-100 kHz), or broadband which are recommended for the high-frequency range (up to 1 MHz) application [185].

### 3.5.3 UHF Methods of PD Detection

Ultra-high frequency (UHF) detection techniques rely on sensing the electromagnetic waves (EM) generated by the partial discharge. The UHF based monitoring system has advantages of higher sensitivity in discarding the background noise and higher signal-to-noise ratio (SNR) [186]–[188]. PD measurement using this technique is quite successful in diagnosing the insulation condition of gas-insulated systems (GIS) [188] and power transformers [186]. Various types of UHF antennas such as Hilbert, cone, patch, spiral etc. are used to detect the



---

EM wave signals [186], [189]. As a drawback, calibration is problematic and the UHF method does not give a reliable measurement of the apparent charge [175], [176].

### **3.5.4 Optical Methods of PD Detection**

The light generated by the ionisation, radiation and recombination processes of a PD event forms the basis of the measurement using optical method [41], [190]. This method is generally carried out in a darkened room where the optical signal produced by an electric discharge is detected by a sensitive photosensor [176]. The detection range is also extendable by using photo-multipliers or image intensifiers. The optical signal after a discharge occurrence has a spectrum varying from the ultraviolet to infrared range [176], [190].

### **3.5.5 Chemical Methods of PD Detection**

Chemical methods are widely employed in detecting PDs in oil-paper or gas-insulated systems. PDs can produce chemical by-products, e.g. hydrocarbon gases dissolved in the oil, decomposition products of SF<sub>6</sub>. Chemical analysis such as gas chromatography can be used to determine the characteristic gas components [41], [176].

### **3.5.6 Hybrid Methods of PD Detection**

In order to determine the instant at which PD occurs and find out its location in the three-dimensional coordinate, it is necessary to employ more than three sensors [175]. To achieve higher accuracy, the acoustic method is sometimes used in combination with other detection methods (HF-CTs or UHF antennas) [175], [176].

## **3.6 Partial Discharge Analysis Techniques**

Characterising PD activities in time-domain is a challenge, and there have been many statistical and graphical approaches to analyse the PD data. In this section, an overview of some popular analysis techniques to evaluate PD activities is presented.

### **3.6.1 Conventional Statistical Analysis**

The conventional statistical methods include the assessment of arithmetic mean, skewness and kurtosis of the measured PD data [191]–[194]. In order to express some additional PD characteristics, some analyses such as fractal dimensions and measurement of complexity are also proposed [195], [196]. Pattern recognition by neural networks has also been used to identify the features of different PD sources and differentiate between them [197], [198]. Weibull distributions have been applied to analyse the phase distribution of PD occurrence, and the apparent charge originated from certain discharge sources [199].

---

### 3.6.2 Phase-resolved Analysis

A common technique used in the data analysis is the phase-resolved partial discharge (PRPD) pattern [42], [44], [62]. It provides information about the discharge magnitudes and the number of discharge occurrence in relation to the phase of the applied voltage [31], [44], [46]. The discharge pattern helps to characterise the insulation defects under varying frequency excitations [43]. The phase-resolved analysis technique has been extensively applied in literature; for example, studying the frequency-dependent behaviour of PDs within cylindrical and spherical cavities [44], [45], [62], [166], the influence of cavity size, numbers and locations [200], [201], the insulation degradation at various stages of the operation, the detection and location of PD activity in the high voltage system [160], [178], the classification of different types of discharge sources [194] and the behaviours of surface and corona discharge under variable frequency voltage [168], [202].

### 3.6.3 Pulse Sequence Analysis (PSA)

The correlation between successive discharges – each discharge event with its immediately preceding and following discharges – conveys information relating to the defect. Pulse sequence analysis (PSA) has been used to diagnose the insulation condition by studying the time sequence of individual PD pulses [203]–[205]. The method computes the time or voltage magnitude difference between two consecutive discharge events. Since the local enhancement of electric field at a defect site causes the electric discharge; thus, the discharge sources and the severity of degradation can be distinguished by interpreting the recorded pulse sequences. By offering the information about the relative time shift, the PSA analysis also has the advantage of measuring the effects of space charge after any PD event [203], [206].

### 3.6.4 $\Phi$ -q-n Analysis

The  $\Phi$ -q-n analysis provides both qualitative and quantitative information about PD data through graphical representations in three-dimensional (3D) view [62], [160], [207]. The parameters  $\Phi$ , q, and n represent the phase of PD occurrence, discharge magnitude and repetition rate. Comparing with other approaches, this method provides a more effective visualisation to evaluate the PD nature and activities [62].

In summary, Figure 3.9 shows the graphical presentations of various PD analysis techniques.

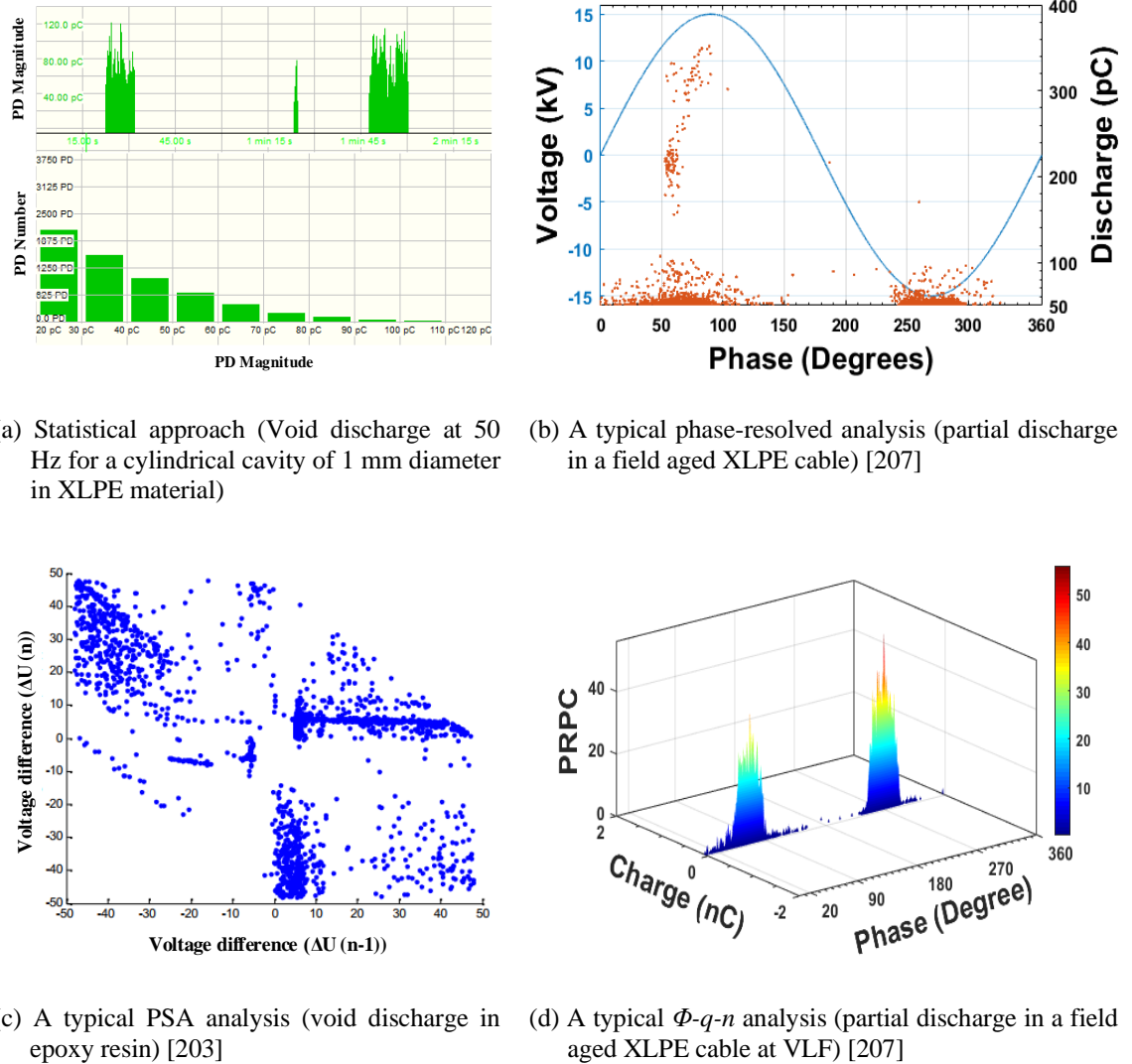


**Figure 3.9.** Graphical representation of various analysis techniques

## 3.7 Physical Parameters Affecting PD Activities

### 3.7.1 Initial Free Electrons Availability

The availability of initial free electrons is a must to initiate a PD event [8], [10], [42]. The initial electron generation rate is strongly dependent on the supply voltage amplitude and frequency, material characteristics, geometries, etc [44], [63], [208]. The free electrons are usually generated from two main sources: surface emission and volume ionisation [42], [143].

#### 3.7.1.1 Surface Emission

Surface emission is the major source of providing free electrons in which under the influence of electric stress and temperature, free electrons are generated from the insulation surface, cavity wall or the electrode surface [33], [208], [209]. Surface emission can be originated from the detrapping of electrons from shallow traps within the insulation, the injection from boundary electrodes, the impact of ionisation process etc.

---

During the cavity and surface discharge process, electrons liberated from the cavity wall and the insulation surface provide a source of free electrons, while for corona discharge, it mainly comes from the electrodes [63], [83]. As time progresses, the emission rate increases because the trapped electrons find it easier to escape from the shallow traps. Moreover, the increased electrical stress and temperature are responsible for enhancing the surface-emitted electron rate [210]. For a relatively narrow cavity, an electron avalanche may also develop along the void surface and parallel to the local electric field due to the release of free electrons by photo-ionisation. This process causes more free electrons to be concentrated with higher density on a small region of the cavity wall and also offers similar effects as imposed by the positive space charges.

### 3.7.1.2 Volume Ionisation

Volume ionisation also provides free electrons via a radioactive reaction process due to collision between energetic photons and neutral gas molecules [208], [211]. The ionisation process largely depends on the gas pressure, gas volume subjected to the ionisation, and the gas contents. This process is considered as the main source of providing initial free electrons for an insulation material which has not been affected by PDs before. This is because as the energy required for detrapping initial electrons in an un-aged surface is comparatively much higher than the aged material [143]. Photo-ionisation is another source whereby gas molecules absorb sufficient light energy to free their loosely-bound electrons [211].

## 3.7.2 Time Constant during a PD Process

The space charges generated after electron avalanches can decay through various physical processes [12, 47, 50]. In order to describe the charge transport and decay rate, the three time constants (material time constant  $\tau_{mat}$ , surface time constant  $\tau_{sur}$ , and effective charge decay time constant  $\tau_{decay}$ ) are usually considered which are strongly dependent on the electric field distributions in the tested material [42], [143], [156]. These parameters have influential roles in varying the PD magnitude and phase distributions.

### 3.7.2.1 Material Time Constant $\tau_{mat}$

Surface charges after PDs may move into the bulk material through volume conduction and result in a decrease of their quantity along the cavity wall or the degraded surface. The decay rate can be modelled with  $\tau_{mat}$  which mostly depends on the material conductivity [44], [62]. A lower  $\tau_{mat}$  implies a faster surface charge decay rate; however, this mechanism is not significant due to a very low value of volume conductivity in some dielectric materials [62].

### 3.7.2.2 Surface Time Constant $\tau_{sur}$

This parameter defines the decay rate of free charges along the cavity surface or the insulation surface and is mainly dependent on the surface conductivity [33], [150]–[154]. A

---

higher conductivity favours faster decay and reduces the availability of initial free electrons between two consecutive discharge events. This time constant is significant when the period of the applied voltage is much larger, and in this case, all the surface charges are expected to decay before the waveform polarity reversal occurs [33], [62], [212]. The surface conductivity can also be increased by the chemical deterioration of the cavity wall due to the repetitive discharges or due to the ageing effects [140], [213].

### 3.7.2.3 Charge Decay Time Constant, $\tau_{decay}$

After PDs, some free charges in a cavity wall or the surface tend to trap in shallow traps within the solid insulation. As time progresses, they may move into deeper traps in proximity of the cavity surface. The deposition of surface charges from a shallow to a deeper trap is controlled by the charge decay time constant,  $\tau_{decay}$  [143], [156], [157]. The smaller  $\tau_{decay}$  means a faster charge decay rate through the deposition process into deeper traps. More movement of surface charges to the deeper traps indicates a lesser electron generation rate [143], [156].

### 3.7.3 Statistical Time Lag & Formative Time Lag

After exceeding the PDIV level, the supply voltage cannot trigger a PD instantly because free electrons may or may not be available at that time to initiate an electron avalanche. To account for this, a small delay time, so-called statistical time lag  $\tau_{stat}$ , is introduced which is defined as the time difference between the instant at which the electric field exceeds  $E_{inc}$  and that when the actual PD happens [143], [156], [208]. Sometimes, due to a longer time lag  $\tau_{stat}$ , PD may be observed at some voltage levels which are fairly higher than the actual PDIV value. The statistical time lag is very much noticeable when the applied voltage frequency is relatively lower [208]. As discussed earlier, at very low frequencies, the free charges (space ions and electrons) from previous PD events are less likely to stay for triggering the next PDs. As a result,  $\tau_{stat}$  is very large and a PD might not onset immediately at the instant when the PDIV is exceeded.

Conversely, in the case of higher frequencies (i.e. 50 Hz), the time interval between two consecutive PD events is quite short which reduces the statistical lag, and as a result, PD may happen relatively earlier [61], [208]. However, the statistical time lag might not be always consistent for subsequent discharges. Usually, the first PD takes a relatively long time for its occurrence than the following discharges under the same ac cycle of the supply voltage.

On the other hand, the formative time lag is defined as the time delay that is required to develop an electron avalanche to cause a PD event [214]. This parameter is a frequency dependent quantity and is fairly negligible for the case of higher frequency excitation.

### 3.8 Importance of Filter Bandwidth Setting

Sometimes, because of the higher repetition rate, a pulse-free zone can be observed in a PD cluster, and the conventional detectors may fail to recognise these discharge pulses [10], [58]. Theoretically, by Fourier series, the continuous time domain response of a single discharge event can be transformed into a discrete frequency spectrum of some periodic pulses. The repetition frequency of such pulses is assumed as  $N_{PD}$ . Also, if a burst of PD pulses are equally spaced in the time domain, in the frequency domain it will exhibit a continuous spectrum with multiple peaks regularly spaced at  $N_{PD}$  interval as depicted in Figure 3.10.

In some cases, a PD burst with a very high repetition rate ( $N_{PD}$ ) may exceed the limit of 1 MHz. To recognise these PD signals as well as to perform the quasi-integration in order to estimate the discharge magnitude, the applied filter bandwidth is recommended to be adjusted in such a way that it must capture one or more peaks of the obtained frequency response [10], [41], [215]. An imperfect adjustment of the filter bandwidth (e.g. in the case of narrow-band measurement) may sometimes lead to incorrect interpretation of measurement results. Moreover, the instability of capturing PD events may cause superposition errors, which is likely to provide incorrect measurement reading in the time-domain [10].

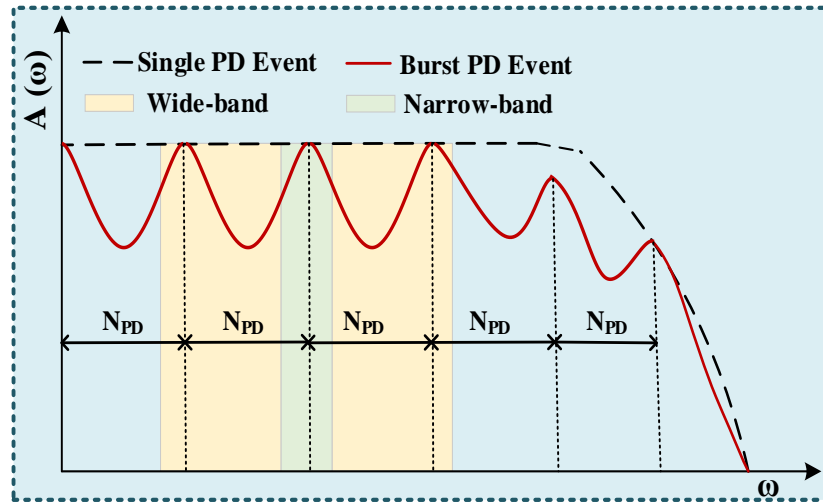


**Figure 3.10.** Frequency spectrum of PD current pulses

The IEC 60270 standard provides a guideline to adjust the filter bandwidth by setting the lower cut-off frequency ( $f_1$ ) and upper cut-off frequency ( $f_2$ ) and there must have adequate attenuation below the frequency  $f_1$  and above  $f_2$ . The recommended filter settings for the wide-band ( $\Delta\omega_w$ ) and narrow-band ( $\Delta\omega_N$ ) measurements are as follows [10], [41]:

$$\text{Wide-band: } \begin{cases} 30 \text{ kHz} \leq f_1 \leq 100 \text{ kHz} \\ f_2 \leq 1 \text{ MHz} \\ 100 \text{ kHz} \leq \Delta\omega_w \leq 900 \text{ kHz} \end{cases} \quad \text{and narrow-band: } \begin{cases} 9 \text{ kHz} \leq \Delta\omega_N \leq 30 \text{ kHz} \\ 50 \text{ kHz} \leq f_m \leq 1 \text{ MHz} \\ f_m = \frac{f_1 + f_2}{2} \end{cases} \quad (3.11)$$

---

The output response of a wide-band PD detector is typically a damped-oscillatory signal with a small resolution time varying from 5  $\mu$ s to 20  $\mu$ s [41], [58]. On the other hand, the output signal of a narrow-band filter is a transient oscillation including the positive and negative peak values varying proportionally to the apparent charge. In this case, the pulse resolution time is comparatively large, typically above 80  $\mu$ s [41], [58]. In the case of higher repetition rate (if more than the set bandwidth), the filter output is an oscillatory waveform which cannot be relied on to interpret the PD signal that is actually generated [215].

### **3.9 Instruments for VLF PD Diagnosis**

For diagnosing insulation over the very low frequency range, a majority of work reported in the literature deploys some commercial test equipment developed according to IEEE 400.2, IEEE 400.3 and IEC 60270 standards for PD measurement [10], [33], [41], [44], [62], [215], [216]. There are many commercially available PD instruments in the market. In this section, only those which have been used in the majority of previous studies are described to get familiarised with their features, sensitivity levels and applications in the VLF range.

#### **3.9.1 Omicron Group Commercial System**

The MPD 600 instrument from Omicron has a variable bandwidth ranging from 9 kHz - 3MHz [217]. It provides a time resolution of 2 ns during PD acquisition. PD measurements e.g. phase-resolved PD pattern (PRPD), ellipse visualisations, PD distribution in multi-phases and individual PD events are possible to measure with this device. Moreover, it provides multi-frequency measurements, detections of fault location in power cable insulation, phase sequence analysis and also can be integrated with the dissipation factor measurement system.

#### **3.9.2 HV Diagnostics PD Test System**

HV diagnostics offers PD30E and PD60-2 portable systems for PD measurements and detections. Both can be used with various VLF power supplies (0.01-0.1 Hz) and can also be integrated with the tan-delta measurements. The test instruments have the features of 125 MHz sampling rate, 100 MHz bandwidth and measurement sensitivity of 5 pC [218].

#### **3.9.3 PD Test Equipment from Baur**

For PD measurement, it comes mainly with two types of detectors: PD-TaD 62 and PD-TaD 80. Both are portable diagnostic systems, operated in parallel with the BAUR VLF generator for PD measurement and location. The systems can acquire PD data from 1 pC to 100 nC [219]. Moreover, these can detect variable PD levels, inception and extinction voltage, PD occurrence frequency. They have high noise immunity, handy for field measuring PDs in the cable insulation, joints and terminations.

---

### 3.9.4 PD Test Equipment from Megger

It includes products like PDS 62-SIN for PD detection and localisation in medium voltage cables. It has advantages of data evaluation and display of PD results in real time and also, recognition and discrimination of PRPD patterns for different types of PD defects such as corona or internal PDs, especially in cable terminations and joints. The PDS 62-SIN is suitable for voltage range up to 62 kV and has a frequency range of 0.01-0.1 Hz and PD range of 2 pC - 100 nC [220].

### 3.9.5 PD Test Equipment from b2HV

It provides PD30-E, PDTD60-2, PDTD90-2, and PDTD120-2 for PD measurements. These instruments can be expandable to the tan-delta assessment and follow the diagnostic approaches documented in IEEE.2-2013 and IEC 60270 standards. These also have the features of PD mapping, phase resolution to categorise different faults, inception and extinction voltage and load-independent frequency ability. All of these have a sampling rate of 125 MHz and operating frequency ranging from 0.01-0.1 Hz with a step of 0.01 Hz [221].

### 3.9.6 PD System from Power Diagnostix

The ICMsystem from Power Diagnostix is basically used as a digital partial discharge detector. The instrument has a variable operating range of supply voltage frequency, including the power frequency (50/60 Hz) and VLF (0.1 Hz). As a non-destructive condition measurement instrument, the system offers high-resolution digital PD patterns for characterising different PD defects in a high voltage insulation system [222].

A summary for comparing products from various manufacturers is given in Table 3.3.

**Table 3.3.** A comparison among various commercial products

Products	Supply Frequency	Bandwidth and Sensitivity	System Portability
MPD 600: Omicron	0.01-2.16 kHz	9 kHz-3 MHz; > 0.015 pC	No
PD 30E: HV Diagnostics	0.01- 0.1Hz	100 MHz ; > 5 pC	Yes
PD-TaD 62: Baur	0.01- 0.1Hz	100 MHz ; > 1 pC	Yes
PDS 62-SIN: Megger	0.01-0.1 Hz	3 KHz- 20MHz ; > 2 pC	Yes
PD30-E: b2HV	0.01-0.1 Hz	100 MHz; > 0.1 pC	Yes
ICMsystem: Power Diagnostix	a wide range including 50 and 0.1 Hz	40 kHz-2 GHz; > 1 pC	No



---

### 3.10 Chapter Conclusion

Various aspects of partial discharge measurements have been presented in this chapter and summarised as follows.

- It reviews challenges associated with HV testing at power frequency, advantage of testing with very low frequency, the importance of diagnostic testing, basic principles of partial discharge occurrence, test techniques, excitation frequency.
- It reviews interpretation of various physical parameters which influence the discharge process under different test frequencies, the necessity of PD filter bandwidth settings, and the applicability of various commercial PD instruments considering their advantages, limitations, sensitivity and applications.
- It describes challenges in interpreting parameters to characterise PD activities, measurement standards, modelling techniques, their comparative analysis, suitability and applications.
- It presents the applicability or suitability of various detections and analysis techniques to diagnose the insulation condition under partial discharge defects.

---

## Chapter 4.

# Dissipation Factor Measurement and PD Influence

Chapters 2 and 3 provide the literature review on the dielectric response and partial discharge measurement respectively; the new findings from this research are presented in the remaining chapters of the thesis. This chapter presents a comparative analysis of the dielectric dissipation factor (DDF) or  $\tan\delta$  measurement for 11-kV cross-linked polyethylene (XLPE) cables. Laboratory experiments are reported on testing at different applied voltage levels at both power frequency (50 Hz) and VLF. Also, differential tangent delta (DTD) and correlation of DDF values are calculated to incorporate with experimental results. In addition, experiments are conducted to investigate the influence of partial discharge on DDF measurement. The work in this chapter has been published in [13], [16] as shown in the List of Publications.

### 4.1 Motivation of the Work

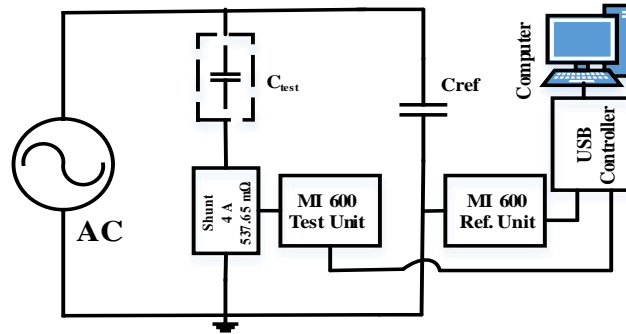
In [81], [223], Hernandez-Mejia *et al.* performed DDF measurement on service-aged and non-aged XLPE cables and demonstrated a relationship between DDF values at 0.1 Hz and power frequency for different voltage, time and protocol sequences. The work was further investigated by Kim *et al.* in 2012 [224] who conducted a diagnostic analysis using the Weibull distribution function for medium-voltage cables. They introduced one-dimensional and two-dimensional matrix patterns and identified the degradation of insulated cable. Afterwards, Perkel *et al.* interpreted the dielectric loss data of service-aged medium-voltage cables from 2007 to 2011 to determine which cables needed replacement or further assessment [5].

As the DDF is found to be dependent on the applied voltage amplitude and frequency; it is of interest to examine  $\tan\delta$  measurement over the frequency range from 50 Hz to 0.1 Hz. This requires performing DDF measurement as a function of applied voltage and providing physical explanations about the discrepancy at various frequencies. Also, the effects of PD on DDF measurement is needed to be examined. This is the motivation for the research performed in this chapter.

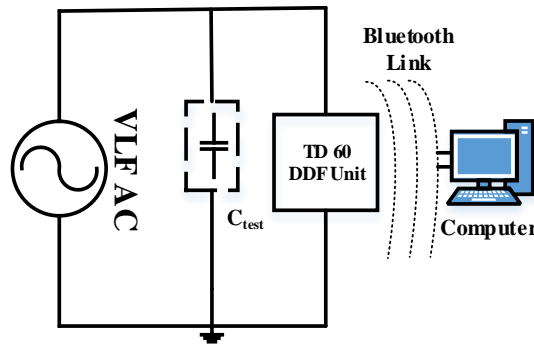
---

## 4.2 Experimental Setup of DDF Measurement

The DDF measurement circuit used for the experiment is depicted in Figure 4.1. The circuit follows the conventional DDF detection techniques well documented in the IEEE 400.2 Standard. The laboratory test setup is shown in Figure 4.2.



(a) From 50 Hz to 5 Hz



(b) 0.1 Hz

**Figure 4.1.** Block diagram of DDF measurement circuit

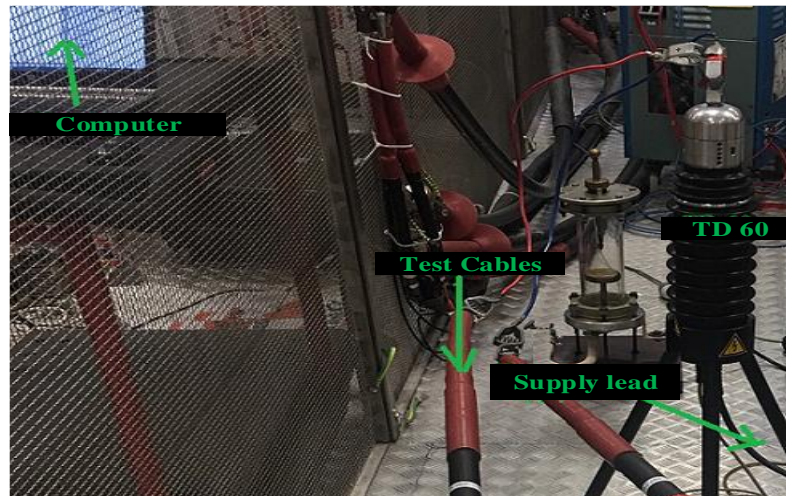
The measurement is divided into two parts. In the first part, the dielectric loss from 50 Hz to 5 Hz is measured by a commercial Mtronix MI 600 universal current measuring system shown in Figure 4.1a and Figure 4.2a.

The measuring system consists of two MI 600 sensor units (reference and test unit), an MCU 502 USB controller and a PC running with Mtronix software. Initially, voltage signals (from 5-50 Hz) are generated from an Agilent waveform generator and then amplified 2000 times by a TREK power amplifier. After that, the amplified signal is fed to a parallel-branched circuit in which one arm contains a reference capacitor (109 pF gas-filled with negligible loss), and the other arm has a series configuration consisting of a test cable and a small shunt resistance. The reference sensor is placed in the reference capacitor branch. Conversely, the test-object sensor is installed in the series branch. The reference capacitor enables the system to extract the ideal capacitive current (i.e. leading the applied voltage by 90°) for reference; its phase angle difference with the current through the test object enables determination of the DDF

value. In the final step, signals from the sensors are transferred to a USB controller circuit via a high-speed optical fiber link. The controller unit connects to the control station (i.e. computer) where all the raw data are processed and stored in real-time for visualisation and monitoring. The recording frequency is one sample per second.



(a) From 50 Hz to 5 Hz

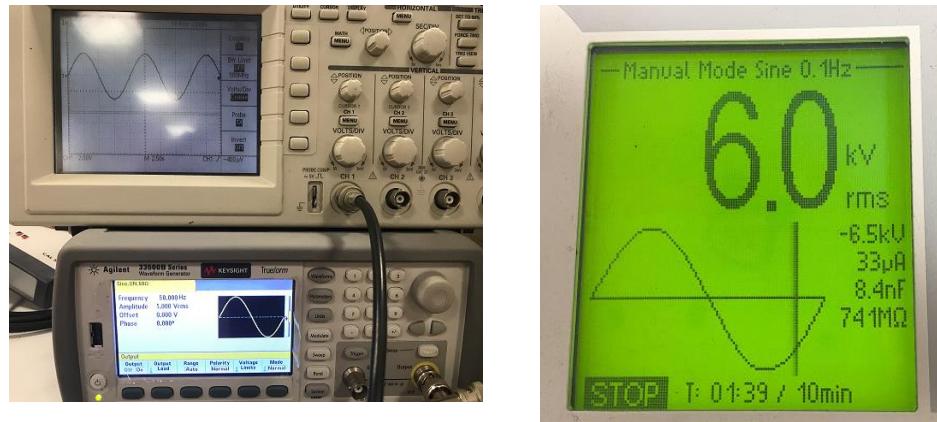


(b) At 0.1 Hz

**Figure 4.2.** Practical laboratory setup of measurements

The Mtronix MI 600 instrument is not intended for DDF measurement at a frequency below 5 Hz. Therefore, another commercial instrument was used for VLF measurement. The block diagram and practical setup for measuring the DDF at 0.1 Hz are shown in Figure 4.1b and Figure 4.2b respectively. Here, the VLF high voltage supply is generated by a commercial HV Diagnostics HVA-60 test instrument. The signal then goes to a versatile tan-delta measuring system, TD-60. The tan-delta value is later measured and recorded to a standard computer running with HVATD software. The system uses a wireless Bluetooth link for transmitting the measured data, thus eliminates the direct physical connection between the TD-60 and the control

unit (computer). The recording frequency is one sample per ten seconds. The waveform generators in the measurements are shown in Figure 4.3.



(a) From 50 Hz to 5 Hz

(b) At 0.1 Hz

**Figure 4.3.** Front Panel of waveform generator

### 4.3 Descriptions of All Test Objects

Different short sections of 11-kV service-aged XLPE cables were used as test objects. These cable samples were provided by a local distribution utility and divided into two groups: Set-1 and Set-2. These two sets were obtained from two different environments. Since the samples of each set are from the same field environment; it is assumed the environmental impacts (e.g. temperature, pressure and moisture) to the samples in the same set are similar.

It should be noted that Chapter 4 and Chapter 5 only describe the experiment analysis of Set-1 cables, while Set-2 cables are not included to avoid redundancy as the latter show the same dielectric characteristics under an AC voltage. However, different ambient temperature conditions (303 K–338 K) were investigated on Set-2 cables by placing them inside a temperature-controlled oven. This is because it is easier to fit these Set-2 samples inside the oven. More details of experimental analysis performed on Set-2 cables are reported in Chapter 6 and Chapter 7.

Figure 4.4 shows all cable samples that were used in this research and their descriptions are listed in Table 4.1.



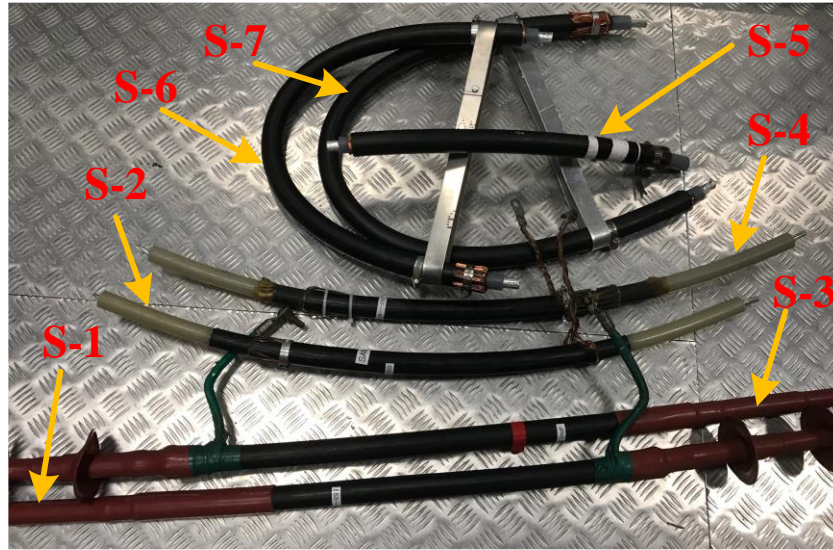


**Figure 4.4.** Photo of all cable samples for dielectric response measurement

**Table 4.1.** Descriptions of cable samples

Cables	Specifications						
	Set-1				Set-2		
	S-1	S-2	S-3	S-4	S-5	S-6	S-7
Cable type	11- kV XLPE Cable						
Core Type	Single Core and Aluminium Stranded						
Length (m)	1.50	1.02	1.47	1.27	0.65	1.01	1.15
Capacitance (pF)	294.20	80.46	298.31	87.73	186.04	346.58	460.08
Core Diameter (mm)	15	7.7	15	7.8	15	15.4	15.4
Insulation Thickness (mm)	7.5	8.3	7.5	8.1	7.5	9.6	9.2
Conductor Cross-section (mm <sup>2</sup> )	176	46.6	176	49.01	176	186	181

In this chapter, DDF measurement is carried out on S-1 to S-4 as a function of the applied voltage amplitude and frequency. As can be seen, two samples (S-1 and S-3) have a capacitance of around 300 pF, while the other two have a relatively lower value of around 100 pF. In addition, partial discharge effects on DDF measurement are investigated in S-3 which has some defects with a PDIV value of around 12 kV. The experiment is carried out at room temperature within 20-25<sup>o</sup> C. The measurement is performed with an excitation voltage of 6 kV, 8 kV, 10 kV and 12 kV.

## 4.4 Formulation of Dissipation Factor Measurement

Conventionally, any electrical insulation can be modelled by a resistor  $R$  and a parallel capacitor  $C$ , and can be represented by a simplified equivalent circuit as shown in Figure 4.5.

Here,  $R$  represents the overall dielectric loss (conduction, polarisation, ionisation losses) and  $C$  represents the lumped capacitance of the cable insulation [10],[29]. Detailed explanations of all losses are provided in Section 2.6.

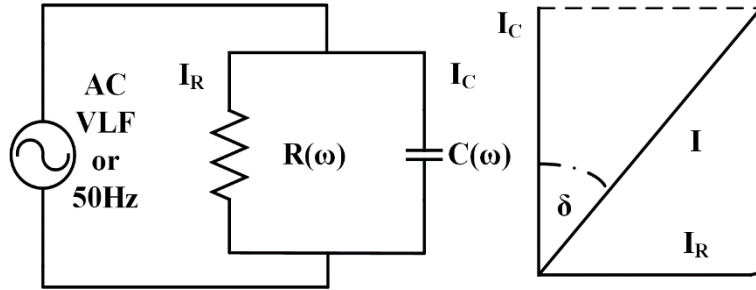


**Figure 4.5.** Equivalent model of cable insulation

$\tan \delta$  values are typically obtained from the phase difference between the applied voltage and the resultant current waveform. The phase angle of the current can be resolved into charging and leakage components. Therefore, the dissipation factor can be defined as the ratio of the leakage current  $I_R$  to the capacitive current  $I_C$ , and their relationship can be derived from Figure 4.5, as shown in the following expression:

$$DDF = \tan \delta = \frac{I_R}{I_C} = \frac{1}{\omega RC} \quad (4.1)$$

where,  $\omega$  denotes the applied voltage angular frequency. Equation (4.1) suggests that unless the dielectric loss is frequency-dependent (i.e. if  $R$  is constant in the equivalent model), under the same applied voltage, the measured DDF value would exhibit a very simple direct inverse relationship with the applied test frequency.

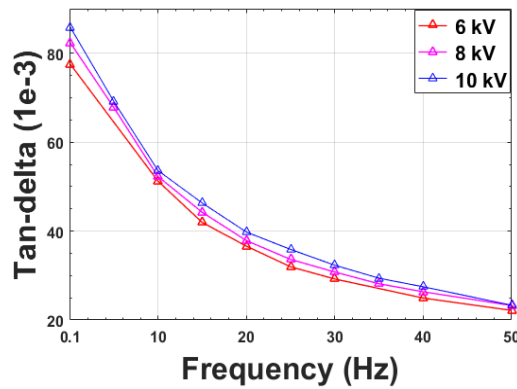
In this present work, all experimental work are performed based on the list of parameters shown in Table 4.2. At each test voltage, more than 6 measurements are performed in order to comply with the recommendation of IEEE Standard 400.2.

**Table 4.2.** Parameters used in the DDF experiment

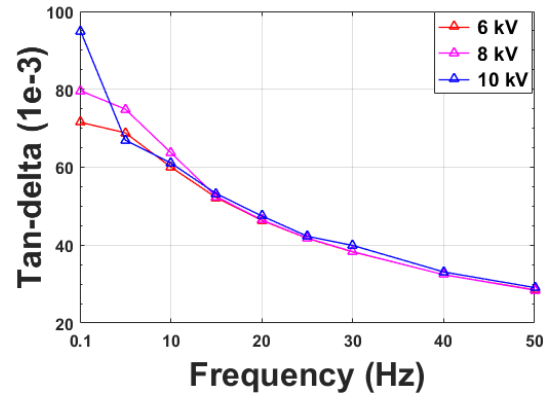
Description	Value
Frequency	50 - 5 Hz and 0.1 Hz
Voltage	6 kV, 8 kV, 10 kV and 15 kV
Reference Capacitance ( $C_{ref}$ )	106.4 pF at 50 Hz
Shunt Resistance	537.65 mΩ
Recording Time	10 minutes
Waveform	Sinusoidal

## 4.5 DDF Measurement as a Function of Applied Voltage

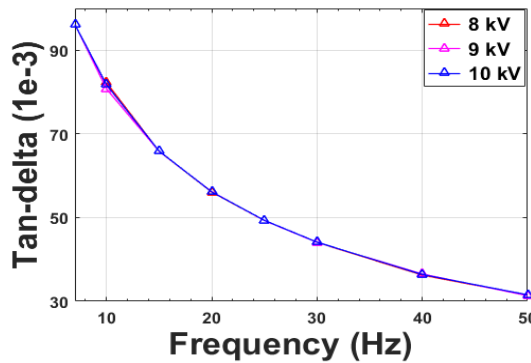
Figure 4.6 shows the dielectric loss measurement of all cable samples in terms of the dissipation factor  $\tan\delta$ . These samples had been in service and so exposed to electric stress. The experimental results of S-1 and S-3 from 50 Hz to 0.1 Hz are depicted in Figure 4.6a and Figure 4.6b respectively. On the other hand, S-3 and S-4 experimental results are shown from 50-5 Hz.



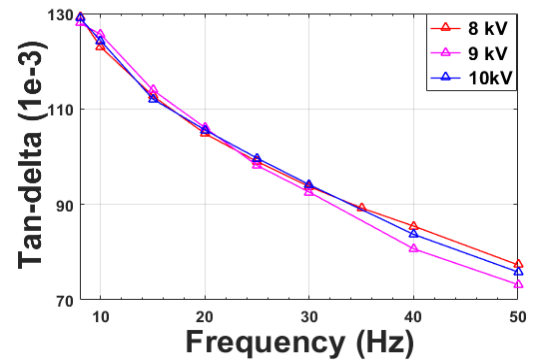
(a) S-1



(b) S-3



(c) S-2



(d) S-4

**Figure 4.6.** DDF vs. excitation frequency of cable samples

This is because the HV-TD60 system has a tendency to show inaccurate DDF value when the test-object capacitance is small. It should be noted that all commercial high voltage DDF equipment for VLF application are designed for large capacitance test objects, typically a minimum capacitance of 3000 pF. Since the capacitance of S-2 and S-4 is lower than 100 pF (listed in Table 4.1), due to uncertainty about the accuracy, DDF values at VLF are excluded from the following plots. This was verified with the real measurements and it was found that the  $\tan$ -delta curve over the lower frequency zone fails to follow conventional trend with HV-TD60 system. Another issue for these two samples is that the leakage current at 6 kV is likely to be very small and as a result, the MI 600 system was not able to determine DDF value over the 5 Hz to 50 Hz range.



Here, the average DDF value at any frequency over the measurement period is presented. From Figure 4.6, it can be observed that the dielectric loss is highly dependent on the excitation frequency and is much increased at lower frequencies. At 6 kV and 8 kV, S-1 and S-3 show almost identical incremental trends of DDF values because both samples possess almost the same capacitance value. However, at 10 kV, S-3 exhibits a higher DDF value than S-1 for 0.1 Hz applied voltage. As mentioned before, S-3 contains some internal defects, and possible occurrence of PDs may be responsible for a higher DDF value. On the other hand, due to low capacitance, S-2 and S-4 show a higher DDF value. Also, S-4 presents a higher dielectric loss, possibly because of the presence of a termination joint at one end.

The voltage-dependent responses of S-1 and S-3 for various frequencies are depicted in Figure 4.7. It can be seen that the DDF values for all voltage levels at 50 Hz are the same. On the other hand, an increase of dissipation factor with excitation voltage at 0.1 Hz is also noticed.

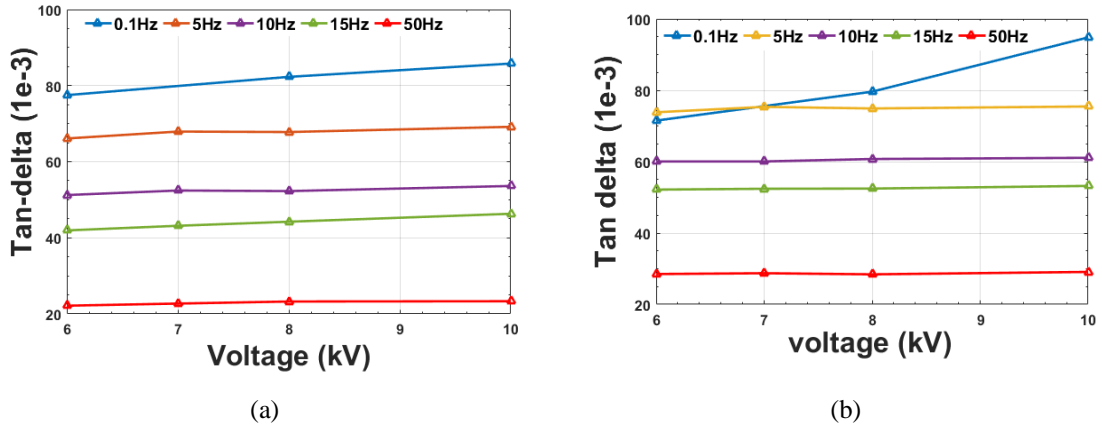


**Figure 4.7.** Voltage dependency (in rms): (a) S-1 (b) S-3

It can be observed that the DDF value at 50 Hz is not exactly 500 times less than that at 0.1 Hz. This may be explained by several factors. One factor is the complex nature of the polarisation effect of the dielectric material. When an external electric field is applied, the material will be polarised, and the polarisation current along with the conduction current will flow through the material. Therefore, the conventional  $R$ - $C$  circuit for DDF measurement in Figure 4.5 is rather simplistic. It should be expanded and modelled by a parallel equivalent circuit as shown on the top-left corner of Figure 4.8. This modified circuit is popularly known as the extended version of the Debye model [66]. Here  $C_0$  denotes the geometric capacitance, and  $R_0$  denotes the DC conductivity resistance. Here the excitation is considered to be below the partial discharge inception voltage (PDIV); hence, discharge activities are ignored in the figure.

The circuit comprises multiple parallel branches where each branch contains a series connection of resistor and capacitor. Each branch describes an independent polarisation event such as interfacial polarisation, polarisation in bulk material, polarisation in an amorphous interface, polarisation due to the charge carriers, etc. Under the influence of an electrical field,

the electric dipoles will try to align with the field, resulting in a delay in their response [10], [39], [58]. This relaxation delay can be characterised by different time-dependent charging and discharging constants such as ( $\tau_1=R_1C_1$ ,  $\tau_2=R_2C_2\dots$ ), which are associated with the different polarisation events. Depending on the applied frequency, these constants respond differently to the excitation frequency and introduce a certain amount of time delay in the equivalent circuit [38].

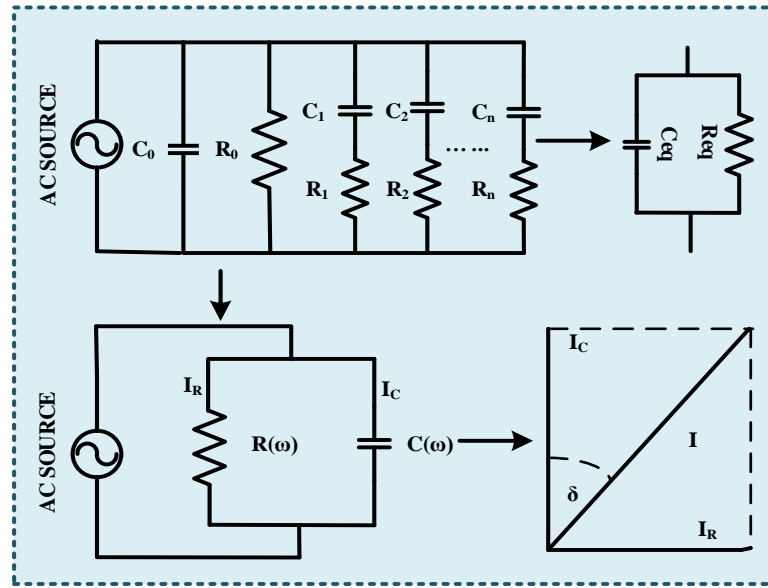


**Figure 4.8.** Equivalent circuit of dielectric and simplified form

In short, the polarisation process is highly dependent on the excitation frequency, and so is the polarisation loss associated with friction between the oscillating dipoles. At lower frequency, there are less oscillations and thus less polarisation loss and so the total dielectric loss is dominated by the contribution from the conduction loss.

On the other hand, if the frequency is high enough, some classes of dipoles may not respond quick enough to follow the changing field. In addition to this, the capacitor charges itself in first-quarter half-cycle of voltage waveform then it needs to be discharged before the next cycle of the waveform. However, if the time constant is much longer than the time period of the voltage waveform, it gets less time to discharge completely. Therefore, when a new cycle of voltage appears, still there is a significant amount of residual voltage remains in the capacitor. On the other hand, at lower frequency, the capacitor gets enough time to discharge completely within the one cycle of the applied voltage. Therefore, during the next cycle, it again starts charging from the zero-crossing. This complex circuit can be simplified to an equivalent circuit and illustrated by two characterised parameters ( $R_{eq}$  and  $C_{eq}$ ) in the top-right corner. Here,  $R_{eq}$  represents the overall dielectric loss (conduction and polarisation), and  $C_{eq}$  represents the lumped capacitance of the insulation [40], [51], [54].

Therefore, the dielectric loss can be formulated as

$$\tan \delta = \frac{\sigma_{eq}}{\omega C_{eq}} = \frac{\frac{1}{\omega R_0} + \sum_{i=1}^n \frac{C_i \omega \tau_i}{1 + (\omega \tau_i)^2}}{C_0 + \sum_{i=1}^n \frac{C_i}{1 + (\omega \tau_i)^2}} \quad (4.2)$$

The derivation is provided in Appendix A.1. Here,  $i$  denotes the number of the polarisation process, and  $\tau_i$  implicates the time constant of the associated process. In practical applications, the polarisation effect is usually ignored by field engineers and the model is simplified as a single R-C circuit as shown in the bottom-left corner of Figure 4.8. The resultant current has two components: the leakage ( $I_R$ ) and charging ( $I_C$ ) components, and their relationship is shown in the phasor diagram. Ignoring the polarisation terms, the final  $\tan \delta$  can be obtained as

$$DDF = \tan \delta = \frac{I_R}{I_C} = \frac{1}{\omega R_0 C_0} \quad (4.3)$$

A possible solution to satisfy the requirement of large capacitance ( $> 3$  nF) when using commercial VLF DDF equipment for testing small capacitance sample like in this research is to add a dummy capacitance load in parallel. The modified circuit for tan-delta measurement is shown in Figure 4.9.

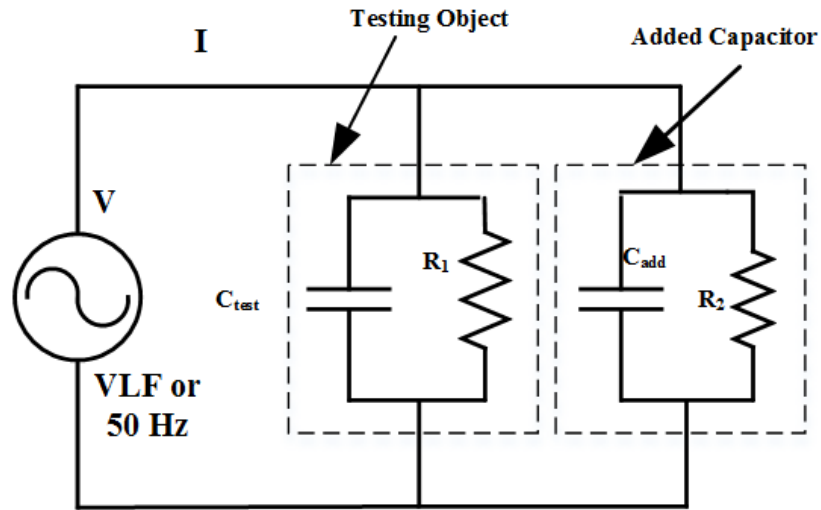


**Figure 4.9.** Modified circuit for low capacitance test sample

In this configuration, the actual tan-delta value of test object can be calculated from the total tan-delta value. If  $\tan \delta_{tot}$  and  $\tan \delta_{test}$  denote the DDF value of the modified circuit and the test object respectively, then the actual tan-delta value of the test object can be obtained by the following equation. The derivation is provided in Appendix A. 2.

$$\tan \delta_{test} = \frac{\beta \tan \delta_{tot}}{1 - \omega R_{tot} C_{add} \tan \delta_{tot}} \quad (4.4)$$

where  $R_{tot} = R_1 || R_2$  and  $\beta = \frac{R_2}{R_1 + R_2}$

If the dummy capacitor is perfectly ideal (i.e.  $R_2 = \infty$ ) then equation (4.4) can be written as follows:

$$\tan \delta_{test} = \frac{\tan \delta_{tot}}{1 - \omega R_1 C_{add} \tan \delta_{tot}} \quad (4.5)$$

## 4.6 Correlation and Differential Tan-Delta Assessment

The overall DDF results of S-1 and S-3 allow establishing a correlation between measurements at power and very-low-frequency for different voltage levels. The correlation plot is shown in Figure 4.10, which is not a strong 1:1 relation. Nevertheless, this information could potentially be of some use in translating diagnostic features from one frequency to another. It can be also noted that the applied voltage has little influence in the correlation. Further testing on more cables with specific insulation defects should be carried out.

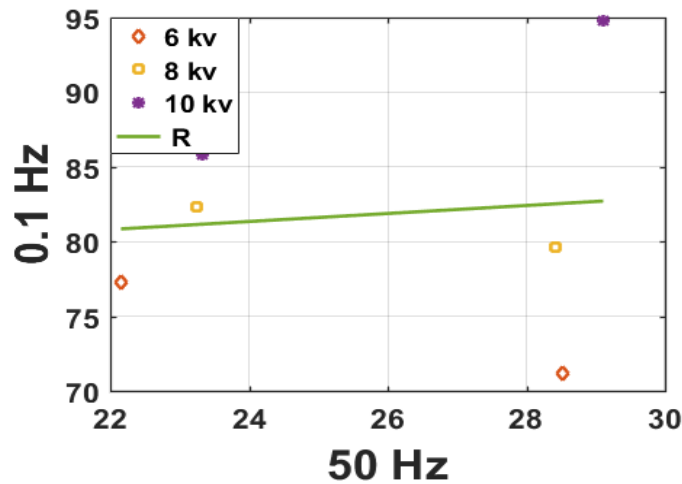


**Figure 4.10.** Correlation of DDF between 50 Hz and 0.1 Hz Frequency

Differential tangent-delta (DTD) measurement is popularly known as the delta tangent-delta or tip-up method. A higher change in DDF value implies a greater degradation of the insulation quality. For measuring DTD values,  $\tan \delta$  values are separately measured at  $1.0 U$ , and  $1.5 U$  and calculated by the following equation:

$$DTD = DDF(1.5U) - DDF(1.0U) \quad (4.6)$$

where  $U$  denotes the rated voltage of the cable. The graphs of DTD values for S-1 and S-3 are shown in Figure 4.11. As expected, the DTD values at 0.1 Hz are much higher than at 50 Hz.

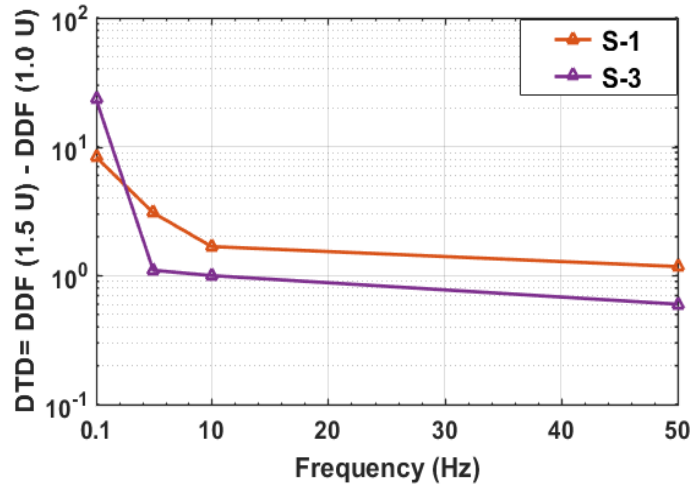


**Figure 4.11.** Comparison of DTD Values with Frequency

## 4.7 Influence of Partial Discharge to the Dissipation factor

### 4.7.1 Relationship between Polarisation and Ionisation Loss

As discussed in Section 2.6, the dielectric loss can be attributed to three different mechanisms: conduction loss, polarisation loss and ionisation loss. The ionisation loss is mainly influenced by partial discharges [58], [225]. If the loss angle ( $\delta$ ) in each case is very small, the resultant dielectric dissipation factor or loss-factor can be described as:

$$\tan \delta_{tot} = \tan \delta_{cond} + \tan \delta_{pol} + \tan \delta_{ion} \quad (4.7)$$

It is also worthwhile to mention that, if various polarisation processes are present in the dielectric, then according to the extended Debye model, the summed contribution due to the conduction loss and the polarisation loss can be formulated and expressed in equation (4.2). From equation (4.7), the total dielectric loss can be simplified as:

$$\tan \delta_{tot} = \frac{\frac{1}{\omega R_0} + \sum_{i=1}^n \frac{C_i \omega \tau_i}{1 + (\omega \tau_i)^2}}{C_0 + \sum_{i=1}^n \frac{C_i}{1 + (\omega \tau_i)^2}} + \tan \delta_{ion} \quad (4.8)$$

However, at very low frequency, the polarisation process is less likely to occur in the dielectric; therefore, the effects due to dipoles are negligible. Hence, the polarisation terms of the total dielectric loss can be ignored. As a result, equation (4.8) can be rewritten as:

$$\tan \delta_{tot} = \frac{\sigma_0}{\omega C_0} + \tan \delta_{ion} \quad (4.9)$$

where  $\sigma_0$  represents the DC conductivity of the material. The inverse-relationship of the total DDF with the excitation frequency explicitly implies the dominance of the conduction process at lower frequencies, which increases linearly with the applied voltage.

---

### 4.7.2 Test Arrangement for Investigating the Effects of PD

The overall experimental work followed can be divided into two parts. Firstly, an AC voltage excitation of either VLF or power frequency is applied to test sample S-3 which has internal voids. After that the resultant partial discharge activities due to the excitation at PDIV are measured. The detailed description of the PD measurement circuit is provided in Chapter 8.

For tan-delta measurement, two different laboratory setups are used. One is for testing at power frequency, whilst the other is for measurement at VLF. The test arrangement for the former is the same as the setup described in Section 4.2. On the other hand, a commercial Baur Frida TD system is used for tan-delta measurement over the VLF range. The Baur Frida system has both the power supply and the DDF measuring tool packaged in an integrated form as shown in Figure 4.12, which provides an excellent means for cable diagnostic testing in the field. The recording rate is 10 sec. per sample.

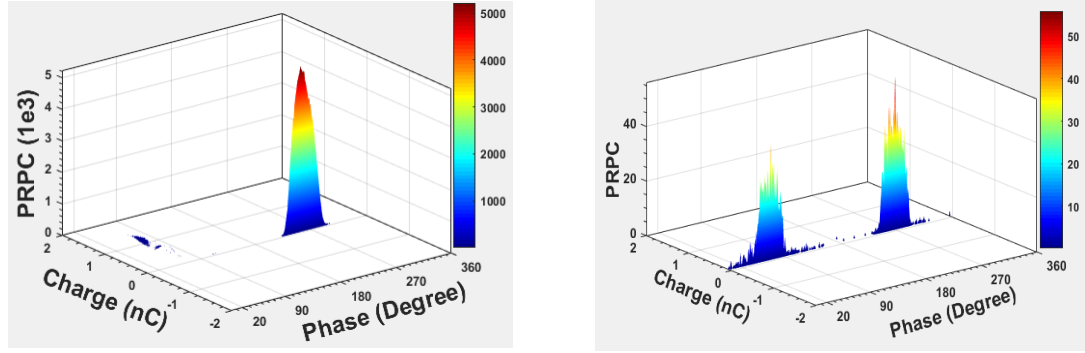


**Figure 4.12.** Front panel view of Baur setup

Comparing the partial discharge at power frequency with VLF, the inception voltage is observed at around 12.9 kV for both cases. To facilitate comparison, all the PD test sequences are performed at 14 kV of the applied voltage. On the other hand, the DDF assessment at both frequencies is carried out from 3 kV to 15 kV. Measurement over a wide voltage range can reveal any tip-up point which suggests the onset of PD activity. In order to avoid any possible environmental influence, all the experiments were performed on the same day at room temperature and pressure. The PD data were recorded for 15 minutes, which corresponds to 45,000 consecutive cycles of 50 Hz or 90 cycles of 0.1 Hz excitation. Conversely, the data of the dissipation factor measurement are recorded for 40 consecutive cycles.

### 4.7.3 Partial Discharge Measurement Results

The phase-resolved analysis of partial discharge at PF and VLF is shown in Figure 4.13. For both frequencies, experimental results are presented for the sinusoidal excitation.



(a) PD at 50 Hz

(b) PD at 0.1 Hz

**Figure 4.13.**  $\phi$ -q-n plot of partial discharge at 50 Hz and 0.1 Hz

The 3D plot of the PDs is presented in the popular  $\phi$ -q-n form, where the symbols represent the applied voltage phase angle, discharge magnitude and discharge repetition rate (PRPC) respectively. To quantify the PRPC in the measurement period, it has been calculated from the ratio of the total number of observed discharge pulses and the number of AC cycles. Due to possible contamination of the smaller discharges by the background noise and interference, a threshold was set so that all the discharge pulses computed here are more than 50 pC.

As can be observed from Figure 4.13, PD activities occur in the positive and negative half-cycles of the applied voltage waveform; however, their phase distribution exhibits non-identical scattering in the two half-cycles. Despite differences in their scattering, the pattern obtained at both frequencies provides similar information. During positive half-cycles of 50 Hz, most of the discharges are concentrated on the rising period (i.e.  $< 90^\circ$  of the applied voltage). However, the discharge pattern obtained at 0.1 Hz continues up to the peak of the applied voltage. Meanwhile, the phase distribution during the negative half-period in all cases is approximately symmetrical around 270 degrees.

A summary of IEC 60270 parameters to characterise PD activities at 50 Hz and 0.1 Hz excitations is tabulated in Table 4.3. Comparing the experimental results with VLF, the power frequency dominantly exhibits a larger PD magnitude (either maximum  $Q_{max}$  or average  $Q_{avg}$ ) and a higher repetition rate per second (PRPS). The trend is also similar in either the positive half-cycle (PHC) or the negative half-cycle (NHC) period. However, the PHC of 50 Hz excitation yields much larger  $Q_{max}$  as compared to the NHC, and the same at VLF. With a change of frequency from 50 Hz to 0.1 Hz, the average discharge of the NHC decreases from 57 pC to 51 pC. On the other hand, the PHC shows a greater change of around 1 nC to 62.5 pC although the repetition rate is smaller in that period.

**Table 4.3.** Characterised parameters for PD

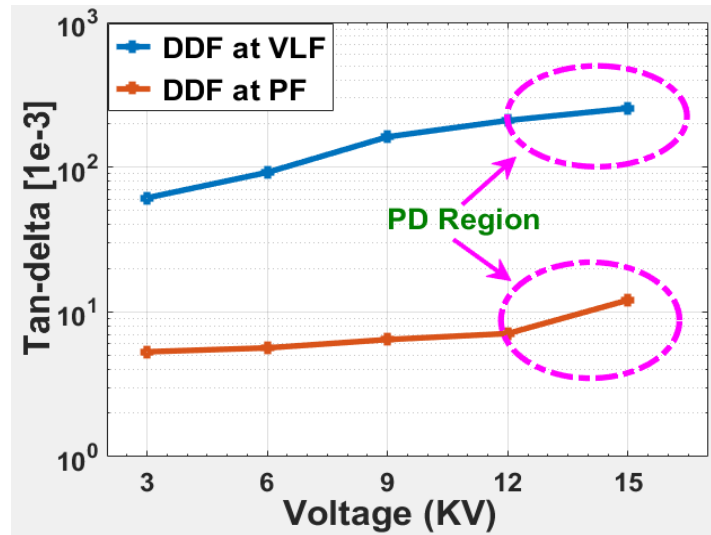
Parameters	50 Hz		0.1 Hz	
	PHC	NHC	PHC	NHC
$Q_{\max}$ (pC)	1517.9	97.25	254.46	54.58
$Q_{\text{avg}}$ (pC)	1001.4	57.30	62.54	51.07
PRPS (PDs/s)	1.561	280.75	0.521	0.111
PRPC (PDs/cycle)	0.0312	5.615	5.211	1.111

\*PHC-Positive half-cycle; NHC-Negative half-cycle

To interpret the presence of discharge source in the test object, the explanations in [31], [83] clearly reveal that during the NHC of VLF, the PD magnitude and PRPS due to corona source are much likely to be higher as compared to the same parameters obtained at 50 Hz. In this experiment, however, PF exhibits much higher value of these quantities than VLF. From the suggestion of literature [31], [33], it can be remarked that the obtained discharge pattern here are mainly due to other discharge types (i.e. cavity or surface).

#### 4.7.4 Dielectric Dissipation Factor Measurement Results

To investigate the dielectric loss, tan-delta measurements were performed on the cable in steps of 3 kV from 3 kV to 15 kV. Based on IEEE 400.2 guidelines, measurements were consecutively taken at 50 Hz and 0.1 Hz. The experimental results are plotted in Figure 4.14.

**Figure 4.14.** Tan-delta measurement at 50 Hz and 0.1 Hz

For every voltage step, the test results presented the mean value of 40 consecutive recorded samples. To provide clear visualisation, after 12 kV, PD inception regions are marked with a pink circle. From the figure, it can be recognised that the resultant dissipation factor due to dielectric loss is strongly dependent on the excitation frequency and exhibits much higher



values at very low frequency. To facilitate a better understanding, a comparison of tan-delta measurements is presented with the boxplots. The measurement results at 15 kV are depicted in Figure 4.15a and Figure 4.15b for 50 Hz and 0.1 Hz excitations, respectively.

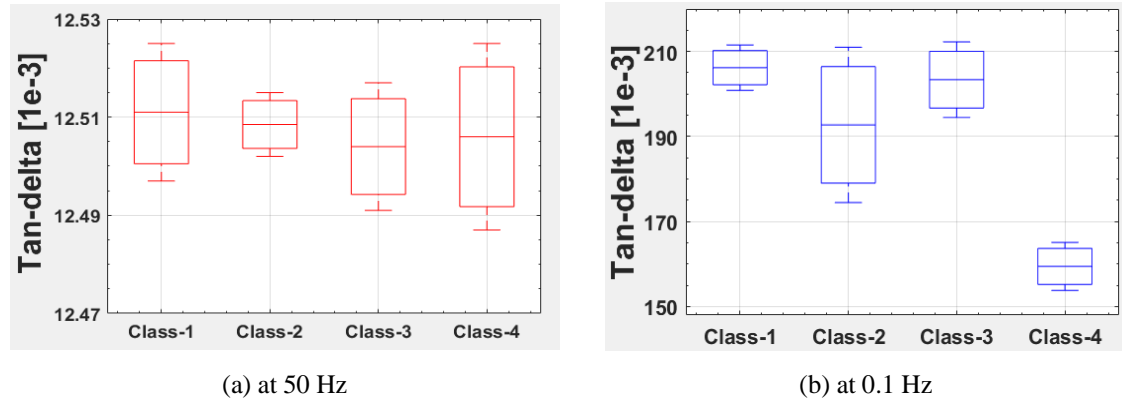


**Figure 4.15.** Box plot of tan-delta values at 50 Hz and 0.1 Hz

All the recorded samples are split into four groups, where each consists of 10 consecutive recorded data. At 50 Hz, for all classes, it can be noticed that the variation of tan-delta value with the mean value is quite negligible ( $< 5\%$ ). However, a comparatively higher percentage change of the DDF value from the mean value is observed at the VLF.

### 4.7.5 Interpretations of Measurement Results

Comparatively higher value of DDF at 0.1 Hz can be explained by the physical processes of dielectrics described in Section 4.5. Below the inception voltage, at higher frequency, the polarisation process is considered to be dominant, and in conjunction with the conduction process, contributes to the total dielectric loss. On the contrary, due to the absence of oscillating dipoles, the total dissipation factor at VLF mostly depends on the conduction loss and increases linearly with the applied voltage. In short, lowering the frequency means increasing the DDF; therefore, measurement at 0.1 Hz is more sensitive than at 50 Hz. As a result, an increase of tan-delta value with 0.1 Hz excitation (till 12 kV) is clearly noticeable in Figure 4.15, whereas, the loss factor at 50 Hz remains almost constant for all voltage levels.

Now if the supply voltage exceeds the PDIV limit (i.e. after 13 kV), the PD loss comes into action and contributes to the total dielectric loss as per equation (4.7). In this case, it can be seen from Figure 4.14 that the slope of the 0.1 Hz tan-delta curve mostly remains unchanged, whereas the slope of the 50 Hz graph exhibits a clear increasing trend after PDIV. In fact, the difference in the obtained shapes is the result of different discharge physical processes occurring at different excitation frequencies. The power frequency produces a comparatively larger magnitude of discharge (nC range in some cases), which contributes to the tip-up of the tan-delta graph. On the

---

other hand, due to the smaller discharge magnitudes, the influence of partial discharges on dissipation factor measurement at VLF tends to be negligible.

## 4.8 Chapter Conclusion

This chapter describes a comparative diagnostic analysis of dielectric loss measurements for medium-voltage cable from frequency 50 Hz to 0.1 Hz. The relatively higher DDF values when measured at VLF are expected because of the lower capacitive charging current. This is obvious because at VLF, the capacitive reactance goes up significantly. However, the polarisation loss of material is very much likely to disappear at very-low-frequency. Consequently, the DDF value at 0.1 Hz is not showing exactly 500 times of that at 50 Hz. In other words, the correlation is not a straightforward direct inverse relationship with the applied frequency due to contribution from the frequency-dependent polarisation loss. Furthermore, the ionisation loss due to dielectric breakdown is influenced by the applied electric field, but the breakdown mechanisms are also frequency dependent.

This chapter also presents a comparative diagnostic study to investigate the influence of partial discharges on dissipation factor measurements. PD measurement results are presented with  $\phi$ -q-n plots and reveal that the larger discharge magnitude at 50 Hz dominantly contributes to the increasing tan-delta value. On the other hand, due to the lower magnitude, the discharge process at VLF makes a negligible change in the dissipation factor curve.

---

## Chapter 5.

# Modelling of Dielectric Dissipation Factor Measurement

This chapter presents an experimental study and modelling of DDF measurement over the frequency range from 1 mHz to 50 Hz. Three different short sections of service-aged 11-kV cross-linked polyethylene (XLPE) cable are used as the test specimens. Low-voltage polarisation/depolarisation current and frequency domain spectroscopy techniques are employed in the investigation. Following the experimental work, numerical analysis is carried out utilising the Debye, Cole-Cole (C-C), Davidson-Cole (D-C) models. To optimise the final parameters of the model, numerical simulation is performed using 3 or 4 R-C branches with different values of Jonscher and D-C constants. The work in this chapter has been published in [1], [14] as shown in the List of Publications.

### 5.1 Previous Relevant Work

As a non-destructive test, the  $\tan \delta$  method was also previously employed in the condition assessment of service-aged XLPE cables and measured the dielectric response in the time and frequency domain [51], [226]. Moreover, their non-linear behaviours under water-tree condition were extensively investigated through experimental analysis in several researches [82]. Recent evidence in [227] reveals that the deterioration of cable under DC/AC excitation is largely influenced by the ageing process and hence yields increasing dielectric loss. The correlation between water-tree growth and ageing has been explored by Gang *et al.*; they remarked that water-tree has an influential role in DDF assessment [54]. Dong *et al.* clearly distinguished the effects of ageing and moisture content of oil-paper insulation and introduced conduction and polarisation losses to the frequency domain spectroscopy analysis [53]. This view is supported by A. Pradhan *et al.* who extended the approach with non-linear modelling under non-sinusoidal excitations [109]. Further along, an experimental study [11] determined the degradation due to the thermal ageing and estimated the consequent conductivity and dielectric loss. Some studies conducted on a wide range of frequencies [129], [228], [229] also suggest that the polarisation

---

process is less likely to contribute to the loss factor at very low frequency.

Because of the difficulty of interpretation, presumably due to the complex behaviour and dynamic properties of dielectrics, DDF modelling was not widely explored. The relationships between various fundamental dielectric parameters and associated physical processes under an applied AC electric field are not fully understood by the experts even now [38], [51], [226]. Thus, it is of interest to explore equivalent circuit modelling based on popular dielectric response theory to simulate dielectric loss measurement over the very low to power frequency range.

## 5.2 Principle of Dielectric Modelling

When a dielectric material is subjected to an electric field, it exhibits various physical phenomena, which are known as the dielectric response. The main losses are due to conduction and polarisation. There is a continual interest in modelling these physical processes by some equivalent circuits. Over the years, many researchers have proposed a number of modelling circuits. In this research, the modelling is based on the Davidson-Cole (D-C) model and Cole-Cole (C-C) model which are a modified form of the popular extended Debye model.

### 5.2.1 Application of Extended Debye model for DDF Modelling

In polymeric insulation, every polar group has a different molecular structure, thus they interact differently with the neighboring molecules, and their response time varies. To explain these physical behaviours, the model extensively followed in dipolar relaxation is the extended Debye circuit. The complex permittivity is expressed in complex form as:

$$\varepsilon^*(\omega) = \varepsilon_\infty + \sum_{i=1}^n \frac{\varepsilon_s - \varepsilon_\infty}{1 + j\omega\tau_i} \quad (5.1)$$

Here,  $\varepsilon_s$ ,  $\varepsilon_\infty$  are the permittivity under DC voltage excitation and at optical frequency respectively [56]. In principle, the model is realised by multiple R-C relaxation branches as separately depicted in Figure 5.1 and discussed in Section 4.5. In the presence of an electric field, their non-identical response of each branch can be characterised by a finite time constant.

It should be noted that a conduction current will flow through the fundamental DC resistance  $R_0$ ; the bulk capacitance is denoted by  $C_0$ . A simplistic equivalent circuit can be derived, as illustrated in Figure 5.1, which comprises primarily an arrangement of lumped capacitance ( $C_{eq}$ ) and loss ( $\sigma_{eq}$ ) components. Here, the relaxation constant is represented by  $\tau = RC$ .

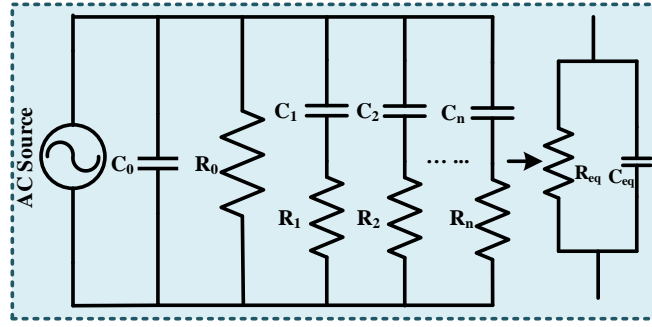


**Figure 5.1.** Extended Debye circuit (left) and simplified equivalent circuit (right).

These lumped parameters can be expressed as (details in Appendix A.1):

$$\begin{aligned}
 C_{eq} &= C_0 + C'_1 + C'_2 + \dots + C'_n = C_0 + \sum_{i=1}^n C'_i \\
 &= C_0 + \sum_{i=1}^n \frac{C_i}{1 + (\omega\tau_i)^2}
 \end{aligned} \tag{5.2}$$

and

$$\begin{aligned}
 \sigma_{eq} &= \sigma_0 + \sigma'_1 + \sigma'_2 + \dots + \sigma'_n = \sigma_0 + \sum_{i=1}^n \sigma'_i \\
 &= \frac{1}{R_0} + \omega \sum_{i=1}^n \frac{C_i \omega \tau_i}{1 + (\omega\tau_i)^2}
 \end{aligned} \tag{5.3}$$

The symbols  $n$ ,  $\sigma$  denote the number of parallel R-C series branches and the conductivity respectively. Additionally, the frequency-dependent terms are introduced to realise the overall polarisation loss. Up to now, the Debye model is generally considered as the fundamental basis for other polarisation-based techniques to assess the dielectric loss in the insulation.

### 5.2.2 Application of Davidson-Cole Model for DDF Modelling

The Davidson-Cole (D-C) model introduces a slight modification of the Debye equations to explain dielectric relaxation. As discussed in Section 2.10.3, a numerical D-C constant  $\beta$  is included in the D-C modelling loss-factor expressions, which contributes significantly to the convergence rate and shape of a tan-delta curve. For a unity value of D-C constant, the model converges sufficiently to the conventional Debye model. For  $n$  polarisation branches, the empirical equation suggested by Davidson and Cole can be written as [26]:

$$\varepsilon^*(\omega) = \varepsilon_\infty + \sum_{i=1}^n \frac{\varepsilon_s - \varepsilon_\infty}{[1 + j\omega\tau_i]^\beta}; \quad 0 \leq \beta \leq 1 \tag{5.4}$$

Segregating the real and imaginary parts and after some manipulation, the simplified form can be expressed as:

$$\varepsilon' - \varepsilon_\infty = (\varepsilon_s - \varepsilon_\infty) (\cos \alpha_i)^\beta \cos(\alpha_i \beta) \tag{5.5}$$

$$\varepsilon'' = (\varepsilon_s - \varepsilon_\infty) (\cos \alpha_i)^\beta \sin(\alpha_i \beta) \quad (5.6)$$

where  $\alpha_i = \tan^{-1}(\omega \tau_i)$

In the D-C modelling, the significance of the  $\beta$  parameter is remarkable due to two reasons. Firstly, for the case of real permittivity ( $\varepsilon'$ ), when the  $\beta$  value increases from 0 to 1, the high-frequency part of the spectrum decreases while the low-frequency part remains unchanged. On the other hand, the imaginary permittivity ( $\varepsilon''$ ) decreases with  $\beta$  in the high-frequency part and increases in the low-frequency part of the spectrum.

### 5.2.3 Application of Cole-Cole Model for DDF Modelling

As mentioned earlier in Section 2.10.2, a Cole constant ( $N$ ) is introduced in the Cole-Cole modelling and contributes significantly to the relaxation process. The model sufficiently converges to the Debye model only if the Cole constant shows null value. For a given material, the characterised parameters for the case of  $n$  branches can be described as [56]:

$$C_{eq} = C_0 + \sum_{i=1}^n c_i \left[ \frac{1}{2} \left( 1 - \frac{\sinh ms_i}{\cosh ms_i + \sin(N\pi/2)} \right) \right] \quad (5.7)$$

and,

$$\sigma_{eq} = \frac{1}{R_0} + \omega \sum_{i=1}^n c_i \left[ \frac{1}{2} \frac{\cos(N\pi/2)}{\cosh ms_i + \sin(N\pi/2)} \right] \quad (5.8)$$

where  $s = \ln(\omega \tau)$ ,  $m = N - 1$ , and  $0 \leq N \leq 1$

### 5.2.4 Relation among Different DDF Modelling

The summary in Table 5.1 shows the relationship between the parameters of the Debye and non-Debye models, and the corresponding complex-plane diagram is depicted in Figure 5.2.

**Table 5.1.** Relation among different modelling parameters

Case	Debye Model	D-C Model	C-C Model
$\frac{\varepsilon' - \varepsilon_\infty}{\varepsilon_s - \varepsilon_\infty}$	$\frac{1}{1 + (\omega \tau)^2}$	$(\cos \alpha)^\beta \cos(\alpha \beta)$	$\frac{1}{2} \left( 1 - \frac{\sinh ms_i}{\cosh ms_i + \sin(N\pi/2)} \right)$
$\frac{\varepsilon''}{\varepsilon_s - \varepsilon_\infty}$	$\frac{\omega \tau}{1 + (\omega \tau)^2}$	$(\cos \alpha)^\beta \sin(\alpha \beta)$	$\frac{1}{2} \frac{\cos(N\pi/2)}{\cosh ms_i + \sin(N\pi/2)}$

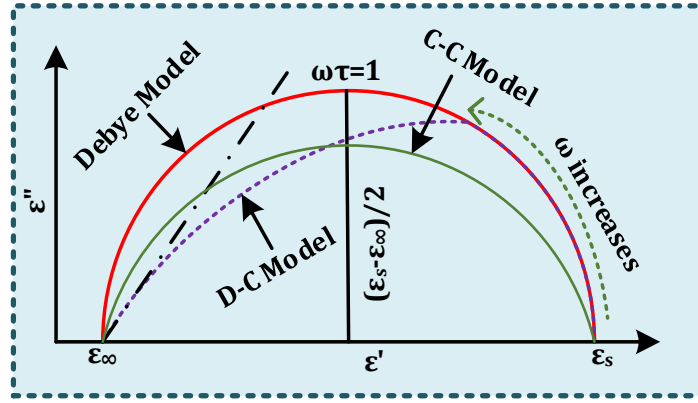


**Figure 5.2.** Difference between Debye and non-Debye models

It can be clearly seen that the geometrical presentation of the D-C curve produces a skewed arc, in which the low-frequency response is likely to follow a semicircle curve whereas, at higher frequencies, it has a quasi-linear response.

### 5.2.5 Jonscher Power Law

Under an alternating voltage, the current density across a material can be realised with an AC component and a DC component. The alternating current is primarily the result of the polarisation effect while the displacement of ionic charge carriers yields the DC current [129]. The relationship between the complex AC conductivity  $\sigma^*_{ac}$  and the permittivity  $\epsilon''$  is given by:

$$\sigma^*(\omega) = \sigma'(\omega) + j\sigma''(\omega) = \omega\epsilon_0 [\epsilon'' + j(\epsilon' - \epsilon_\infty)] \quad (5.9)$$

For a material with a pure conductive loss, the term  $(\epsilon' - \epsilon_\infty)$  becomes negligible. To follow up with the previous discussion, the total conductivity can be summed up as:

$$\sigma(\omega) = \sigma_{dc} + \sigma_{ac} = \sigma_0 + \omega\epsilon_0 \epsilon'' \quad (5.10)$$

To generalise, Jonscher formulated a universal power law, which represents the total conductivity effect on the dielectric response as a function of frequency.

$$\sigma_{ac} = \sigma_0 + a\omega^j; \quad 0.6 \leq j \leq 1 \quad (5.11)$$

### 5.2.6 Dielectric Dissipation Factor

The dielectric dissipation factor (DF) is a widely used parameter to measure the dielectric loss in high voltage apparatus. From the equivalent circuit in Figure 5.1 (right), the generalised expression for the loss factor or  $\tan \delta$  measurement can be written as:

$$DDF = \tan \delta = \frac{\sigma_{eq}}{\omega C_{eq}} \quad (5.12)$$

According to the Debye and D-C models, equation (5.12) can be modified, respectively, as follows:

$$\tan \delta_{debye} = \frac{\frac{1}{R_0} + \omega \sum_{i=1}^n \frac{C_i \omega \tau_i}{1 + (\omega \tau_i)^2}}{\omega \left( C_0 + \sum_{i=1}^n \frac{C_i}{1 + (\omega \tau_i)^2} \right)} \quad (5.13)$$

$$\tan \delta_{C-C} = \frac{\frac{1}{R_0} + \omega \sum_{i=1}^n C_i \left[ \frac{1}{2} \frac{\cos(N\pi/2)}{\cosh ms_i + \sin(N\pi/2)} \right]}{\omega \left[ C_0 + \sum_{i=1}^n C_i \frac{1}{2} \left( 1 - \frac{\sinh ms_i}{\cosh ms_i + \sin(N\pi/2)} \right) \right]} \quad (5.14)$$

and,

$$\tan \delta_{D-C} = \frac{\frac{1}{R_0} + \omega \sum_{i=1}^n C_i (\cos \alpha_i)^\beta \sin(\alpha_i \beta)}{\omega \left( C_0 + \sum_{i=1}^n C_i (\cos \alpha_i)^\beta \cos(\alpha_i \beta) \right)} \quad (5.15)$$

After ignoring the polarisation circuit, it can be seen that the complex circuit converts into the simplistic form of traditional measurement circuit (i.e.  $\tan \delta = 1/(\omega R_0 C_0)$ ).

## 5.3 Experimental Analysis

### 5.3.1 Measurement of Polarisation/Depolarisation Current

To investigate the slow polarising effect in the time domain, the polarisation/depolarisation current (PDC) method is commonly employed for diagnostic analysis. The basic circuit for PDC assessment is shown in Figure 5.3. In principle, the polarisation current involves a charging and conduction current while the depolarisation current contains the discharging component. The responses are then translated to the time-domain spectroscopy, which corresponds to the lowest dielectric loss at the respective frequencies.

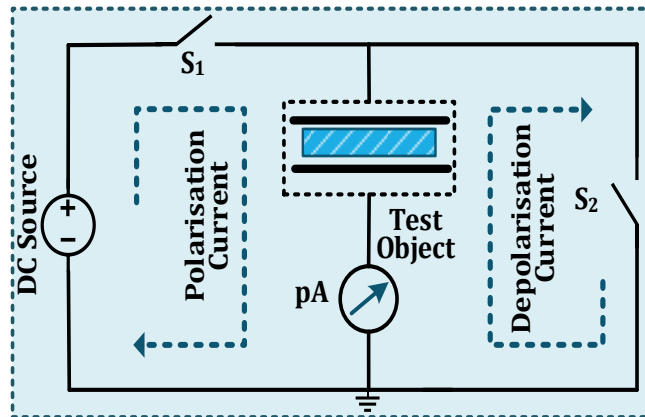


**Figure 5.3.** Basic circuit for the PDC measurement



For PDC measurement, an external DC voltage ( $U_0$ ) is applied to the test object by closing switch  $S_1$  and opening switch  $S_2$ , and the resultant current is measured by an electrometer or a highly sensitive ammeter. For a sufficiently long period ( $T_c$ ), the power supply stimulates the charging process with different time constants. Charging of the primary capacitance  $C_0$  lasts for a few seconds and is then assumed to be almost fully charged. After that, the system is deliberately short-circuited by closing switch  $S_2$  and opening switch  $S_1$ . This automatic switching operation, in fact, initiates the depolarisation process in the opposite direction and the charge stored in the test object begins to decay more or less exponentially to a steady-state DC value. This DC current, depending on the dielectric resistance, continues till the end of the measurement period [10], [71].

Since the system cannot switch instantaneously, a small delay time (up to 5 seconds) is included before both measurements to avoid possible damage to the electrometer due to the abrupt rise of DC voltage. The analytical expressions of polarisation and depolarisation currents are derived from equation (2.8) and expressed as follows. Here  $\varphi(t)$  denotes the response function:

$$I_{pol}(t) = C_0 U_0 \left[ \frac{\sigma_0}{\varepsilon_0} + \varphi(t) \right] \quad (5.16)$$

$$I_{dep}(t) = -C_0 U_0 [\varphi(t) - \varphi(t + T_c)] \quad (5.17)$$

### 5.3.2 DDF Measurement Using Frequency Domain Spectroscopy

Frequency domain spectroscopy (FDS) is a useful diagnostic tool to study the polarisation and conduction loss in the frequency domain. The schematic diagram of FDS measurement is shown in Figure 5.4.

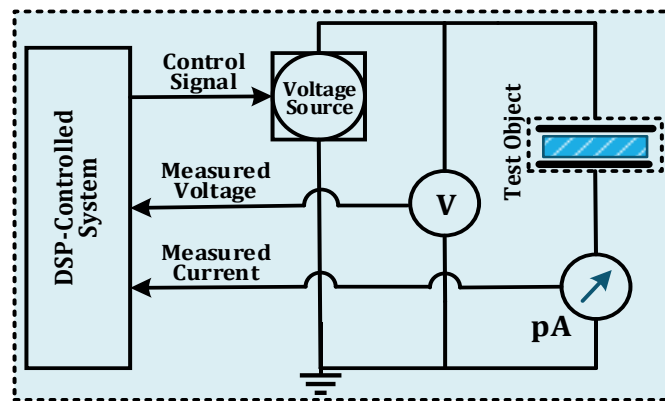


**Figure 5.4.** Basic circuit for FDS measurement

In this method, a sinusoidal AC voltage excitation  $U^*(\omega)$  with varying frequency is applied to the test specimen, and the corresponding capacitive current  $I^*(\omega)$  is measured. Due to the dielectric loss, the phase angle between the applied voltage and the generated current is

not precisely  $90^\circ$ , rather the current shows a slight deviation/phase delay with the quadrature component. The current passing through a homogeneous dielectric can be expressed as:

$$I^*(\omega) = j\omega C^*(\omega)U^*(\omega) \quad (5.18)$$

where  $C^*(\omega)$  is the complex capacitance of the dielectric and is represented by:

$$C^*(\omega) = [\varepsilon'(\omega) - j\varepsilon''(\omega)]C_0 = C'(\omega) - jC''(\omega) \quad (5.19)$$

Here,  $\varepsilon'$  and  $\varepsilon''$  denote the real and imaginary permittivity respectively. Based on the phase delay, the real and imaginary capacitances of the dielectric as a function of frequency are measured and subsequently used to quantify the corresponding loss factor. Usually, this can be done by deploying a DSP-based control system, which in general involves the fast Fourier or Laplace transform of the captured signals. Based on this interpreted quantity, the working principle of tan-delta measurements is given by:

$$\tan \delta(\omega) = \frac{C''(\omega)}{C'(\omega)} = \frac{\varepsilon''(\omega)}{\varepsilon'(\omega)} \quad (5.20)$$

### 5.3.3 Practical Experimental Setup

The practical laboratory setup for the experiment is shown in Figure 5.5. An Omicron Dirana system was used for the measurement. As test objects, S-1, S-2, and S-3 and also their parallel arrangement were employed, this is denoted as S-P. A short description of S-1, S-2 and S-3 is provided in Table 4.1. Here, the test object S-P is not tabulated since it consists of the parallel arrangement of the other three samples. The whole experimental work was carried out over two days at room temperature within 20-25  $^\circ\text{C}$ . For PDC analysis, a step of 200 V DC was applied to energise the cable specimen and initiate the polarisation process. The measurement period was set for 1000 seconds while the recording rate was one sample/second. In the FDS study, a sinusoidal voltage with a maximum amplitude of 200 V was swept over the frequency range from 1 mHz to 50 Hz.

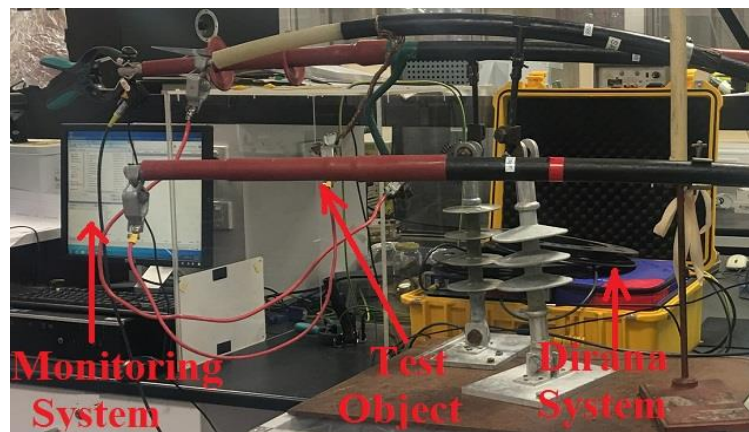


**Figure 5.5.** Practical setup for PDC experiments

## 5.4 Computation Process

The working procedures of DDF modelling are illustrated with a flowchart in Figure 5.6. By using the Debye and D-C models, the whole process is simulated over the required range of frequencies in MATLAB. For simulation, total numbers of 3-4 branches are considered to give reasonable modelling. Data processing involves a suitable set of polarisation and depolarisation currents as input. The following sections describe various steps to evaluate the measured loss-factor.

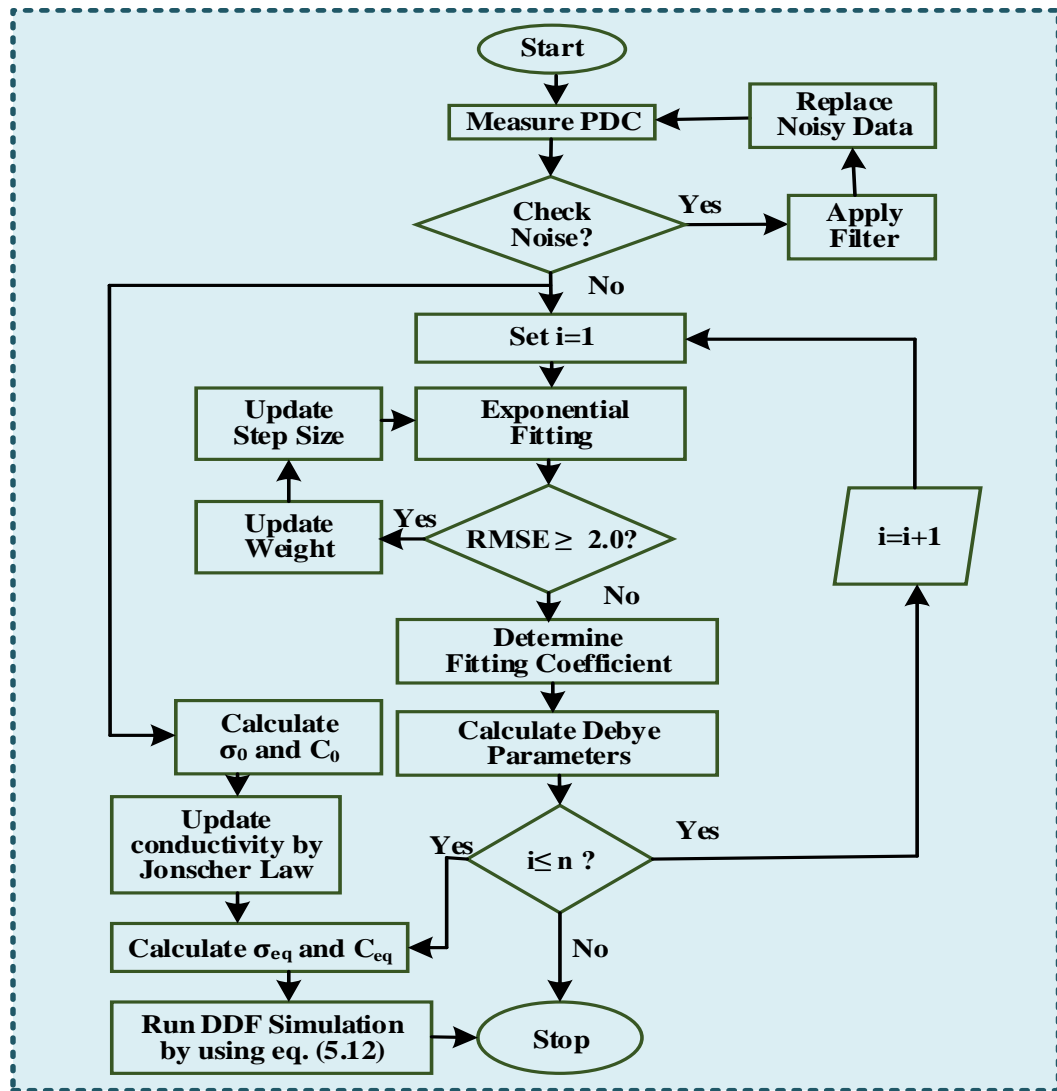


Figure 5.6. Flowchart of working algorithm. \*RMSE - root-mean-square error

### 5.4.1 Effects of Noise and Filtering

As mentioned earlier, the presence of noise or interference is unavoidable in practice. Some possible sources can be the coupling of AC currents from nearby energised power equipment, high-frequency ripple from the DC power supply, electromagnetic or electrostatic inductive effects from high-voltage installations. In addition, the cable insulation resistance

sometimes exceeds  $10^{12} \Omega$ , and so the measured polarisation/depolarisation current would be in the pA or nA range. Such a small signal exacerbates the undesirable impact caused by the superimposed noise. A low-pass filter can be used to improve the performance. Generally, this is done by deploying a digital filter, as the filter characteristics can easily be adjusted through the software operation.

To suppress the high-frequency random noise, a software-based Butterworth filter was implemented in this work. The applied second-order filter had a passband frequency of 2 Hz and a 6 dB cut-off frequency of 10 Hz. This can also be characterised by unity gain in the passband and 15 dB attenuation in the stopband. The sampling rate was 200 Hz.

Figure 5.7 shows the pre-filtered and post-filtered depolarisation currents for various cable specimens. For clearer visualisation, the filtered response of S-3 is not shown. This is because the depolarisation currents from S-1 and S-3 are almost identical; hence, one overlaps with the other. Instead of sweeping over the whole period, the filter operation was carried over a duration slightly longer than the noisy part. After that, the original data were replaced with the filtered current. Comparing with other samples, the depolarised current of S-2 tends to exhibit smaller value than other specimens. The plots of Figure 5.7 also reveal that measured currents decay with time and are highly affected by interference at the end of the measurement period.

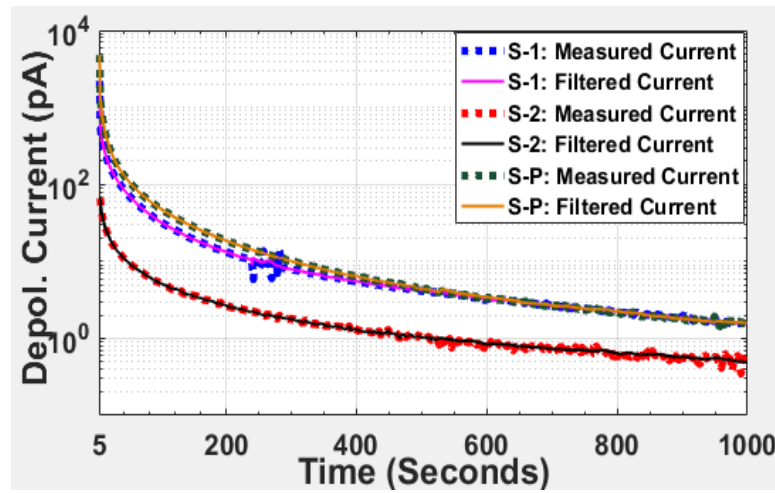


**Figure 5.7.** Pre- and post-filter plot of depolarisation current

### 5.4.2 Elementary Parameters Estimation

As seen in equation (5.16), the polarised current has conductive and charging components. For a longer charging period, the response term  $\varphi(t+T_c)$  is able to decay completely and therefore, it can be approximated as  $\varphi(t+T_c) \approx 0$ . After removal of the DC excitation, the conductive current, as shown in Figure 5.8, can be obtained explicitly from the difference between the polarisation and depolarisation currents.

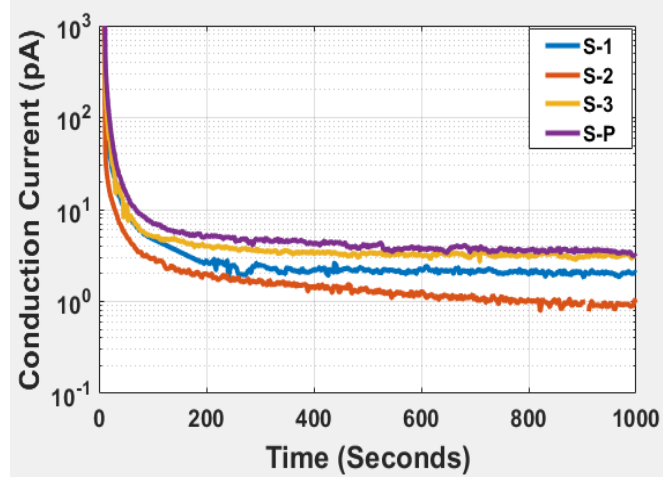


**Figure 5.8.** Conduction currents of various test samples

It is also apparent that the measured currents show an almost time-independent behaviour most of the time. Ideally, it should be consistent. However, a little inconsistency as observed at the very beginning may be attributed to the non-linear response of practical dielectric systems. Of interest is the corresponding DC conductivity which can be estimated as:

$$\sigma_0 = \frac{\varepsilon_0}{C_0 U_0} [I_{pol}(t) - I_{dep}(t)] \quad (5.21)$$

where  $\varepsilon_0$  denotes the permittivity of free space. A common approach to determine the primary capacitance  $C_0$  is to measure it at power frequency using a capacitance meter. In the experiment, this can be readily obtained from the Dirana setup. These elementary parameters are summarised in Table 5.2.

**Table 5.2.** Elementary parameter estimations

Cable	Lossy Part		Bulk Insulation $C_0$ pF
	$\sigma_0$ ( $10^{-15}$ s)	$R_0$ (T $\Omega$ )	
S-1	0.778	1285.8	294.31
S-2	0.506	1974.4	80.40
S-3	0.827	1223.8	298.3
S-P	1.042	959.31	679.5

Evidently, the tabulated values support the experimental results in Figure 5.8. As can be clearly seen, the higher  $\sigma_0$  value makes larger DC current in polymeric insulation. This is why the parallel configuration has a higher conduction current than the other test cases.

### 5.4.3 Exponential Fitting

Various polarisation events contribute to the dielectric loss, and in the absence of an electrical field, their physical characteristics relax considerably with time. Due to the nature of

these relaxations, the discharging current for polymeric insulation can mathematically be described as:

$$I_d = \sum_{i=1}^n A_i e^{-t/\tau_i} \quad (5.22)$$

Here, the parameter  $i$  denotes the number of R-C branches as mentioned in equation (5.1). The expressed time-dependent decay can be empirically obtained with the exponential fitting for 3-4 branches. For the case of three branches, Figure 5.9 depicts the fitting plots of depolarisation currents for various test objects. Basically, the depolarised data after filtering are transferred to MATLAB to get a reasonable curve fitting. For evaluation, the Levenberg-Marquardt algorithm was used and iteratively tested. Furthermore, the fitting goodness was evaluated through multiple performance functions such as RMSE, regression coefficient  $R^2$  etc. To achieve higher accuracy, these functions were monitored after every iteration and followed by updating both the step size and weight of the algorithm. A lower value of RMSE ( $\leq 2\%$ ) and a higher value of  $R^2$  ( $\geq 0.99$ ) implicate a strong agreement between experimental results and the fitted curve.

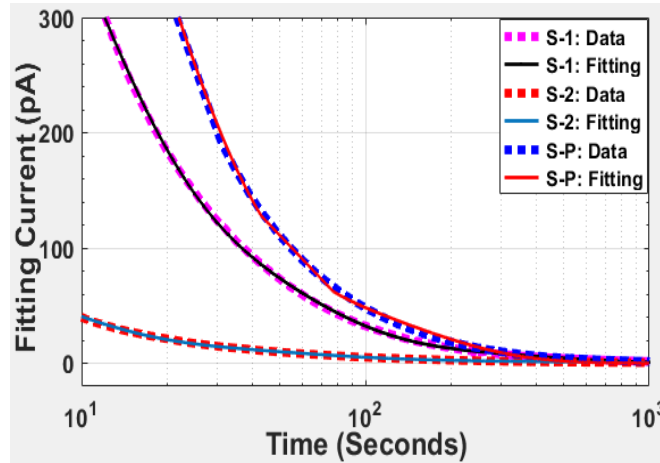


**Figure 5.9.** Exponential fitting of the measured depolarisation currents

#### 5.4.4 Debye Parameters Estimations

The fitted results are post-processed to determine the Debye circuit parameters. Here, the estimated values convey the corresponding time-constant information for different branches. The formulas used for calculating the Debye parameters are:

$$R_i = \frac{U_0}{A_i} (1 - e^{-t_c/\tau_i}) \quad \text{and} \quad c_i = \frac{\tau_i}{R_i} \quad (5.23)$$

The R-C equivalent circuit parameters with three and four branches for the tested cable samples are listed in Table 5.3.

**Table 5.3.** Debye parameters estimation for the DDF modelling

Cable		$R_1$ (T $\Omega$ )	$C_1$ (pF)	$R_2$ (T $\Omega$ )	$C_2$ (pF)	$R_3$ (T $\Omega$ )	$C_3$ (pF)	$R_4$ (T $\Omega$ )	$C_4$ (pF)
<b>S-1</b>	<b>Branch-3</b>	0.316	26.64	9.293	35.33	1.167	37.42	-	-
	<b>Branch-4</b>	0.315	26.54	9.305	35.33	1.165	37.42	1680	0.318
<b>S-2</b>	<b>Branch-3</b>	36.78	7.693	5.468	4.157	295.8	0.005	-	-
	<b>Branch-4</b>	1.068	3.069	6.419	2.479	75.45	8.245	20.11	4.067
<b>S-3</b>	<b>Branch-3</b>	0.312	44.08	10461	5.078	2.667	44.84	-	-
	<b>Branch-4</b>	1.094	35.45	10461	5.653	7.824	32.13	0.235	34.59
<b>S-P</b>	<b>Branch-3</b>	804.41	3.728	0.221	68.45	1.887	65.17	-	-
	<b>Branch-4</b>	0.1582	71.41	1.376	71.84	228.9	0.016	2848	0.0019

## 5.5 Modelling Results with C-C Model

Figure 5.10 illustrates a comparative analysis of dissipation factor measurement for the S-1 and S-3 samples ranging from 0.1 Hz to 50 Hz. The modelling scenario has been considered for a three-branch R-C circuit. Here, the measured tan-delta from FDS and PDC techniques is compared with the simulation result.

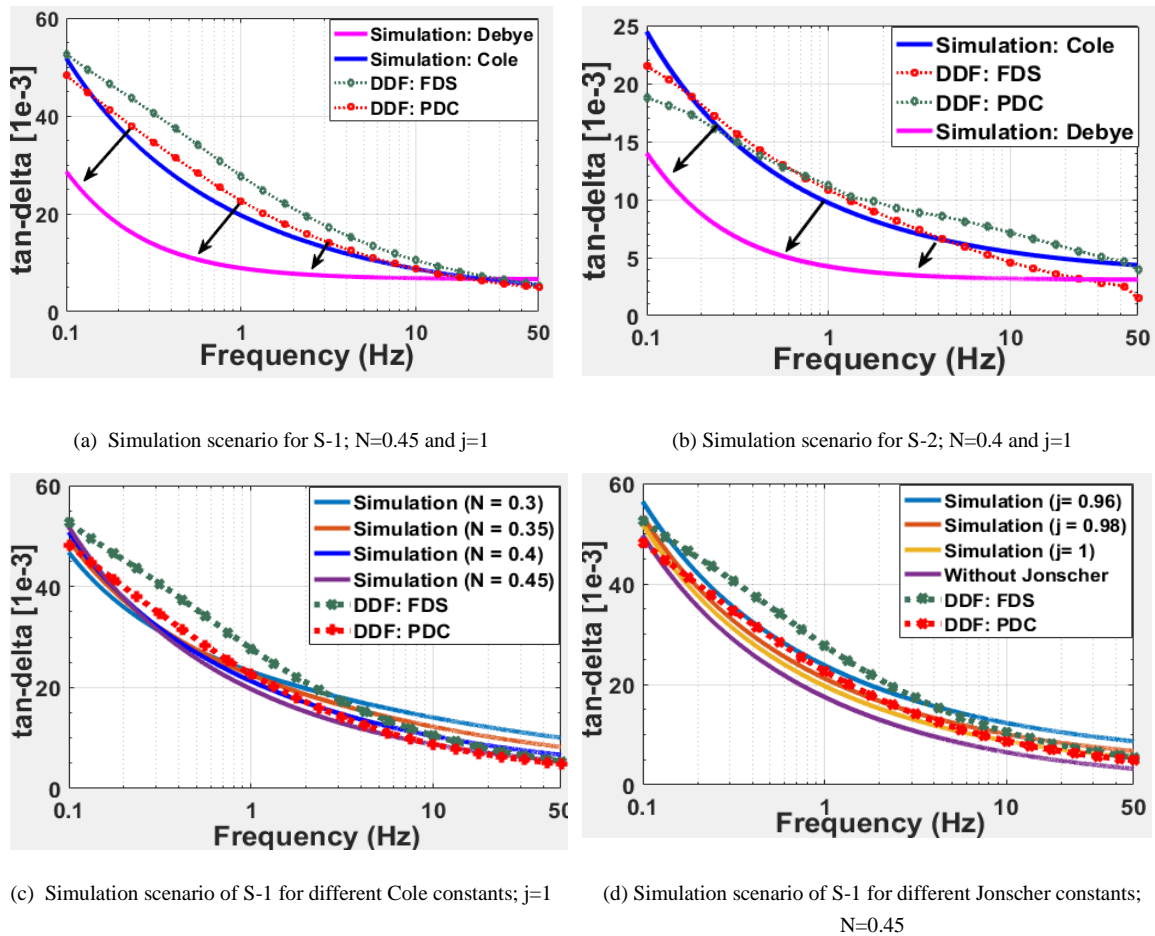


**Figure 5.10.** Comparison of DDF values between the experimental and simulation result

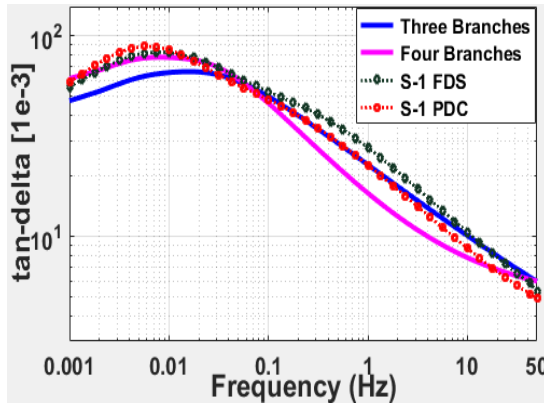
For lower frequency, it can be seen that the Debye model is unable to follow the measured curve, whereas the Cole model matches fairly well over the whole concerned frequency range. To verify the influence of different modelling constants, one can examine Figure 5.10c and Figure 5.10d. Here, the results are only presented for S-1 to avoid redundancy. It is apparent from Figure 5.10c that the best performance is achieved for Cole constant  $N=0.4$ . This result, in fact, suggests that a wise selection of  $N$  can enhance the modelling performance. Additionally, the plot of Figure 5.10d reveals that any ignorance of the Jonscher constant can induce a significant deviation in the calculated curve.



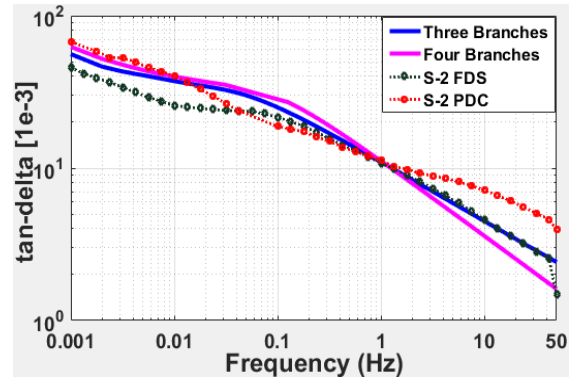
In summary, based on the Debye and Cole-Cole relaxation process, this section investigates dielectric response measurement of XLPE cables from very low frequency to power frequency range. Comparing with the Debye process, the calculated tan-delta from the latter model matches well with the measured data. Moreover, the additional use of Cole and Jonscher constants improves the simulation performance. Nevertheless, it is still required to modify the model in order to investigate the dielectric loss beyond the frequency range considered here; therefore, the DDF simulation based on D-C model has been introduced and discussed in the next section.

## 5.6 Modelling Results with D-C Model

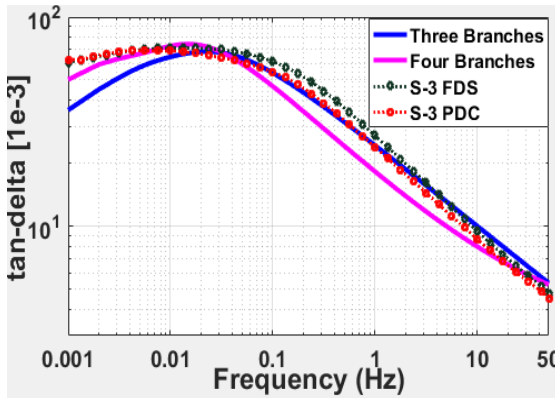
A comparative analysis of dissipation factor modelling along with measurement results for samples 1-3 and their parallel arrangement are shown in Figure 5.11. Here, the simulation results are compared with the experimental FDS and PDC techniques for 3 branches and 4 branches.



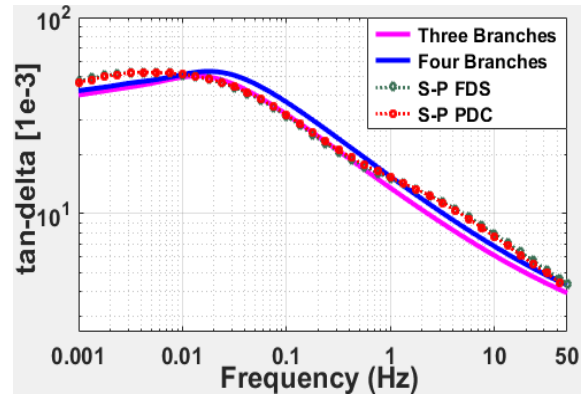
(a) Simulation scenario for S-1;  $\beta=0.45$  and  $j=1$



(b) Simulation scenario for S-2;  $\beta=0.45$  and  $j=1$



(c) Simulation scenario for S-3;  $\beta=0.45$  and  $j=1$



(d) Simulation scenario for S-P;  $\beta=0.45$  and  $j=1$

**Figure 5.11.** Comparison between the experimental and simulation results based on D-C modelling

---

Most of the local loss-peak frequencies from the experiment are observed around 0.01 Hz, and so as with the simulation. These might be caused by the accumulated charge at the polymeric interface or due to the space-charge polarisation [56]. The only exception can be noticed for S-2 in which the loss factor exhibits a more varying pattern but the modelled results manage to track the experimental trends. A slight discrepancy at the lower frequencies in modelling could be due to the inadequacy of assessing the exact conductivity from the numerical fitting below 1 Hz. This is because the polarisation processes at very low frequency are less likely to occur. Therefore, the total dielectric loss tends to depend substantially on the conduction process. On the other hand, the polarisation current contributes dominantly to the loss at the higher frequencies.

The polarisation currents are the results of oscillating dipoles, usually originated from their angular or linear movement under the application of an alternating field. The originated dipoles usually follow the Debye model and relax according to an exponential law ( $e^{-t/\tau}$ ) [56], [129]. In general, this polarisation process is called Debye polarisation. Possible sources of the Debye polarisation are the oscillating dipoles inside the bulk insulation, the bounded charges at the interface of the cable semi-con and insulation layers, the trapped charges due to localised defects present in a dielectric, etc. Higher frequencies will result in higher oscillations; whereas, at lower frequencies, there are less oscillating dipoles, and the frequency-dependent polarisation term of equation (5.15) tends to become negligible. As a result, this equation can be rewritten as:

$$\tan \delta_{D-C} = \frac{1}{\omega R_0 C_0} = \frac{\sigma_0}{\omega C_0} \quad (5.24)$$

The conductivity term ( $\sigma_0/\omega$ ) is very sensitive to the frequency change and increases substantially as the frequency becomes lower. Moreover, an increase of the conductivity due to the bounded/trapped charges at the semi-con/insulation interface or the localised sites dramatically increases the dissipation factor at lower frequencies [11], [56], [66]. On the other hand, due to the lower value of ( $\sigma_0/\omega$ ) at higher frequencies, the conductivity has less influence on the loss factor, and the loss factor mostly depends on the polarisation process. In the Debye circuit, the higher frequency electric field dominates the capacitance of the insulation; whereas, at lower frequencies the resistance plays a more important role [66].

From studying the influence of different D-C and Jonscher constants on the modelling, a comparison is presented in Figure 5.12 and Figure 5.13. To avoid redundancy, both experimental and modelling analyses presented here are only for S-1 and S-P. It can be seen that the best performance is achieved for the D-C constant  $\beta = 0.4-0.5$ . It is also apparent from Figure 5.12b and Figure 5.12b that the Jonscher constant has a significant influence on the

modelling. Omission of the Jonscher constant causes abnormality to the calculated tan-delta curve. In all cases, the value of parameter  $a$  has been chosen in such a way that it follows the quantity  $KE_0$ ; where  $0.3 \leq K \leq 0.6$ . The results from the illustrated figure further suggest that a careful selection of  $\beta$ ,  $j$  and  $i$  can enhance the modelling performance in loss factor measurements.

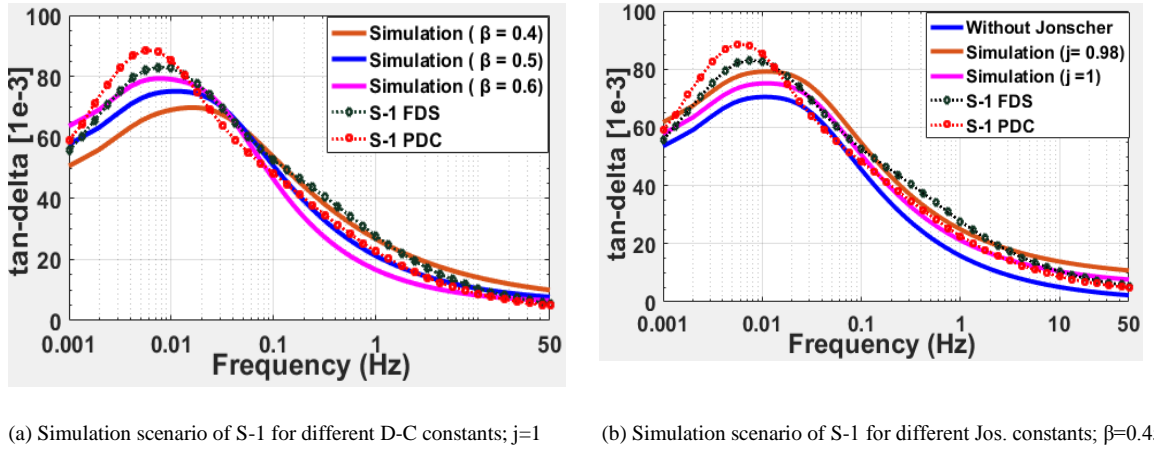


**Figure 5.12.** Influence of D-C and Jonscher (Jos) constant for S-1

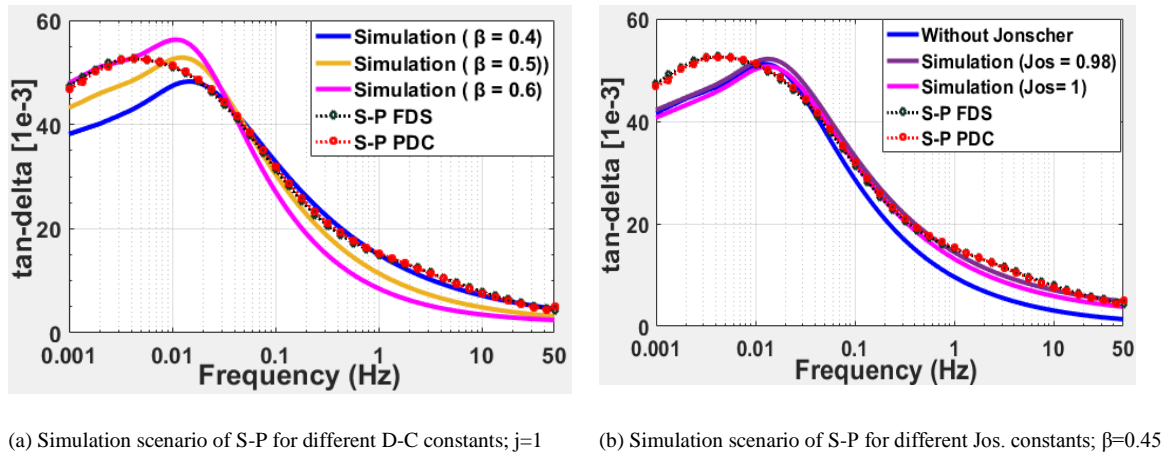


**Figure 5.13.** Influence of D-C and Jonscher (Jos) constant for S-P

Figure 5.14 depicts comparison of the D-C model with other popular models (e.g. Debye, Cole-Cole) in tan-delta measurements. The illustrated results are shown only for S-1. It can be clearly seen that the Debye model deviates substantially at higher frequencies whereas the modelled results from Cole-Cole simulation diverge significantly at frequencies below 0.1 Hz. Comparing with other models, the employed D-C model follows fairly well over the tested frequency range.

In this research, the measurement and modelling of  $\tan\delta$  are carried out over the VLF to power frequency range. This is because most high voltage power networks operate at the power frequency. The motivation is to investigate physical behaviours of the insulation under VLF excitations and compare their dielectric response with that at the power frequency. This is why the

frequency sweeping in the FDS measurement was stopped at 50 Hz. It would be of interest to investigate how far the developed model is applicable beyond the power frequency. The dipole behaviours are expected to vary with the increasing frequency and the modelling based on the equivalent Debye circuit needs to be modified to correlate with the experimental results.

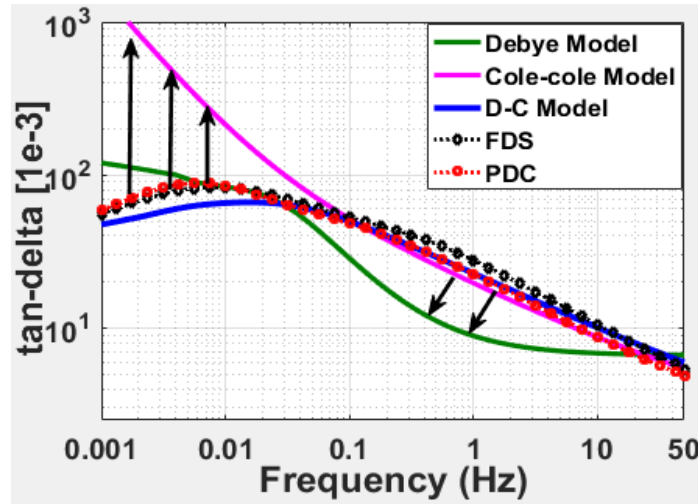


**Figure 5.14.** Comparison of D-C model with other models

## 5.7 Field Aspects of Measurements

To date, there is a lack of documented diagnostic study on XLPE cables which discusses the field aspects of FDS and PDC measurements in terms of cable length and applied voltage magnitude over the tested frequency range. Due to the lower  $\tan \delta$  value, testing with power frequency excitation is probably not a suitable option to study the dielectric response. The IEEE 400.2 Standard provides an insight on field measurements for XLPE cables below 1 Hz (0.01 -1.0 Hz) [68]. The cable length considered here is in between 0.5 m -105 m. In this FDS study, the assessment criteria are summarised in Table 5.4.

**Table 5.4.** Assessment Criteria of field aged XLPE cable [68]

Cable	Mean $\tan \delta$ [ $10^{-3}$ ]	
	North America (at $U_0$ )	Other Countries (at $2 U_0$ )
No action required	<4	<1.2
Further Study	4 to 50	1.2 to 2
Action required	>50	>2

\* $U_0$  – rated rms phase-to-ground voltage

PDC tests usually are performed at a lower voltage, typically 100 - 1000 V [54], [229]. The higher voltage might cause ionisation loss in the test specimen and also increase the complexity of the measurement circuit [207]. In this method, the cable length may vary from 0.2 m -100 m. It

---

---

should also be noted that comparing with time domain measurements, the FDS methods are more robust in tackling noise and requirement of complicated hardware [51], [230].

For  $\tan \delta$  modelling, Hamon's approximation is well recognised, but the approximation is generally applicable for a dielectric in which the discharging current follows a power law ( $\propto t^{-k}$ ;  $0.3 < k < 1.2$ ) and has a single polarisation event. However, the dielectric response current (either polarisation or depolarisation) here mostly follows exponential law, decays more or less exponentially with time and having multiple polarisation events. Therefore, Hamon's approximation might not be a suitable approach to extrapolate  $\tan \delta$  from PDC measurements for XLPE cables. Moreover, according to CIGRE TB493 [105], Hamon's transformation is valid as long as the dielectric response current is voltage independent. Here, both the polarisation and depolarisation currents are found to be voltage dependent; therefore, D-C, C-C and Debye dipolar models are adopted to perform  $\tan \delta$  modelling over the very low to power frequency range.

## 5.8 Chapter Conclusion

In this chapter, an experimental study followed by empirical modelling for tan-delta measurement over the frequency range of 1 mHz - 50 Hz is presented. A physical explanation is presented which deals with the process of conduction and polarisation losses. The Davidson-Cole model is implemented which realised the finite time constants by a number of parallel R-C relaxation branches. In this respect, the extracted characteristic parameters through exponential fitting make the modelling simpler to realise. It is found that the modelling results, when considering Jonscher and D-C constants, assist appreciably in matching the measured tan-delta curve. For lower frequencies, the tan-delta characteristics are primarily influenced by the conduction loss, whilst at higher frequencies the polarisation loss comes into effect and contributes to the tan-delta.

---

---

## Chapter 6.

# Dielectric Response Measurement under Ambient Temperature Conditions

Chapter 5 described the modelling of dielectric dissipation factor measurement over the very low frequency (1 mHz) to power frequency (50 Hz) range under room temperature conditions. This chapter examines the dielectric response at various ambient temperatures (293 K-338 K) using frequency domain spectroscopy (FDS) method. It includes the measurement of the loss peak frequency, mean relaxation time, DC conductivity, activation energy etc. Frohlich's analysis is also included to investigate the distribution of dissipation factors under room temperature conditions. Some challenges to the FDS measurement, such as the edge effects, termination's influence, impacts of voltage amplitudes and the necessity of guarding are reported. The work in this chapter has been published in [3] as shown in the List of Publications.

### 6.1 XLPE Polymer Geometry and Features

XLPE materials exhibit good electrical, mechanical and thermal properties. They are widely used as the primary insulation in extruded HVAC power cables. For industrial production, the process mostly followed is to crosslink the base polymer, such as low-density polyethylene (LDPE), with a commercial peroxide (e.g. Dicumyl peroxide -DCP) [56], [231]. The main chemical reactions during the crosslinking of LDPE with DCP are illustrated in Figure 6.1.

As can be observed, the cross-linked polyethylene has an interconnected network of main chains, in which numerous secondary branches are attached. When the material is subjected to an external electric and thermal field, the dipoles originating from primary and side chains are also excited and react in different ways, which are collectively known as the dielectric response. The dielectric response is mainly contributed by the conduction and polarisation processes of molecules. However, the study of dielectric response in XLPE insulated power cable is different

from that for thin film. This is mainly for three reasons: (i) the difference in morphological structure, (ii) the semicon layers, prepared from carbon black, have unique dielectric properties and cannot be replicated into thin films, (iii) the trapping distribution is also different.

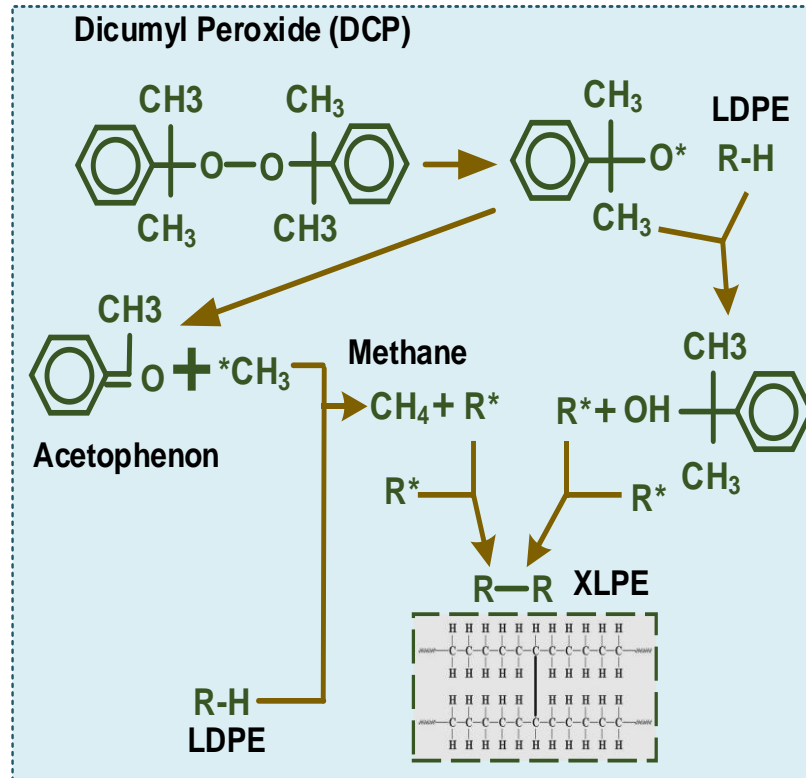


**Figure 6.1.** The cross-linking process of LDPE with DCP.

To interpret the dielectric loss at a constant frequency, the influence of temperature can be considered as a variable. The physical structure at different temperatures also has an influential role [232], [233]. Morphologically, at room temperature, XLPE material exhibits a semi-crystalline structure, in which low-crystalline areas are mostly surrounded by bulk amorphous regions. In contrast to LDPE, XLPE shows lower crystallinity and is ideally assumed to be free of individual imperfect rotational side groups (e.g.  $-CH_3$ ). In the presence of an electric field, the originated dipoles may execute three different relaxation processes as illustrated in Figure 6.2.

Apart from the melting point ( $T_m$ ), the glass transition temperature ( $T_g$ ) is of interest to explain the thermal response. For semi-crystalline materials,  $T_g$  is the intermediate temperature at which the dielectric changes its phase from glassy to a super-cooled/amorphous state. However, the XLPE's base polymer LDPE has a reasonably low  $T_g$  value (typically  $-120^\circ\text{C}$ ). This is because of (i) the absence of intermolecular cohesive forces and (ii) the low mass of the  $C-H$  bond [56].



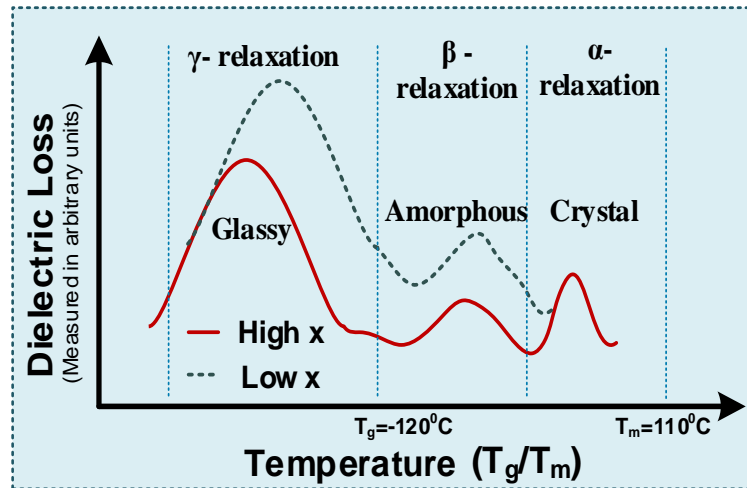


**Figure 6.2.** Relaxation processes in semi-crystalline XLPE material; \*x= crystallinity fraction (the proportion of crystallinity in the semi-crystalline material)

In this research, the experimental investigation is carried out from 293 K-338 K; therefore, it is highly expected to observe  $\alpha$ - and  $\beta$ - relaxations in this temperature range [56]. The  $\beta$ -relaxation may show its peak near room temperature, whereas the  $\alpha$ -relaxation may onset with increasing temperature progressing to the melting point (110°C). Thus, the different relaxation processes at different temperatures stimulate continuing interest to measure the dielectric dissipation factor in service-aged power cables.

## 6.2 Descriptions of Ambient Condition Investigations

The Omicron Dirana system was used for FDS measurements. As discussed earlier, frequency domain spectroscopy (FDS) method involves sweeping a sinusoidal voltage excitation over a wide range of frequencies and later quantifying the corresponding loss factor. An estimation of amplitude and phase delay between the applied voltage and the generated current due to physical processes is subsequently used to interpret the complex capacitance and the corresponding loss-factor.

For this part, Set-2 cable samples (S-5, S-6 and S-7) were used as test objects to investigate the effects of ambient temperature conditions. The experiment was carried out for each cable sample individually but measurement was also performed for two cable samples connected in parallel (S-5 and S-6) denoted as S56-P. These cables had been exposed to the same field environment; therefore, their ageing conditions were assumed to be similar. The FDS study was conducted with a sinusoidal voltage of 200 V peak amplitude and swept over the frequency range from 1 mHz to 50 Hz. Different ambient temperatures (293 K-338 K) were achieved by placing the test samples inside an electric oven. The oven temperature was maintained constant during the experiment. Each FDS study takes around 5 hours, and the



complete experiment was carried out over four weeks. Figure 6.3 shows the laboratory setup for the experiment.

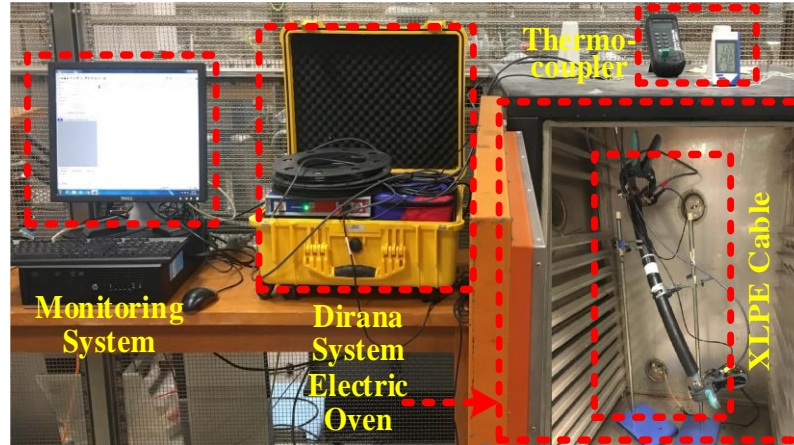


**Figure 6.3.** Practical laboratory setup for the experiment

A summary of test sequences is given in Table 6.1. The short description of all samples is also provided in Table 4.1. The cable capacitance  $C_0$  at power frequency 50 Hz can be readily obtained from the Dirana measurement and shown in Table 4.1. Note that the test object S56-P is not tabulated as it consists of the parallel arrangement of S-5 and S-6.

**Table 6.1.** Analysis of different cable samples

Cable	Frohlich Analysis	$\tan \delta$ (2D View)	$\tan \delta$ (3D View)	Activation Energy	Pol/ Depol. Current
S-1	√	-	-	-	√
S-3	√	-	-	-	√
S-5	√	√	-	√	√
S-6	√		√	√	√
S-7		√		√	√
S56-P (S-5   S-6)	-	-	√	√	√

## 6.3 Frohlich's Analysis

As discussed earlier, molecules of XLPE material are not spherical; instead, they constitute a long chain in their formation. Under an external field, their axis of rotation creates dipoles and contributes to the dielectric response and the dielectric loss. Moreover, in the solid phase, the dipoles are more likely to be interactive in their responses. Also, with the frequency change of the alternating electric field, the responses are not identical and show different values over a wide range of frequencies.

To understand the different dynamicity, Frohlich introduced a dipolar model to show the relationship among the relaxation time, excitation frequency and dissipation factor. Frohlich generalised the model by assuming that the transition of dipoles from one energy level to another is limited and requires a potential energy, usually supplied by the external environment. This energy is popularly known as the activation energy, expressed in terms of electron volts (eV) and can be defined as a DC energy barrier separating two equilibrium positions. It was also assumed that the transition follows Arrhenius expression and the relaxation times corresponding to energy  $v_1$  and  $v_2$  are given by [56] :

$$\begin{cases} \tau_1 = \tau_0 \exp\left(\frac{v_1}{kT}\right) \\ \tau_2 = \tau_0 \exp\left(\frac{v_2}{kT}\right) \end{cases} \quad (6.1)$$

Here,  $k$  and  $T$  denote the Boltzmann constant (8.617 eV/K) and ambient temperature respectively. Also,  $\tau_0$  is a constant measured at absolute temperature. For generalisation, the dependence of the dielectric loss on the angular frequency ( $\omega$ ) has been simplified to a factor ( $\varepsilon''/\varepsilon''_{max}$ ) and calculated as a function of the normalised frequency ( $\omega/\omega_p$ ) according to:

$$\frac{\varepsilon''}{\varepsilon''_{max}} = \frac{\tan^{-1}\left(\frac{\omega}{\omega_p} \sqrt{\frac{\tau_1}{\tau_2}}\right) - \tan^{-1}\left(\frac{\omega}{\omega_p} \sqrt{\frac{\tau_2}{\tau_1}}\right)}{\tan^{-1}\left(\sqrt{\frac{\tau_1}{\tau_2}}\right) - \tan^{-1}\left(\sqrt{\frac{\tau_2}{\tau_1}}\right)} \quad (6.2)$$

Here,  $\omega_p$  is the local peak frequency where the maximum loss  $\varepsilon''_{max}$  occurs. Table 6.2 summarises the experimental  $\omega_p$  values and corresponding  $\varepsilon''_{max}$  values of different samples.

**Table 6.2.** Loss peak frequency and values of different samples

Cable	Loss Peak, $\omega_p$ (mHz)	Peak value $\varepsilon''_{max}$
S-1	10.00	$82 \times 10^{-3}$
S-3	12.50	$73 \times 10^{-3}$
S-5	4.26	$11 \times 10^{-4}$
S-6	3.52	$9.8 \times 10^{-4}$

Figure 6.4 shows a comparison between the distributions of loss factors using equation (6.2) with the experimental results. Here, the comparison has been shown for three  $\sqrt{\tau_2/\tau_1}$  values: 0.15, 25, 50 at room temperature from 50 Hz to 1 mHz. It can be observed that the curves of experimental distribution follow the same shape as the distribution obtained from

Frohlich analysis. The experimental distribution matches very well with the frequency close to the peak value, whereas at the higher frequency, it deviates significantly from the calculated results. With the increasing relaxation time, the energy gap or activation energy ( $\nu_1 - \nu_2$ ) between dipole states also increases and widens the loss factor curve.

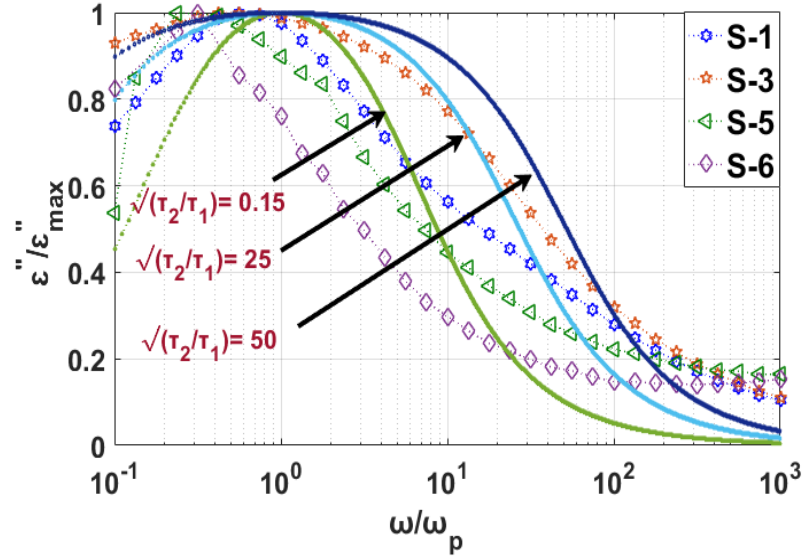


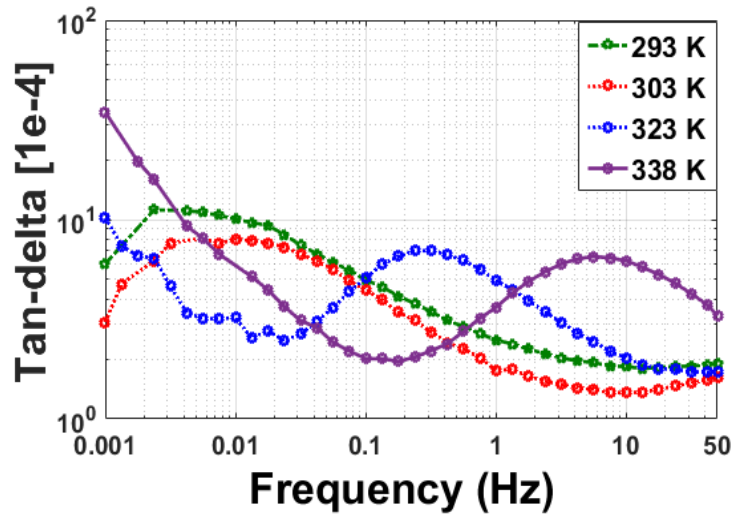
**Figure 6.4.** Comparison of experimental values with Frolich analysis

However, it is a drawback that dipoles are assumed to be confined between two constant energy positions and orientate either parallel or anti-parallel to the equilibrium position as the field alternates. In reality, such occurrences rarely happen in XLPE material; instead, they rotate with different angles and are likely to cause a discrepancy between the experimental and theoretical results [56].

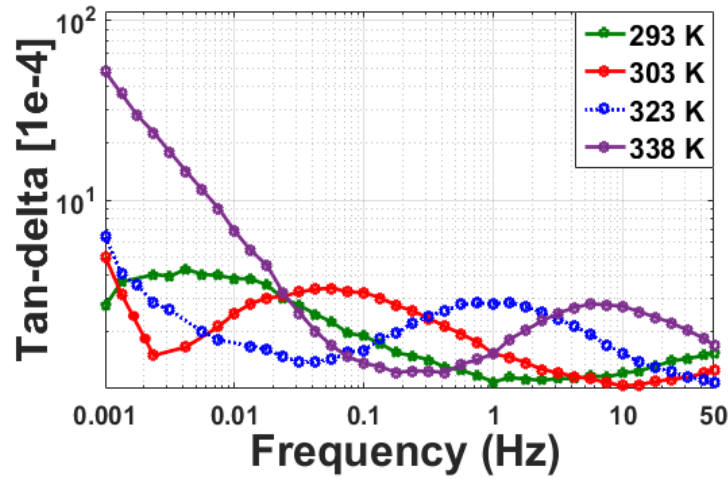
## 6.4 Influence of Temperature on $\tan \delta$ Measurements

### 6.4.1 Two-Dimensional (2D) Visualisation of $\tan \delta$ Response

Different temperatures have different impacts on the dielectric response as revealed in  $\tan \delta$  measurements. Unlike liquid insulation, when the material is thermally excited, several turbulences may occur at the molecular level and at any instant, some dipoles are able to vibrate with greater amplitude than others [234]. Moreover, according to studies on FDS, different polarisation and conduction processes are likely to dominate the dielectric response. Figure 6.5 plots the frequency spectrum of  $\tan \delta$  measurement at different temperatures. Here, the experimental results are shown with 2D views for S-5 and S-6 from very low (1 mHz) to power frequency (50 Hz). At lower temperature, the dielectric loss at power frequency has a comparatively much lower value than the loss at VLF. This can be explained by the behaviours of different polarisation processes at various frequencies.



(a) S-5



(b) S-7

**Figure 6.5.** 2D view of  $\tan \delta$  measurements at different temperatures

From the dielectric response theory, the dipoles under very low frequency excitation have enough time to oscillate or relax; therefore, the Debye (or generalised polarisation) process is negligible at lower frequency and contributes little to the total dielectric loss. Nevertheless, the higher  $\tan \delta$  value speculated in that frequency range can be reasoned by the increasing conduction process and so is the DC conductivity, which makes an increasing contribution to the loss factor through interfacial or space charge polarisation. On the other hand, as the frequency becomes higher, the total dielectric loss tends to depend substantially on the polarisation process [52], [129]. It is apparent from the literature [235], [236] that the dielectric losses observed here are the results of  $\alpha$ - and  $\beta$ - relaxations. As discussed earlier, the cross-linked polymeric chains of XLPE material at room temperature mostly arrange themselves into more conductive crystalline sheets or lamellae. On the other hand, the less conductive amorphous region may contain additives, imperfect cross-linked branches, different side chains connected to adjacent lamellae, impurities and so on. When the material is electrically excited,

these side branches tend to align with the electric field and result in different  $\beta$ -relaxations in the amorphous region. The literature in [56], [233] also remarks that  $\beta$ -relaxation occurs above the glass transition temperature and continues to onset till the material is completely crystallised.

Also, it is interesting to note that the loss-peak of  $\tan \delta$  in all cases exhibits a shifting to the higher frequency region with increasing temperature. This is probably due to the  $\alpha$ -relaxation, generally produced by the twisting of the main chain in the crystalline region. With an increase in temperature, the lamella-amorphous interface begins distorting and allows an increase of free volume in the amorphous segment. This extended volume in fact favors greater freedom of chain movement and subsequently leads to an increase of the  $\alpha$ -response [11].

Another noticeable feature is that at the maximum temperature (338 K), the loss factor increases linearly in the low frequency zone (below 0.1 Hz). This is possibly due to an intensified interfacial polarisation effect, which implies that the conductivity of tested samples has improved dramatically at higher temperatures [56]. The samples in this condition, instead of acting as a perfect semi-crystalline, are assumed to start behaving as a single crystal.

#### 6.4.2 Three-Dimensional (3D) Visualisation of $\tan \delta$ Response

The FDS experimental results can be graphically presented in 3D as a bivariate function of temperature and frequency. In fact, such a visualisation facilitates analysis of the dielectric loss in a more focused and precise way. For example, Figure 6.6 depicts the 3D view of  $\tan \delta$  measurements for S-6 and S56-P. However, comparing the measurement results with various previous analyses and reproducing the prior results are not easy. This is mainly due to trapping and non-identical chain branching that ultimately result in a discrepancy of different samples in their morphological structure.

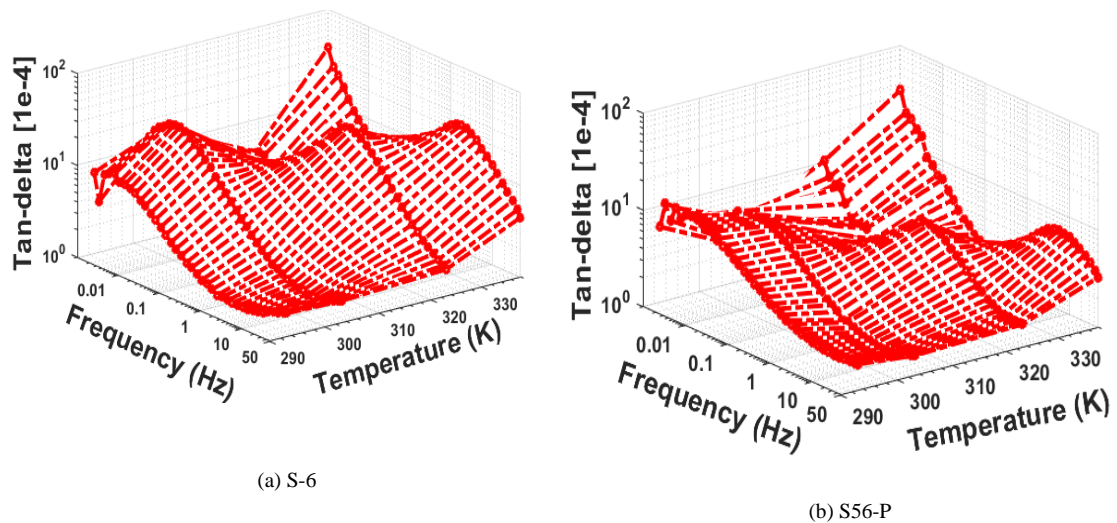


**Figure 6.6.** 3D view of  $\tan \delta$  measurements

## 6.5 Activation Energy and Mean Relaxation Time

The shifting of the peak to a higher frequency with the change of temperature can be used to calculate the activation energy. Primarily, the parameter can be interpreted with the Arrhenius expression, which corresponds to an exponential relationship between the loss-peak frequency ( $f_{max}$ ) and temperature ( $T$ ). The expression can also be used to measure the mean relaxation time ( $\tau_m$ ). The generalised expression of Arrhenius theory is given by:

$$f_{max} = \varphi_0 \exp\left(-\frac{w}{kT}\right); \quad w = v_1 - v_2 \quad (6.3)$$

The factor  $\varphi_0$  is much less sensitive to the ambient conditions, whereas the exponential term contains the critical energy of the dipoles for a jump. After some numerical manipulations, the expression can be simplified as:

$$\ln f_{max} = \ln \varphi_0 - \frac{w}{kT} \quad (6.4)$$

According to equation (6.4), the activation energy can be determined by plotting  $f_{max}$  as a function of  $1/T$ . The calculated energy subsequently defines the mean relaxation time as follows:

$$\tau_m = \tau_0 \exp\left(\frac{w}{kT}\right); \quad \tau_0 = \frac{1}{2\pi\varphi_0} \quad (6.5)$$

The results of  $\tan \delta$  measurement in different samples, including the loss-peak frequency and corresponding  $\tan \delta$  value are listed in Table 6.3. Here, the mean values of the parameters  $f_{max}$  and  $\tan \delta$  are presented. To ensure accuracy, the measurements were performed three times on each sample at the same operating condition. The three data sets obtained show a deviation of less than 0.5% from the mean value.

**Table 6.3.**  $f_{max}$  and corresponding  $\tan \delta$  values of different samples

Cable		293 K	303 K	323 K	338 K
S-5	$f_{max}$ (Hz)	0.004	0.01	0.316	5.623
	$\tan \delta \times 10^{-4}$	11.11	7.961	6.991	6.528
S-6	$f_{max}$ (Hz)	0.003	0.004	0.023	1.778
	$\tan \delta \times 10^{-4}$	9.127	23.97	23.42	23.26
S-7	$f_{max}$ (Hz)	0.004	0.056	1.00	5.623
	$\tan \delta \times 10^{-4}$	4.301	3.409	2.827	2.817
S56-P	$f_{max}$ (Hz)	0.001	0.005	0.237	0.562
	$\tan \delta \times 10^{-4}$	7.349	13.04	11.74	11.37

In this research, a linear fitting technique was employed in MATLAB to interpret the measurement results. After that, the slope and Y-axis intercept were used to estimate the activation energy and the mean relaxation time respectively. Figure 6.7 shows the fitting results of experimental data for various samples by using the least square method. Each linear fitting has a negligible root-mean-square error (RMSE) and sum-of-squared errors (SSE), typically  $\leq 1$  %. These metrics were used to evaluate the fitting goodness.

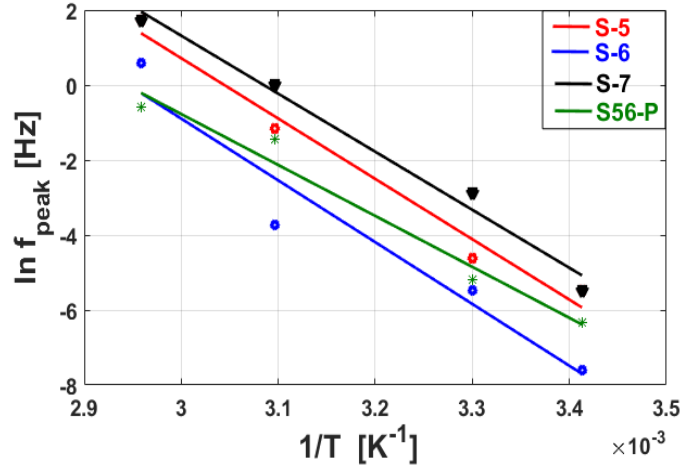


**Figure 6.7.** Linear fitting of different samples for determining the activation energy

The insignificant error evidently indicates that the fitting curves are in good agreement with the measurement results. Hence, for activation energy measurement, the fitting method and the FDS study are considered to be an effective and suitable analysis technique. The fitted results are post-processed and deployed later to perform further analysis.

Table 6.4 summarises the activation energy and the mean relaxation time of S-5 to S56-P. As can be observed, the mean relaxation time decreases with increasing temperature. On the other hand, the lower activation energy of S-P implies greater flexibility to the dipolar movement and energy distribution, and easier transition of molecular chains in the amorphous state as compared to other tested samples.

**Table 6.4.** Activation energy and mean relaxation time

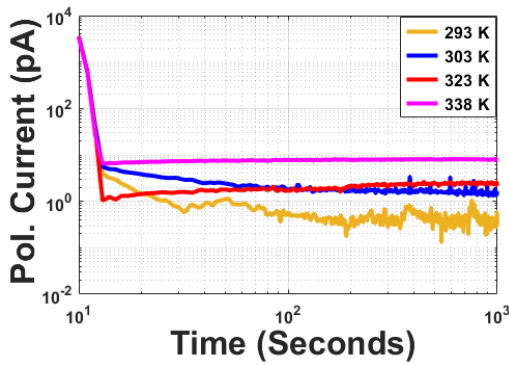
Cable	Mean relaxation time $\tau_m$ (Sec.)				W (eV)
	293 K	303 K	323 K	338 K	
S-5	59.97	9.785	0.364	0.039	2.773
S-6	220.89	34.52	1.191	0.123	2.839
S-7	25.48	4.457	0.188	0.022	2.667
S56-P	94.36	20.41	1.271	0.196	2.341



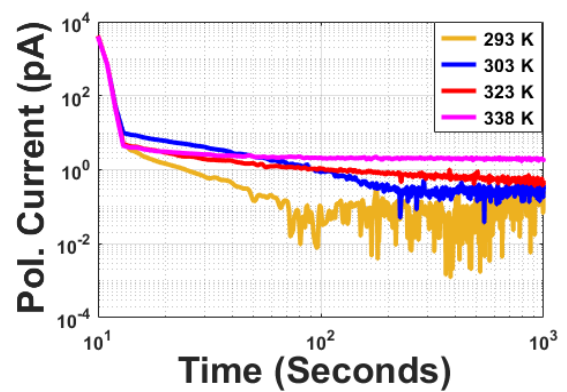
## 6.6 Influence of Temperature on Pol/depolarisation Current

Apart from dissipation factor measurement, the polarisation and depolarisation currents (PDC) are also measured to evaluate the dielectric response. PDC analysis is performed in the time domain with a DC excitation. In principle, the excitation yields a charging current while the short-circuiting of the voltage source results in the discharging or depolarisation current of the test object. For diagnostic analysis, the larger pol/depolarisation current corresponds to a higher dielectric loss in the time domain. In practical PDC measurement, a step of 200 V DC was applied to the test objects, and the corresponding dielectric loss was measured over the desired temperature range 293 K - 338 K.

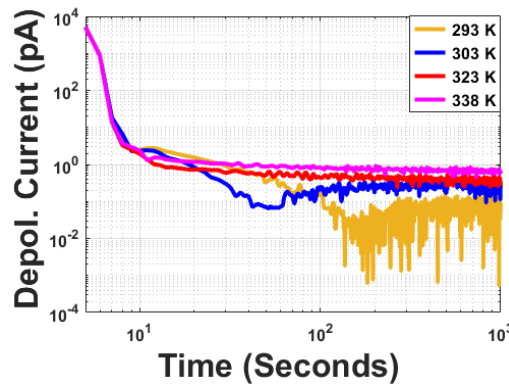
Figure 6.8 shows the polarisation and depolarisation currents of different test specimens obtained at various temperatures. Analysis of these currents as a function of temperature helps to diagnose the health condition of the insulation. It can be seen that these characteristic currents decay dramatically with the progressing time. With the rising temperature, the magnitude of both currents shifts to higher values.



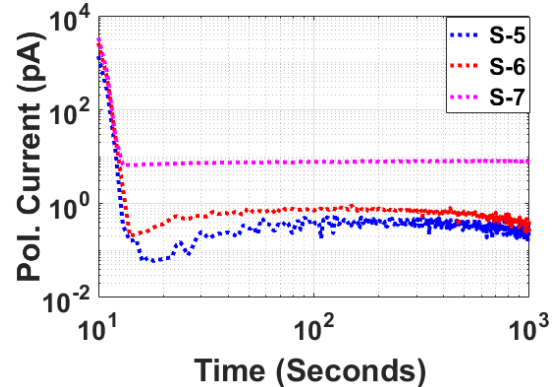
(a) Polarisation current of S-7 sample



(b) Polarisation current for S56-P sample



(c) Depolarisation current of S-5 sample



(d) Comparison of polarisation currents at 338 K

**Figure 6.8.** Comparative analysis of dielectric response in the time-domain



When the test objects are thermally excited, the resultant increasing currents in both charging and discharging periods are assumed to be due to the growth of charge carriers and space charge polarisation [54]. However, the depolarisation currents are very small in magnitude and very sensitive to temperature variation; possible variations during the measurement period may introduce some uncertainty in the accuracy of the results.

It is also important to note that the conductivity  $\sigma$  of the cable samples can vary in the range of  $10^{-15}$  -  $10^{-30}$  siemens. In reality, such a small signal is likely to be contaminated by background noise. This is clearly visible for both polarisation and depolarisation currents of different samples at room temperature condition as shown in Figure 6.8. In all cases, the measured currents decay with time and are highly affected by interference at the end of the measurement period. This noise effects can be reduced using a low-pass digital filter.

A comparison of different samples is also shown in Figure 6.8d which presents the polarisation currents of S-5 to S-7 measured at 338 K. Comparing with other samples, the polarisation current of S-5 tends to be smaller than other specimens. The conduction current can also be obtained from the difference between the polarisation  $I_{pol}(t)$  and depolarisation currents  $I_{dep}(t)$ , which can be subsequently used to obtain the DC conductivity  $\sigma$  according to equation (5.21).

In Figure 6.9, the change of conductivity, caused by both electrical and thermal excitation, is also shown. Under the transition from a lower to higher temperature, the conductivity of any test sample is higher than the corresponding values obtained at room temperature. At increased temperature, the increasing mobility of the charge carriers in the polymeric insulation causes this change of conductivity.

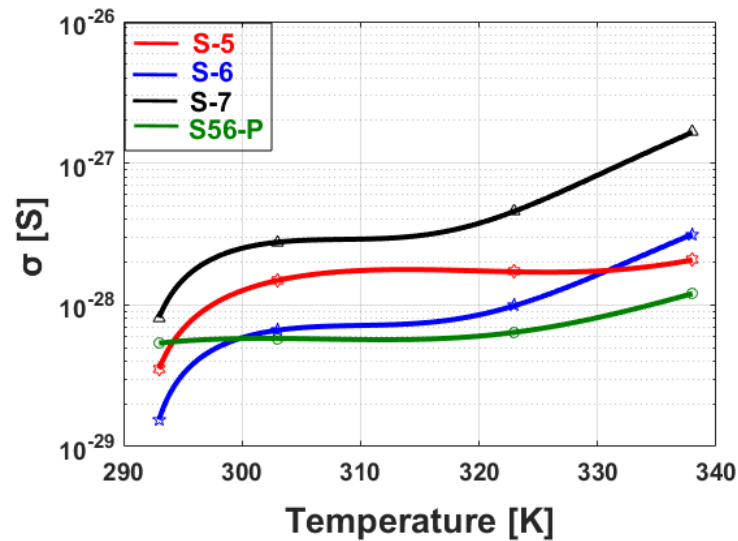


**Figure 6.9.** Change of conductivity with the increasing temperature

---

## 6.7 Some Challenges in Frequency Response Measurement

### 6.7.1 Edge Effects

In [116], it has been reported that when testing a high voltage cable, the edge effect from the measurement electrode may arise. In order to perform accurate dielectric response measurements, the electrodes need to be protected from this effect; otherwise, it could introduce some inaccuracy to the measurement results. To investigate, P. Werelius performed testing on an approximately 10 m long XLPE cable (2.1 nF) with and without guarding [116]. The test was performed at 3 kV and 8.5 kV voltage level and found that the real and imaginary permittivity increase significantly if the test specimen is not properly guarded.

In this work, the tested specimens used are less than 1.5 m in length and have a maximum capacitance of 300 pF. Unlike most of the tested samples in P. Werelius experiment, these short sections of cable are taken after some time in service but not subjected to any water tree effects. The frequency sweeping is performed from very low frequency (1 mHz) to power frequency (50 Hz) and according to CIGRE TB493 [105], an AC voltage of 200 V (peak) was applied. It is advised that performing any high voltage testing below 0.1 Hz requires limiting the maximum field stress below ( $<10$  kV/mm) to avoid any risk of space charge formation which may remain in the insulation after testing. Furthermore, such a small applied voltage (i.e. 140 Vrms) is unlikely to generate any significant leakage current that flows along the insulation surface due to the edge effect.

To investigate how significant the leakage current influences the loss factor measurement over a wide range of frequency, further experiments were conducted. Two short sections of cable samples (0.75 m and 0.70 m) were prepared from an 11-kV XLPE cable. For each sample, the PVC sheath, armour and outer semicon layer were removed from both ends to expose an unscreened bulk XLPE section of 10 cm as shown in Figure 6.10.

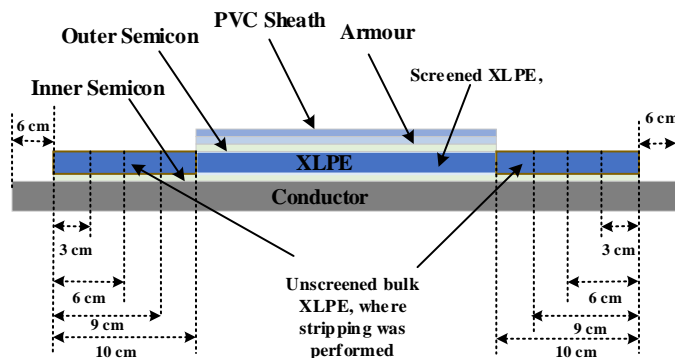
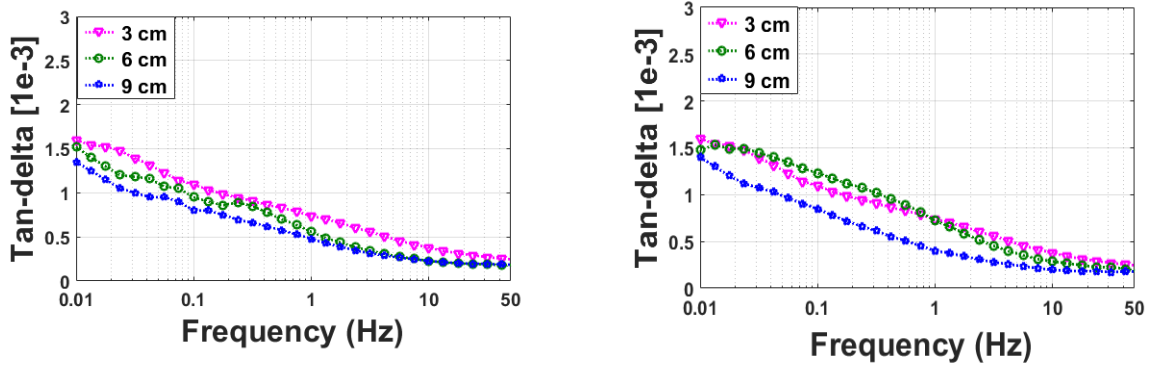


**Figure 6.10.** Cross-section of the test sample to explore the impact of leakage current

After that the unscreened bulk insulation and inner semicon layer were cut off and stripped away 3 cm inwards to the screened insulation. Then 140 V (rms) voltage is applied and swept from 0.01 to 50 Hz. The test was then repeated twice with a further stripping of 3 cm each time. As expected, and seen in Figure 6.11, there is no major change of the loss-factor graph after stripping the bulk insulation. This implies the influence of leakage current from edge effects is quite negligible under 140 V AC excitation.



(a) 0.70 m cable section with 190 pF capacitance (before stripping)

(b) 0.75 m cable section with 194 pF capacitance (before stripping)

**Figure 6.11.** Edging effects of short length cable section when exposed to 140 V (rms) voltage

Since the tested samples (S-1 to S-7) are also short in length, open guarding might introduce some effects to the measurement results. As reported in [116], the loss current of an R-C circuit can be maximum  $(1/\sqrt{2})$  times of the capacitive current without providing a resistor. Now if a small capacitive guarding (let assume 1.5 pF) is introduced in S-3, that will cause an additional loss of  $3.5 \times 10^{-3}$  ( $1.5/(\sqrt{2} \times 296)$ ) which is undesirable. Most of the experiments were performed in the aluminum shielded cage, where the test specimen and measurement electrodes were placed inside a metal oven. Hence, the effects of not shielding are expected to be not too pronounced.

### 6.7.2 Effects of Termination

Referring to CIGRE TB493, the effect of termination is very significant for the water tree aged cable. At 0.1 Hz frequency and rated voltage ( $U_0$ ), it was found that some selected terminations could contribute a loss-factor value ranging from  $10^{-3}$  and  $10^{-1}$ . Here in the experiment, all tested samples mostly show a loss factor value ranging from  $10^{-3}$  to  $10^{-4}$  at 140 V voltage (rms) and are not affected by any previous water-tree effect. Since all experiments were carried out at low voltage (140 V as compared to the kV range); it is less likely to generate any leakage current due to the parasitic effects resulting from accessories like terminations. It is also found from Figure 6.11 that there is not much change occurred in the loss-factor graph when it is subjected to an applied voltage of 140 Vrms under varying insulation screen to the

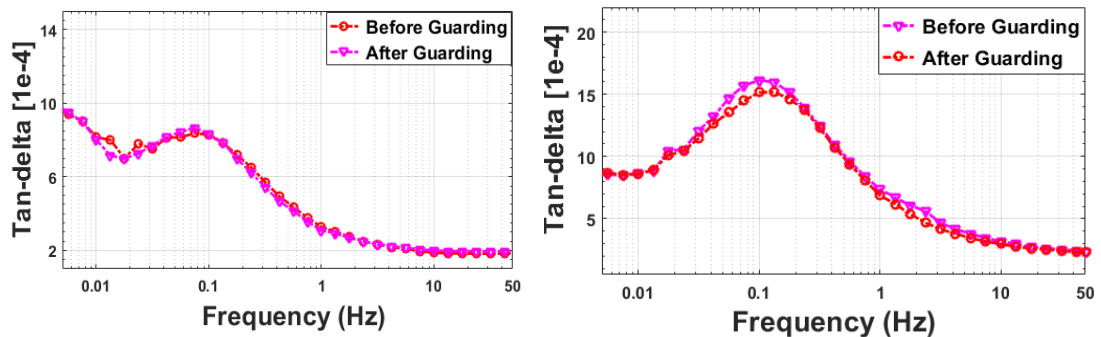
measurement electrode distances. However, it would be of practical interest to consider the cable system as a whole; but, for simplicity, the research only focused on the cable insulation itself.

### 6.7.3 Effects of Voltage Change

Since the cable sections tested are short in length, to compromise between the cable accessories effects and the accuracy of the results, the test voltage level was chosen as 140 V<sub>rms</sub>. Moreover, according to CIGRE TB493, for a wide frequency range from 1 mHz to 1000 Hz, the prescribed maximum voltage level for a low voltage system is 200 V. This is because increasing voltage level ( $> 15$  kV/mm) below 0.1 Hz frequency might introduce space charge in the insulation. When power frequency is re-applied, such residual space charges could increase the local field and impose the same adverse effects on the insulation as the high voltage DC test. Some other scopes of this research are to determine the activation energy and mean relaxation time, which might not be accurately interpreted if the voltage level is raised too high. Also, increasing the voltage level may introduce surface discharge which can affect the accuracy of the test results.

## 6.8 Necessity of Guarding Arrangement

Two different short sections of 11-kV XLPE cable sample with a guarding arrangement were also prepared according to P. Werelius work as recommended in [116]. The dissipation factor measurements of the test samples before and after guarding at 200 V (peak) applied voltage are shown in Figure 6.12. As can be observed, after guarding with this small voltage level there is no significant difference found in the trending of loss-factor graph. It can be adduced that the leakage current due to the edging effects at 200 V is negligible.



(a) 0.75 m cable section (capacitance of 196 pF before guarding)

(b) 0.8 m cable section (capacitance of 198 pF before guarding)

**Figure 6.12.** Comparison of loss-factor with the guarding arrangement

However, the necessity of guarding should not be ignored. For this purpose, before and after guarding, DDF testing on prepared samples at different voltage levels were performed. Two different setups (Omicron MI 600 and Baur Frida) were used to check the DDF response at 50 Hz and 0.1 Hz applied voltage respectively. Three voltage levels (2.0 kV, 1.0 kV and 0.6 kV) were applied to investigate the impact on the leakage current with increasing voltage level. As expected and seen in Figure 6.13, at higher voltages the guarding effects are more pronounced and introduce inaccuracy to the measurement results if ignored.

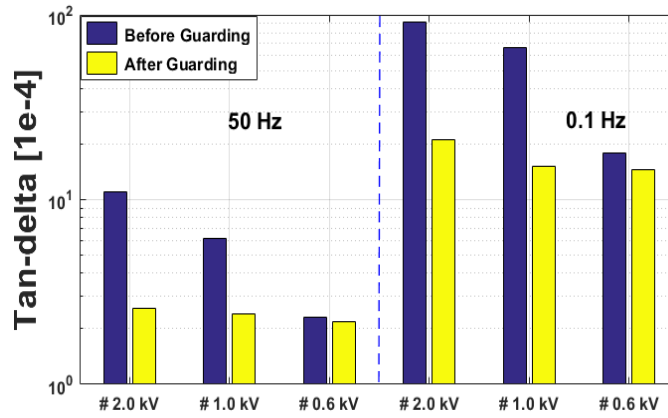


**Figure 6.13.** Difference in tan-delta value at different voltage levels

On the other hand, at lower voltage level (e.g. 600 Vrms), the difference between with and without guarding is found to be less which in turn suggests that the influence of leakage current becomes negligible with decreasing voltage level. Therefore, guarding is highly recommended if testing is performed at elevated voltage level.

## 6.9 Chapter Conclusion

In this chapter, the dielectric responses are obtained over the frequency range from 1 mHz to 50 Hz with different diagnostic measures including  $\tan \delta$ , Frohlich's analysis, activation energy, and pol/depolarisation current. Furthermore, the tests are also carried out for different ambient temperatures (293 K - 338 K).

Based on the dielectric response theory, the physical explanations of the relaxation processes and their behaviour as a function of temperature are first introduced. With the transition of temperature from a lower to a higher value, it is found that the loss-peak of  $\tan \delta$  shifts to a higher frequency and vice-versa. This feature is the result of  $\alpha$ - and  $\beta$ - relaxations. The  $\beta$ -mode relaxations are caused by the movement of imperfect chain segments in the amorphous region, whereas the  $\alpha$ -mode relaxations are the result of main chain twisting in the crystalline zone.

---

---

The activation energy calculated from the Arrhenius expression also provides an idea of the energy distribution in the oscillatory dipoles. Finally, the PDC analysis facilitates the dielectric response interpretation in the time-domain, which is subsequently used to estimate the DC conductivity and it shows that the increased conductivity is the result of the upward transition of temperature.

---

---

## Chapter 7.

# Dielectric Response Measurement in the Time Domain

The dielectric behaviours in the frequency domain using FDS method have been examined in Chapter 6. In this chapter, dielectric response measurement in the time domain based on the polarisation and depolarisation current (PDC) method is presented. Firstly, the physical explanations of various polarisation processes at low and high frequencies are reported using the clustering model. The main contributions of the chapter are Daniel's normalisation, determining the number of polarisation branches and equivalent  $\tan \delta$  modelling, the relationship between individual loss factors and the overall loss factor. Measurements of AC activation energy and testing under varying electrical stresses and ambient conditions are also carried out. A methodology to construct the RVM response based on the PDC measurement is proposed and demonstrated. The work in this chapter has been published in [4] and [5] as shown in the List of Publications.

### 7.1 Motivation of Pol/Depolarisation Current Measurement

Comparing with frequency domain measurements, the PDC method is more attractive in terms of short test duration and accuracy [10], [226]. The time constant of pol/depolarisation currents has a good correlation with the ageing and varies accordingly depending on the insulation deterioration [80]. Also, without requiring much knowledge on physico-chemical-electrical characteristics, it eases the way of analysis as compared to other methods such as partial discharge measurement, frequency response analysis, recovery voltage measurement [10], [226]. Moreover, the PDC technique forms the basis of dielectric spectroscopy measurement and the dielectric loss factor (or  $\tan \delta$ ) spectrum can be readily obtained by transforming the time domain response into the frequency domain equivalent [10], [56]. Moreover, PDC method facilitates the basis of recovery voltage measurement (RVM), which is also a non-destructive insulation diagnostic method [237]–[239]. These advantages provide the motivation to investigate dielectric behaviours in time domain using PDC method.

---

## 7.2 Dipoles Behaviours and Clustering Distribution

A practical dielectric insulation system in solid phase is not homogeneous; instead it has some form of structural disorder. Under the influence of an electric field, this geometrical randomness creates locally coupled vibration zones and so is the physical relaxation process [240], [241]. In order to understand the physical behaviour of solid dielectrics, Dissado and Hill [56], [240] introduce a theory which serves as a realistic picture of a polymeric material that has imperfect order.

According to this theory, the dipoles arrange themselves into some localised regions over which a partially regular geometric order can be observed; these regions are broadly known as clusters. With the interactions among them, the clusters tend to form an array having at least a long-range chain of partial regularity. Under the application of an electric field, the orientation or position of individual dipoles inside each unit cluster may change and cause dipolar relaxation. Depending on the dipolar displacement (either angular or location), such a relaxation can be classified as inter-cluster and intra-cluster polarisation. These two processes are dominant at the higher frequencies. Figure 7.1 shows a schematic diagram of the clustering model for dielectric relaxation.

Intra-cluster polarisation involves the movement of individual dipoles within a cluster following the Debye law. In this process, dipoles usually link one to another through the geometrical structure and consequently affect the field seen by other neighbouring dipoles. The overall contribution can be assumed to be a single dipole relaxation.

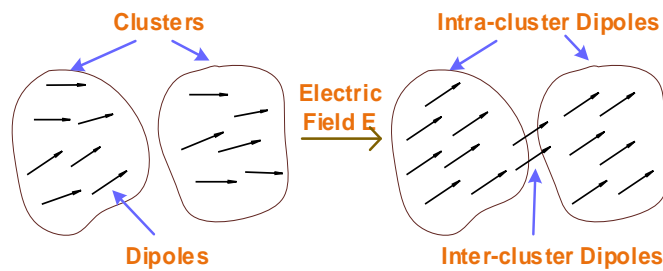


**Figure 7.1.** Clustering model proposed by Dissado-Hill

On the other hand, inter-cluster polarisation occurs between adjacent clusters, especially on those dipoles (usually a few in numbers) which reside at the edges of neighbouring cluster sites. The inter-cluster motion is attributed to have a broader range, and in conjunction with intra-cluster movement, exhibits a frequency-dependent dielectric response.

Another possible source of polarisation is trapping/defect effects due to several localised sites existing in a dielectric. Dipoles residing in such sites contribute to the total dielectric loss at lower frequencies that must be taken into consideration [56].



Interfacial or space charge polarisation also can occur as a result of localised charges, mainly bounded at the interface of the semi-con and insulation layers in an XLPE cable. This polarisation usually takes a long time and makes an increasing contribution to the dielectric loss as the frequency becomes lower [54], [226]. In the absence of water trees, moisture or electrical treeing, the various dielectric relaxation processes, including their magnitude intensity and dominance over the frequency range, can be summarised in Table 7.1. The “↑” and “↓” symbols denote higher and lower values of any parameter respectively.

**Table 7.1.** Various polarisation processes

Polarisation	Magnitude ( $A_i$ )	Frequency ( $\omega_i$ )	Time Constant ( $\tau_i$ )
Interfacial	↑	↓	↑
Intra-cluster	↑	↑	↓
Inter-cluster	↓	↑	↓
Trapping	↓	↓	↑

### 7.3 Descriptions of the Experiment

The same practical laboratory setup is used for the PDC experiment as shown in Figure 6.3. For PDC measurement, the DC excitation was set at a level of 200 V to energise the test specimen. Each PDC test sequence was set for a duration of 1000 seconds, while the recording rate was one sample/second. The test samples were divided into two sets denoted as PSet-1 (S-1 and S-3) and PSet-2 (S-5 and S-7).

In this chapter, several graphical illustrations or analyses of experimental results for some test samples were not included simply to avoid redundancy. Description and analysis of different cable samples are provided in Table 7.2.

**Table 7.2.** Description and analysis of cable samples

Cable		Daniel Normalisation	Number of Branches and $\tan \delta$ Measurement	Activation Energy	Pol. / Depol. Current Analysis
PSet-1	S-1	√	√		√
	S-3	√	√		√
PSet-2	S-5	√		√	√
	S-7	√		√	√

---

## 7.4 Daniel's Normalisation

Morphologically, XLPE insulation has a semi-crystalline structure, where polymeric/crosslinking long chains twist themselves into crystalline regions or lamellae and imperfect side chains into amorphous zones. Due to the arrangement of the chains in such a complex array of molecular segments, this polymeric material has a number of different relaxation times and is assumed to follow a distribution function  $G(\tau)$ . For an infinitesimal relaxation time  $\Delta\tau$ , the function  $G(\tau)$  of all dipoles is given by [56]:

$$\int_0^{\infty} G(\tau) d\tau = 1 \quad (7.1)$$

On the other hand, the imaginary permittivity ( $\varepsilon''$ ) of any dielectric can be derived from equation (5.1) and is written as:

$$\varepsilon'' = (\varepsilon_s - \varepsilon_{\infty}) \sum_{i=1}^n \frac{\omega\tau_i}{1 + (\omega\tau_i)^2} \quad (7.2)$$

Daniel's normalisation is usually applied to quantify the permittivity difference ( $\varepsilon_s - \varepsilon_{\infty}$ ) [56]. The parameter ( $\varepsilon_s - \varepsilon_{\infty}$ ) can be achieved by integrating  $\varepsilon''$  as a function of frequency, and the area under the  $\varepsilon'' - \ln\omega$  is expressed as follows:

$$\int_{\ln\omega_p}^{\infty} \varepsilon'' d(\ln\omega) = (\varepsilon_s - \varepsilon_{\infty}) \int_0^{\infty} \int_{\ln\omega_p}^{\infty} \frac{G(\tau)\omega\tau}{1 + (\omega\tau)^2} d\tau d(\ln\omega) \quad (7.3)$$

Here,  $\omega_p$  denotes the loss-peak frequency of test specimen. Using equation (7.1) and after some manipulations, equation (7.3) can be rewritten as:

$$\int_{\ln\omega_p}^{\infty} \varepsilon'' d(\ln\omega) = \frac{\pi}{2} (\varepsilon_s - \varepsilon_{\infty}) \quad (7.4)$$

To estimate the permittivity difference ( $\varepsilon_s - \varepsilon_{\infty}$ ), the analytical statement is popularly known as Daniel's normalisation expression and is applied to all test samples to calculate that dielectric parameter. The area under the master curve  $\varepsilon'' - \ln\omega$  readily provides the value of ( $\varepsilon_s - \varepsilon_{\infty}$ ).

Figure 7.2 shows the experimental measurement of dielectric loss  $\varepsilon''$  for various samples over the 1 mHz to 50 Hz frequency range. It can be seen that PSet-1 gives comparatively higher loss than PSet-2 over the whole tested frequency zone. At higher frequencies, the values of the factor  $\ln(\varepsilon'')$  are quite negligible.

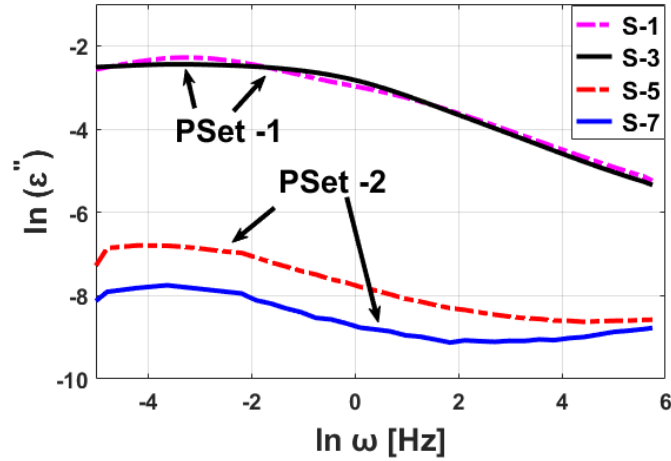


**Figure 7.2.** Dielectric loss measurements of different samples

Table 7.3 summarises the experimental loss-peak frequency of various samples and the corresponding  $(\epsilon_s - \epsilon_\infty)$  values calculated according to equation (7.4). As can be observed, S-7 has the lowest Daniel's parameter, while S-1 has the highest value among all test specimens.

**Table 7.3.** Dielectric characteristic parameters of different samples

Cable	Loss Peak, $\omega_p$ (mHz)	Daniel's Parameter $(\epsilon_s - \epsilon_\infty)$
S-1	10.00	0.3494
S-3	12.50	0.3403
S-5	4.26	0.0036
S-7	8.42	0.0015

It should be noted that the normalisation is assumed to apply for a material that follows Debye relaxation and shows a local loss peak in the  $\epsilon'' - \ln \omega$  characteristic curve. However, without performing an in-depth study, the method had been shown to be quite successful in determining the dielectric responses of various polymeric materials such as PVC, PET [56]. Therefore, the same approach is used in this study to measure  $\epsilon_s - \epsilon_\infty$  of XLPE insulation.

## 7.5 Number of Polarisation Branches

The dipole's displacement due to the external applied voltage causes different polarising processes, and in the absence of that field, their physical characteristics are assumed to decay more or less exponentially with respect to time. The nature of the relaxing or depolarising current for polymeric insulation can be mathematically expressed as:

$$I_d = \sum_{i=1}^n A_i e^{-t/\tau_i}; \quad A_i = \frac{U_0}{R_i} (1 - e^{-t_c/\tau_i}); \quad R_i = \frac{\tau_i}{c_i} \quad (7.5)$$

---

The annotation “ $n$ ” represents the number of R-C parallel relaxation branches as mentioned in equation (7.5). The “ $n$ ” value can be determined by simulating depolarisation currents for different integer values until the measured and simulated results match each other. Usually, this can be performed by deploying a Debye equivalent circuit corresponding to XLPE insulation and the governing equations as discussed earlier.

The whole simulation was iteratively carried out through exponential fitting in MATLAB. The Levenberg-Marquardt algorithm was also employed to improve the iterating process performance. As inputs, the depolarised data after filtering were used to get a reasonable curve fitting. The fitting goodness is evaluated with different performance functions (PFCs) such as the sum of squared errors (SSE), regression coefficient ( $R^2$ ), and root mean squared errors (RMSE) [242] and listed as follows:

$$PFC = \begin{cases} SSE = \sum_{i=1}^n w_i (y_i - \bar{y}_i) \\ R^2 = 1 - \frac{SSE}{SST} \\ RMSE = \sqrt{\frac{MSE}{V}} \end{cases} \quad (7.6)$$

The measurement results of the depolarisation current for PSet-1 at room temperature and fitted curves for various branch numbers ( $n=1$  to  $n=6$ ) are plotted on a logarithmic scale and illustrated in Figure 7.3 and Figure 7.4.

As can be observed, S-1 and S-3 show no significant difference between their decaying trends. The measured currents here are in the pA or nA range owing to large insulation resistance, sometimes exceeding values of  $10^{12}$ - $10^{14} \Omega$ . To avoid redundancy, results of PSet-2 are not shown here. These cable samples have much lower conductivity and their measurements were excessively contaminated by background noise at the end period of the measurement.

To evaluate the accuracy of the fitting process, Table 7.4 lists the performance functions of S-1 and S-3 for various numbers of branches. From the results, it can be easily recognised that the numbers of parallel relaxation branches that are most suitable to represent the polarising process for PSet-1 test specimens are  $n=3$  and  $n=4$ , where  $n=4$  shows the best fitting performance, as the fitted results much more closely resemble the depolarising currents during the measurement period. On the other hand, the fitting simulation for other branch numbers deviates quite significantly from the baseline depolarisation current.

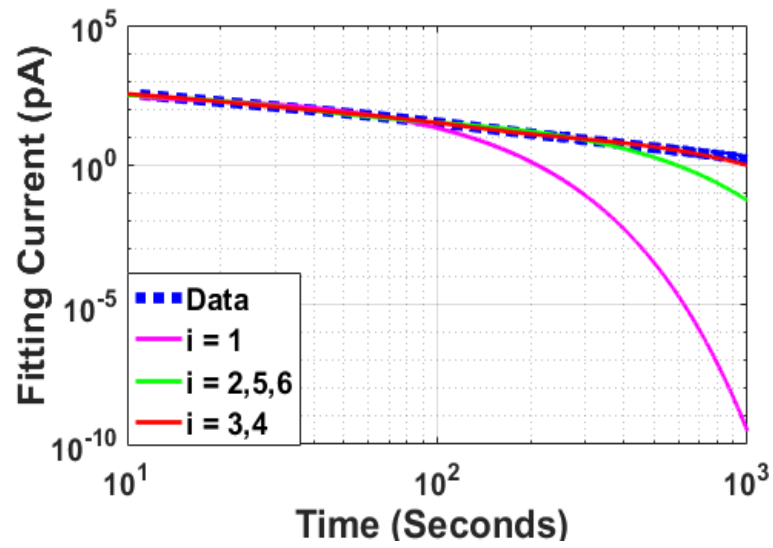


Figure 7.3. Fitting curves for various polarisation branches in S-1

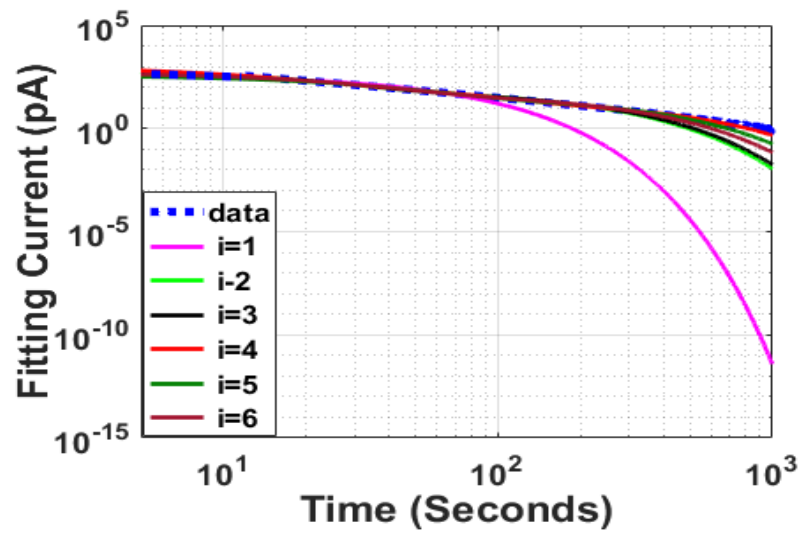


Figure 7.4. Fitting curves for various polarisation branches in S-3

Table 7.4. Estimation of different performance functions

	S-1			S-3		
	SSE	R <sup>2</sup>	RMSE	SSE	R <sup>2</sup>	RMSE
n=1	6× 10 <sup>4</sup>	0.936	8.097	6× 10 <sup>4</sup>	0.940	8.221
n=2	6× 10 <sup>4</sup>	0.993	2.585	5× 10 <sup>3</sup>	0.995	2.439
n=3	384	0.999	0.625	1× 10 <sup>3</sup>	0.998	1.209
n=4	384	0.999	0.626	248	0.999	0.503
n=5	6× 10 <sup>3</sup>	0.993	2.593	4× 10 <sup>3</sup>	0.995	2.238
n=6	6× 10 <sup>3</sup>	0.993	2.595	2× 10 <sup>3</sup>	0.997	1.624

It is also interesting to note that for  $n=4$ , the discharging magnitude ( $A_i$ ) and decay constant ( $\tau_i$ ) of each parallel R-C branch can be readily obtained from the exponential fitting. As discussed in Section 7.2, according to Table 7.1, the estimated values of such parameters can also help in interpreting the different physical polarising processes and is tabulated in Table 7.5.

**Table 7.5.** Interpretation of different polarisation processes

Physical Process	S-1			
	i=1	i=2	i=3	i=4
$A_i$	644.2	20.49	172.2	0.119
$\tau_i$	8.271	328.4	43.44	0.485
Comments	Intra-cluster	Trapping	Interfacial	Inter-cluster
	S-3			
	i=1	i=2	i=3	i=4
$A_i$	182.7	0.019	25.08	849.4
$\tau_i$	38.80	0.531	251.4	8.149
Comments	Interfacial	Inter-cluster	Trapping	Intra-cluster

It is noteworthy that a low-pass second-order Butterworth digital filter was employed here to suppress the interference superimposed on the measured depolarising currents. To sum up, an extended Debye circuit can empirically provide a baseline to determine the number of branches or polarisation events occurring in a dielectric under the influence of applied voltage.

## 7.6 $\tan \delta$ Measurement and Modelling

The Debye model assumes that molecules of any dielectric material are in a spherical shape. However, in reality, the molecules of XLPE form a long chain in their geometrical arrangement. Under an external field, the dipoles are likely to be interactive, and some dipoles tend to oscillate with much greater amplitude than others. For the purpose of understanding these physical behaviours and dynamicity, Davidson-Cole (D-C) introduces a modified form of Debye dipolar model that explicitly establishes the relationship between the excitation frequency and the dielectric loss [56], [234].

### 7.6.1 Relation between Debye and D-C $\tan \delta$

Each branch of the extended Debye circuit, consisting of a series connection of  $R_i$  and  $C_i$  ( $i=1, 2, 3, \dots, n$ ), can be converted into an analogous parallel circuit as shown in Figure 7.5. For

the Debye and D-C models, the equivalent parameters ( $R_i'$  and  $C_i'$ ) can also be expressed as listed in Table 7.6.

**Table 7.6.** Relationship among analogous modelling parameters

Case	Debye Model	D-C Model $\alpha_i = \tan^{-1}(\omega\tau_i)$
$C_i'$	$\frac{C_i}{1 + (\omega\tau_i)^2}$	$C_i(\cos \alpha_i)^\beta \cos(\alpha_i\beta)$
$\sigma_i = \frac{1}{R_i'}$	$\frac{\omega C_i \omega\tau_i}{1 + (\omega\tau_i)^2}$	$\omega C_i(\cos \alpha_i)^\beta \sin(\alpha_i\beta)$

According to the Debye model, the generalised expression of the loss-factor for any branch can be written as:

$$DF_{debye} = \tan \delta_i = \frac{V_{Ri}}{V_{Ci}} = \omega R_i C_i = \omega \tau_i \quad (7.7)$$

On the other hand, the dissipation factor of any branch in the D-C model can be quantitatively interpreted through the analogous parallel circuit and given by:

$$\begin{aligned}
 DF_{D-C} = \tan \delta_i &= \frac{I'_{Ri}}{I'_{Ci}} = \frac{\sigma_i}{\omega C'_i} = \frac{(\cos \alpha_i)^\beta \sin(\alpha_i\beta)}{(\cos \alpha_i)^\beta \cos(\alpha_i\beta)} \\
 &= \tan(\alpha_i \beta) \\
 &= \tan[\beta \tan^{-1}(\omega \tau_i)] \\
 &= \tan[\beta \tan^{-1}(DF_{debye})]
 \end{aligned} \quad (7.8)$$

## 7.6.2 Total $\tan \delta$ and Individual Branch $\tan \delta$

With the aid of the extended Debye circuit and the analogous model depicted in Figure 7.5, it is also possible to establish a relationship between the  $\tan \delta$  contribution of each individual polarisation process and the total dielectric loss.

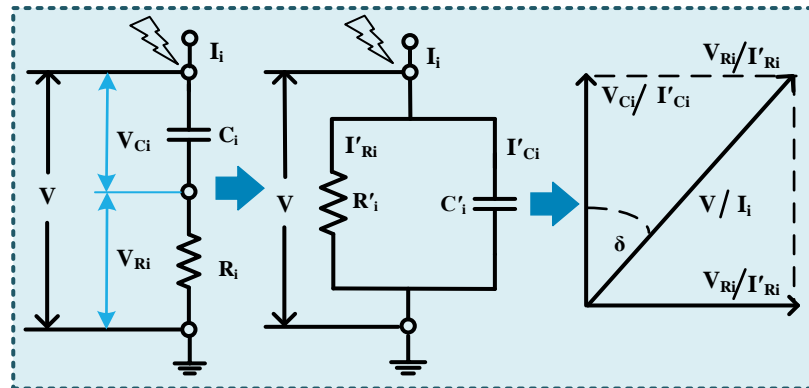


**Figure 7.5.** Analogous circuit of each series branch

For simplicity, the impedance of the Debye circuit can also be expressed as a parallel arrangement of lumped capacitance ( $C_{eq}$ ) and resistance ( $R_{eq}$ ), as shown in the right side of Figure 7.5.

After applying Kirchhoff's current law (KCL), the total current ( $I$ ) of that equivalent circuit is given by:

$$I = I_0 + I_1 + I_2 + \dots + I_n$$

$$\frac{V}{R_{eq} \sin \delta} = \frac{V}{R_0 \sin \delta_0} + \frac{V}{R_1} \sin \delta_1 + \frac{V}{R_2} \sin \delta_2 + \dots + \frac{V}{R_n} \sin \delta_n \quad (7.9)$$

When  $\delta \rightarrow 0$ , by using the approximation  $\sin \delta \approx \tan \delta$ , the total loss factor ( $\tan \delta_{tot}$ ) can be written as:

$$\frac{1}{R_{eq} \tan \delta_{tot}} = \frac{1}{R_0 \tan \delta_0} + \frac{1}{R_1} \tan \delta_1 + \frac{1}{R_2} \tan \delta_2 + \dots + \frac{1}{R_n} \tan \delta_n$$

$$\tan \delta_{tot} = \frac{1}{R_{eq}} \left[ \frac{1}{R_0 \tan \delta_0} + \sum_{i=1}^n \frac{1}{R_i} \tan \delta_i \right]^{-1} \quad (7.10)$$

As discussed earlier, for the total number of R-C branches  $n=4$ , equation (7.10) can be sufficiently applied to quantify the total dissipation factor of S-1 and S-3. After fitting once the parameters  $A_i$  and  $\tau_i$  are obtained, the corresponding values of  $R_i$  and  $C_i$  for each branch are also determined by using equation (7.5). Table 7.7 summarises the estimated  $\tan \delta_{tot}$  of PSet-1 samples from the very low (1 mHz) to the PF (50 Hz) range by using the Debye model and D-C model ( $\beta=0.5$ ). As can be observed, the Debye model deviates considerably at higher frequencies whereas the D-C model matches reasonably well with the experimental results over the tested frequency range.

**Table 7.7.** Modelling results of Debye and D-C models

$\omega$ Hz	S-1 [ $\tan \delta_{tot} * 10^{-3}$ ]			S-3 [ $\tan \delta_{tot} * 10^{-3}$ ]		
	Experiment	Debye	D-C	Experiment	Debye	D-C
<b>0.001</b>	59.14	78.78	57.79	62.26	65.56	67.05
<b>0.01</b>	85.35	82.90	75.08	68.22	86.36	78.06
<b>0.1</b>	48.26	27.43	50.61	54.76	27.39	58.93
<b>1.0</b>	22.61	7.688	21.17	23.86	2.941	25.19
<b>10</b>	8.723	5.642	10.47	8.664	0.401	10.15
<b>50</b>	4.911	5.460	7.687	4.529	0.175	5.387



## 7.7 Activation Energy Measurement

The activation energy (AcE) is generally defined as the DC potential barrier (eV) separating two equilibrium positions over which dipoles limit their displacement. The relationship between AcE ( $\Delta w$ ) and the insulation resistance  $R_{eq}$  can be determined from Arrhenius expression and expressed as:

$$R_{eq} = R_0 \exp\left(\frac{\Delta w}{kT}\right) \quad (7.11)$$

Here,  $R_0$  represents a DC resistance considered to be at an infinitely high temperature and  $k$  is the Boltzmann constant. As of interest, the variations of insulation resistance with the ambient temperatures for PSet-2 test objects are shown in Figure 7.6 and Figure 7.7. The figures clearly show that with the increasing temperature, the resistivity of the test specimen decreases considerably, especially in the low-frequency zone. This can be attributed to the greater availability of free electrons after introducing the temperature change.

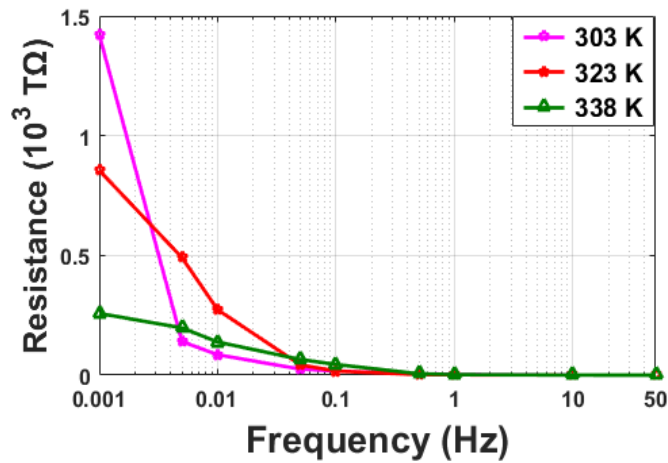


Figure 7.6. Influence of temperature on the resistivity of S-5

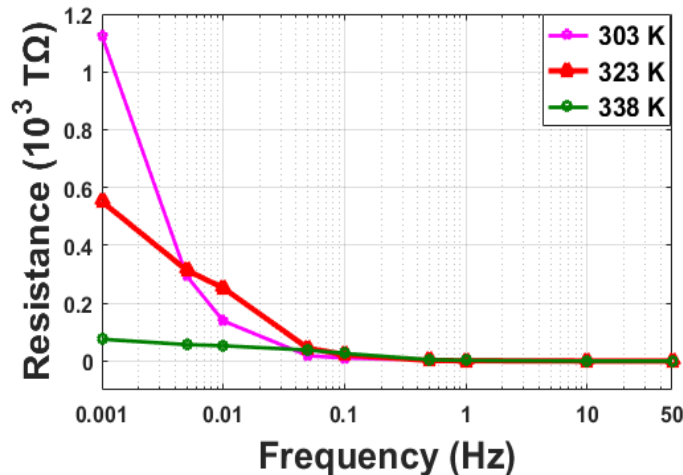
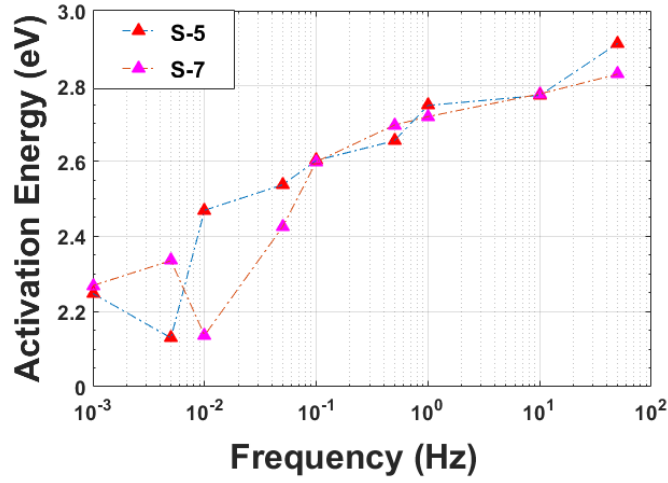


Figure 7.7. Influence of temperature on the resistivity of S-7

The decrease of resistivity with increasing temperature can aid to construct the spectrum of the activation energy (AcE) of the AC conduction as shown in Figure 7.8.



**Figure 7.8.** Activation energy of AC conduction process

Here, the AcE is calculated from the logarithm of  $R_{eq}$  versus the inverse of the ambient temperature. Measurement results suggest that the lower activation energy eases the process of AC conduction at very low frequency; thus, contributes to the increasing dielectric loss in this frequency range.

## 7.8 Stress Effects and Ambient Conditions

The influence of various voltage levels (100 V and 200 V) on the polarisation (pol.) and depolarisation (depol.) currents is illustrated in Figure 7.9 and Figure 7.10. For clear visualisation, the experimental results are shown only for S-1 and S-3. As expected, the increasing electrical stress yields higher pol/depolarisation currents and so is the dielectric response. In principle, the larger response current corresponds to a higher dielectric loss in the time domain.

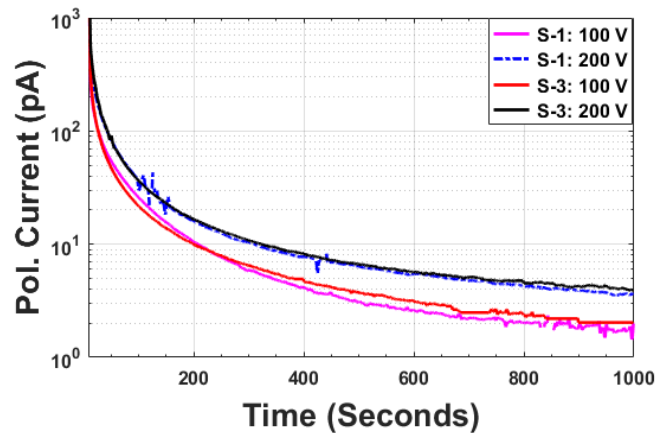


**Figure 7.9.** Polarisation currents of PSet-1 for different stresses

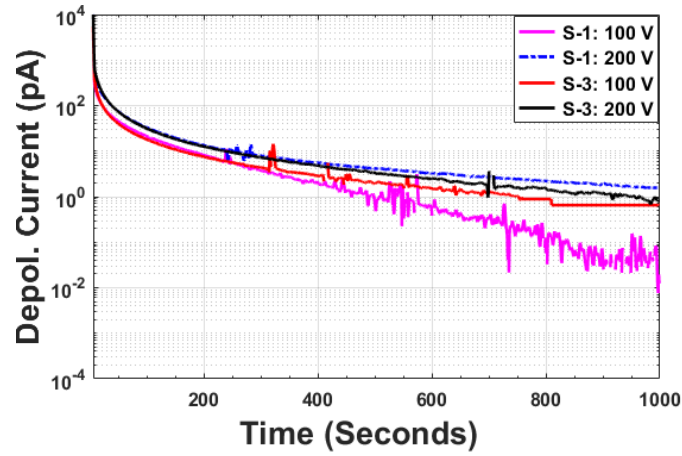


**Figure 7.10.** Depolarisation currents of PSet-1 for different stresses

Figure 7.11 depicts the polarising currents of S-5 over the measurement period obtained at various temperatures. It can be recognised that with increasing temperature, the magnitude of the polarisation currents shifts to a higher value due to a change of the DC conductivity and space charge polarisation.

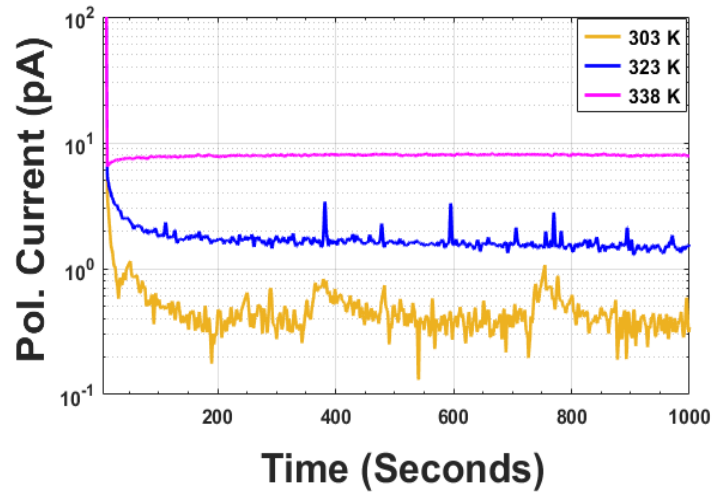


**Figure 7.11.** Influence of temperature on polarisation currents of S-7

Apart from different electric stresses, the temperature variation also assists to interpret the trapping effect due to the macroscopic defects in polymeric insulation. The product of the depolarising current  $I_{dep}(t)$  and the measurement time instant  $t$  correlates with the trap level distribution function  $N(E)$  [54], i.e.

$$I_{dep}(t) * t \propto N(E) \quad (7.12)$$

The trapping intensity of S-5 at various temperatures is shown in Figure 7.12. Basically, as time progresses, more traps are likely to be formed due to the increasing temperature; thus, they capture more space charge and contribute to the gradual rise of the depolarisation currents.

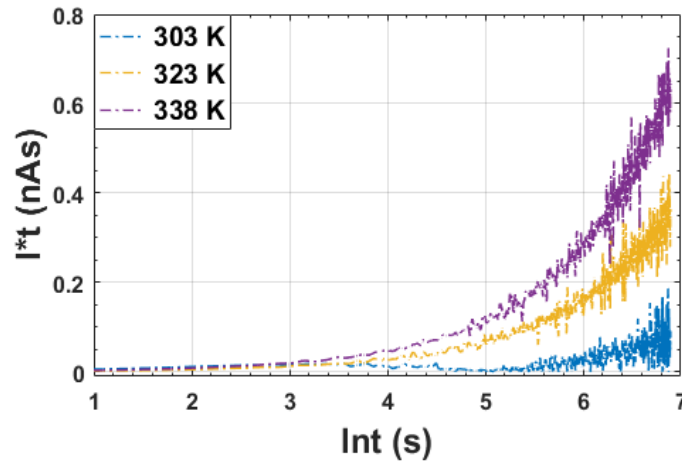


Figure 7.12.  $I_{dep}(t)*t$  vs.  $\ln(t)$  curves

## 7.9 Recovery Voltage Response

Recovery voltage (RV) measurement was initially developed for the condition monitoring of oil-paper insulation in the transformer but was later found to be able to detect ageing effects in polymeric insulation systems [243], [244]. In principle, the method quantifies the polarisation time constant in the low frequency region of the dissipation factor or  $\tan\delta$  spectrum [237], [245]. Additionally, the analysis provides two other dielectric response parameters, namely the ‘slope of the curve’ (the first derivative of the initial RV response), and the ‘peak time’ (the time at which the recovery voltage reaches its peak) [66], [245].

Several researches reported field studies of RV measurement for oil-paper insulation [66], [245], [246]. However, there has been a lack of investigations on polymeric insulation and in particular XLPE medium voltage cables [244], [247]. Moreover, there is a need for research on the modelling of the recovery voltage in XLPE cables under aged conditions [237]. In this regard, the extended Debye circuit is an attempt to model an insulation system by an equivalent circuit having a number of  $R$ - $C$  relaxing polarisation branches [66], [245].

### 7.9.1 Principle of Recovery Voltage Measurements

#### 7.9.1.1 Definition of Recovery Voltage (RV)

Following application of an external voltage which produces an electric field in an insulator, the dipoles align themselves in the direction of the field and as a result, a polarisation current occurs. When the applied voltage is removed, the dipoles get relaxed and return to their original states following a specific time constant [10], [54]. During this dipole relaxation period, the process of relaxation results in a recovery voltage developed across the insulator which is measurable. The recovery voltage and the relaxation time constant are considered as two useful

indicators for assessing the insulation condition [10]. Deterioration of the insulation due to ageing will influence the polarisation process.

### 7.9.1.2 Working Principle of Test Circuit

In order to explain the recovery voltage measurement (RVM) process, it is necessary to understand the physical process occurring in a dielectric under the influence of an electric field. In this regard, the equivalent circuit representation of a dielectric material is shown in Figure 7.13.

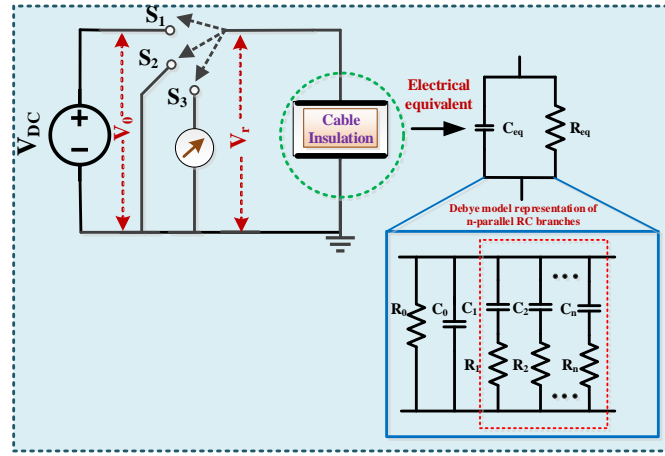


**Figure 7.13.** RVM measurement and Debye equivalent model

The  $R$ - $C$  combination formed by  $R_0$  and  $C_0$  typically has a much smaller time constant, i.e. the charging/discharging happens very quickly, and thus does not have any significant contribution to the pol/depolarisation process. On the other hand, the higher time constants of other  $R$ - $C$  branches make them following a certain finite time lag in their charging/discharging process [129], [245]. The operating principle of the RVM circuit can be explained by the following three steps.

Firstly, the test sample is directly connected to a DC voltage source  $V_0$ , by closing switch  $S_1$  while switches  $S_2$  and  $S_3$  remain open as shown in Figure 7.13. During this period, the deposit of charges on the insulation surface initiates the polarisation process of the excited molecules.

After completion of the polarisation period ( $t_0$ - $t_2$ ), the discharging process is initiated by short-circuiting the test sample using switch  $S_2$  at  $t_2$ .

Finally, in the third step, both switches  $S_1$  and  $S_2$  are opened, while  $S_3$  is closed. The residual bounded charges due to the depolarisation process inside the dielectric are converted to free charges on the sample surface which usually recharge the primary capacitance  $C_0$ . As a result of this charging, the return or recovery voltage appears across the terminal, which can be

measured using a high input impedance voltmeter with high sensitivity. The generated recovery voltage attains its maximum value at  $t_5$  and then follows more or less an exponential decay before reaching zero. Degradation of the insulation may shift the peak to a lower value [17]. The charging mode, switching instances and development of the recovery voltage are illustrated in Figure 7.14.

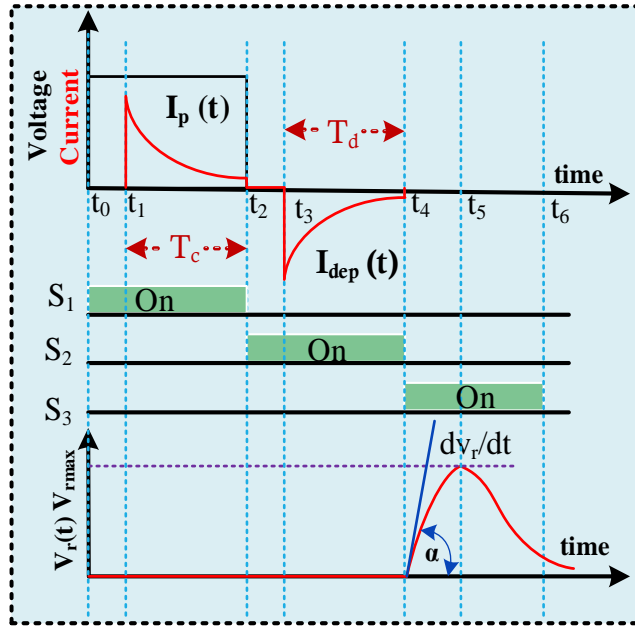


**Figure 7.14.** Working principle of the RVM method

Time domain analyses like PDC and RVM mostly follow the Debye circuit in their operation, and the circuit parameterisation forms the basis of the modelling. The Dirana instrument used in the laboratory experiment is able to perform the PDC measurement only. However, the measured pol/depolarisation currents can be utilised for constructing the RVM spectrum through the developed circuit modelling. Thus, without carrying out the actual RVM measurements, the modelling offers a novel alternative to obtain the RVM results which can save time and the hardware requirement.

## 7.9.2 Analytical Expression of RVM Measurement

In the RVM measurement, a series of repeated measurements is carried out to assess the insulation condition. After this, the associated dielectric responses help in constructing the polarisation spectrum from which, the determination of the recovery voltage peak value ( $V_{rmax}$ ) and the corresponding time instant ( $T_p$ ) is of interest. With the degradation of insulation, the peak value slightly shifts to a lower value [10].

The step-by-step process of developing an analytical expression for RVM modelling is as follows. Following the DC excitation, the polarisation currents flow in the circuit which enable the charging of all capacitors. The voltage developed across any capacitor ( $C_i$ ) can be written as:

---



---


$$V_{Ci}(T_c) = V_0 \left[ 1 - \exp\left(-\frac{T_c}{\tau_i}\right) \right] \quad (7.13)$$

After the charging period, the short-circuiting of the dielectric (by changing the switch position to 2) causes the depolarisation current, and the residual voltage across any polarising capacitor  $C_i$  can be expressed as:

$$V_{Ci}(T_c, T_d) = V_0 \left[ 1 - \exp\left(-\frac{T_c}{\tau_i}\right) \right] \exp\left(-\frac{T_d}{\tau_i}\right) \quad (7.14)$$

The duration of both the polarisation ( $T_c$ ) and depolarisation current ( $T_d$ ) is the same. Therefore, equation (7.14) can be rewritten only as a function of the charging period ( $T_c$ ). As soon as the switch is moved to position 3, the residual voltages stored in all capacitors ( $n$ ) result in the recovery voltage ( $V_r$ ) developed across the terminals of the test specimen. However, the geometric capacitance  $C_0$  does not make any significant change to the measured recovery voltage as it discharges very quickly.

Let's assume, only one polarisation mechanism is occurring in a dielectric. Therefore, a single charging capacitor ( $C_1$ ) is present in the equivalent circuit. For a given charging period ( $T_c$ ), the maximum value of across this capacitor can be written as follows (relevant derivation of  $V_{rmax}$  is provided in Appendix B):

$$\begin{aligned} V_{rmax}(T_c) &= \hat{A}_1(T_p) V_{C1}(T_c) \\ &= \hat{A}_1(T_p) V_0 \left[ 1 - \exp\left(-\frac{T_c}{\tau_1}\right) \right] \exp\left(-\frac{T_d}{\tau_1}\right) \end{aligned} \quad (7.15)$$

where,

$$\hat{A}_1(T_p) = k \left[ A_{1,1} \exp(T_p p_1) + A_{1,2} \exp(T_p p_2) \right]$$

Here,  $T_p$  is the time instant at which the maximum value of the polarisation spectrum is achieved. The formulation derived above is applicable for a dielectric containing a single polarisation event. However, this is not sufficient in explaining the modelling of RVM measurements in most practical cases. A dielectric may contain more than one polarisation branch, and their contribution must be considered in the modelling in order to improve the accuracy.

To generalise, the final form of the RVM response for  $n$  branches is given by

$$\begin{aligned} V_{rmax}(T_c) &= \hat{A}_1(T_p) V_0 \left[ 1 - \exp\left(-\frac{T_c}{\tau_1}\right) \right] \exp\left(-\frac{T_d}{\tau_1}\right) + \dots \\ &\dots + \hat{A}_n(T_p) V_0 \left[ 1 - \exp\left(-\frac{T_c}{\tau_n}\right) \right] \exp\left(-\frac{T_d}{\tau_n}\right) \end{aligned} \quad (7.16)$$

where,

$$\hat{A}_i(T_p) = A_{i,1} \exp(T_p p_1) + \dots + A_{i,n+1} \exp(T_p p_{n+1})$$

$$A_{i,m} = \frac{k_i \prod_l (p_m - z_{i,l})}{p_m \prod_{x \neq m} (p_m - p_x)}$$

$$k_i = \frac{N_{n,i}}{D_{n+1}}$$

$$i, l = 1, 2, \dots, n; \quad m, x = 1, 2, \dots, n+1$$

### 7.9.3 Computation Process of the RVM Response

The working procedures of the RVM modelling are depicted by the flowchart in Figure 7.15. The whole simulation process is iteratively carried out over a wide range of charging period in MATLAB. As mentioned earlier, the Dirana system does not measure the recovery voltage. However, the measured polarisation and depolarisation currents from this setup are utilised as input data to construct the RVM spectrum.

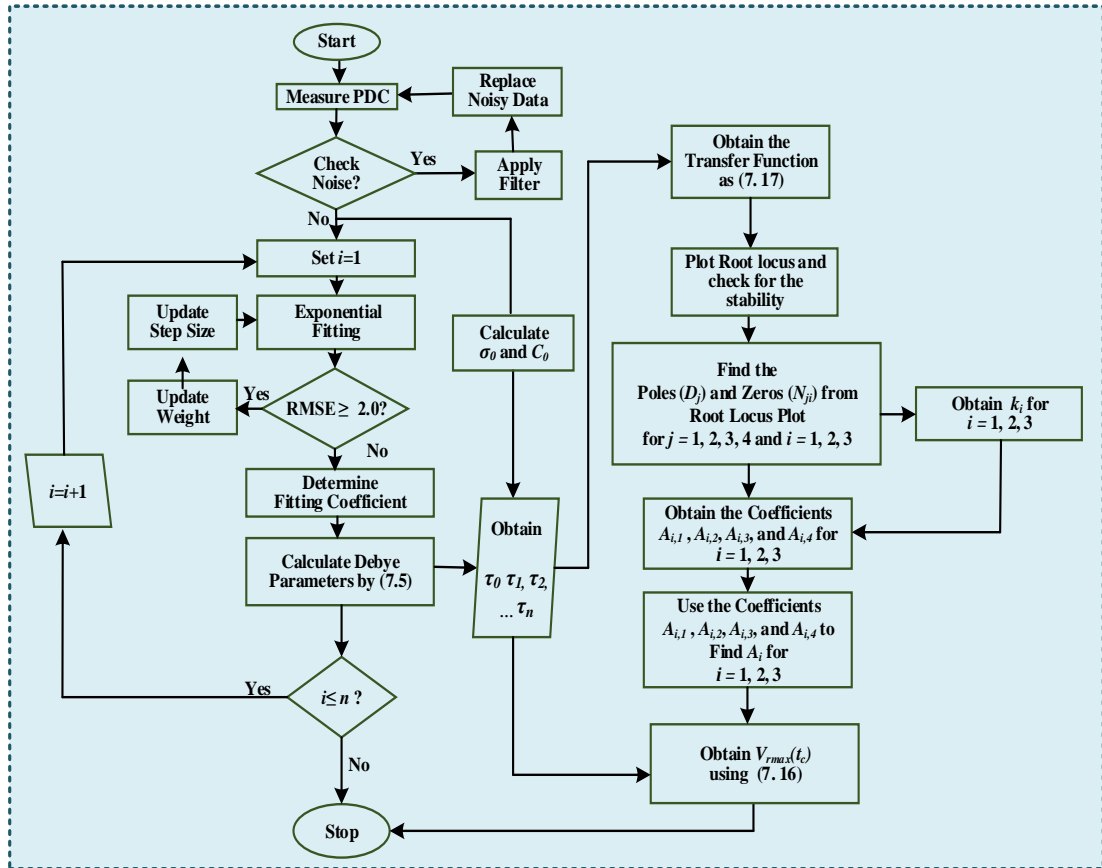


**Figure 7.15.** Flowchart of the working algorithm in the RVM simulation

Although the best fitting is achieved for  $n=4$  as reported in Table 7.4, for the simplicity of RVM modelling, the total number of relaxation branches chosen here is  $n=3$ . A higher number of branches increases the convergence time and makes it difficult to find a suitable solution for the RVM modelling.



### 7.9.3.1 Poles and Zeros Analysis

The transfer function for the Debye circuit having three parallel  $R$ - $C$  branches is given by:

$$F(s) = \frac{V_r(s)}{V_k(s)} = \frac{s^3 N_{3,i} + s^2 N_{2,i} + s N_{1,i} + N_0}{s^4 D_4 + s^3 D_3 + s^2 D_2 + s D_1 + D_0} \quad (7.17)$$

where,

$$\begin{aligned} D_4 &= \tau_0 \tau_1 \tau_2 \tau_3 \\ D_3 &= \tau_0 \tau_1 \tau_2 \tau_3 + \tau_0 (\tau_1 \tau_2 + \tau_2 \tau_3 + \tau_3 \tau_1) + \\ &\quad R_0 (\tau_1 \tau_2 C_3 + \tau_2 \tau_3 C_1 + \tau_3 \tau_1 C_1) \\ D_2 &= \tau_0 (\tau_1 + \tau_2 + \tau_3) + \tau_1 \tau_2 + \tau_2 \tau_3 + \tau_3 \tau_1 + \\ &\quad R_0 [(\tau_1 + \tau_2) C_3 + (\tau_2 + \tau_3) C_1 + (\tau_3 + \tau_1) C_2] \\ D_1 &= \tau_0 + \tau_1 + \tau_2 + \tau_3 + R_0 (C_1 + C_2 + C_3) \\ D_0 &= 1 \end{aligned}$$

On the other hand, the coefficients of all the terms in the numerators of  $F(s)$  can be determined from the superposition principle. In the RVM modelling, three capacitors ( $C_1$ ,  $C_2$  and  $C_3$ ) are considered. Thus, the total effect of these energy storage components at an instant can be calculated by the sum of their individual contributions at that moment. Considering the residual voltage across  $C_1$  is  $V_k = V_{C1}$ , the coefficients in equation (7.17) can be written as:

$$\begin{aligned} N_{3,1} &= R_0 C_1 \tau_2 \tau_3; & N_{2,1} &= R_0 C_1 (\tau_2 + \tau_3) \\ N_{1,1} &= R_0 C_1; & N_0 &= 0 \end{aligned} \quad (7.18)$$

Similarly, for  $V_0 = V_{C2}$  and  $V_0 = V_{C3}$ , the coefficients are:

$$\begin{aligned} N_{3,2} &= R_0 C_2 \tau_1 \tau_3; & N_{2,2} &= R_0 C_2 (\tau_1 + \tau_3) \\ N_{1,2} &= R_0 C_2; & N_0 &= 0 \end{aligned} \quad (7.19)$$

$$\begin{aligned} N_{3,3} &= R_0 C_3 \tau_1 \tau_2; & N_{2,3} &= R_0 C_3 (\tau_1 + \tau_2) \\ N_{1,3} &= R_0 C_3; & N_0 &= 0 \end{aligned} \quad (7.20)$$

For each parallel  $R$ - $C$  branch, the Bode plots of the transfer functions for various branch numbers are shown in Figure 7.16. The magnitude and phase contribution for each pole-zero pair corresponds to each RC-parallel branch. As can be observed, the pole locations are fixed for all branches which imply the denominator of the transfer function is independent from the  $R_i$  and  $C_i$  parameters and also, the system is stable. However, the zeros are observed to be located at different positions for various  $R$ - $C$ -branches. The frequency responses for both samples are almost similar. For the Bode plot of sample S-3, the initial magnitude for branch 2 ( $i=2$ ) is less (near to  $-60$  dB) compared to that of sample S-1 (near to  $-40$  dB) as shown in red colour. In the phase response, till the corner frequency  $10^{-3}$  rad/s, all branches ( $i = 1, 2, 3$ ) show equal phase

shift while after that the phase shift is different till 1 Hz. This is due to the fact that the slopes added by the poles in these frequency ranges are different for different  $R$ - $C$ -branch parameters. Due to different corner frequencies, the magnitude responses also deviate from each other.

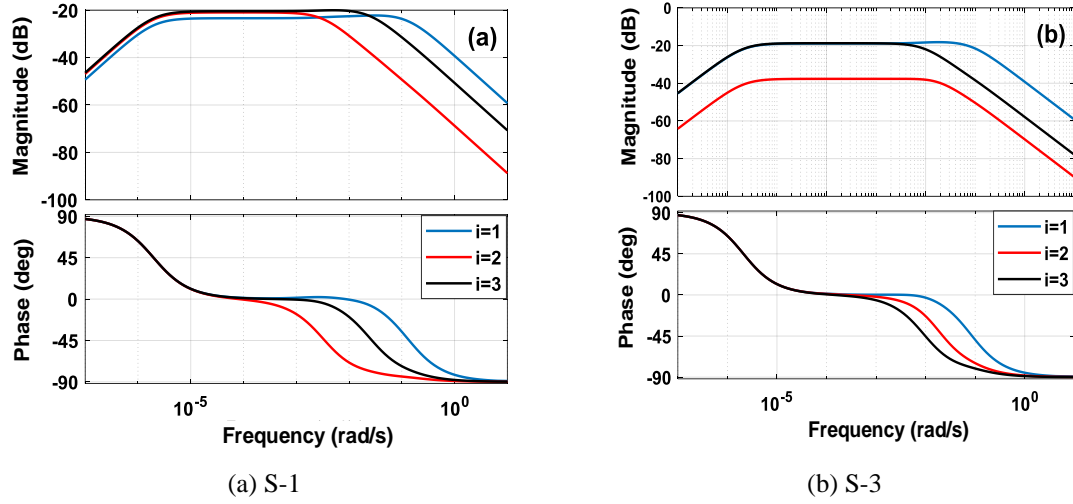


**Figure 7.16.** Bode plots of the transfer functions for S-1 and S-3

Once the poles and zeros are obtained, the next step is to calculate the coefficients of  $V_{rmax}$  ( $T_c$ ) in equation (7.16). Each parallel branch represents one coefficient ( $A_i$ ) and each coefficient is divided into four sub-coefficients ( $A_{ij}$ ). These coefficients are evaluated by each  $R_i$ - $C_i$  pair. The calculated coefficients are provided in Table 7.8.

**Table 7.8.** Calculated coefficients of the transfer function for S-1 and S-3

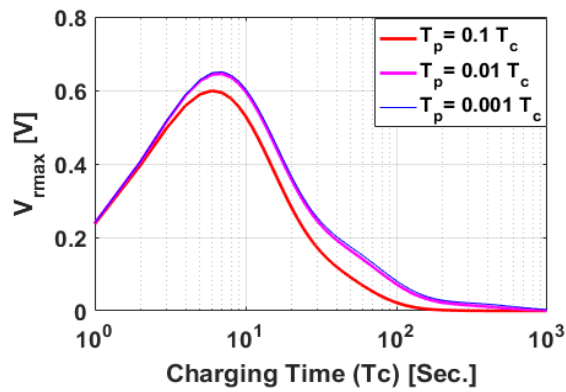
Coefficients	Samples		Location of poles
	S-1	S-3	
$A_{11}$	0.0112	0.0112	<b>Poles for S-1</b> $p_1 = -0.132$ $p_2 = -0.025$ $p_3 = -0.003$ $p_4 = -1.97 \times 10^{-6}$
$A_{12}$	$9.31 \times 10^{-6}$	$9.31 \times 10^{-6}$	
$A_{13}$	$-1.16 \times 10^{-7}$	$-1.16 \times 10^{-7}$	
$A_{14}$	$8.32 \times 10^{-10}$	$8.32 \times 10^{-10}$	
$A_{21}$	$3.28 \times 10^{-5}$	$2.91 \times 10^{-5}$	
$A_{22}$	$-1.30 \times 10^{-6}$	$-1.16 \times 10^{-6}$	
$A_{23}$	$1.55 \times 10^{-6}$	$1.37 \times 10^{-6}$	<b>Poles for S-3</b> $p_1 = -0.084$ $p_2 = -0.019$ $p_3 = -0.009$ $p_4 = -2.1 \times 10^{-6}$
$A_{24}$	$1.10 \times 10^{-9}$	$9.81 \times 10^{-10}$	
$A_{31}$	0.0003	0.0001	
$A_{32}$	$-8.90 \times 10^{-5}$	$-3.87 \times 10^{-5}$	
$A_{33}$	$-1.86 \times 10^{-7}$	$-8.09 \times 10^{-8}$	
$A_{34}$	$1.16 \times 10^{-9}$	$5.08 \times 10^{-10}$	

### 7.9.3.2 Results and Discussion

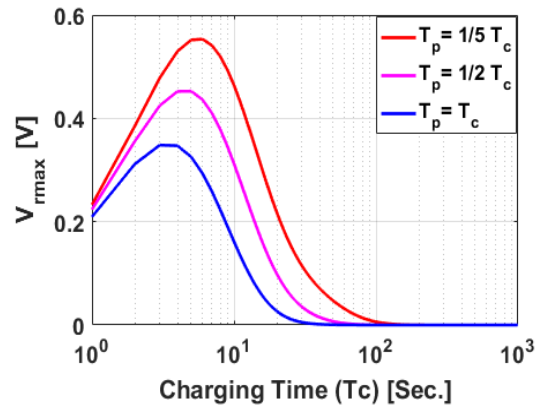
The RVM modelling of S-1 and S-3 as a function of the charging time ( $T_c$ ) is illustrated in Figure 7.17. Here, two cases including the relationship between the peak time ( $T_p$ ) and the polarising period ( $T_c$ ) are analysed. Different literature suggests that as ageing progresses, the peak time of the RVM curve follows almost a linear relation with the charging period and has a comparatively lower slope value [238], [245], [247].

Hence, in one case, it is considered that the  $T_c$  value is increasing by a factor of 10 to the  $T_p$ , while the other case assumes the ratio between  $T_p$  and  $T_c$  to be 20%, 50% and 100%. Both cases are expressed as follows:

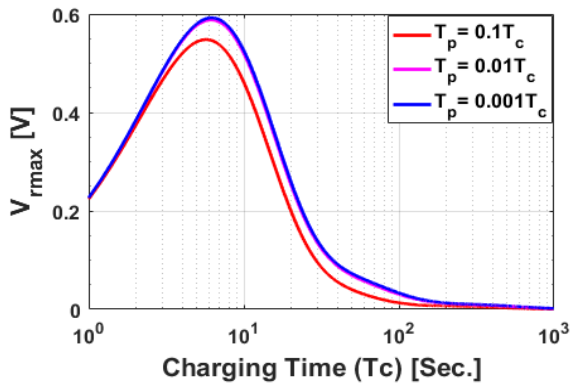
$$\text{Case 1: } \begin{cases} T_p = 0.1 T_c \\ T_p = 0.01 T_c \\ T_p = 0.001 T_c \end{cases} \quad \text{and} \quad \text{Case 2: } \begin{cases} T_p = \frac{1}{5} T_c \\ T_p = \frac{1}{2} T_c \\ T_p = T_c \end{cases}$$



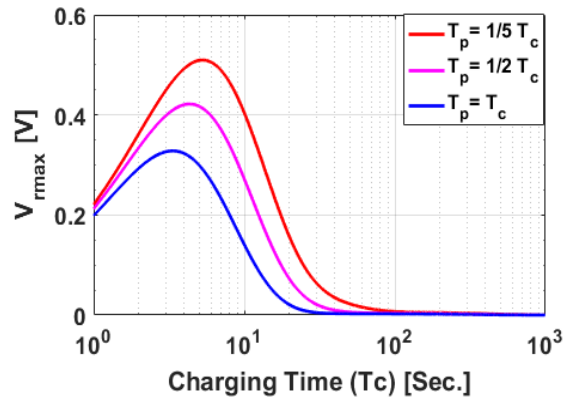
(a) RVM response of S-1 for Case-1



(b) RVM response of S-1 for Case-2



(c) RVM response of S-3 for Case-1



(d) RVM response of S-3 for Case-2

**Figure 7.17.** RVM response of the test cable samples

---

---

As can be observed, the modelled RVM responses of S-1 and S-3 follow similar trends for both Case-1 and Case-2. Here, the peak of the  $V_{max}$  response is decreasing when  $T_p$  value is progressively increasing to the  $T_C$  value. This is because the coefficients of  $V_{max}$  ( $A_1$ ,  $A_2$  and  $A_3$ ) in equation (7.16) are a function of  $T_p$  i.e.  $\exp[(T_p - p_i)]$ , and the poles are also negative; therefore, an increased value of  $T_p$  causes a noticeable change to the peak value in the recovery voltage response.

For Case-1, when  $T_p$  is 100 times less than  $T_C$  or lower than that factor, the resultant curves overlap with each other for both samples. On the other hand, for Case-2, with the increasing  $T_p$ , the peak of the  $V_{max}$  curve is shifting towards the lesser charging time. Moreover, the magnitude difference under different conditions is comparatively larger as compared to Case-1. Another noticeable feature in all the cases is that  $V_{max}$  is gradually dying out when the charging period exceeds 100 seconds. This is obvious as the recovery voltage is mostly dependent on the pol/depolarisation currents where these currents are more likely to decay at an exponential rate with the increasing time.

The modelling results shown here are derived from three  $R$ - $C$  polarisation branches for both test samples. In accordance with the Debye circuit, the acquired pol/depolarisation currents from experimental measurements form the basis of the RVM modelling. Also, the exponential fitting of the pol/depolarisation currents is justified with performance functions. Hence, it can be said that this modelling approach based on the Debye circuit and the PDC current provides an alternative solution to predict or construct the recovery voltage response without performing the actual measurements. The obtained RVM curves show almost similar trends as reported in existing literatures [10], [66], [238], [239], [246]–[248]. Some discrepancy observed in other studies can be attributed to additional polarisation processes associated with the contamination, moisture and trapping/defects in the test samples, which would require more  $R$ - $C$  relaxation branches to obtain the desired RVM response [243], [245].

## 7.10 Chapter Conclusion

In this chapter, an experimental study on several short sections of service-aged XLPE cable has been carried out using various analyses including Daniel's normalisation,  $\tan \delta$  measurement and modelling (from 1 mHz to 50 Hz), activation energy measurements, electrical stress impacts, etc.

For thin films, the Dissado-Hill clustering model has been well established and widely used; however, for service-aged XLPE cables, this model is applied here for the first time to identify the physical polarisation process due to the clustering, interfacial and trapped dipoles from the measured depolarisation current. Moreover, the applied model mathematically

---

---

correlates the dielectric response and associated polarising events generally occurred in XLPE cable in the absence of major defects (e.g. water trees).

Daniel's normalisation is applied to interpret the permittivity difference between DC and optical frequency. The modelling approach based on the relationship between the individual  $\tan \delta$  due to distinct polarisation events and the overall  $\tan \delta$  follows the experimental measurements very well over the tested frequency range.

The lower AC activation energy at VLF physically corresponds to the increasing conduction process in this frequency range. Finally, PDC analysis with different ambient conditions (303 K - 338 K) provides knowledge about trapping defects with the rising temperature. To sum up, the information obtained from measurement and analysis of the PDC current will be a potential resource to better understand the dielectric response in polymeric insulation.

An empirical approach to model the recovery voltage of XLPE cables based on the polarisation and depolarisation current (PDC) method is also elucidated. Based on the Debye circuit, the time-domain responses are transferred to the frequency domain to obtain the peak value of recovery voltage. For modelling, a mathematical relationship is developed among different  $R$ - $C$  relaxation branches, the charging period and the time when the recovery voltage is at its maximum. The developed model considers three relaxation branches and is justified with several performance functions. The RV response from this modelling correlates the charging time and the peak time and supports the results in previous studies elsewhere.

---

---

## Chapter 8.

# Cavity Discharge Measurement and Modelling

The previous chapters (Chapters 4-7) documented research on dielectric response measurement. The increasing application of VLF testing for insulation condition assessment also requires understanding the partial discharge behaviours at this frequency. To this end, this is the first contribution chapter on cavity discharges. In this chapter, a comparative study including measurement and modelling of partial discharge for various void geometries (cylinder, block, prism, rhombus) at VLF and PF voltage is carried out. Results from experiments and simulations are presented with phase-resolved discharge patterns and integrated parameters (maximum/average discharge magnitudes, repetition rates, etc.). Dynamic simulation, achieved using a combination of finite element analysis and MATLAB, is included to incorporate with the experimental results. The work in this chapter has been published in [6], [11], [18] as shown in the List of Publications.

## 8.1 Physical Process of Cavity or Void Discharge

### 8.1.1 Definition of Void or Cavity Discharge

In practice, solid dielectrics are not perfectly homogeneous; instead there are some cavities/voids, imperfections or defects built up within the insulation due to the long-term in-service operation or flaws in the manufacturing process. The cavities are gas-filled (relative permittivity = 1) and usually have lower breakdown strength as compared to the surrounding solid dielectric medium. When subjected to a high external applied voltage, the electrical stress inside the cavity rises considerably, and after exceeding the gas breakdown strength, PDs are expected to be incepted [8], [10], [144]. However, for a cavity discharge, the availability of free electrons inside the void is one of the prerequisite conditions [62], [154], [156], [208]. Under the force caused by interaction of the electric field with the charged electrons, these free electrons get accelerated and gain sufficient energy to collide with the neutral gas molecules and

---

---

make ionisation. This phenomenon causes more release of free electrons and eventually generates an electron avalanche [8], [10], [203].

In principle, the cavity discharge resulting from an electron avalanche is a short duration current pulse flowing from one end to the other end of the cavity, momentarily bridging insulation through the void. The gas content inside the cavity transiently changes its state from the non-conducting to conducting, and subsequently causes a sudden drop of electrical stress across the cavity volume [44], [144], [156].

#### **8.1.1.1 Effects of Cavity Discharge**

Partial discharge has injurious effects to any high voltage system because repetitive discharges occurring in the long-term can eventually lead to complete failure of the whole system [179], [206], [249]–[251]. The repetitive discharges may alter the composition or microstructure of chemical compound, resulting in an increase of the conductivity across the void surface [250], [251]. Gaseous by-products generated after an electron avalanche may also change the gas pressure inside the cavity [14]. It has been experimentally observed that the cumulative effects of PDs result in electrical treeing process, which is the formation of numerous bush or filament-shaped partially conductive channels in the tested material [179], [206], [249].

#### **8.1.1.2 Discharge Type**

During the cavity discharge process, the electron avalanche may grow significantly until it forms a momentarily conductive channel in the cavity. The discharge pulses are typically in the duration of 1-100 ns. The discharge process is the streamer type, and the magnitude is around 10 pC or so [252], thereby can be detected by most of the PD measurement systems [178]. It should also be noted that as the streamer develops, the electric field inside the cavity drops considerably [58], [144].

### **8.1.2 Physical Mechanism of Discharge Occurrence**

The physical mechanism of PD phenomena, including the triggering process, causes and effects inside cavities, has been extensively discussed in the literature [143], [156], [159], [167]. The basic concepts and associated explanations are discussed as follows.

Figure 8.1 illustrates the sequence of physical processes that happen inside a cavity under application of a sinusoidal voltage excitation. Prior to a cavity discharge event (Figure 8.1a), the cavity electric field ( $E_{int}$ ) closely correlates with the external field ( $E_0$ ) at the boundary electrodes through a suitable modification factor ( $f_m$ ). Depending on the material permittivity and cavity geometry, the factor changes the electric stress across the cavity accordingly. The

field  $f_m E_0$  is known as the Laplacian field, and before any PD events, the electric field inside the cavity is equal to that value [44], [167].

During a discharge event (Figure 8.1b), a charge transfer occurs at the cavity wall, and as a result, the opposite polarity space charges generated from an electron avalanche begin to build up at the other end of the cavity surface. The accumulated space charge at the cavity wall thereby develops a residual field in the opposite direction of the applied stress. This opposing field due to space charges is known as Poissonian field [156]. The resultant cavity field can be now expressed as the sum of the external field and residual field, and written as:

$$E_{in}(t) = f_m E_0 + E_{res}(t) \quad (8.1)$$

After a PD event (Figure 8.1c), the leftover space charges start to decay on the cavity surface through the drift/recombination process. Therefore, the residual field due to the space-charge decreases and the total cavity field approaches to a field contributed only by the external voltage. In reality, PD events occur very quickly, typically in a duration of few micro-to-nanoseconds; therefore, the field inside the cavity drops suddenly over a very short period of time [8], [33], [216]. If the cavity field is sufficiently low, ideally below the extinction level, the PD activities are expected to cease completely.

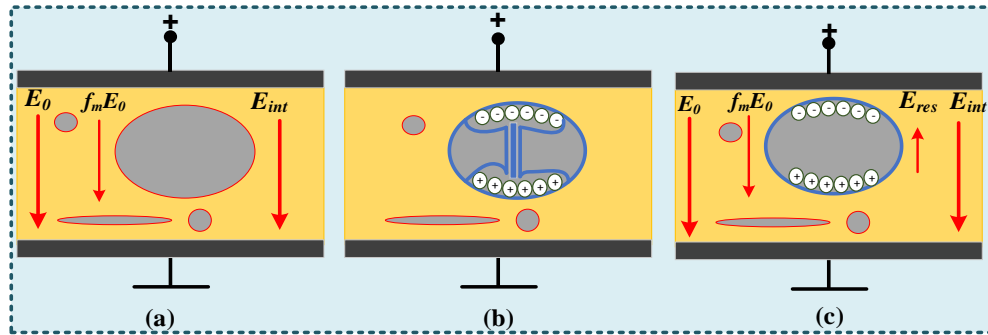


**Figure 8.1.** Schematic diagram of a PD event (a) before PD (b) during PD (c) after PD

A conceptual visualisation of cavity discharge at four different phase angle positions of a sinusoidal waveform is depicted in Figure 8.2.

- 1) For position (a), the residual field due to positive space charges opposes the external field, thereby reduces the effective cavity field and so is the PD magnitude.
- 2) For position (b) at which the transition of the voltage polarity across the zero-crossing just occurred, the space charge field and external field both are in the same direction. Thus, in this case, the effective field across the cavity increases which ultimately provides a rise in the PD magnitude.



- 3) Same physical process as position (a); however, only for PDs occurring during the negative half-cycle.
- 4) Same physical process as position (b); however, only applicable for PDs in the positive half-cycle.

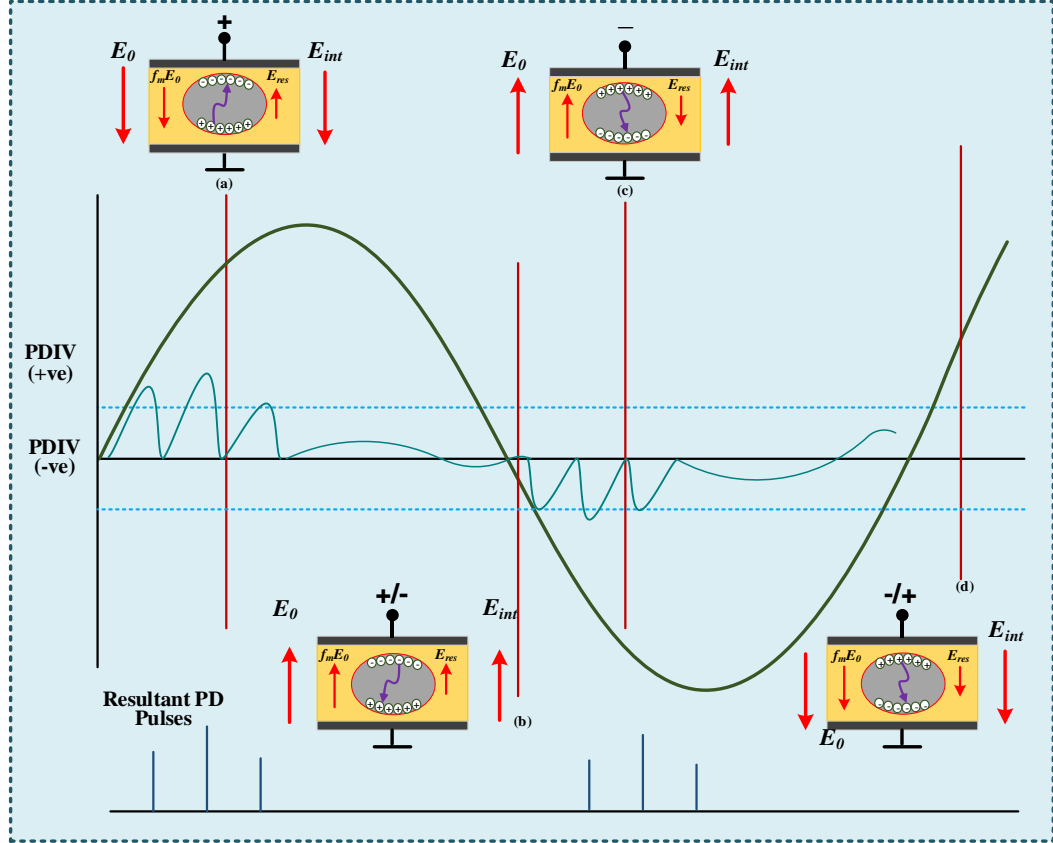


**Figure 8.2.** Physical process of cavity discharge with the impacts of space charges

## 8.2 Motivation of Cavity Discharge Measurement

A number of experimental studies has been conducted to investigate the characteristics of void discharges under variable applied frequency excitations in different insulation materials such as epoxy resin [33], [44], ABS insulation [46], polycarbonate [62], polyester resin [42], and PE insulation [140], [167]. Experimental results showed that the PD characteristics (inception voltage, magnitude, repetition rate, etc.) and the phase-resolved discharge patterns change with the applied voltage frequency and materials and thus not easy to generalise. Based on the three capacitance model, investigations by [140], [253] provide a basic theory of PD occurrences inside different cavity shapes and the effects of discharge areas in an isolated void bounded by solid insulation. However, the experimental measurement, as well as numerical modelling under power frequency voltage, was not included.

---

---

To date, the PD characteristics under VLF test voltage get little attention, especially for the diagnosis of voids in cross-linked polyethylene (XLPE) insulation [62], [208], [254], [255]. Furthermore, there is limited research conducted on the modelling of PD behavior under VLF excitation and matching the simulation with the experimental results [44], [63]. The test voltage frequency and cavity shapes have influences on various physical phenomena associated with a PD event [46], [254]. These include the recombination, conduction and decay process of free electrons (which is responsible for the PD inception). Space charges, usually generated after a PD event inside the cavity or at the cavity surface, play a role in causing discrepancy between the discharge characteristics at VLF and power frequency. For varying cavity shapes and test frequencies, the diagnosis of PD behaviors by both measurement and modeling is an area yet to be explored. It is of research interest to obtain as much diagnostic knowledge as possible [16].

Majority of research was based on fabricated cylindrical or spherical cavities for PD source and results from PD measurement and modelling were found inconsistent, especially at VLF voltage. To explore such changes of PD characteristics in relation to the void geometry as well as frequency, different void structures are here examined for testing. Measurement and modeling results are interpreted with the phase-resolved analysis and comparisons of integrated parameters (inception voltage, magnitude and repetition rate etc.) at VLF and 50 Hz. Good agreement of experimental and simulated PD characteristics as a function of cavity geometry at VLF and PF voltage is the main contribution of this research.

## **8.3 Experimental Descriptions of PD Measurement**

### **8.3.1 Power Supply and PD measurement system**

Figure 8.3 illustrates the schematic diagram of a time-resolved PD measurement system that has been used to conduct the laboratory experiment. The measurement system, detection technique and measurement procedure comply fully with the approach documented in IEC 60270 Standard. The test setup basically consists of a high voltage supply and the measurement system. For both measurements (either 50 Hz or 0.1 Hz), the experimental arrangement is similar to the circuit shown in Figure 8.3 except that the high voltage supply to provide AC voltage excitation for the test object is different.

In the experiment, two different power sources are used to provide VLF (0.1 Hz) and power frequency (50 Hz) test voltage. A commercial Baur-Frida instrument was used for the VLF excitation. For power frequency, a conventional test setup was used: a 25 kVA step-up transformer with its low voltage input side fed from a 240 V variable auto-transformer (variac).

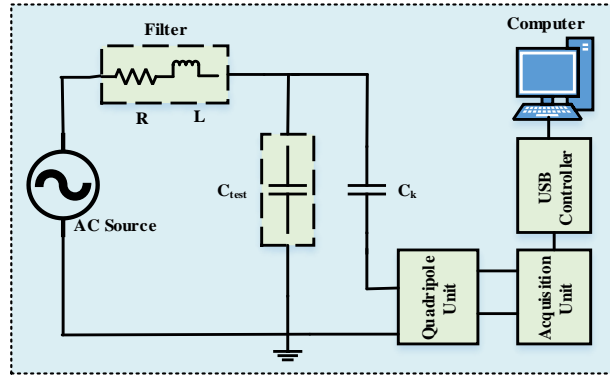


**Figure 8.3.** Schematic diagram of the measurement circuit

For PD measurement, a commercial Mtronix MPD 600 system was employed. The test setup includes a quadripole unit (CPL 542) connected to the circuit via a 1 nF coupling capacitor ( $C_k$ ). This coupling capacitor is also in parallel to the test object, i.e. cavity discharge test-cell. When a discharge happens in the test object ( $C_{test}$ ), the coupling capacitor transfers charge to it to compensate for the momentary voltage collapse across the test object. On the other hand, the quadripole unit acts as the measuring impedance where both the PD and voltage signal can be extracted.

The acquisition unit is the main module of the PD detection system which captures and digitises the output PD signal. Through an MCU 502 USB controller and fibre optic cables, the digitised signals are transferred to a computer so that data can be saved for subsequent processing and analysis. This can be done using the MPD 600 software and also, the stored data can be post-processed with custom programs in MATLAB. The test setup also includes a high voltage filtering unit that consists of a resistor (50 k $\Omega$ ) and inductance (20 mH) to block the high-frequency noise from the supply and for the protection in case of full breakdown.

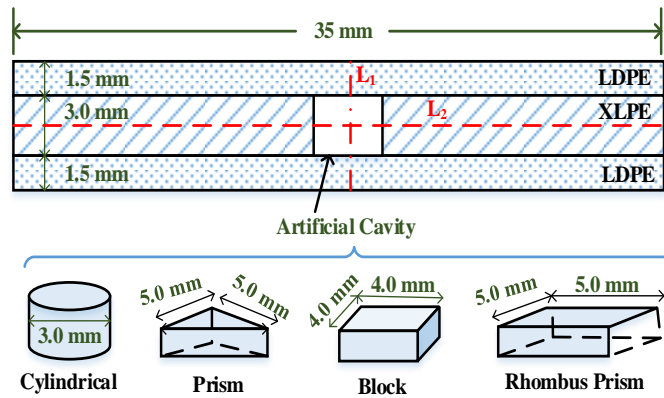
### 8.3.2 Description of Test Samples

The test-objects are small disks of solid dielectric materials containing an isolated cavity. The cross-sectional view of the test samples is depicted in Figure 8.4. The middle layer is an XLPE sheet with a thickness ( $d$ ) of 3 mm. A hole was then punched into its center. After that, an LPDE sheet of 1.5 mm thickness was stacked over the top and the bottom. The desired shape of the hole was precisely provided in the central layer using a computer numerically controlled tooling machine. The XLPE layer was then thermally fused with the top and bottom LDPE layers at about 110<sup>0</sup> C in a thermostat-controlled oven for two hours. Each test sample has a diameter of 35 mm and an overall height ( $D$ ) of 6 mm. The description of test samples is provided in Table 8.1. To facilitate comparison, each test specimen is characterised in terms of the geometry factor ( $GF$ ) which is defined as the ratio of its void volume ( $V_s$ ) and the smallest void volume ( $V_{min}$ ) among the tested specimens.

**Table 8.1.** Description of all test samples

Samples	Void Geometry	GF= $V_s/V_{min}$	Dimensions (mm)
T-1	Cylindrical	1.0	$d = 3.0$ ; $c = 3.0$
T-2	Prism	1.5	$a = b = 5.0$ ; $c = 3.0$ ;
T-3	Block	2.25	$a = 4.0$ ; $b = 4.0$ ; $c = 3.0$
T-4	Rhombus Prism	3.0	$a = 5.0$ ; $b = 5.0$ ; $c = 3.0$

\*a = length; b = width; c = height and d = diameter

**Figure 8.4.** Front view and cavity shapes of all test samples

### 8.3.3 Description of Measurement Procedures

The test specimen is placed between two brass electrodes that follow a pseudo-Rogowski profile, i.e. the electrodes comprise flat plates with a rounded edge to reduce enhanced stress at the edge. The whole structure is completely immersed in a transformer oil-filled housing to prevent unwanted interference from surface discharges (discharges not in the cavity) during the testing. The image of all test objects along with the test-cell that have been used is shown in Figure 8.5. As a check of this arrangement, no discharges were observed when the setup was stressed to the test voltage with a dummy test specimen of same dimension but no void in the middle layer.

Depending on the actual inception voltage (PDIV) value, PD activity is measured under sinusoidal excitation of frequency 50 Hz or 0.1 Hz and sequentially at different applied voltage levels: 1.1, 1.25 and 1.5 PDIV. For conditioning purpose, all samples are pre-stressed at the test voltage for 1 hour and after that measurement results are recorded for 60 consecutive AC cycles at frequency of 0.1 Hz and for 6000 cycles of 50 Hz excitation. Prior to each test sequence, the measurement circuit was calibrated by injecting a known charge of 50 pC from an MPD 542 calibrator. After calibration, it was established that the background noise level generated from

the test circuit supply including the use of filtering is about 20 pC. This interference level is acceptable as it is much smaller as compared to the discharge magnitude occurring in the cavity, typically in order of several hundreds of pC.

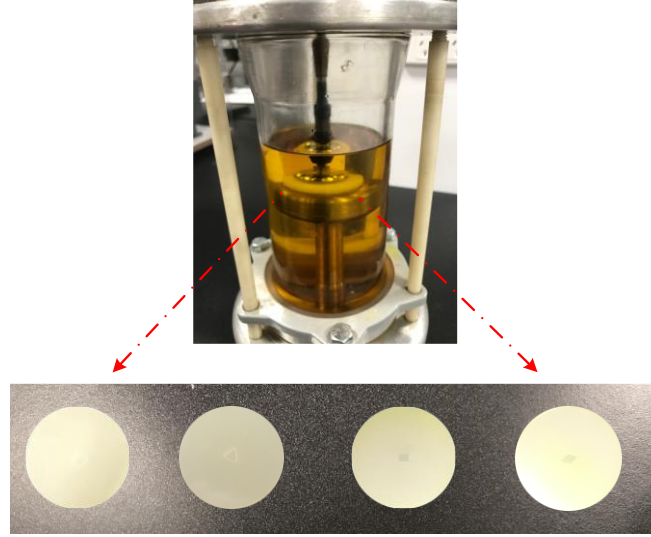


**Figure 8.5.** The test-cell and top-view of test samples

To achieve a consistent test environment, all measurement sequences of the same test sample were conducted continuously; there is a concern that the interruption between two consecutive applied voltage levels or frequencies (50 Hz measurements first then VLF) might affect the measurement results. With the constant frequency, when the applied voltage is raised it was seen that the average time interval between two consecutive PD events is almost constant. This suggests that any change of local conditions inside the cavity or at the cavity surface is relatively small. Note that the total test duration of each sample was around 6 hours.

## 8.4 Inception Voltage and Field Calculation

Partial discharges occurring in the cavity are streamer type. The inception voltage and field mostly depend on the void geometry, shape, inside gas pressure, permittivity of the solid insulation that bounds the cavity and the ionisation characteristics of gas during a PD event [156]. An empirical formula for calculating inception voltage is given by [256]

$$V_{inc} = \frac{\beta p}{\ln(pd)^\eta + k} \left[ \frac{D + d(\epsilon_r - 1)}{\epsilon_r} \right] \quad (8.2)$$

$$k = 3.513(pd)^{0.0059}; \quad 0.2 \leq pd \leq 100 \quad [kPa - cm] \quad (8.3)$$

It is assumed that the field inside the cavity is sufficient enough to initiate a discharge process and the gas inside the void is ambient air at atmospheric pressure  $p$  (1 atm). Here,  $D$  is the thickness of the total insulation,  $d$  is the depth of the void, and  $\epsilon_r$  is the relative permittivity

of the solid insulation. The constant  $\beta$  and  $\eta$  represent the ionisation process which depends on the gas content inside the void. For air, the values are 273.7 V/Pa-m and 0.5 respectively [63], [156].

The relative permittivity of XLPE and LDPE is similar, approximately 2.3-2.4. Thus, for simplicity, the permittivity  $\epsilon_r$  is considered as 2.3 for both materials. The inception voltage was then calculated by equation (8.2) and (8.3) and found to be 15.16 kV. It should be noted that the empirical formula was developed for cylindrical/spherical void samples in which the field inside the void was considered uniform. In reality, field distortion and enhancement occur around cavity edges. Moreover, multiple discharge concentration points may exist that generate free electrons and influence the PD process.

To measure the inception voltage, the test voltage was raised quickly to 75% of the estimated inception value and then increased slowly in steps of 200 V to acquire the first repetitive PDs in the test circuit. Each test sample was tested for 5 times and the average value was considered. The variations of experimental PDIV for all tested samples are illustrated with the error bar plot of Figure 8.6.

As can be observed, the PDIV values show a dependency on the cavity geometry and the supply voltage frequency. The rhombus geometry provides the lowest PDIV value. In all cases, the PD under VLF excitation incepts comparatively at a lower voltage than that at PF. This can be attributed by the lower statistical time of initial free electrons which are responsible to ignite a discharge process comparatively earlier in the VLF [208]. Note that the experimental PDIV value of cylindrical geometry agrees with the theoretical inception voltage value as calculated earlier.

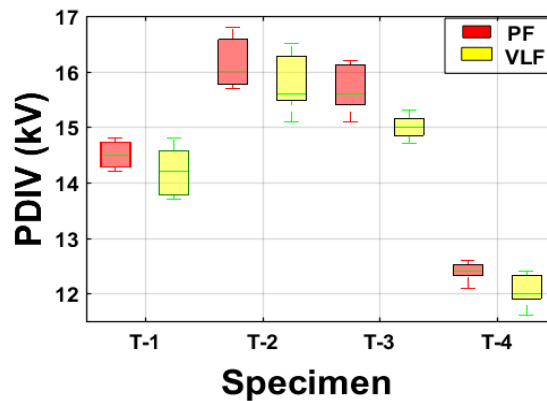


**Figure 8.6.** PDIV values of all tested samples in the experiment

The critical inception field ( $E_i$ ) for an air-filled insulated cavity can be approximated as:

$$E_{inc} = (E/p)_{cr} p \left[ 1 + \frac{B}{(pd)^\eta} \right] \quad (8.4)$$

For air, the parameters  $(E/p)_{cr}$  and  $B$  are found to be  $24.2 \text{ VPa}^{-1}\text{m}^{-1}$  and  $8.6 \text{ Pa}^{1/2} \text{ m}^{1/2}$  [63], [156]. After substituting all the parameters, the inception field for a cylindrical cavity test sample is estimated as  $3.65 \text{ kV/mm}$ . As discussed earlier, the same formula is not applicable to other geometries. For the modelling purpose, the inception field of other test samples ( $E_{incX}$ ) is evaluated as follows:

$$E_{incX} = E_{inc(cylindrical)} \frac{PDIV_X}{PDIV_{cyl}} \quad (8.5)$$

Here,  $PDIV_{cyl}$  and  $PDIV_X$  denote the experimental inception voltage value of the cylindrical and other test samples respectively.

## 8.5 Phase-Resolved Study of Cavity Discharge

For phase-resolved studies, PD activities occurred in the cavity were recorded over 60 consecutive AC cycles at a frequency of  $0.1 \text{ Hz}$  and for 6000 cycles of  $50 \text{ Hz}$  excitation. In the following section, the phase-resolved images of data acquired at  $1.1 \text{ PDIV}$  level are shown.

### 8.5.1 PRPD of Cylindrical Void Geometry

The PD phase-resolved scatter plots of the cylindrical void sample at PF and VLF are shown in Figure 8.7. Here, the patterns were acquired after one-hour conditioning under the voltage level of  $1.1 \text{ PDIV}$ . For PF excitation, it can be seen that discharge activities occur in both positive and negative half-cycles and mostly scatter across the rising quadrant ( $0-90^\circ$  and  $180^\circ-270^\circ$ ) of the voltage waveform, whereas in the VLF case, these are more likely to concentrate around the peak region. Comparing the discharge pattern obtained at  $50 \text{ Hz}$  with VLF, the PF excitation exhibits much denser PD scattering. Interestingly, the patterns obtained here are similarly observed in other studies [46], [62]. Additionally, with the transition of frequency from  $50 \text{ Hz}$  to  $0.1 \text{ Hz}$ , the maximum and minimum discharge magnitude decrease from around  $1600 \text{ pC}$  and  $52 \text{ pC}$  to below  $1200 \text{ pC}$  and  $50 \text{ pC}$  respectively.

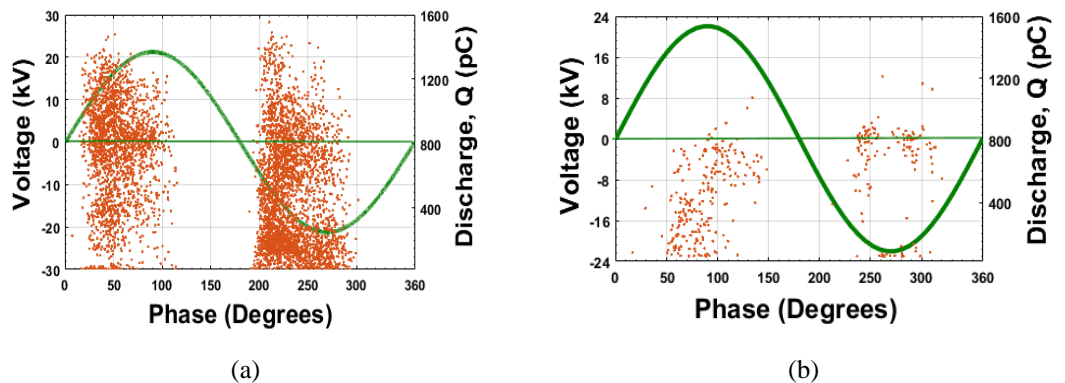


**Figure 8.7.** PRPD patterns of T-1 (a) at  $50 \text{ Hz}$ , and (b) at  $0.1 \text{ Hz}$

---

### 8.5.2 PRPD of Prism Void Geometry

Figure 8.8 shows the phase-resolved PD patterns of the prism void test specimen. The patterns for PF and VLF excitations correspond to 2 minutes and 10 minutes recording time respectively. In each case, as expected, void discharges as a function of the phase angle show approximately symmetrical distribution during positive and negative halves of the AC cycle. However, few discharges with small magnitude are occasionally observed in the zero-crossing region for VLF excitation. Also, a high number of PDs are over 800 pC for 50 Hz, whereas for the VLF case, two intermediate discharge levels (i.e. below 50 pC and above 350 pC) can be clearly distinguished.

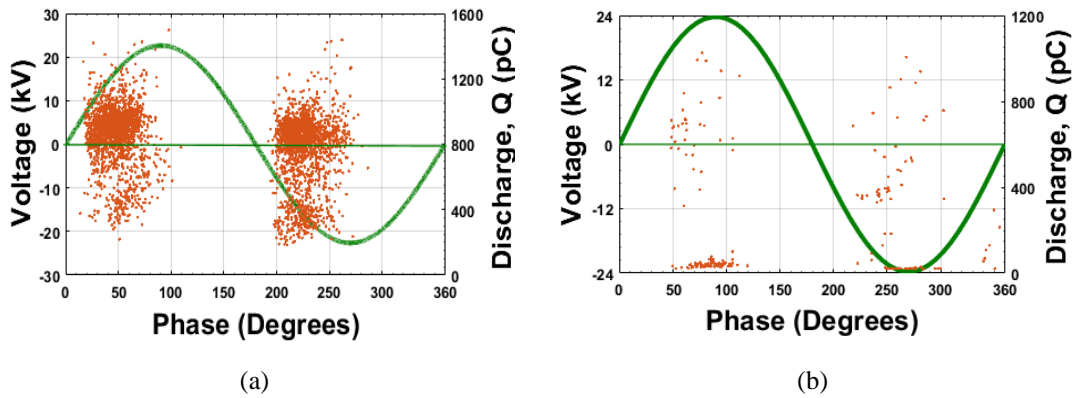


**Figure 8.8.** PRPD patterns of T-2 (a) at 50 Hz, and (b) at 0.1 Hz

### 8.5.3 PRPD of Block Void Geometry

For the block cavity test sample, PDs are also captured with phase-resolved patterns shown in Figure 8.9.

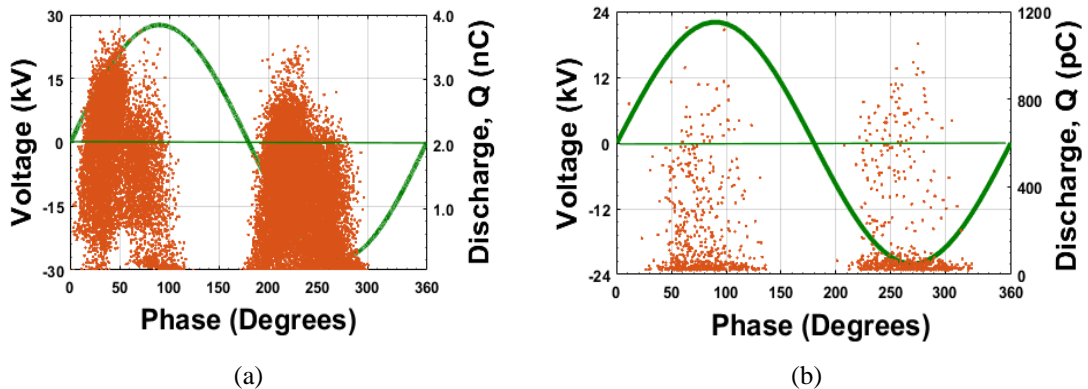


**Figure 8.9.** PRPD patterns of T-3 (a) at 50 Hz, and (b) at 0.1 Hz

Both excitations produce similar patterns over approximately the same phase window during the positive and negative half-cycles. In T-3, larger discharge magnitudes are noticeable, and in particular, the PD activities at PF are scattered over the phase range between the zero-



crossing and peak instantaneous voltage. Also, a high number of discharges are in the nC range, whereas PDs are mostly below 1 nC magnitude with VLF excitation. The maximum discharge magnitude for PF excitation is about 4.0 nC, while in the case of VLF, it is around 1.2 nC.

#### 8.5.4 PRPD of Rhombus Prism Void Geometry

The void discharge patterns as a function of excitation frequency in the rhombus-prism cavity sample are shown in Figure 8.10. Comparing with other test samples at 50 Hz, this specimen exhibits much intensified discharge activity across the zero-crossing of instantaneous voltage. Also, the occurrence rate of PDs above 1 nC magnitude under VLF excitation is comparatively higher. The maximum PD magnitude increased to around 2 nC and 5 nC for the case of 0.1 Hz and 50 Hz, respectively.

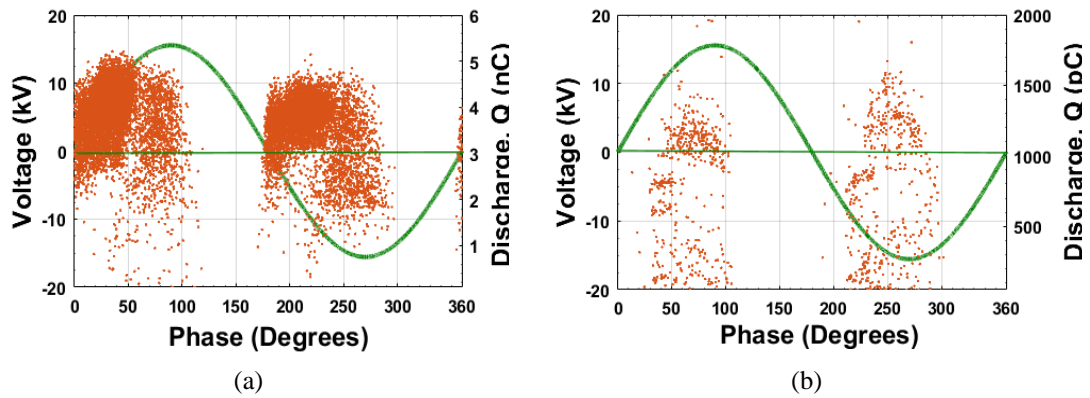


Figure 8.10. PRPD patterns of T-4 (a) at 50 Hz, and (b) at 0.1 Hz

### 8.6 PD Physical Model

#### 8.6.1 Model Geometry and Field in 3D View

The three-dimensional (3D) model of all test objects has been developed in COMSOL Multiphysics® finite element analysis (FEA) software. Note that for modelling purposes, some previous researches consider the 2D axis-symmetric geometry. However, the assumption of axis-symmetry is unrealistic for small cavities. To simplify the model, the dielectric materials inside the sample are assumed as non-dispersive which means the permittivity does not change with the applied voltage frequency. In the 3D model, the top surface of the sample is connected to the high voltage supply, whilst the bottom surface is grounded.

To show the electric field distribution inside the cavity, two cut-lines (L1 and L2) have been drawn in each sample as depicted in Figure 8.4 and Figure 8.11. L1 is a vertical line (i.e. along the z axis) passing through the center of the void. On the other hand, the horizontal line L2 bridges the diameter of the sample through the cavity centre and traverses along the longest

distance of cavity parallel to the x-axis. A cavity surface layer of 0.5 mm thickness has been considered around the void geometry to simulate the charge decay via various physical processes (charge drift recombination, conduction through the cavity wall, etc).

The electric potential distribution in the test object is governed by the following partial differential equations (PDE) and from which the local electric field  $\vec{E}$  can be solved:

$$\varepsilon_0 \varepsilon_r \nabla \cdot \vec{E} = \varepsilon_0 \varepsilon_r \nabla \cdot (-\nabla V) = 0 \quad (8.6)$$

$$\nabla \cdot \left( \sigma \nabla V + \varepsilon_0 \varepsilon_r \frac{\partial}{\partial t} (\nabla V) \right) = 0 \quad (8.7)$$

where,  $\sigma$  is the conductivity of the material,  $V$  is the electric potential, and  $\varepsilon_0$  is the vacuum permittivity. Depending on free electrons availability, it has been assumed that PDs occur when the applied electric stress at the void centre exceeds the critical inception value and during a PD event, the electrical charges propagate along the line L1. Also, the space charges generated after a PD event dissipate or decay on the cavity surface. Therefore, two boundary conditions can be applied to the cavity surface where  $V_{surf}$  and  $\sigma_s$  denote the potential of the cavity surface and surface conductivity respectively.

$$\begin{cases} \nabla \cdot \sigma_s \nabla V_{surf} = 0 \\ V = V_{surf} \end{cases} \quad (8.8)$$

The electric potential and field distribution of all test specimens is calculated in each time step of the measurement period by the finite element method (FEM) as shown in Figure 8.11.

Here the field is calculated for the moment when the PDIV voltage reaches its peak. From the distribution, it can be observed that the comparatively higher field stress is concentrated on the edge and corner of the block and rhombus-prism geometry. This may be the reason for multiple charge concentration points in T-3 and T-4.

## 8.6.2 Cavity Discharge Occurrence

From the basic theory, partial discharge within a void bounded by solid insulation occurs if the two conditions are satisfied. These are: (1) the field magnitude at the centre of cavity needs to be larger as compared to the critical inception field, and (2) there must have free electrons available to initiate a discharge process. Initial free electrons are mainly generated from two possible sources: surface emission ( $N_{esur}$ ) and volume ionisation ( $N_{evol}$ ) [33], [156]. Hence, the total electron generation rate (EGR) can be expressed as:

$$N_{total}(t) = N_{evol} + N_{esur}(t) \quad (8.9)$$

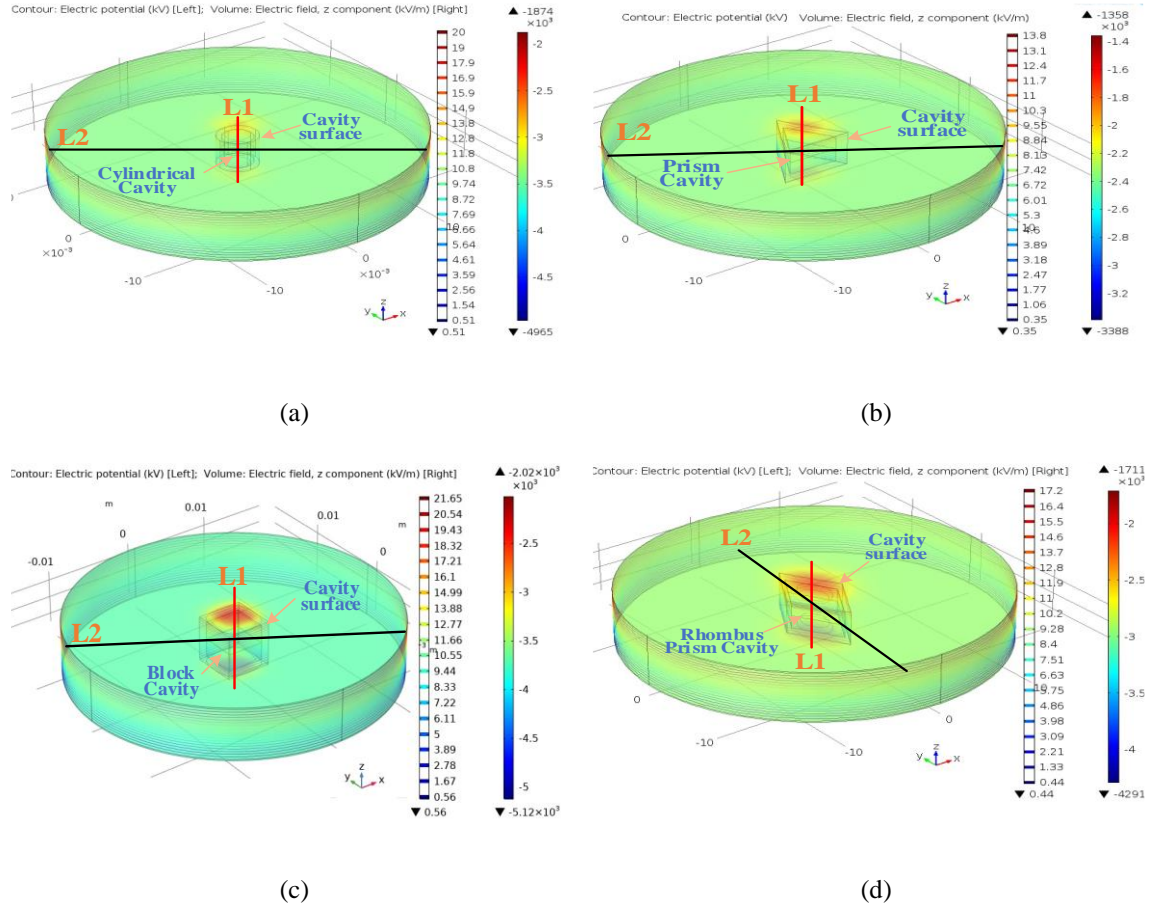


**Figure 8.11.** Electric field of all test specimens

The parameter  $N_{evol}$  correlates with the photo-ionization impacts and is unlikely to have a significant change within the measurement period. Therefore, it is assumed constant during the whole simulation. At the beginning, the total EGR depends on the volume ionisation ( $N_{evol}$ ) but as time progresses and PD starts to occur, the EGR value starts to rely on  $N_{esur}$  [44], [167]. The total electron generated from surface emission is assumed as the result of detrapped charges on the cavity surface due to the previous discharge events. The quantity of detrapped charges is subjected to the electric field in the void centre ( $E_{cav}$ ) for that instant at which the occurrence of the very last PD is accomplished ( $t_{PD}$ ). The generated electron rate due to the last PD event  $N_{PD}$ , is given by:

$$N_{PD} = N_{esur0} |E_{cav}(t_{PD}) / E_{inc}| \quad (8.10)$$

where  $N_{esur0}$  is the generated electrons per second at  $E_{inc}$ . Therefore, the total free electron generation rate due to the surface emission at any instant can be defined as:

$$\begin{aligned} N_{esur}(t) &= N_{PD} \exp(-\Delta t_{PD} / \tau_{decay}) \\ &= N_{esur0} |E_{cav}(t_{PD}) / E_{inc}| \exp(-\Delta t_{PD} / \tau_{decay}) \end{aligned} \quad (8.11)$$

where  $\Delta t_{PD}$  represents the time elapsed since the last discharge happened and  $\tau_{decay}$  is the

---

charge decay time constant. It should be noted that the incidence of PDs is a stochastic process, therefore, the likelihood of PD occurrence at any instant  $F(t)$  can be calculated from equation (8.12) where  $dt$  is the time interval duration

$$F(t) = N_{total}(t) dt \quad (8.12)$$

For an instant, if the local cavity field exceeds the inception value, then the probability function  $F(t)$  at that moment is calculated and checked with a random number  $R$ . The value of  $R$  is between 0 and 1. A PD may happen when the value  $F(t)$  is greater than  $R$ .

### 8.6.3 Local Cavity Condition During Discharge Process

To realise the dynamic behaviour of a discharge model, the cavity condition is modelled in such a way that it changes its state from non-conducting to conducting during a PD event whilst after a PD event it is the reverse. This dynamicity is implemented by increasing the void conductivity from a fairly low value ( $\sigma_{low}$ ) to a high value ( $\sigma_{high}$ ) during the discharge period and then returning to the initial value when the discharge ceases [44], [62], [63]. The change of cavity condition during and after a discharge process is realised as follows:

$$\sigma_{cav} = \begin{cases} \sigma_{low}; & \text{when there is no PD} \\ \sigma_{high}; & \text{when there is a PD} \end{cases} \quad (8.13)$$

In the modelling, the discharge stops when the cavity field drops below the extinction value  $E_{ext}$ . The assumption in equation (8.13) is quite reasonable because of the much shorter duration of the discharge period (typically in the nano-seconds range) as compared to the longer time period of the applied voltage excitation (either 50 Hz or 0.1 Hz) [44], [62], [63].

On the other hand, to model the surface/space charge decay along the cavity wall, a variable  $\sigma_{sur}(t)$  is introduced for the case when the field due to the surface charge  $E_q(t)$  acts in the same direction to the local cavity field. At any time step, it can be expressed as [44]:

$$\sigma_{sur}(t) = \sigma_{s0} \exp(\alpha | E_{cav}(t) |) \quad (8.14)$$

where  $\sigma_{s0}$  and  $\alpha$  are the initial surface conductivity and the stress coefficient respectively. From equation (8.14), the conductivity on the cavity surface  $\sigma_{sur}(t)$  increases to a very high value due to the increasing  $E_{cav}(t)$  and may cause problem with convergence or fitting in the numerical simulation. To avoid this, the surface conductivity  $\sigma_{sur}(t)$  is set to a high value  $\sigma_{sH}$  which represents the maximum cavity surface conductivity due to the charge conduction along the cavity wall. However, under the condition of  $E_q(t)$  opposing the cavity field, the surface conductivity  $\sigma_{sur}(t)$  is reset to the initial value  $\sigma_{sL}$ , assuming that there is no charge movement on the cavity wall [44], [63].

## 8.6.4 Partial Discharge Magnitude Calculation

Partial discharge magnitude can be calculated numerically from the surface integration of electrical charges on the cavity wall. This can be done in MATLAB by utilising the imported data from COMSOL. The apparent and real discharge magnitudes can be calculated as:

$$q_{PD} = \int_t^{t+dt} I(t) dt \quad (8.15)$$

The current  $I(t)$  flowing through the cavity and at the boundary electrodes results in the real discharge and apparent discharge magnitudes respectively.

## 8.7 Simulation Process of Cavity Discharge

### 8.7.1 Initial Simulation Parameters

Table 8.2 provides a description of the global parameters used in the numerical simulation. The time step  $dt$  is set to a value of  $1/500f$  to give a reasonable time increment for the simulation, where  $f$  is the applied voltage frequency. Also, the time interval during a PD event ( $\Delta t$ ) is set as 1ns to model the short discharge period. If it is too long, the cavity field  $E_{cav}(t)$  will decay too fast and reach the extinction field  $E_{ext}$  much earlier, which might influence the accuracy of PD magnitude. Conversely, the setting of comparatively lower  $\Delta t$  time will increase the simulation time excessively. For the air-filled void, the relative permittivity of the cavity is set as 1.

**Table 8.2.** Descriptions of global parameters used in the simulation

Parameters	Value	Unit
Number of simulation cycles, $n$	40	-
Applied voltage frequency, $f$	50 and 0.1	Hz
Duration of each time step, $dt$	$1/500f$	s
Time step during a PD, $\Delta t$	1.0	ns
Applied voltage, $U_{rms}$	1.0 -1.5 PDIV	kV
Material relative permittivity, $\epsilon_r$	2.3	-
Cavity relative permittivity, $\epsilon_{cav}$	1.0	-
Cavity surface lower conductivity, $\sigma_{sL}$	0	S/m
Cavity surface relative permittivity, $\epsilon_s$	2.3	-
Cavity surface high conductivity, $\sigma_{sH}$	$10^{-9}$ : PF; $10^{-11}$ : VLF	S/m
Cavity conductivity without PD, $\sigma_{low}$	0	S/m
Cavity conductivity during a PD, $\sigma_{high}$	$5 \times 10^{-3}$	S/m
Extinction field, $E_{ext}$	$2.5-3.0 \times 10^6$	V/m
Charge decay constant, $\tau_{decay}$	$2 \times 10^{-3}$ : PF ; 2.0: VLF	s
EGR from volume ionisation, $N_{evol}$	50: PF; 1.0 : VLF	$s^{-1}$
EGR from surface emission, $N_{esurf0}$	$1.5 \times 10^3$ : PF ; 10: VLF	$s^{-1}$

---

The values of  $N_{evol}$ ,  $N_{esur0}$  and  $\tau_{decay}$  depend on each other and are adjusted in such a way that the simulation results agree with the measurement data. For example, the value of  $\sigma_{sH}$  is adjusted to match with the repetition rate in the laboratory measurement. If this value is set too large, the charge decay along the cavity wall will be accelerated, resulting in a faster decrement of  $E_q(t)$  which reduces the subsequent number of PD pulses per cycle. On the other hand, if  $\sigma_{sH}$  is set too low, the free charges are unlikely to decay, resulting in an insufficient decrement of  $E_q(t)$  [44], [63], [167]. The extinction field  $E_{ext}$  is appraised from the minimum measured discharge.

For the lower frequency, the time interval between two consecutive discharges is much longer and the free charges get enough time to decay via charge recombination or drifting into the bulk insulation. Therefore, the values of  $N_{evol}$  and  $N_{esur0}$  are set to a lower value as compared to 50 Hz. Also, the value of  $\sigma_{sH}$  is relatively lower at very low frequency. This is reasonable as the slower rate of voltage change at VLF offers a less chance of free charges available on the cavity surface and the free charges might recombine with the free electrons and reduce the mobility rate on the cavity surface.

### 8.7.2 Simulation Flowchart of the Modelling

The working principle of cavity discharge modelling is provided in Figure 8.13. The COMSOL Multiphysics software builds up different models in order to calculate electric field magnitudes and electric currents throughout the simulation process. MATLAB simulations then compare the results obtained from COMSOL and apply this information to determine whether partial discharges occur or not. It should be noted that some important indicators such as apparent charge magnitudes and real charge magnitudes could not be obtained directly from COMSOL and thereby, calculated numerically in MATLAB simulation.

At the very beginning, all the initial parameters are assigned, and MATLAB sends commands to COMSOL Multiphysics to build up the required model with the predefined dimensions, materials and applied voltages. In each time step, the model is meshed and simulated in COMSOL to provide the output electric field magnitude at the cavity center. When this magnitude is larger than the pre-defined inception value, the probability of partial discharge occurrence is initiated and by calculating the initial electron generation rate, the likelihood of the partial discharge occurrence is subsequently determined. After the simulation, discharge magnitudes, occurrence phase and all other important parameters are saved for further processing and the processed simulation results are then compared with the experiment results.

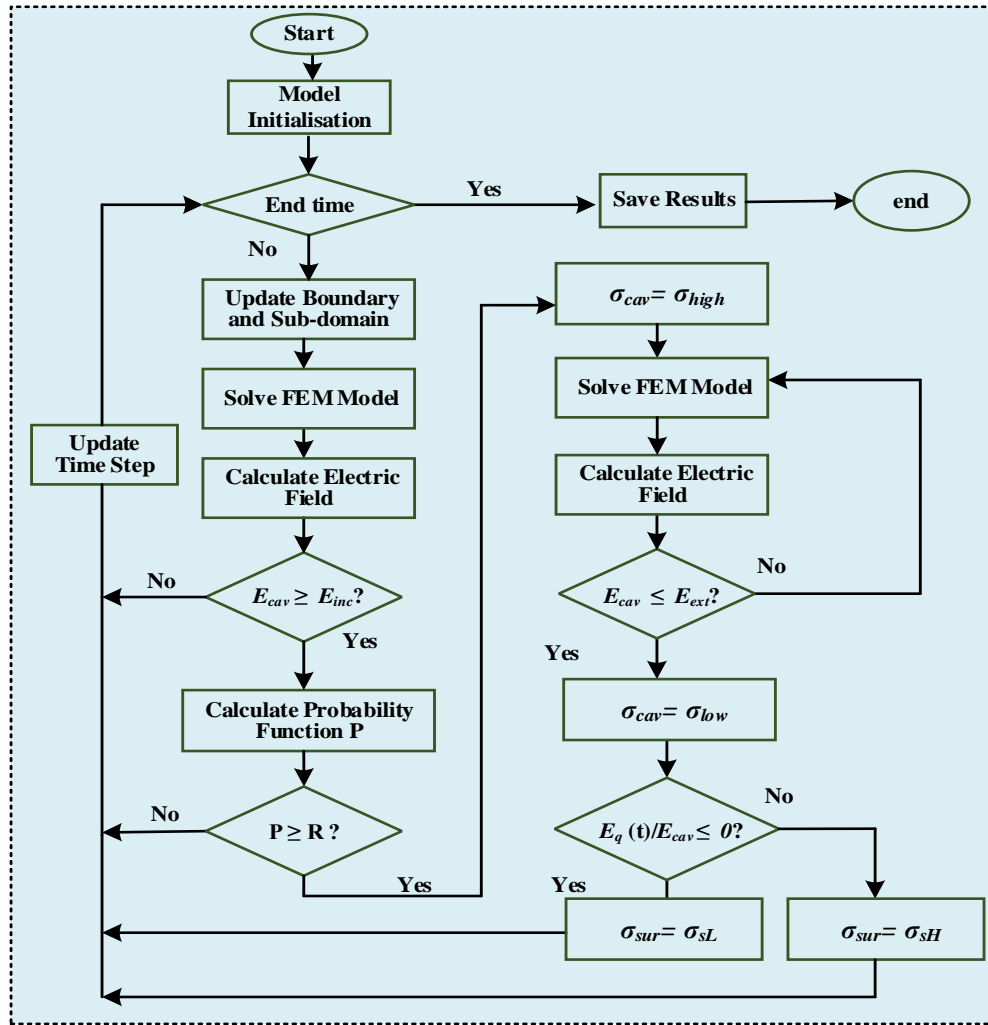


**Figure 8.12.** Flowchart of the cavity discharge simulation

## 8.8 Field before and after a PD Event

The electric field along the L2 is shown in Figure 8.13. Here, the field distributions are shown at 1.1 PDIV level before the first PD occurrence. As can be observed, along the L1 and L2, the field increases dramatically at the void centre. This is because the relative permittivity of the void is lower than the surrounding solid insulation which causes the increasing field stress in the cavity. Because of the geometrical shape and the respective inception voltage value, the prism geometry at 50 Hz shows the highest field stress at the cavity centre. On the other hand, the lowest field stress can be observed in the block geometry under VLF excitation. Since the PD occurs along the vertical z-axis, the non-uniformity of the electric field along the L1 before and after a PD event is shown in Figure 8.14 and Figure 8.15 respectively. As expected, the field distribution is not homogenous but symmetrical along the line L1.

Before the first PD occurrence, the regions of the cavity closest to the electrodes have shown the maximum stress than that observed at the void centre. Once the first PD occurs, the electric field distribution inside the cavity is greatly influenced by the electric charge movement



along the cavity surface. The charge density increases on the cavity surface during the PD event, resulting in a significant decrement of the cavity field as shown in Figure 8.15.

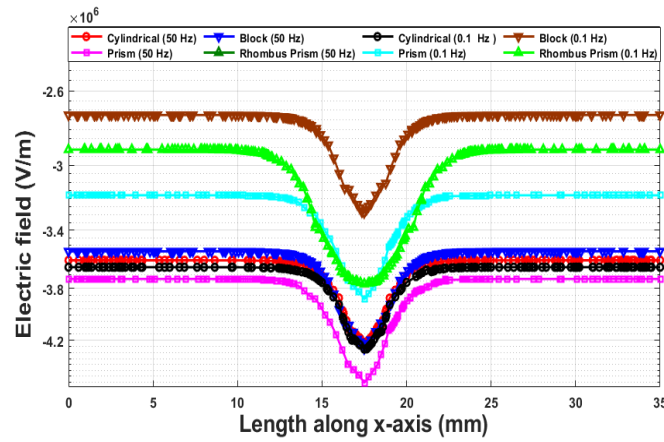


**Figure 8.13.** Field plot along the x-axis at 1.10 PDIV level

At the same time, the magnitude of the electric field on the void surface closer to the electrodes increases considerably due to the charge accumulation on the cavity wall. As a result, the field distribution inside the cavity still remains non-uniform and that influences the occurrence and magnitude of the subsequent discharges.

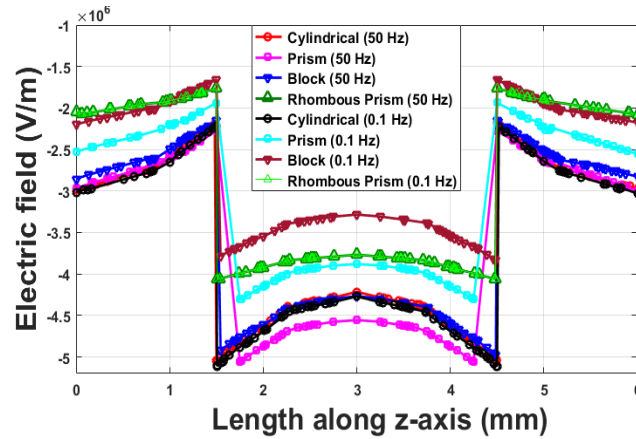


**Figure 8.14.** Field plot before a PD occurrence along the z-axis

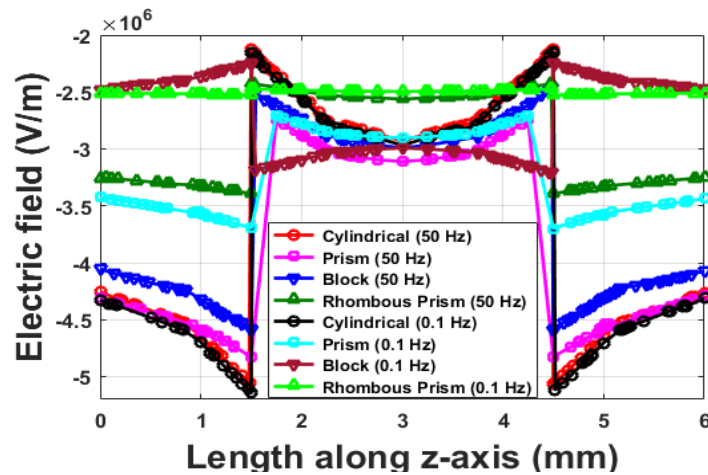


**Figure 8.15.** Field plot after a PD occurrence along the z-axis



---

## 8.9 Comparison between Measurement and Simulation

The phase-resolved images of PD pattern obtained by both measurement and simulation under PF and VLF excitations are shown in Figure 8.16 to Figure 8.23.

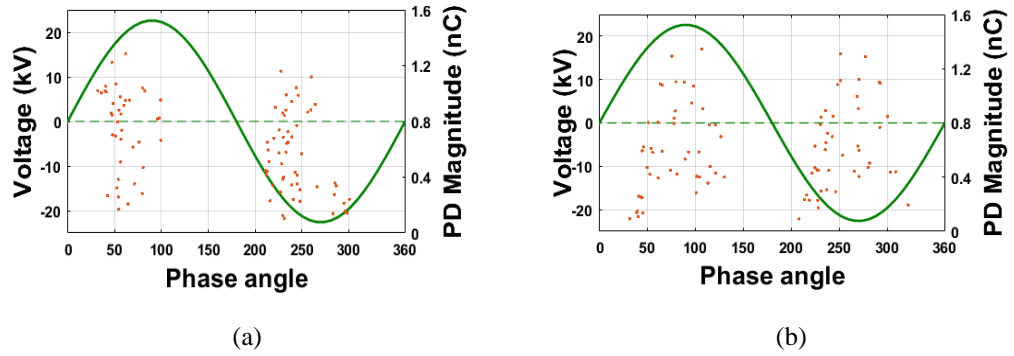


**Figure 8.16.** PRPD patterns of T-1 at 50 Hz (a) Measurement (b) Simulation

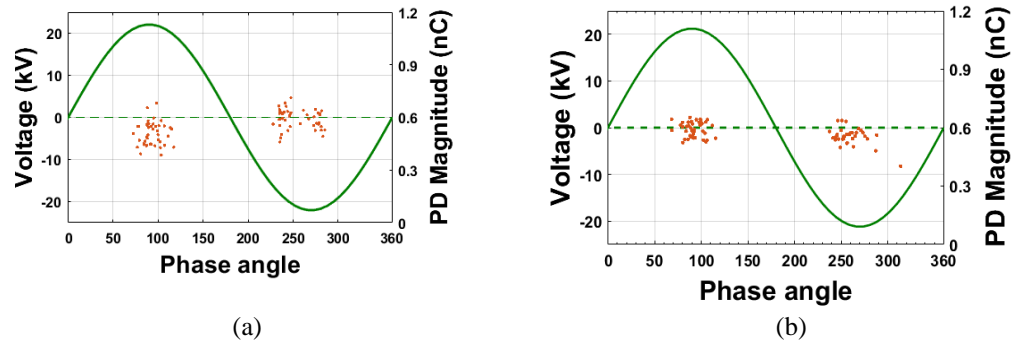


**Figure 8.17.** PRPD patterns of T-1 at 0.1 Hz (a) Measurement (b) Simulation

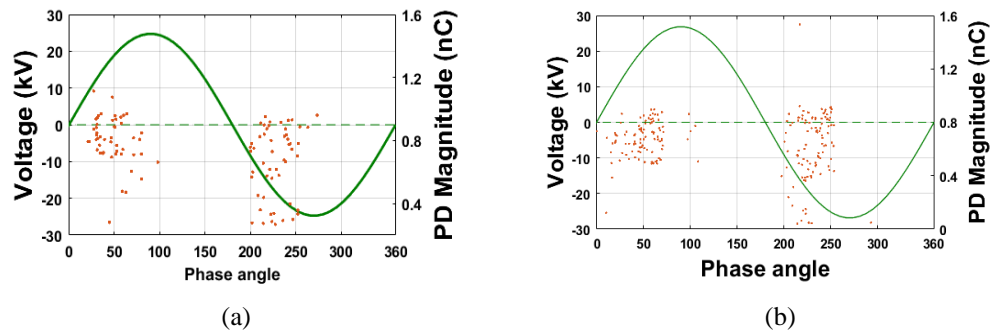


**Figure 8.18.** PRPD patterns of T-2 at 50 Hz (a) Measurement (b) Simulation

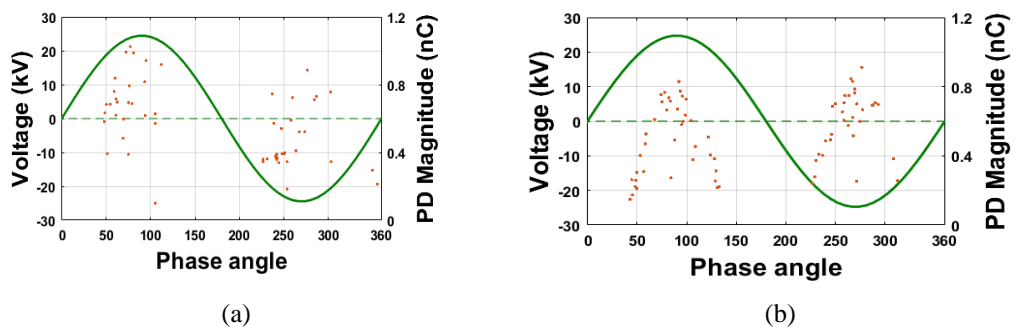
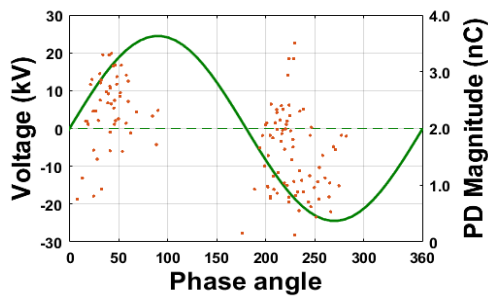
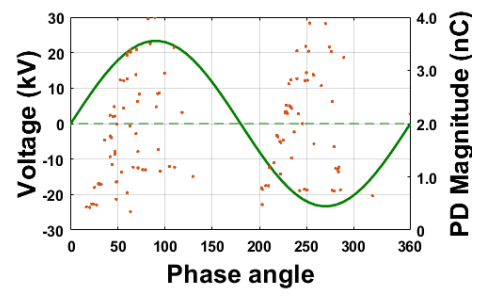


**Figure 8.19.** PRPD patterns of T-2 at 0.1 Hz (a) Measurement (b) Simulation

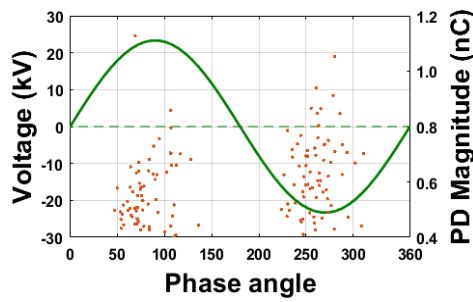


(a)

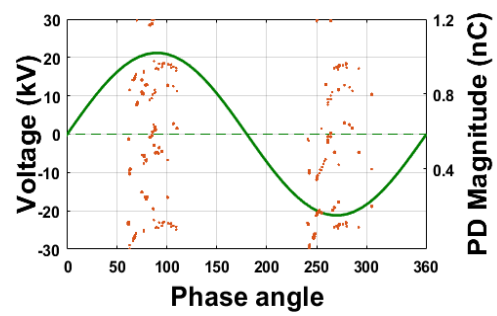


(b)

**Figure 8.20.** PRPD patterns of T-3 at 50 Hz (a) Measurement (b) Simulation

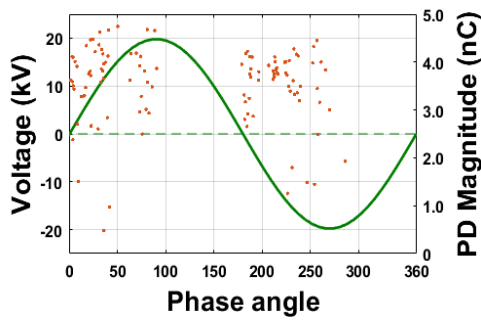


(a)

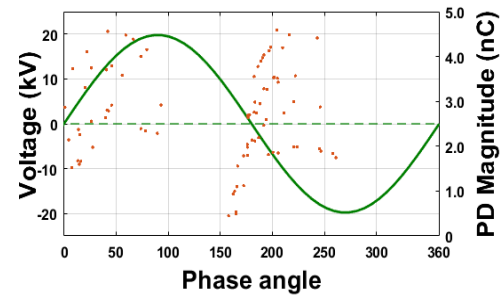


(b)

**Figure 8.21.** PRPD patterns of T-3 at 0.1 Hz (a) Measurement (b) Simulation

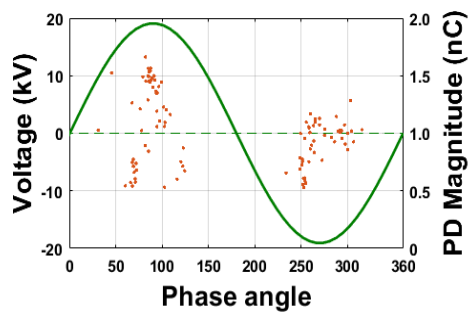


(a)

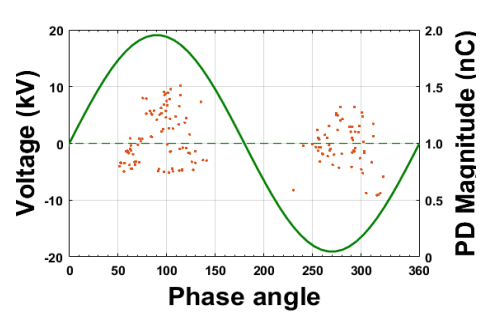


(b)

**Figure 8.22.** PRPD patterns of T-4 at 50 Hz (a) Measurement (b) Simulation



(a)



(b)

**Figure 8.23.** PRPD patterns of T-4 at 0.1 Hz (a) Measurement (b) Simulation

---

---

To avoid repetitions, here the images are only shown for the case of 1.10 PDIV. For power frequency, it can be observed that the discharge activities mostly occur in the rising quadrant ( $0-90^\circ$  and  $180^\circ-270^\circ$ ) of the voltage waveform. For ease of comparison, here discharge magnitudes in both positive and negative half-cycles are shown with the same polarity. Comparing with other test samples, T-3 and T-4 tend to concentrate more around the zero-crossing region of the power frequency voltage.

In the numerical modeling, each simulation set requires very long computation time. Therefore, the simulation is carried out for 40 consecutive AC voltage cycles, and these are sufficient to obtain a phase-resolved discharge pattern. As can be observed, the patterns from the numerical simulation, in the majority of cases, agree fairly well with the measured results in terms of the discharge magnitude and phase distribution. A possible cause for the difference may be associated with the fitting error in adjusting the simulation parameters.

Comparing with power frequency excitation, the PD phase distribution at VLF scatters less within the voltage cycle and is more likely to occur at the later phase rather than sooner near the zero-crossing. This may be due to the relatively higher surface charge decay and reduced availability of free electrons at very low frequency. The much longer VLF period allows fewer charges (either free electrons or space charges) to populate within the void and thus, contributes little to the local cavity field. Therefore, at the frequency of 0.1 Hz, the free electrons need some time to develop a complete avalanche process across the cavity again, resulting in the later phase of PD occurrence [62], [254].

## 8.10 Comparison among Discharge Characteristics

Figure 8.24, Figure 8.25 and Figure 8.26 provide a comparison between the measured and simulated PD data as a function of cavity geometry at different PDIV levels. It can be seen that the simulation results show reasonable agreement with the measurement results at all geometries and test frequencies. The differences could be due to either the choice of the simulation parameters or measurement errors (background noise, external interference). Further tuning of such parameters or modifying the electron generation rate from the surface emission or volume ionization are some possibilities for improving the modelling performance.

Referring to the experimental results, the maximum discharge magnitude and repetition rate per cycle (prpc) become larger as the applied voltage increases. This can be attributed to local field enhancement of the cavity due to the increased voltage, resulting in a lower statistical time lag and larger EGR which subsequently produce a higher repetition rate at increased PDIV levels [44], [167]. Also, the maximum discharge increases since the higher applied voltage leads to a significant voltage drop in the void when a discharge happens [33]. Meanwhile, the average

discharge magnitude increases when the voltage rises from 1.10 PDIV to 1.25 PDIV; however, the value sometimes decreases when the test voltage changes to 1.50 PDIV level.

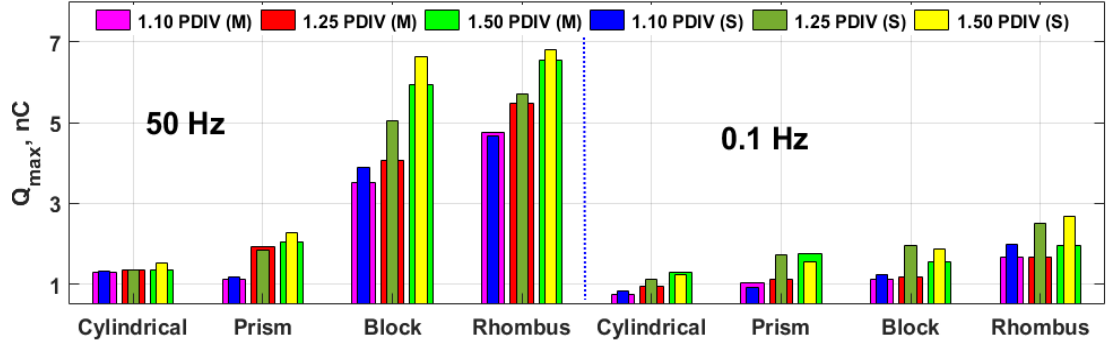


Figure 8.24. Measurement (M) and simulation (S) of maximum discharge ( $Q_{max}$ )

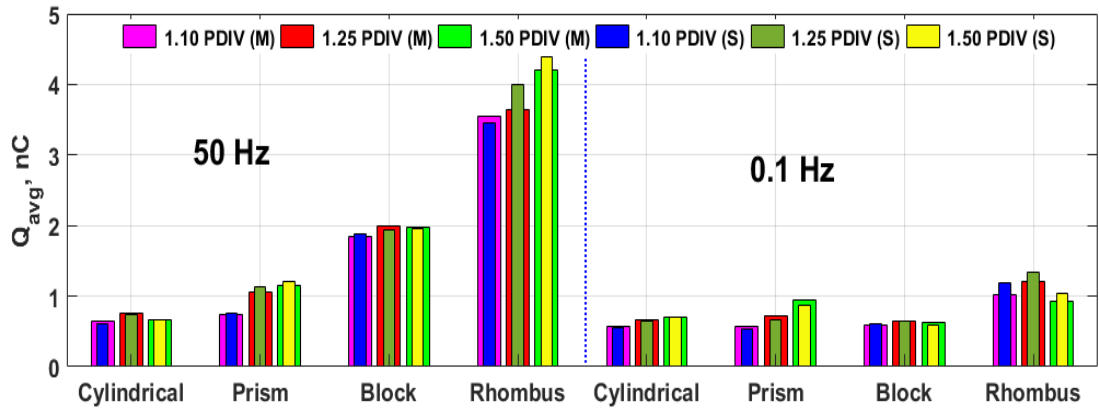


Figure 8.25. Measurement (M) and simulation (S) of average discharge ( $Q_{avg}$ )

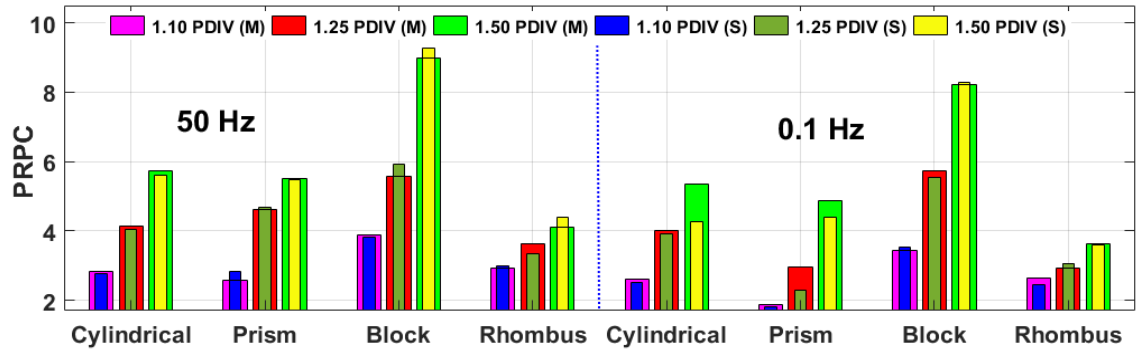


Figure 8.26. Measurement (M) and simulation (S) of pulse repetition per cycle (prpc)

In all cases, the discharge magnitude and repetition rate are comparatively higher at PF excitation. Basically, the shorter time period of 50 Hz applied voltage presents a situation where space charges get less time to decay and remain unchanged after the polarity reversal of the voltage waveform. Consequently, these enhance the local cavity field and so is the discharge magnitude [33], [46]. Also, the shorter time period increases the chances of getting free electrons available on the cavity surface or in local shallow traps between two consecutive

---

---

discharges. The increased availability of free electrons promotes PD inception almost immediately after the test voltage exceeds the inception voltage level, resulting in a higher repetition rate at power frequency [44]. On the other hand, the higher statistical time lag at lower frequency reduces the electron generation rate, and thereby, causes a reduction in the number of PDs per cycle of the VLF applied voltage [33], [254].

Under the excitation of the same test frequency and PDIV level, the block-void sample T-3 shows a higher repetition rate per cycle. The likelihood of free electrons available from volume ionisation is larger in the bigger cavity as more photoionisation or radiation is expected to occur within a larger void [46], [140]. Another possible explanation is that the local cavity field is more likely to be distorted around its corners or edges and thus, yields multiple points inside the void at which the electric stress is intensified. These points act as a discharge source and, with the aid of intensified stress, enable multiple discharges to be incepted within a voltage cycle [46], [254]. On the other hand, sample T-4 has the highest cavity surface area as compared to other test samples. This favors the discharge process by restricting the decay mechanism of space charges through recombining with free electrons [62], [140]. The increased availability of space charges is probably the reason why sample T-4 shows the largest PD magnitude among all the test specimens at the same test voltage and frequency.

It should also be noted that some of the simulation parameters to describe the physical process may not truly reflect the real discharge mechanisms occurring in the cavity. Nevertheless, the implemented model is adequate to produce the phase-resolved patterns and corresponding discharge characteristics close to the measured values. Thus, it probably confirms most parameters have been chosen and adjusted appropriately, i.e. their values are accurate and correlate well with what happens in the cavity during a PD event.

## 8.11 Correlate with Real Application

One of the objectives here is to show the trending of PD characteristics and integrated parameters under the application of VLF applied voltage and reveal the changes that differ from normal power frequency. Due to fabricating problems, the size exceeds that of a cavity observed in power cables. Therefore, attempts were taken to perform further simulations with more realistic cavity size. The calculated field distribution is shown in Figure 8.27. Here,  $r$  denotes the radius of cylindrical cavity.

As can be observed from Figure 8.27a, the electric field is trending to be uniform along the  $x$ -axis for the reduced diameter. On the other hand, along the  $z$ -axis in Figure 8.27b, a higher electric field is observed at the point where the cavity depth starts. At these points, the electric field is intensified, and the local cavity field is distorted.

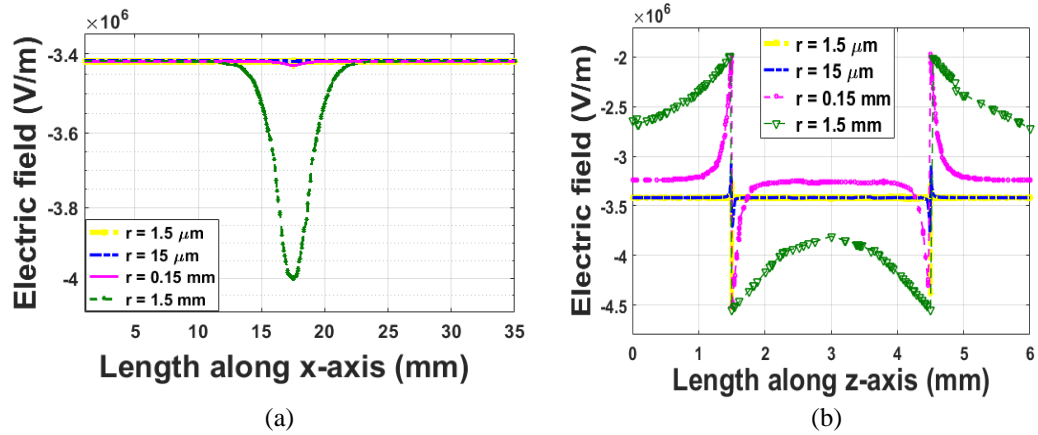


**Figure 8.27.**Electric field distribution at 15 kV; (a) along L2 (b) along L1.

## 8.12 Chapter Conclusion

A comparative study of PD measurements on test samples containing an artificial void of different geometry (cylindrical, prism, block etc.) embedded in XLPE under different applied voltage amplitude at very low (0.1 Hz) and power (50 Hz) frequency excitation is presented. Measurement results reveal that the discharge characteristics such as the magnitude (maximum and average) and repetition rate are sensitive to the void structure. These values are influenced by the cavity surface area, charge concentrating points and intensified electric stress. The PD magnitudes and repetition rate are comparatively lower at VLF. This may be attributed to the fact that the availability of space charges, electron generation rate and free charge decay rate after a PD event are more significant at very low frequency and consequently, influence the physical discharge process in the different void geometries.

A three-dimensional physical model describing the PD behaviours as a function of cavity geometry and test frequency has been also developed. Using finite element analysis (FEA), the implemented model dynamically simulates the discharge occurrences in the cavity and closely reproduces the measurement results from experiments. The phase-resolved discharge patterns obtained from experiments and numerical simulations are in agreement. The non-uniform charge distribution on the cavity wall at VLF excitation affects the electric field within the void and governs the differences in the discharge characteristics as compared to the power frequency.

---

---

## Chapter 9.

# Surface Discharge Measurement and Modelling

Chapter 8 investigated PD characteristics in an artificial void bounded in solid insulation, while in this Chapter, a comparative study of surface discharges and their characteristics under power frequency (50 Hz) and very low frequency (0.1 Hz) excitation is presented. As the surface discharge process is mainly resulted from the enhanced electric stress; it is necessary to know how the field distributes on the solid dielectric surface when it is exposed to a high voltage AC excitation. To this end, the surface electric field before, during and after a PD event at VLF and PF test voltage is reported. Finite element analysis (FEA) based numerical simulation is also included to model the surface discharge. The contributions from this chapter have been published in [7] and [12] as shown in the List of Publications.

## 9.1 Background Study of Surface Discharge

### 9.1.1 Motivation of the Work

Partial discharges due to surface degradation are unavoidable, especially in HV cable terminations and joints. For diagnostic purpose, surface discharge (SD) measurement at power frequency voltage had been extensively investigated. However, there is still a lack of knowledge of SD behaviours and the associated electric field distribution before, after and during a PD event [33], [257], [258], especially for the VLF test voltage. Therefore, it is desirable to know how the insulation surface degradation is dependent on the applied frequency. Insulation diagnosis through SD measurement at VLF excitations is still a challenging and complicated matter [9], [27], [28]. Thus, the motivation to conduct experimental and simulation studies of SD in XLPE and acquire diagnostic information.

---

### 9.1.2 Surface Discharge Physical Process

One of the major causes for insulation degradation is surface discharge (SD). To understand the physical phenomena, an IEC-B electrode configuration for SD measurement is shown in Figure 9.1. The setup consists of an HV electrode with a curved edge to trigger SD. The flat electrode placed below is grounded and a solid insulating material is placed between the two electrodes.

A surface discharge occurs when the localised electric field along the insulation surface exceeds the certain stress level, known as inception field, and the corresponding voltage is the inception voltage (SDIV). Depending on availability of free electrons, the SD process usually originated from a triple point junction, which is the interface between the HV electrode edge and the solid/gaseous dielectrics. After a discharge, an amount of space charges is generated; they then decay in the insulation surface via various physical processes (e.g. charge drift recombination, conduction etc.) and depending on the applied voltage frequency, significantly influence the local surface field.

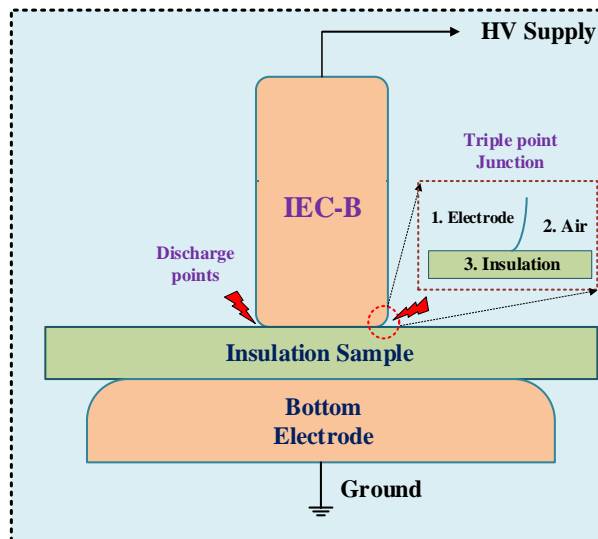


**Figure 9.1.** Surface discharge occurring in an IEC-B electrode arrangement

## 9.2 Surface Discharge (SD) Measurement

The schematic diagram of the SD measurement circuit is almost the same as the cavity discharge measurement circuit as shown in Figure 9.2. The only difference is the AC supply which is provided by an Agilent 33500B waveform generator and a TREK 20/20C high voltage amplifier (Figure 4.3a). More details of the measurement circuit are included in Chapter 8.



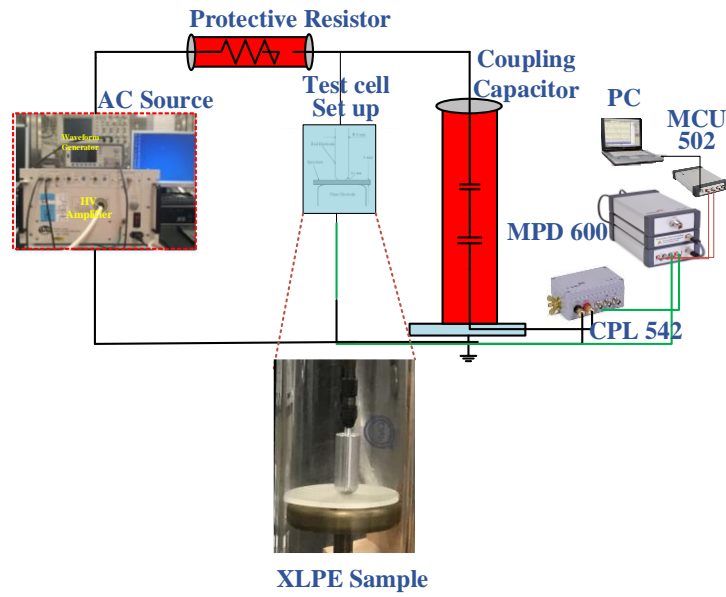


**Figure 9.2.** Block diagram of the surface discharge measurement circuit

The test specimen is a circular disk of XLPE insulation, with diameter of 35 mm and thickness of 4 mm. Its measured capacitance is 11.42 pF. The test sample is placed between a semi-sphere / plane electrode arrangement. The semi-sphere electrode is connected to the HV terminal, while the plane electrode having a diameter of 78 mm is earthed. The sphere electrode is made of steel having 7 mm cross-sectional diameter, and the lower curvature that touched the test object is of 5 mm diameter.

### 9.2.1 Phase Resolved Partial Discharge (PRPD) Study

The localised field enhancement at the triple point junction initiates surface discharges. Theoretically, the larger discharge magnitude is an indication of more degraded dielectric surface condition. The SD patterns at VLF and 50 Hz are shown in Figure 9.3 and Figure 9.4 respectively for 6 kV applied voltage. The surface discharge inception voltage (SDIV) is measured at around 4.8 kV for 50 Hz and 5.5 kV for 0.1 Hz.

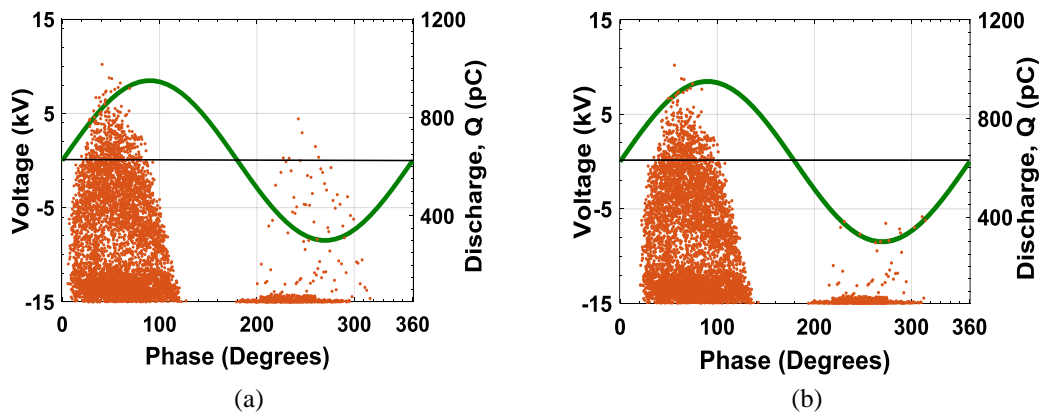


**Figure 9.3.** VLF PRPD pattern at (a)  $t = 1$  hr. (Left) (b)  $t = 6$  hrs. (Right)

Measurements are made periodically at the last 10 minutes of every hour, and the test is for a total ageing time of 6 hours. The pattern obtained at each frequency shows similar trends of PD distribution.

After exceeding SDIV level, the increasing surface electric field strength generates more charge species (ions and free electrons) and contributes to more ionisation processes [10]. Moreover, PD occurrence is found to be less in the positive half-cycle as compared to the negative half-cycle at both VLF and 50 Hz supply. This can be attributed to the different mobility of the positive ions and electrons [63], [207].

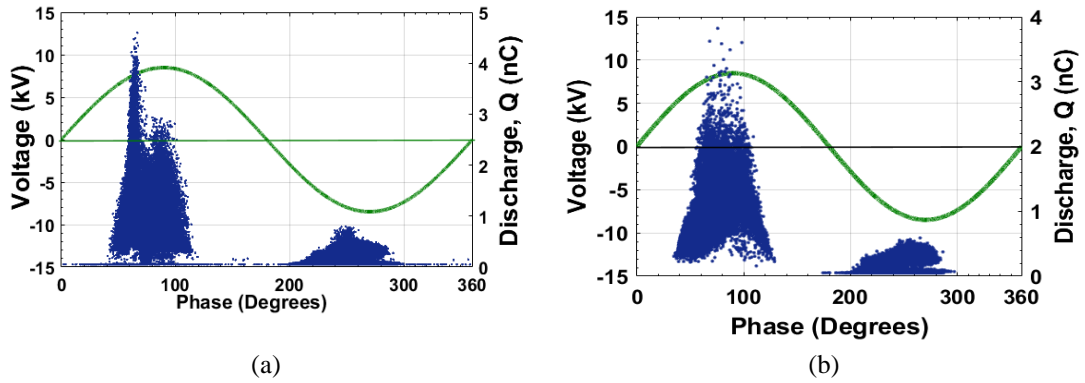


**Figure 9.4.** PF PRPD pattern at (a)  $t = 1$  hr. (Left) (b)  $t = 6$  hrs. (Right)

Measurement is also carried out at 8 kV voltage of PF and VLF excitation. The acquired PD patterns are shown in Figure 9.5 and appear similar as at 6 kV. The patterns are shown for 600 consecutive AC cycles of PF excitation and 60 cycles of VLF respectively.

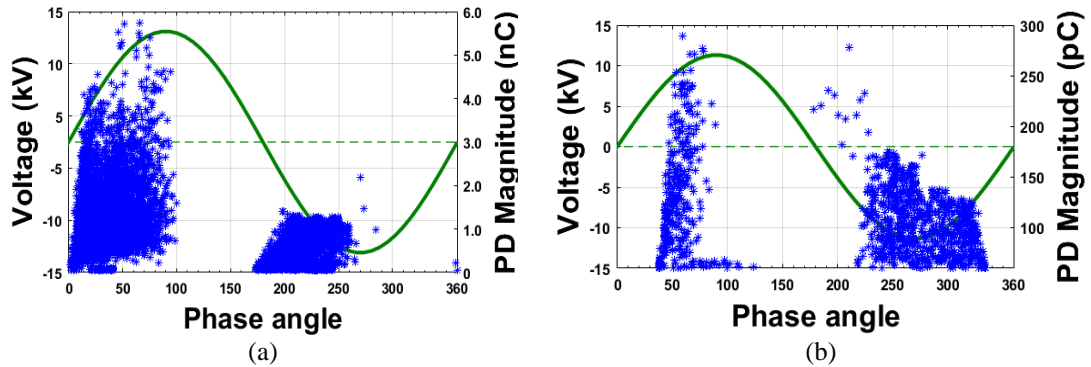


**Figure 9.5.** PRPD pattern at 8 kV voltage (a) 50 Hz (Left) (b) 0.1 Hz (Right)

### 9.2.2 Average Discharge Magnitude

The average discharge magnitude during both positive ( $Q_{avg}^+$ ) and negative half-cycles ( $Q_{avg}^-$ ) at VLF and 50 Hz are plotted in Figure 9.6. As can be observed, the average discharge for 50 Hz excitation during the positive half-cycle is around 1000 pC which is approximately 5 times that of the negative half-cycle. Similarly, for VLF during the positive half-cycle, the average discharge is 400 pC, and in the negative half-cycle, it is around 80 pC. Comparing with

VLF for either positive or negative half-cycle, the average discharge magnitude is found to be higher in the case of 50 Hz.

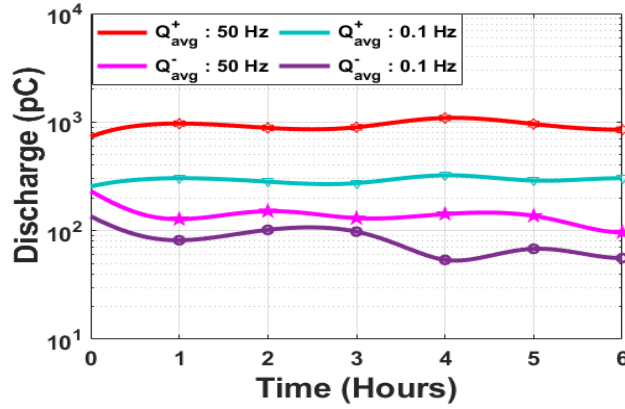


Figure 9.6. Average discharge magnitude at VLF and 50 Hz

### 9.2.3 Pulse Repetition Rate per Second (PRPS)

The pulse repetition rate per second (PRPS) is calculated in every hour over the total test duration and plotted in Figure 9.7.

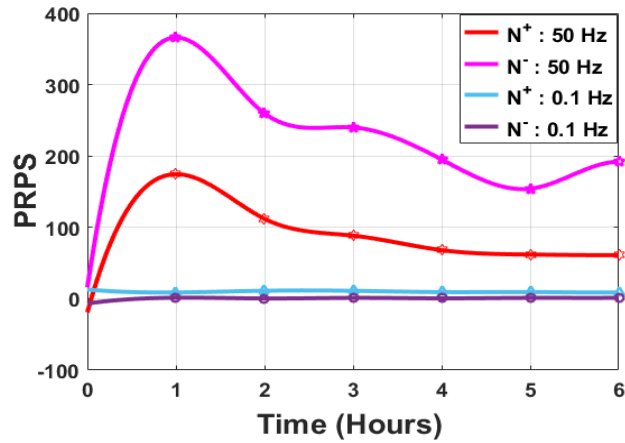


Figure 9.7. Pulse repetition rate per second at VLF and 50 Hz

The PRPS value at 50 Hz is found to be higher than that at VLF excitation in both positive and negative half-cycles. This may be due to the significant charge recombination process in the case of VLF. Again, it has been observed that at 50 Hz, the PRPS in the negative half-cycle is more than that of the positive half-cycle during the whole test period. This may be attributed to that in the negative half-cycle, free electrons are more likely to generate and cause repetitive ionisation. Also, the PRPS is found to be higher during the first hour of the test.

## 9.3 Surface Discharge (SD) Simulation Process

Based on the sample geometry, a model using finite element analysis (FEA) method is developed in COMSOL Multiphysics and integrated with MATLAB to determine the electric

field distribution along the insulation surface before, after or during a discharge occurrence. The simulated model also can effectively reproduce the discharge sequences and agrees with the experimental results.

### 9.3.1 Two-Dimensional (2D) Model Geometry

A physical model as a representation of the test arrangement was developed in an axial symmetric two-dimensional geometry as depicted in Figure 9.8. The whole structure was simulated in the air medium at 6 kV applied voltage. The triple point junction and the critical zone are also provided to simulate the surface discharge. An erosion surface layer of 0.5 mm thickness is introduced in the test sample to represent the surface emission where the detrapping/ trapping of free charges (space ions and free electrons) occurs and also, the space charges decay through conduction and drift-recombination. The electric field distribution is calculated using the same partial differential equations as in (8.6) and (8.7).

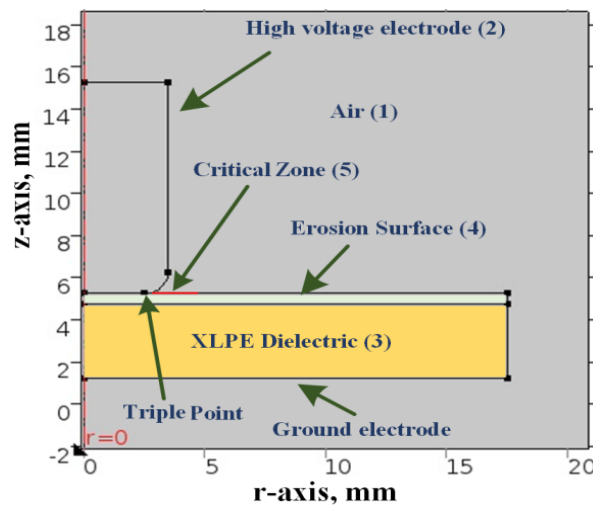


**Figure 9.8.** The axis-symmetric two-dimensional view of the model

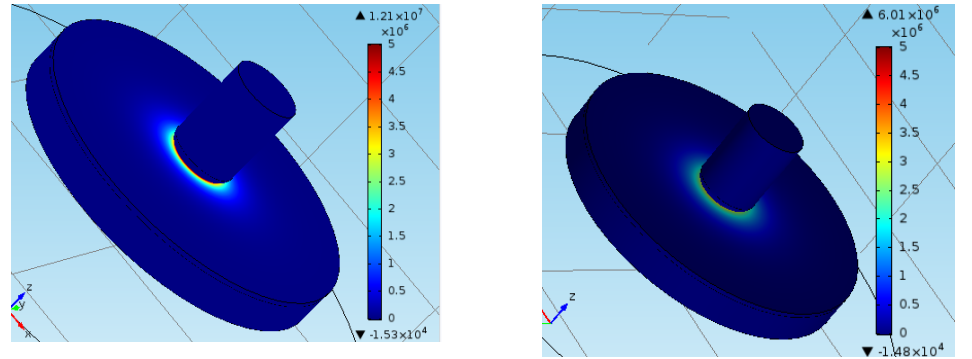
### 9.3.2 Electric Field Distribution along the Surface

Figure 9.9 and Figure 9.10 illustrate the electrical field distribution on the sample surface before and after a discharge event at 50 Hz and 0.1 Hz excitation respectively. For electric field calculation, the same PDEs of equation (8.6) and (8.7) were solved.

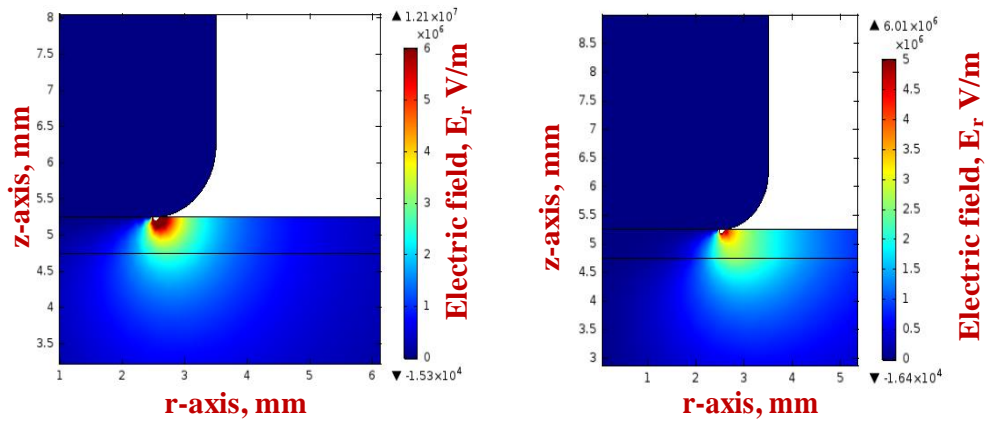
Table 9.1 lists the global parameters that are used in the numerical simulation to model the physical behaviours. Note that the relative permittivity and conductivity of air and HV electrode (steel) are taken from COMSOL materials library.

At higher frequencies, the space charges get relatively lesser time to decay and can be found available during the moment when the voltage waveform changes its polarity. These free charges produce an electric field in the same direction to the external field and thus increase the

local surface field. With the power frequency excitation, the chance of getting initial free electrons also increases since the time interval between two consecutive discharges at higher frequencies is very small and provides the enhanced availability of free electrons to incept a discharge.



a. 3D view before (left) and after (right) a PD event

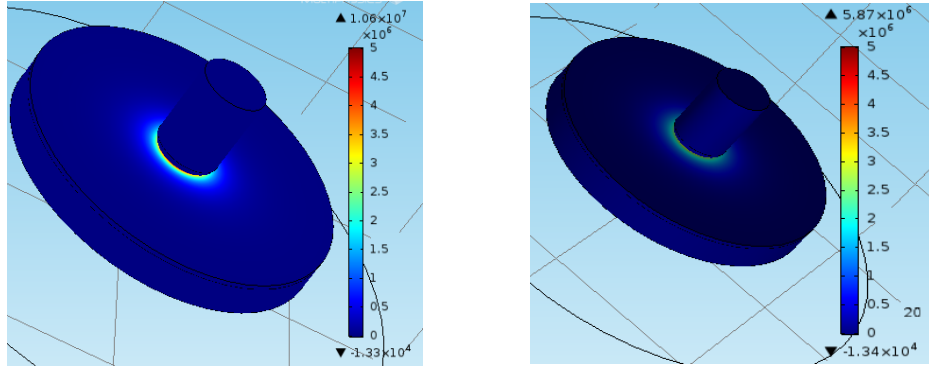


b. 2D view before (left) and after (right) a PD event

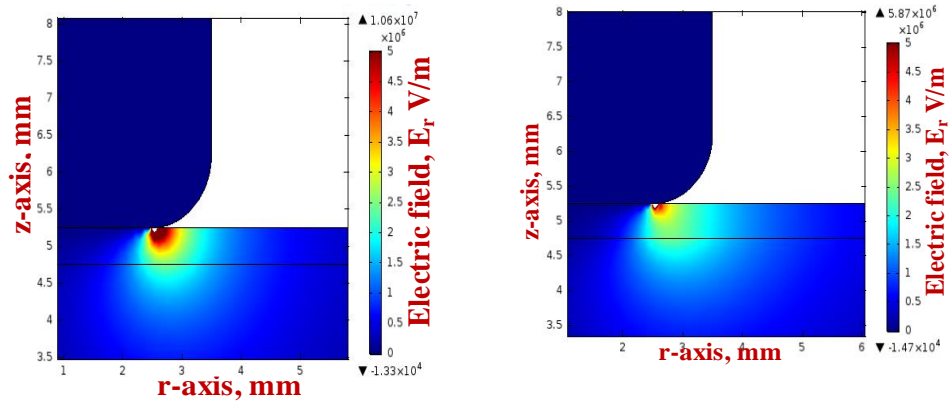
**Figure 9.9.** Simulation of electric field distribution at 50 Hz on the XLPE surface

**Table 9.1.** Descriptions of global parameters used in the simulation

Description	Relative Permittivity, $\epsilon_r$	Conductivity, $\sigma$
Air (Domain 1)	1	0
HV electrode: Steel (Domain 2)	1	$4.03 \times 10^6$ S/m
XLPE dielectric (Domain 3)	2.4	0
Erosion surface (Domain 4)	2.4	varies
Critical zone (Domain 5)	2.4	$5 \times 10^{-3}$ S/m
EGR from surface emission	50/s at 50 Hz (PHC) and 100/s at 50 Hz (NHC); 0.05/s at 0.1 Hz (PHC) and 0.1/s at 0.1 Hz (NHC)	
Inception field $E_{inc}$	1.25 kV/mm at 50 Hz; 5.6 kV/mm at VLF	



a. 3D view before (left) and after (right) a PD event



b. 2D view before (left) and after (right) a PD event

**Figure 9.10.** Simulation of electric field distribution at 0.1 Hz on the XLPE surface

Therefore, the total electron generation rate (EGR) due to surface emission should have a higher value at 50 Hz. On the other hand, at very low frequency (0.1 Hz) an opposite scenario is likely to be observed and because of the longer time period, the free charges are assumed to cease entirely after a discharge event.

As also can be observed in Figure 9.9 and Figure 9.10, the critical zone has the highest electric field and comparing with VLF, the first PD is incepted at a higher magnitude under 50 Hz applied voltage. Basically, the critical zone is the region where the surface discharge mostly occurs. In either case, the electric field drops after a discharge event.

To show how the electric field distributes along the r-axis, Figure 9.11 plots the radial ( $E_r$ ) and vertical component ( $E_z$ ) of the field magnitude on the insulation surface. Here, the radial field  $E_r$  before and after a PD event is shown in Figure 9.11a while the vertical field  $E_z$  is shown in Figure 9.11b. As can be seen, the field distribution is not uniform and decreases more or less exponentially with the increasing distance. Before the first PD occurrence, the highest radial stress  $E_r$ , can be observed in the critical zone, in particular, a short distance after the triple point (i.e. 2.5 mm). Once PDs occur, the free charge movement across the erosion surface

increases, resulting in a significant decrement of the local surface field as shown in Figure 9.11. Accumulation of these free charges on the insulation surface influences the occurrence and magnitude of subsequent PDs.

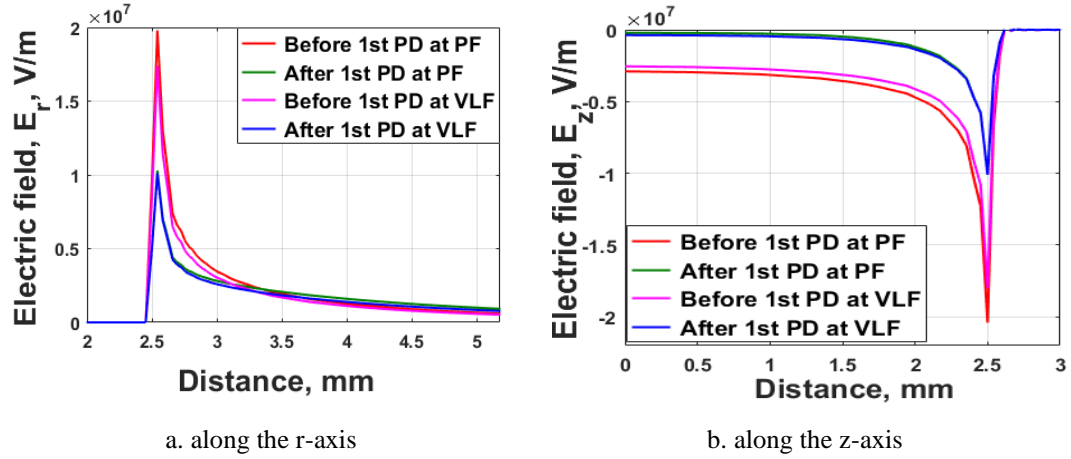


**Figure 9.11.** Field distribution along the insulation surface

### 9.3.3 Simulated Discharge Sequence

The rate of voltage change ( $dv/dt$ ) is proportional to the applied voltage frequency. Hence, the power frequency excitation has a higher  $dv/dt$  which allows space charges less time to be decayed through the insulation surface. As a result, the surface conductivity of space charge or the space charge decay between two consecutive PD events at power frequency is much smaller as compared to VLF. The electric field distributions during a PD event for 7 consecutive AC cycles under PF and VLF excitation are shown in Figure 9.12 and Figure 9.13 respectively. Due to the successive discharges, the charge accumulation on the insulation surface increases.

As discussed earlier, the surface electric field ( $E_{sur}$ ) is the result of the external field that comes from the external supply ( $f_m E_0$ ) and the field due to space charge effects ( $E_q$ ). Initially, the space charge field  $E_q$  is equal to the external field due to the absence of surface charge deposited from PD events. When the first PD occurs,  $E_{sur}$  drops steadily, which causes an increase of  $E_q$  in the opposite direction of the surface field. This can be seen at the first half-cycle of any voltage excitation (position A). When the polarity of  $E_{sur}$  is the same with  $E_q$ , then after a discharge event space charges start to cease through conduction, resulting in the increase of surface conductivity and thus, reducing the space charge field (position B). However, when  $E_{sur}$  is the opposite polarity of  $E_q$ , the charge accumulation along the surface increases and generates larger space charge field magnitude (position C).

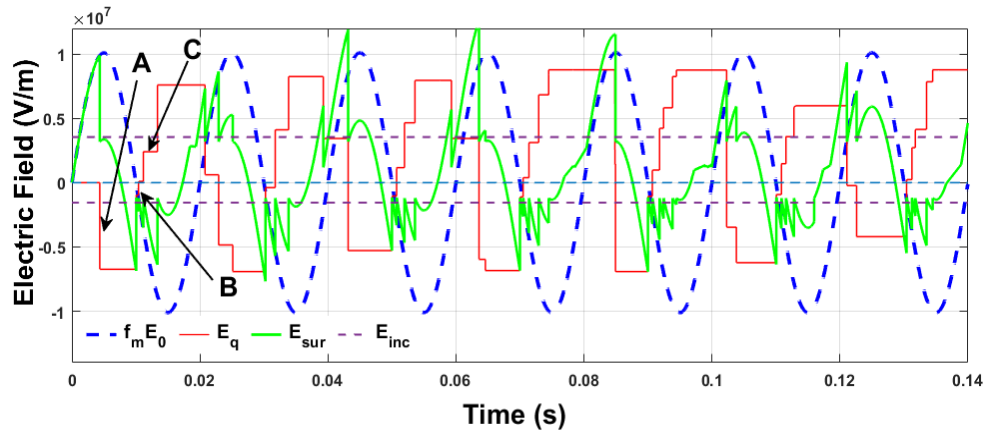


**Figure 9.12.** Simulation of surface electric field at 50 Hz

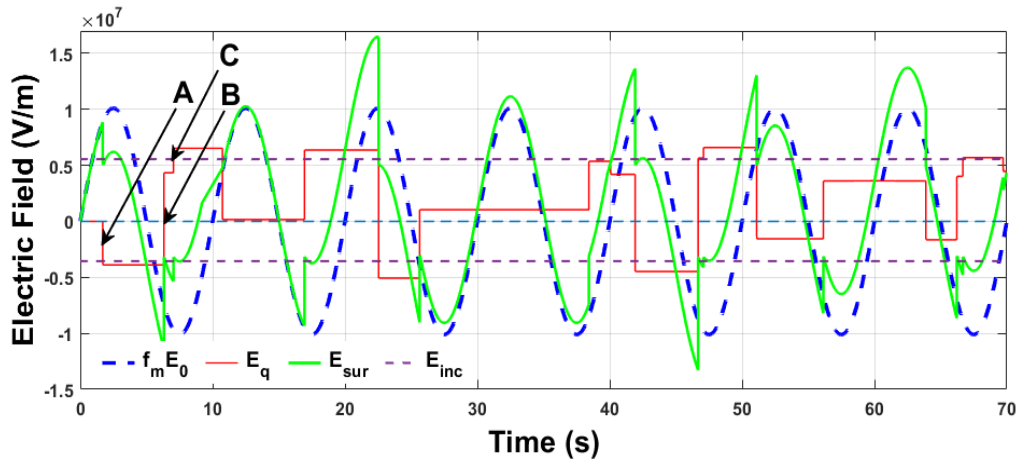


**Figure 9.13.** Simulation of surface electric field at 0.1 Hz

In the case of 50 Hz, due to the higher  $dv/dt$ , the time interval between two consecutive PD events is very short. This short duration allows a higher availability of free charges (free electrons and space ions) to be present on the surface. The next PD event is likely to occur almost immediately after the moment when  $E_{sur}$  exceeds  $E_{in}$ . On the other hand, due to the lower  $dv/dt$  at VLF, the surface charge decay is more significant. Therefore, after a PD event, the space charge and free electrons get enough time to vanish, which in turn results in less PD occurrence. In other words, the space charge field is less dominant at very low frequency as the slower rate of voltage change at VLF enables majority of free charges to dissipate along the insulation surface. The simulation results of 50 Hz and VLF test voltage are shown in Figure 9.14.

The illustrated discharge patterns are for 60 consecutive AC cycles, and the duration is sufficient to obtain enough data points for trending. As expected, the local field enhancement due to free charges causes relatively larger PD magnitudes and a higher number of surface discharges at the power frequency.



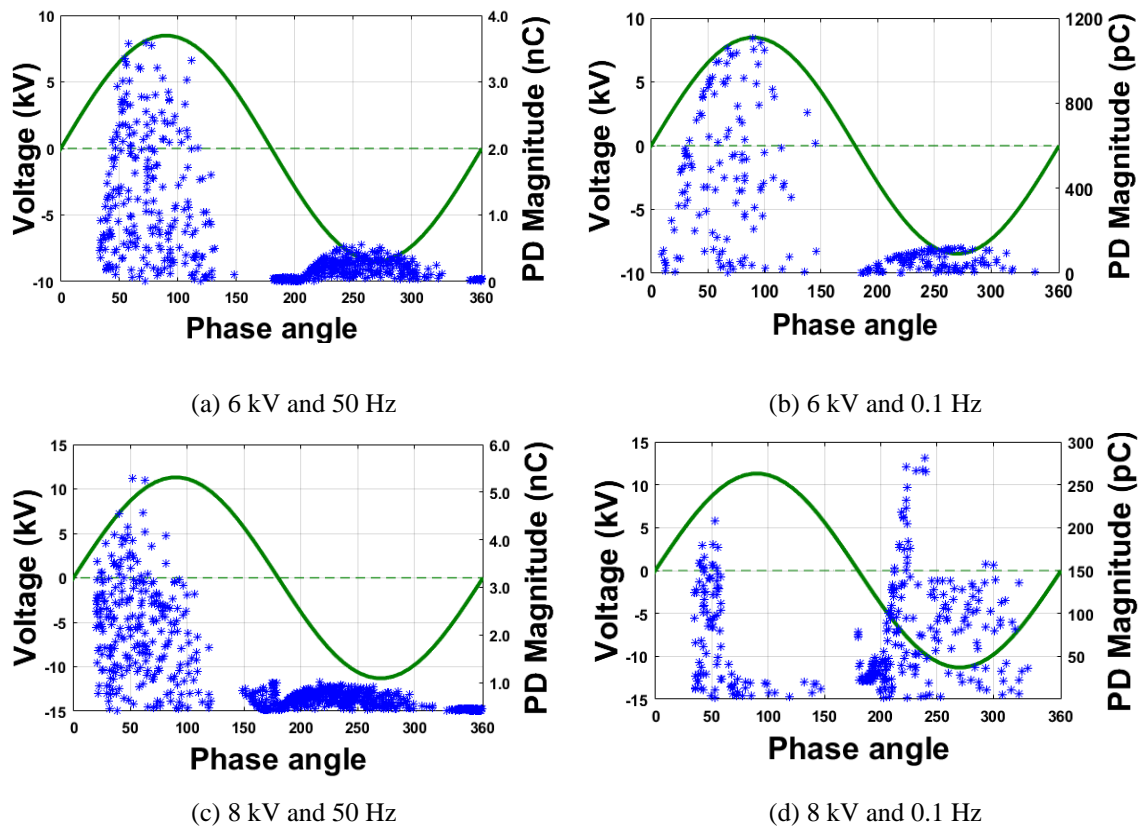


**Figure 9.14.** Simulation results of surface discharge at 50 Hz and 0.1 Hz

### 9.3.4 Comparison between Measurement and Simulation

Table 9.2 and Table 9.3 compare the measured and simulated PD data as a function of applied voltage at different excitation frequencies. It can be seen that the simulation results show reasonable agreement with the measurement results; the mismatch may be due to the choice of values for the adjustable parameters in the simulation model.

**Table 9.2.** Measurement results of all tested samples

Characterised Parameters	Voltage Levels	50 Hz		0.1 Hz	
		PHC	NHC	PHC	NHC
Maximum Discharge, $q_{max}$ (pC)	6.0 kV	4597	791.5	1015	99.40
	8.0 kV	5738	1250	289.3	402.5
Average Discharge, $q_{avg}$ (pC)	6.0 kV	968.7	127.6	304.2	55.92
	8.0 kV	1268	690.4	132.9	150.2
Pulse repetition rate per cycle (prpc)	6.0 kV	3.491	7.322	2.838	1.318
	8.0 kV	7.018	10.73	5.525	6.617

**Table 9.3.** Simulation results of all tested samples

Characterised Parameters	Voltage Levels	50 Hz		0.1 Hz	
		PHC	NHC	PHC	NHC
Maximal Discharge, $q_{max}$ (pC)	6.0 kV	3594	550.5	1104	118.2
	8.0 kV	5271	1008	440.6	563.2
Average Discharge, $q_{avg}$ (pC)	6.0 kV	992.3	146.4	352.9	50.04
	8.0 kV	1295	618	138.5	146.6
Pulse repetition rate per cycle (prpc)	6.0 kV	4.416	8.133	1.447	1.377
	8.0 kV	6.466	8.833	4.115	7.716

It should be noted that one AC cycle of VLF (0.1 Hz) signal takes 500 times longer time than a single cycle of 50 Hz, which means one 0.1 Hz cycle is equivalent to 500 cycles of 50 Hz signal. So, it is of interest to check whether the trend of higher PRPC at PF as compared to VLF will follow the similar trend of higher PRPS under 50 Hz signal. Interestingly, it is found that the listed PRPC values in Table 9.2 and Table 9.3 support the trends of PRPS results illustrated in Figure 9.7 and it is concluded that the repetition rate at PF in either case (whether it is PRPS or PRPC) is relatively higher than that at VLF.

## 9.4 Chapter Conclusion

In this chapter, the measurement and modelling of surface discharges for XLPE insulation are presented. The PD activities obtained from the phase-resolved image along with parameters such as the inception voltage (PDIV), average discharge and repetition rate (PRPS) ease the way of diagnostic interpretations.

A physical model describing the electric field distribution on the surface of XLPE material due to partial discharge is also presented. Using finite element analysis (FEA) the discharge behaviours before, during and after a PD occurrence at very low and power frequency are simulated. The simulated model shows that the increased field due to the space charges at power frequency causes the differences in PD magnitudes and discharge occurrence as compared to the very low frequency.

---

---

## Chapter 10.

# Corona Discharge Measurement at Very Low Frequency

In this chapter, an experimental study of AC corona discharges in air under the application of different applied voltage amplitudes and excitation waveforms (sinusoidal and non-sinusoidal) is presented. Here, a comparative study at both frequencies is carried out based on the phase-resolved PD patterns and various IEC 60270 integrated parameters (the discharge magnitude, repetition rates, current, etc). The work in this chapter has been published in [15] and [17] as shown in the List of Publications.

## 10.1 Motivation of Corona Discharge Measurement

The physical ionisation in air under uniform and quasi-uniform field may onset an electron avalanche and after a while, it leads to the complete breakdown. However, in a non-uniform field, before the breakdown completely sparks over the airgap, several manifestations of luminous and audible discharges are observed. These discharges can be transient or steady state in occurrence, popularly known as corona discharge [8], [10], [58].

The corona discharge process is very much dependent on the rate of rise/fall of the applied voltage, duty cycle and the time lag (e.g. statistical and formative) characteristics of the electrons, which implies that such PD activity is highly influenced by the applied voltage frequency [31], [83], [259]. Hence, the excitation waveforms and frequencies are considered to be influential on the corona discharge characteristics [140], [141], [212].

To date, the sinusoidal voltage waveform as excitation has been extensively investigated. However, there is still limited research conducted on non-sinusoidal waveforms at VLF [260], [261]. Furthermore, it is a timely appeal to understand PD behaviours as some power equipment and electronic devices could be operating under the excitation of non-sinusoidal voltage waveforms such as square, sawtooth, etc [140]. For example, VLF square waveform can be

---

applied for testing plastic/polymeric cable, sheath testing, machine insulation, switching systems etc. Also, it provides potential diagnostic application for power electronics (e.g. inverter, rectifier) insulation. VLF cos-rect waveform can detect weak or critical spots in PE, XLPE.

A number of studies [140], [141], [260], [261] have been conducted to investigate PD behaviours under the application of various waveforms. The analysis reported in [31] compares the phase-resolved partial discharge (PRPD) patterns for sinusoidal and cos-rectangular (cos-rect) waveforms at 50 Hz and 0.1 Hz and concludes that the PRPD pattern for a cos-rect waveform is complicated or even sometimes impossible to characterise as compared to the sinusoidal waveform. The applications of triangular voltage [141], square voltage [140], [261] and trapezoidal voltage [141] have been investigated to examine the various discharge types (surface and cavity) at 50 Hz and it was reported that the PD characteristics are strongly affected by the instantaneous voltage, its rate of voltage change  $dv/dt$ , ramp time, slew rate.

The previous chapters (8 and 9) had examined the characteristics of PDs in void or on insulation surface. Thus, it would be incomplete if corona discharge under VLF and PF excitations is not examined. This chapter provides a comparative phase-resolved study of corona discharge in ambient air as a function of applied voltage amplitude and excitation waveforms (sinusoidal, square, and sawtooth).

## 10.2 Description of Experimental Setup

The practical laboratory setup of corona discharge measurement circuit along with the test-cell is depicted in Figure 10.1.

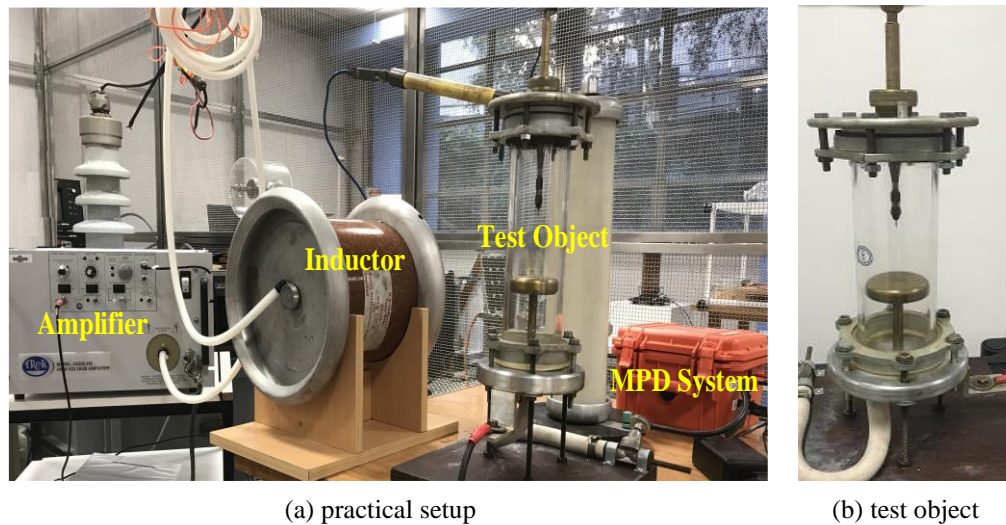


**Figure 10.1.** Laboratory setup of the experiment

---

The experimental work follows conventional PD detection techniques and fully compliant with the well-known IEC 60270 [41]. The measurement circuit is similar to the test circuit that used for surface discharge measurement. The only exception is that the test-object is replaced with a simple needle-plane electrode configuration to produce the corona discharge. The needle is made of steel having a tip radius of 50  $\mu\text{m}$  and connected to the high-voltage supply. The ground electrode is a circular brass metal plate with a diameter of 78 mm. The insulating medium between the electrodes is ambient air. Due to the sharp point tip, high electric stress is concentrated in the vicinity of the tip area and results in corona discharge in air.

## 10.3 Experimental Measurement

### 10.3.1 Inception Field

The inception electric field for corona discharge in air can be obtained from Peek's formula [262]:

$$E_c = 30 \times \delta \left( 1 + \frac{0.301}{\sqrt{r\delta}} \right) \text{ (kV/cm)} \quad (10.1)$$

where  $r$  is the radius of wire electrode in cm,  $\delta$  is the air density factor where  $\delta = T_0 P / TP_0$ ;  $T$  and  $P$  denote the room temperature and pressure respectively whereas  $T_0$  and  $P_0$  denote the standard temperature (20°C) and pressure (1 bar). The corresponding corona inception voltage,  $V_c$  is given by:

$$V_c = E_c \left\{ r \ln \left( \frac{d}{r} \right) \right\} \text{ (kV)} \quad (10.2)$$

where  $d$  is the distance between electrodes. The formulas are derived for parallel wire electrodes with smooth surface. However, the same formulas can be taken into account for a needle-plane geometry by assuming that the mean of the principal radii of curvature of the corona needle tip is equal to the cylindrical radius [263]. For this particular experiment setup,  $r = 50 \mu\text{m}$  and  $d = 45 \text{ mm}$ . The corona inception electric field and voltage are calculated to be 148 kV/cm and 5.09 kV respectively.

On the other hand, the electric stress distribution along the axis of symmetry for a needle-plane geometry can be approximated by the following [264]:

$$E(x) = \frac{2V}{\ln \left( \frac{4d}{r} \right) (2x + r - \frac{x^2}{a})} \quad (10.3)$$

where,  $x$  is the distance from the needle tip to the position in the air gap where corona occurs. This distance is influenced by space charge accumulated in the vicinity of the needle tip. In the experiment, inception voltage (PDIV) for corona discharge was measured at 4.6 kV which is very close to the inception voltage calculated from Peek's formula in equation (10.1).

### 10.3.2 Measurement Considerations of Corona Discharge

The experiment was conducted over consecutive days with relatively negligible humidity change in every day. Each test sequence was carried out for 6 hours at any voltage level. At the end of every hour, discharge activities were recorded. Each recording time was 10 minutes which corresponds to 60 consecutive cycles of 0.1 Hz or 30,000 cycles of 50 Hz. Details about the test setup parameters are shown in Table 10.1.

**Table 10.1.** Parameters used in experiment

Parameters	Value
Filter Bandwidth	300 kHz
Filter Center Frequency	250 kHz
Air Gap	45 mm
Temperature	25-30 °C
Noise Level	42 pC
Waveform	Sinusoidal, Square, and Sawtooth
Voltage	6 kV, 8 kV and 10 kV
Calibration	50 pC
Pulse Counting	$\geq 50$ pC
Coupling Capacitance ( $C_k$ )	1 nF

### 10.3.3 Characterised Parameters of Corona Discharge

Plots of the pulse repetition per cycle (PRPC), average charge magnitude, discharge current and discharge power are shown in Figure 10.2. The measurements were taken for both very low frequency (0.1 Hz) and power frequency (50 Hz) at 6-10 kV of applied voltage. From the experiment, all the corona pulses occurred in the negative half-cycle of the excitation although at the beginning, a small number of corona pulses were observed in the positive half-cycle. The latter are not considered here because these disappeared shortly after the initiation of experiment. Even so, as seen from the graphs in Figure 10.2, the parameter values fluctuate throughout the test duration. This is expected because the PD activity itself is a stochastic process which depends on the probability function of free electron generation rate, space ion-electron recombination rate, etc.

As can be observed from Figure 10.2, the pulse repetition per cycle at VLF for each voltage is much higher than the PRPC for the same voltage level at power frequency. Even the

PRPC for 6 kV at 0.1 Hz is higher than the 6-10 kV excitation of power frequency. The mobility of space charge after the PD event is probably responsible for this physical phenomenon. When an electric field rises significantly in the vicinity of needle tip, the high electrical stress accelerates free electrons to dislodge from electrodes. When the electrons get liberated, they collide with the gas molecules in the nearby high field region of the tip and result in ionisation. Due to ionisation, more electrons are generated and propagate towards the ground electrode where space charges (charges after the collision, mainly positive ions) are drifting slowly. After a PD inception, more space charges left by the avalanche accumulate in the gas region around the tip.

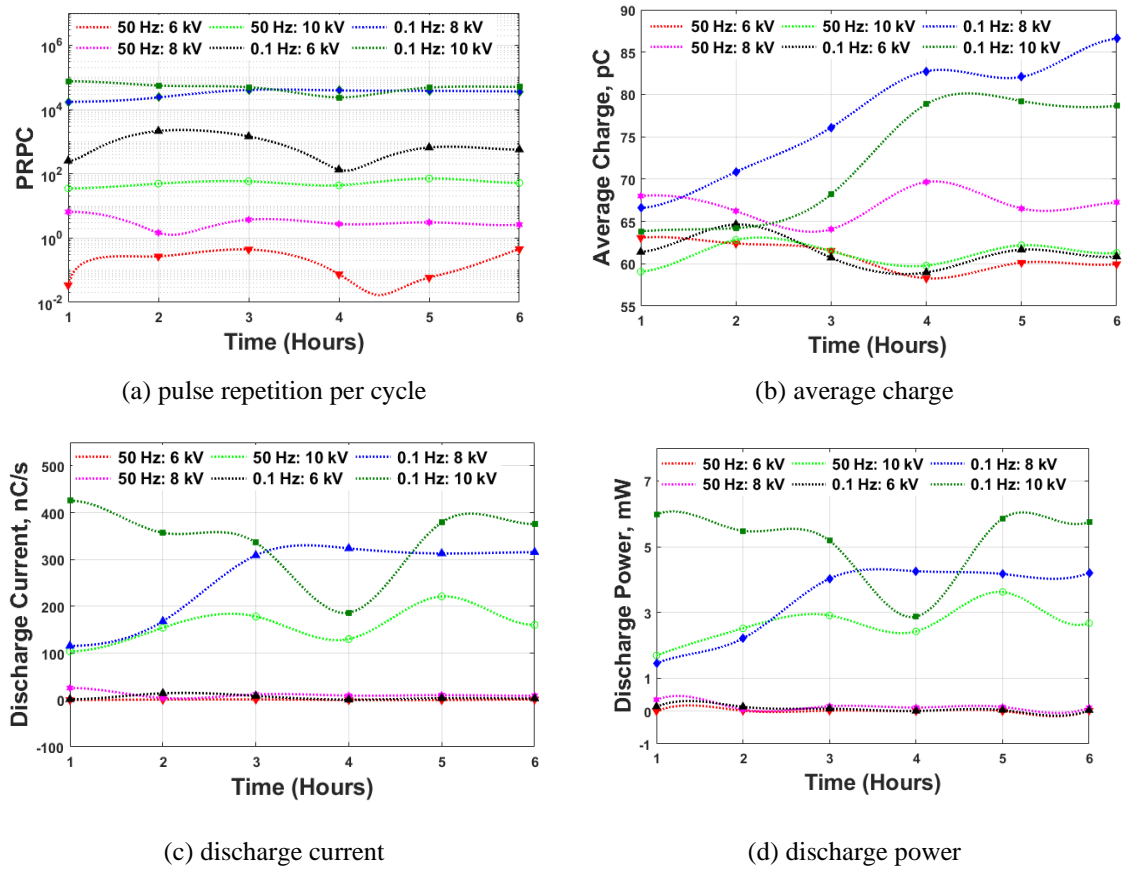


**Figure 10.2.** Corona discharge characterised parameters

Now, if the frequency of the applied voltage is relatively high, the voltage polarity gets a comparatively short time to switch from negative to positive. Therefore, the disappearance of positive ions cannot happen instantaneously while following the polarity change. As a result, the space charges get comparatively less time to recombine with free electrons. Therefore, with high-frequency excitation, a significant amount of space charge from PD events of the previous voltage cycle is still present in the new voltage cycle. As time goes, more space charges are generated, accumulated, and reduce the electric field in the proximity of the needle tip which in



---

turn necessitates an increasing field in order to start a PD during the new cycle. On the other hand, if the voltage excitation period is considerably higher, the voltage waveform changes its polarity after a long time. Therefore, it is reasonable to speculate that this longer period allows the space charge to recombine with electrons. Hence, the positive-ion cloud near the tip is reduced which is unable to make any significant change of electric field during the new cycle of VLF excitation [31], [83], [259]. This may be the reason why the PD repetition rate per cycle for 50 Hz at any voltage level is much lower than the PRPC at 0.1 Hz.

It is also interesting to observe in Figure 10.2b that the average apparent charge magnitude at VLF is almost the same as at power frequency for lower voltage (i.e. 6 kV) whereas, for higher voltage (i.e. 8 kV and 10 kV), VLF exhibits a higher magnitude of discharge than 50 Hz. This may be because the 6 kV excitation is much closer to the PDIV, therefore, throughout the measurement period, the discharge magnitude is almost the same at both frequencies.

On the other hand, at a higher voltage, during one cycle of VLF, the space charge amount rises with the instantaneous excitation of voltage. Besides, the PRPC rate is also higher. As a result, high electric stress is required to trigger a discharge and causes a relatively higher magnitude of PD events [83].

The discharge current and power for 10 minutes recording time as shown in Figure 10.2c and Figure 10.2d respectively are calculated from equation (3.1) and equation (3.2). As expected, the discharge current and power at VLF are higher than those at power frequency since both parameters are highly dependent on the PRPC and the apparent charge magnitude. The discharge current at both 8 kV and 10 kV for VLF hovers around 315-350 nC/s whilst the power is around 4-6 mW. Another observation from Figure 10.2 is that all IEC 60270 parameters (discharge current, and power) at 8 kV are very close to those for 10 kV at power frequency. All results are also investigated for 5 minutes recording time and similar results are found; therefore, these are not included in this chapter to avoid redundancy.

#### **10.3.4 Accumulated Charge Comparison between 50 Hz and 0.1 Hz**

The number of PD events for accumulated charge and charge within a fixed interval described by IEC 60270 are shown in Figure 10.3. Accumulated charge represents the number PD pulse/events when the magnitude exceeds 50 pC, 60 pC, and so forth. Note that in this study, 50 pC was taken to be the threshold because measurements below this value were susceptible to contamination by the high-frequency background noise.

Here, a discharge interval of 10 pC is considered. From both bar graphs, it is clearly evident that the number of PD events for 0.1 Hz in any interval is at least three times higher



than that at 50 Hz. Interestingly, for 50 Hz, the majority of PD events occur within the 50-60 pC interval whereas for VLF they occur at both 70-80 pC and 80-90 pC intervals.

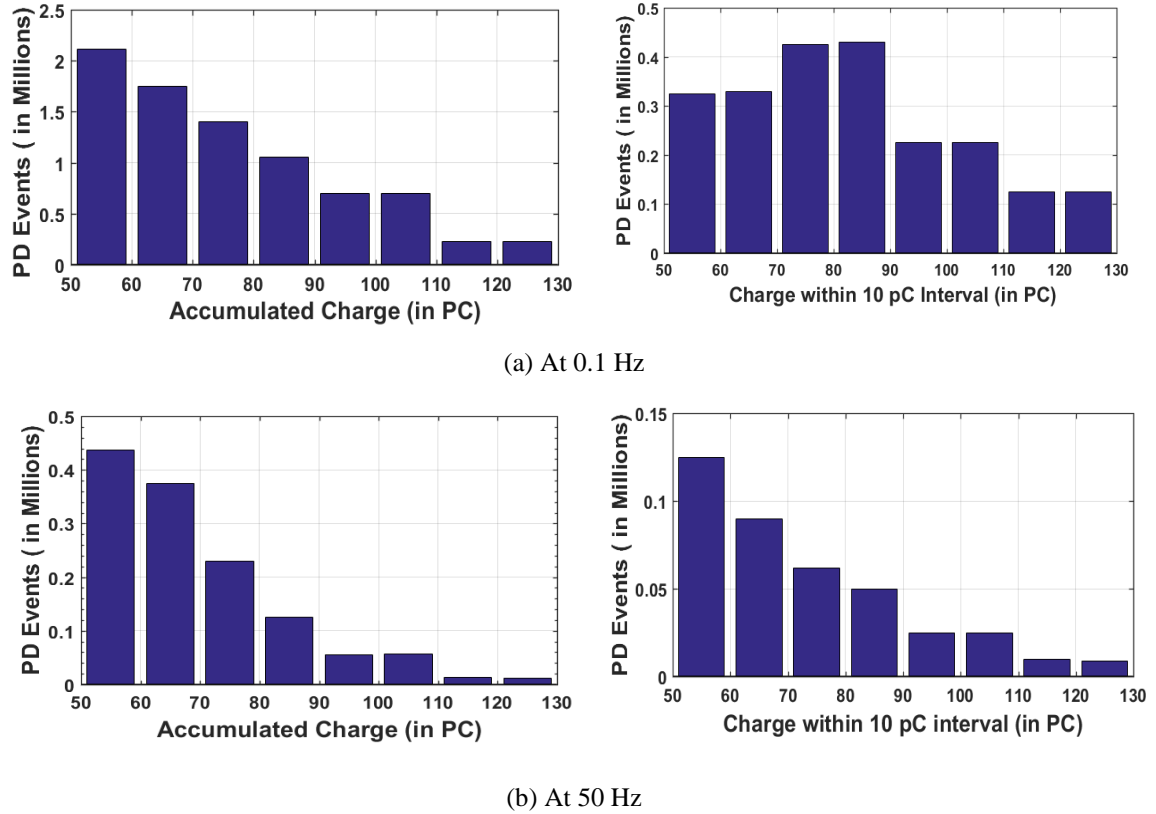


**Figure 10.3.** Number of PD events vs. accumulated charge and charge within 10 pC interval

## 10.4 Influence of Excitation Waveform on Corona Discharge

This section presents a comparative phase-resolved study of corona discharge under sinusoidal and non-sinusoidal voltage excitations. Here, the results are reported for the same applied peak voltage of 8 kV.

### 10.4.1 Sinusoidal Waveform

The PD phase-resolved scatter plots for sinusoidal waveform at 50 Hz and VLF are plotted in Figure 10.4 and Figure 10.5 respectively. The data were captured in the last 10 minutes of the initial and final hour. It can be seen that PD activities occur only in the negative half-cycle and scatter around the peak region of the applied voltage. The patterns acquired from the first hour exhibit a higher number of discharge activities than the final hour. Also, discharge activities at 50 Hz are much less dense than that at 0.1 Hz.

For the case of sinusoidal waveform, IEC 60270 integrated parameters to characterise PD activities are tabulated in Table 10.2. Comparing results with power frequency, the maximum discharge ( $Q_{\max}$ ) and average discharge ( $Q_{\text{avg}}$ ) magnitudes at VLF are larger in general while

other parameters exhibit much higher value. Both frequencies produce similar phase-resolved patterns over approximately the same phase window.

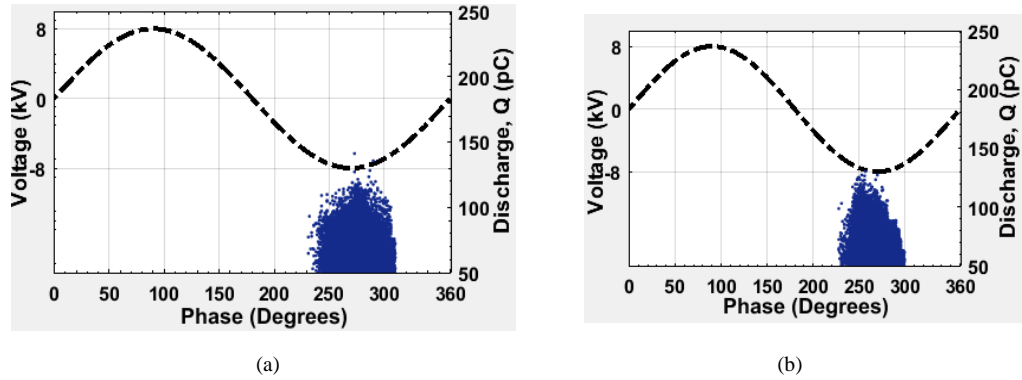


**Figure 10.4.** Sinusoidal excitation at 50 Hz: (a) at 1 hour (b) at 6 hour

**Table 10.2.** Characterisation under sinusoidal waveform

Parameters	50 Hz		0.1 Hz	
	1 Hour	6 Hour	1 Hour	6 Hour
$Q_{\max}$ (pC)	130.14	141.14	273.24	204.89
$Q_{\text{avg}}$ (pC)	64.04	65.71	82.07	86.58
PRPS (PDs/s)	100.00	44.14	3811	3638
PRPC (PDs/cycle)	2.00	0.882	38116	36386
Current, I (nA)	6.40	2.90	312.83	315.05
QR, D (aC <sup>2</sup> /s)	0.423	0.197	27.51	29.83

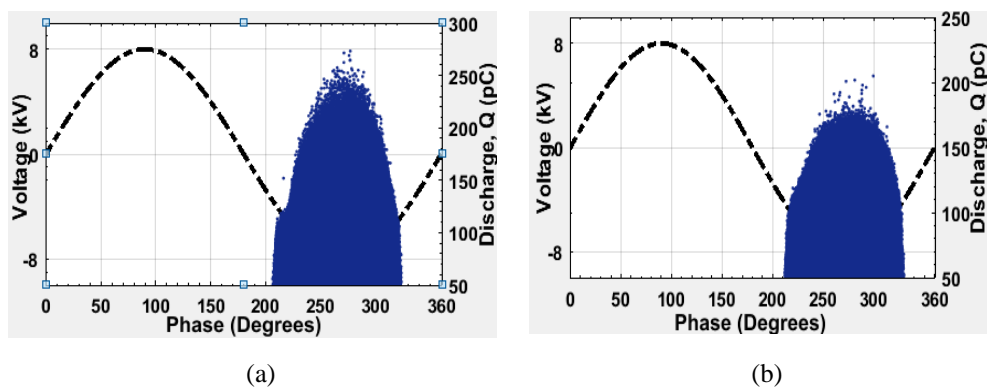


**Figure 10.5.** Sinusoidal excitation at 0.1 Hz: (a) at 1 hour (b) at 6 hour.

## 10.4.2 Square Waveform

The PD patterns for square waveform at very-low and power-frequency are shown in Figure 10.6 and Figure 10.7 respectively. Unlike the sinusoidal waveform in which PDs are concentrated around the negative voltage peak, here the distributions scatter throughout the

whole negative half-cycle from  $180^0$  to  $360^0$  phase angle. Another feature is that larger magnitudes of discharge are noticeable during the transition period where the voltage waveform reverses its polarity.

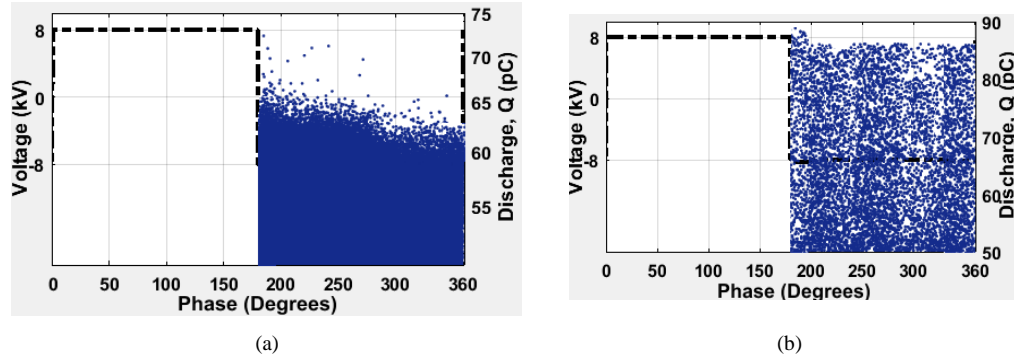


**Figure 10.6.** Square excitation at 50 Hz: (a) at 1 hour (b) at 6 hour.

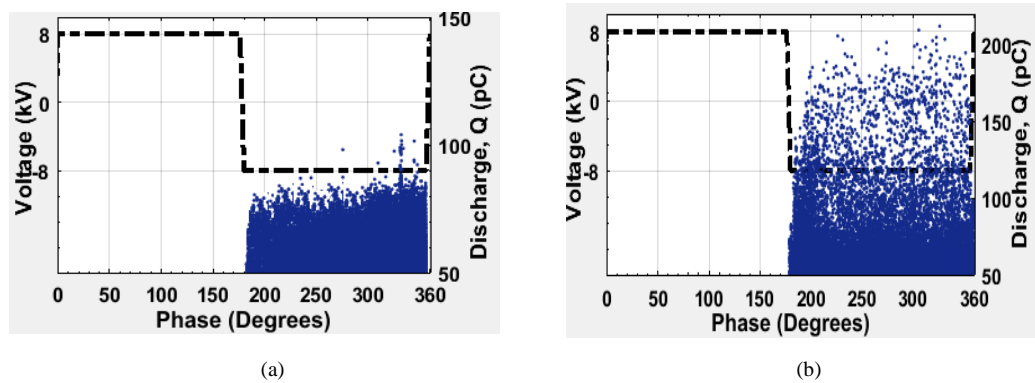


**Figure 10.7.** Square excitation at 0.1 Hz : (a) at 1 hour (b) at 6 hour.

The discharge characteristics for square waveform are summarised in Table 10.3. Comparing with sinusoidal waveform, a relatively lower discharge magnitude is observed in square waveform.

**Table 10.3.** PD characterisation under square waveform

Parameters	50 Hz		0.1 Hz	
	1 Hour	6 Hour	1 Hour	6 Hour
$Q_{\max}$ (pC)	72.29	86.11	309.31	335.12
$Q_{\text{avg}}$ (pC)	53.54	61.36	57.86	67.20
PRPS (PDs/s)	206.74	14.12	121.47	63.67
PRPC (PDs/cycle)	3.13	0.282	1214.7	636.73
Current, I (nA)	37.84	0.866	7.029	4.279
QR, D (aC <sup>2</sup> /s)	2.030	0.054	0.414	0.338

This may be associated with the high ( $dv/dt$ ) from the negligible rise/falling time of square wave. In fact, the trends are not merely observed during the recording period of the first and final hour but also experienced over the six hours of the test sequence. Exhibiting the same

trend as in sinusoidal waveform, square waveform excitation also produces a higher repetition rate (PRPS) and repetition rate per cycle (PRPC) at 0.1 Hz as compared to 50 Hz. The maximum discharge at VLF is around 350 pC whereas, in power frequency, it is around 62 pC.

### 10.4.3 Sawtooth Waveform

Figure 10.8 and Figure 10.9 are discharge scatter plots for symmetrical sawtooth waveform at 50 Hz and 0.1 Hz respectively. Interestingly, the triangular waveform yields quite similar features to those patterns acquired under sinusoidal excitation. PD activities are distributed around the maximum instantaneous voltage.

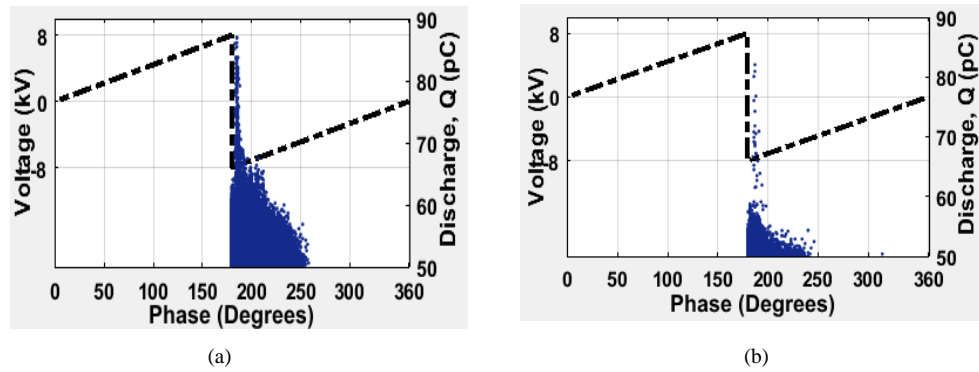


**Figure 10.8.** PRPD pattern of 50 Hz excitation: (a) at 1 hour (b) at 6 hour.

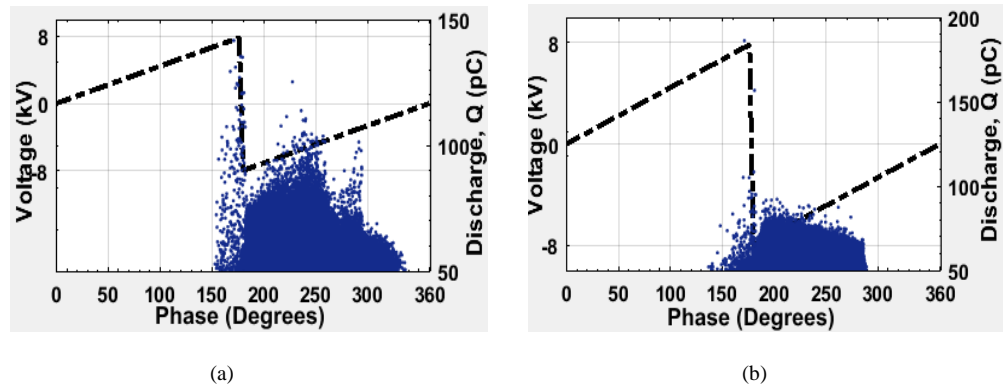


**Figure 10.9.** PRPD pattern of 0.1 Hz excitation: (a) at 1 hour (b) at 6 hour.

A summary of IEC 60270 parameters is tabulated in Table 10.4. From the table, these parameters are fairly comparable in every hour of measurement. The maximum and average PD magnitude increased from around 52 pC and 87 pC to 57 pC and 196 pC, respectively when the frequency was changed from 50 Hz to 0.1 Hz. This is because the faster rate of voltage change at high frequency causes the difference in PD magnitudes.

**Table 10.4.** PD characterisation under sawtooth waveform

Parameters	50 Hz		0.1 Hz	
	1 Hour	6 Hour	1 Hour	6 Hour
$Q_{\max}$ (pC)	86.95	82.05	195.42	186.19
$Q_{\text{avg}}$ (pC)	52.26	51.39	57.33	56.01
PRPS (PDs/s)	315.23	16.97	1241	778.91
PRPC (PDs/cycle)	6.30	0.339	12418	7789
Current, I (nA)	16.47	0.872	71.20	43.63
QR, D (aC <sup>2</sup> /s)	0.862	0.044	4.11	2.46

#### 10.4.4 Explanation of the Phase Distribution

Based on the PRPD patterns presented in the earlier sections, Figure 10.10 illustrates the amount of spreading,  $\Delta\phi$ , of PD activities during the negative half-cycle of the applied voltage for the three waveforms. The square waveform has maximum spread, followed by the sinusoidal waveform whilst the sawtooth waveform has the least scattering, i.e.

$$\Delta\phi_{\text{square}} > \Delta\phi_{\text{sine}} > \Delta\phi_{\text{sawtooth}} \quad (10.4)$$

The extent of spreading of PD phase distribution during the negative half-cycle appears to relate to the rate of voltage change, i.e.  $(dv/dt)$ . A faster voltage change results in PD occurred over a wider phase range. To support this argument, Fourier series can be utilised to represent any periodic non-sinusoidal voltage waveforms  $v(t)$  as an algebraic sum of harmonic sinusoidal functions. One can then work out the time derivative and from which obtain the maximum slew rate. For the same peak voltage  $V_p$ , it can be shown that:

$$\left( \frac{dv(t)}{dt} \right)_{\max} = \begin{cases} \omega V_p & \text{sinusoidal waveform} \\ (2/\pi)\omega V_p & \text{sawtooth waveform} \\ (4/\pi)\omega V_p & \text{square waveform} \end{cases} \quad (10.5)$$

where  $\omega$  denotes the angular frequency. Since  $2\omega/\pi < \omega < 4\omega/\pi$ , it clearly reveals that there is a correlation between the maximum slew rate and the relative spreading of PD activities as expressed in equation (10.4).

Larger PD characteristic parameters in all cases at VLF excitation (as compared to 50 Hz) are due to the physical process of the discharge as previously discussed. In short, it is less likely for positive ions from the previous cycles to stay present under VLF excitation. Indeed, this is the factor which contributes to the differences between two frequencies in tabulated IEC 60270 parameters.

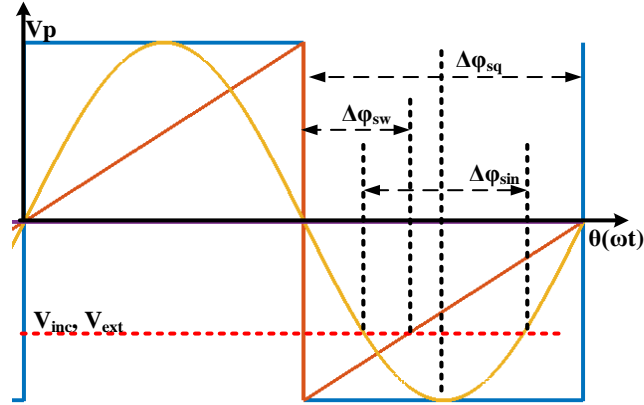


**Figure 10.10.** Phase range where PDs occurred for the three waveforms.

Faster switching period of polarity in the square wave allows the voltage exceeding the critical inception value immediately after the zero-crossing. This quicker transition of polarity generates more discharges, hence more positive space ions. Besides, there is no conducting surface for space ions. As a result, during the constant voltage period, accumulated charges from previous events reduce the electric field in the gas region. In fact, this is why results in Table 10.3 for square wave are considerably smaller as compared to other waveforms. On the other hand, sinusoidal and sawtooth voltages rarely experience this phenomenon because of the non-zero slew rate during their negative period [141], [261].

## 10.5 Chapter Conclusion

In this chapter, a comparative analysis of corona discharge with phase-resolved patterns at power frequency and very low frequency is presented. Measurement results reveal that these discharge characteristics are strongly dependent on the excitation frequency as well as the shape of voltage waveform. The PD phase distribution for a square wave is spread over the whole negative period of applied excitation whereas for sinusoidal and sawtooth waveforms, PD activities concentrate around the peak voltage region. In all tests, VLF excitation yields larger discharge, higher repetition rate and so as other parameters. Such behaviours could be due to the combined influence of the slew rate of the applied voltage as well as the excitation frequency on the physical discharge mechanism.

---

---

# Chapter 11.

## Conclusion and Future Work

### 11.1 Conclusions

To the aim of insulation condition/diagnostic assessment, this thesis provides extensive experimental measurement and modelling work to investigate dielectric response (DR) and partial discharge (PD) in polymeric insulation. For dielectric response, the measurement is carried out under different stress conditions over the very low to power frequency range. The studies include dielectric loss factor measurement and modelling, polarisation and depolarisation current measurement, recovery voltage response, activation energy measurement, trapping effects, Frohlich's distribution and so on. These are performed on service-aged XLPE cables in both time and frequency. Based on the pol/depolarisation current, the modelling of loss factor was implemented using the Debye model, Cole-Cole model and Davidson-Cole model.

On the other hand, partial discharge measurements have been done with three types of discharge sources: corona discharge, surface discharge, and internal discharge in an artificial void. For corona discharge in an air gap, the research was performed with a needle-plane electrode which was stressed at different voltage amplitudes and waveforms at very low frequency (0.1 Hz) and power frequency (50 Hz). The field distributions of surface discharge and how it affects the discharge sequence at VLF and PF have also been investigated. Measurements and modelling of the internal discharge as a function of applied voltage frequency and different cavity geometries (cylindrical, block, prism, rhombus) have been shown for different voltage levels. Based on the finite element analysis (FEA) method, the modelling of cavity discharge determines parameters which affect the discharge characteristics at VLF and PF excitations. The good agreement between the simulation and experimental results implies that the physical discharge process can be characterized by the modelling with the chosen parameter values.

By and large, partial discharge and dielectric response measurements reveal the local and overall insulation degradation respectively. The comparison between experimental and modelling results showed that these are strongly dependent on the applied voltage frequency

---

---

and depending on their relative physical process, contribute to the obtained results accordingly. The experimental, analytical and simulation studies of different diagnostic testing, together with the key findings, are summarised below.

- Chapter 1 identifies the motivation of this research. It explained the reasoning of dielectric testing at VLF excitation and the importance to compare the measurement and simulation results with the conventional power frequency. It also includes information regarding how the overall and local degradation of electrical insulation can be interpreted through dielectric response and partial discharge measurement.
- Literature on dielectric response measurement was reviewed in Chapter 2, including various diagnostic challenges of dielectric loss assessment (e.g. field measurement, processing, standards), different voltage sources and suitability (e.g. online/offline AC testing, VLF, DAC), dynamic properties of polarisation processes (e.g. generalised and external) and their differences, measurement techniques (e.g. in time domain and frequency domain), loss-factor measurement principles (e.g. Schering bridge, C-tan $\delta$  system), and some commercial test instruments (e.g. Baur, Omicron, sebaKMT etc.).
- Different diagnostic aspects of partial discharge measurement were provided in Chapter 3. It starts with introducing various discharge sources, parameters to characterise the PD activities, diagnostic standards and detection techniques. Several discharge models which have been used to simulate discharge activities are also discussed. To model the simulation, critical parameters (the initial electron generation rate, statistical and formative time lags, free charge decay time constant) which influence the discharge occurrence are explained in detail. Finally, PD analysis techniques such as statistical methods, phase-resolved patterns and commercially available systems with VLF test voltage are documented.
- Chapter 4 presented a comparative diagnostic study of dielectric loss measurements for service-aged XLPE cables over very low to power frequency. Measurement results show that higher DDF values are observed at 0.1 Hz as compared to PF. This is because the capacitive reactance of any test cable drops significantly with the increasing frequency. Moreover, the polarisation loss comes into action and contributes to the DDF value. The research also investigates the influence of partial discharge to the DDF value at VLF and PF applied voltage. The key finding is that the larger discharge magnitude at 50 Hz dominantly contributes to the tip-up in tan-delta value. On the other hand, the discharge process at VLF has smaller magnitude and makes a negligible change in the dissipation factor curve.
- An experimental study followed by empirical modelling using the Debye model, Cole-Cole model and Davidson-Cole model for dissipation factor measurement is reported in Chapter 5.



---

---

Experimental results obtained from PDC and FDS methods are modelled with the dipolar relaxation process for a frequency range from 1 mHz to 50 Hz. Comparing with the Debye and Cole-Cole process, the calculated tan-delta from the D-C model matches well with the measured data. Moreover, the additional use of D-C and Jonscher constants improves the simulation performance. For the obtained tan-delta characteristics, the conduction loss is found less dominant at higher frequencies whilst at lower frequencies, the characteristics are highly influenced by the conduction process of dipoles.

- The frequency domain response of dielectric dissipation factor under the influence of different ambient temperatures (293 K - 338 K) is documented in Chapter 6. With the increasing temperature, the loss-peak of  $\tan \delta$  shifts to a higher frequency zone due to  $\alpha$ - and  $\beta$ - relaxations; these two physical processes are the results of main chain and imperfect side chains movement. Frohlich's analysis shows the distribution of the imaginary permittivity as a function of the loss peak frequency at room temperature. The activation energy and mean relaxation time of test samples are calculated using Arrhenius equation. From the polarisation and depolarisation current, the study also shows that the upward transition of the DC conductivity is the result of increasing temperature.
- Dielectric response measurement of electrical insulation based on pol/depolarisation current measurement is extensively investigated in Chapter 7. The main contributions of this chapter are Daniel's normalisation, determining the number of polarisation branches, establishing the relationship between the Debye loss factor and D-C loss factor, the change of activation energy with the applied frequency, electrical stress impacts, etc. Furthermore, an empirical method to model the recovery voltage response is proposed. Modelling response from the analytical simulation correlates the charging time and the peak time and supports the previous study results.
- A comparative study of void discharge under the influence of various cavity geometries (cylindrical, prism, block, rhombus) is presented in Chapter 8. Measurement results reveal that PD characteristics such as discharge magnitude (average, maximum) and repetition rate are sensitive to the void structure for both VLF (0.1 Hz) and power frequency (50 Hz) excitations. The varying behaviours could be due to the availability of space charges and the electron generation rate in different geometries that influence the physical process. Comparing with power frequency, VLF excitation in general provides lower discharge magnitude and repetition rate. This is because the availability of space charges, electron generation rate and free charge decay rate after a PD event are less at VLF. A three-dimensional physical model describing the PD behaviours is also another novelty of the

---

---

research. Finite element analysis (FEA) based numerical model dynamically simulates and reproduces the discharge sequence matching the experimental measurement.

- Chapter 9 reports the measurement and modelling of partial discharge on XLPE insulation surface. Based on the sample geometry, a two-dimensional physical model was developed to describe the surface discharge process and determine the electric field distribution along the insulation surface before, after or during a discharge occurrence. The developed model shows that the local surface field drops after a PD event, and the drop is higher at the power frequency. The model also can effectively reproduce the discharge sequence and agrees with the measurement result.
- Corona discharge and their time-dependent behaviours are presented with the phase-resolved plots in Chapter 10. Experimental results show that the discharge magnitude, repetition rate per cycle, power and current at very low frequency have a higher value than at power frequency for the same applied voltage level. Similar trends are also observed when changing the excitation waveforms.

## 11.2 Future Research Directions

Some aspects of this research can be improved or expanded. Despite the measurement and simulation results in both dielectric response and partial discharge show reasonable agreement, there are still some differences. These differences/errors might be resulted either from the experiment or from the simulations. For instance, switching interferences or background noise might introduce some inaccuracy to the recorded measurement results in the laboratory. For the simulation, the performance may be improved by a better set of adjustable parameters.

Further investigations can examine other dielectrics such as polyester resin, epoxy etc. It is also of interest to check the dielectric behaviour beyond the power frequency range (e.g. kHz) considering most of the power electronics are operating in the higher frequency zone. The dielectric characteristics over kHz frequency range may or may not be similar to that observed in either very low frequency or power frequency. It may be required to modify the model in order to investigate the dielectric loss beyond the tested frequency range considered here.

As the renewable energy sources (PV, wind etc.) are rapidly penetrating and integrating to the grid, the existing transmission or distribution network sees an increasing trend of their capacity [265]. Deployment of various power electronic converters during the operation of AC to DC or DC to AC conversion injects different orders of harmonics (especially, 3<sup>rd</sup>, 5<sup>th</sup> and 7<sup>th</sup>) to the power network. Moreover, some power equipment and electronic devices could be operated under the excitation of non-sinusoidal waveforms and typically have the operating

---

---

frequency of 1 kHz-100 kHz. The mix-up of AC and DC voltage, harmonic distortion, sinusoidal and non-sinusoidal voltage, and high frequency (kHz) and power frequency (50 Hz) impose challenges to the electrical insulation. Therefore, this research can be extended to study the electrical insulations under such voltage conditions.

# Appendix A

## A.1 Dissipation Factor Formulation Using Debye Model

According to the Debye model, the equivalent circuit of a dielectric under an AC excitation can be illustrated as in Figure A. 1a.

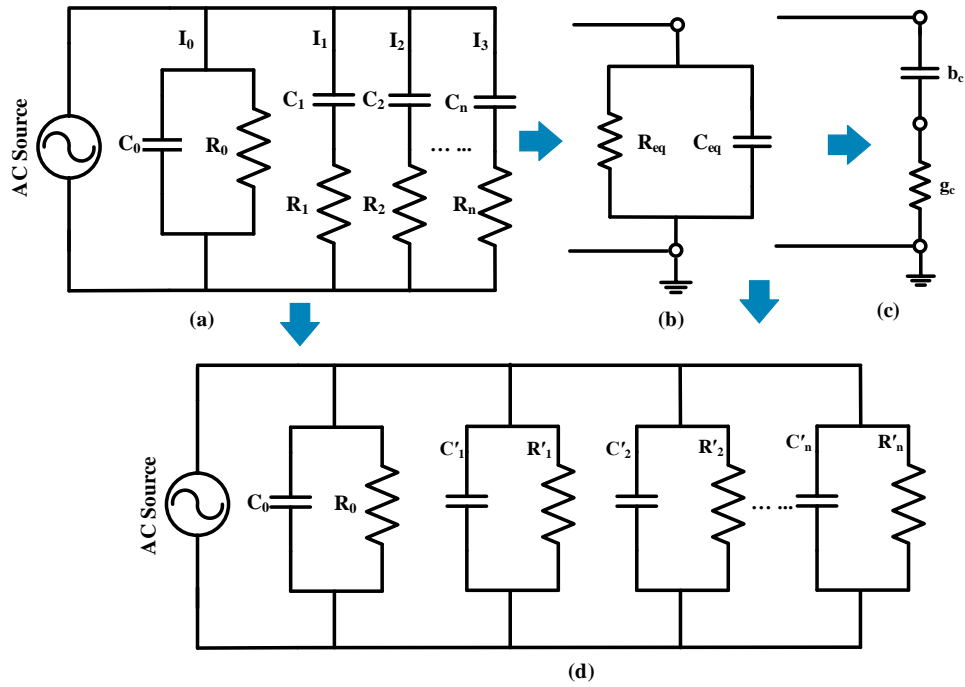


**Figure A. 1:** Step-by-step procedure to simplify the circuit

As can be seen, this complex circuit can also be converted into a parallel equivalent circuit in Figure A. 1b and a series equivalent circuit in Figure A. 1c. Each branch of the Debye circuit can also be modified into a parallel analogous circuit as in Figure A. 1d. The total equivalent admittance of the series circuit in Figure A. 1c can be written as:

$$Y = g_c - jb_c \quad (A1. 1)$$

where  $g_c$  ( $=\sigma_{eq}$ ) represents the equivalent conductance and  $b_c$  ( $=1/X_{eq}$ ) denotes the equivalent susceptance. From Figure A. 1d, the equivalent resistance ( $R_{eq}$ ) and capacitance ( $C_{eq}$ ) can be described as

$$\begin{aligned} \sigma_{eq} &= \sigma_0 + \sigma'_1 + \sigma'_2 + \dots + \sigma'_n \\ \frac{1}{R_{eq}} &= \frac{1}{R_0} + \frac{1}{R'_1} + \frac{1}{R'_2} + \dots + \frac{1}{R'_n} \end{aligned} \quad (A1. 2)$$

and

---



---


$$C_{eq} = C_0 + C'_1 + C'_2 + \dots + C'_n \quad (A1.3)$$

From the basic circuit, the admittance of the first branch ( $i=1$ ) can be expressed as:

$$Y_1 = \sigma_1 - j b_{C_1} = \frac{1}{Z_1} = \frac{1}{R_1 - j X_{C_1}} = \frac{R_1 (\omega C_1)^2}{1 + (\omega R_1 C_1)^2} + \frac{j \omega C_1}{1 + (\omega R_1 C_1)^2} \quad (A1.4)$$

By comparing the real and imaginary part, it can be deduced as:

$$\sigma_1 = \frac{1}{R'_1} = \frac{R_1 (\omega C_1)^2}{1 + (\omega R_1 C_1)^2} = \frac{C_1 \omega^2 \tau_1}{1 + (\omega \tau_1)^2} \quad (A1.5)$$

and

$$C'_1 = \frac{C_1}{1 + (\omega R_1 C_1)^2} = \frac{C_1}{1 + (\omega \tau_1)^2} \quad (A1.6)$$

where,  $\tau_1 = R_1 C_1$ . The formulas (A1.5) and (A1.6) are similar for other polarisation branches ( $i=1, 2, 3, \dots, n$ ). Hence, the final computation formula for the loss factor from equation (A1.1) is given by:

$$\begin{aligned} DDF &= \tan \delta \\ &= \frac{g_c}{b_c} \\ &= \sigma_{eq} X_{eq} \\ &= \frac{\sigma_{eq}}{\omega C_{eq}} \\ &= \frac{\sigma_0 + \sigma'_1 + \sigma'_2 + \dots + \sigma'_n}{\omega [C_0 + C'_1 + C'_2 + \dots + C'_n]} \\ &= \frac{\frac{1}{R_0} + \frac{1}{R'_1} + \frac{1}{R'_2} + \dots + \frac{1}{R'_n}}{\omega [C_0 + C'_1 + C'_2 + \dots + C'_n]} \\ &= \frac{\frac{1}{R_0} + \frac{C_1 \omega^2 \tau_1}{1 + (\omega \tau_1)^2} + \frac{C_2 \omega^2 \tau_2}{1 + (\omega \tau_2)^2} + \dots + \frac{C_n \omega^2 \tau_n}{1 + (\omega \tau_n)^2}}{\omega \left[ C_0 + \frac{C_1}{1 + (\omega \tau_1)^2} + \frac{C_2}{1 + (\omega \tau_2)^2} + \dots + \frac{C_n}{1 + (\omega \tau_n)^2} \right]} \\ &= \frac{\frac{1}{\omega R_0} + \sum_{i=1}^n \frac{C_i \omega \tau_i}{1 + (\omega \tau_i)^2}}{C_0 + \sum_{i=1}^n \frac{C_i}{1 + (\omega \tau_i)^2}} \end{aligned} \quad (A1.7)$$

## A.2 DDF Measurement After Adding a Dummy Capacitor

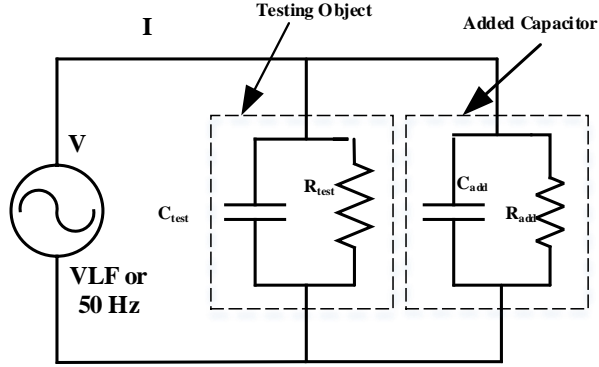


Figure A. 2: Adding an extra capacitor parallel to the test object

After adding a dummy capacitor to a test object, the equivalent resistance ( $R_{tot}$ ) and capacitance ( $C_{tot}$ ) can be written as:

$$R_{tot} = R_{test} || R_{add} \text{ and } C_{tot} = C_{test} + C_{add} \quad (A2. 1)$$

Now, the dissipation factor of test object  $\tan \delta_{test}$  can be derived from total DDF  $\tan \delta_{tot}$  and the derivation is given by

$$\tan \delta_{tot} = \frac{1}{\omega R_{tot} C_{tot}}$$

$$\frac{1}{\tan \delta_{tot}} = \omega R_{tot} C_{tot}$$

$$\frac{1}{\tan \delta_{tot}} = \omega R_{tot} (C_{test} + C_{add})$$

$$\frac{1 - \omega R_{tot} C_{add} \tan \delta_{tot}}{\tan \delta_{tot}} = \omega R_{tot} C_{test} \quad (A2. 2)$$

$$\frac{1 - \omega R_{tot} C_{add} \tan \delta_{tot}}{\tan \delta_{tot}} = \omega \frac{R_{test} R_{add}}{R_{test} + R_{add}} C_{test}$$

$$\frac{1}{\omega R_{test} C_{test}} = \frac{R_{add}}{R_{test} + R_{add}} \frac{\tan \delta_{tot}}{1 - \omega R_{tot} C_{add} \tan \delta_{tot}}$$

$$\tan \delta_{test} = \beta \frac{\tan \delta_{tot}}{1 - \omega R_{tot} C_{add} \tan \delta_{tot}}$$

This is the final form of dissipation factor measurement after adding a dummy capacitor, where,  $\beta = \frac{R_{add}}{R_{test} + R_{add}}$ .

## Appendix B

When switch  $S_3$  of the RVM circuit (in Figure 7.13) is closed, a recovery voltage can be found at the terminal. For a single polarisation event, the circuit in Figure 7.13 can be simplified and illustrated in Figure A. 1. This simplified circuit includes a single polarisation capacitor ( $C_1$ ).

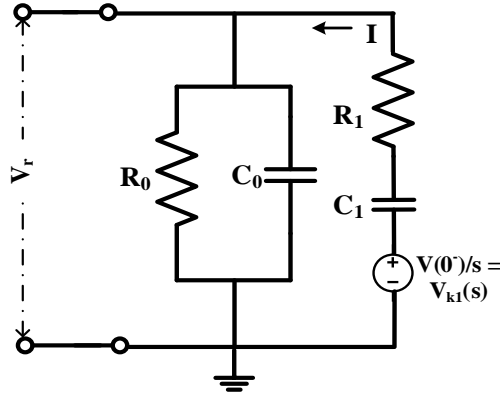


Figure B. 3: Debye equivalent circuit for a single polarising event

By Laplace transformation, the expression of recovery voltage ( $V_r$ ) and the current ( $I$ ) which flows in the circuit can be expressed as follows. The initial voltage at the beginning of discharging period is modelled with a voltage source as  $V_{k1}(s)=V(0)/s$ .

$$V_{k1}(s) = V_r(s) + R_1 I(s) + \frac{I(s)}{s C_1} \quad (B.1)$$

After rearranging (B.1),

$$V_r(s) = V_{k1}(s) - I(s) \left[ R_1 + \frac{1}{s C_1} \right] \quad (B.2)$$

Applying KCL to the parallel branch of  $R_0$  and  $C_0$ ,

$$I(s) = s C_0 V_r(s) + \frac{V_r(s)}{R_0} = V_r(s) \left[ s C_0 + \frac{1}{R_0} \right] \quad (B.3)$$

Substituting  $I(s)$  from (B.3) to (B.2),

$$V_r(s) = V_{k1}(s) - V_r(s) \left[ s C_0 + \frac{1}{R_0} \right] \left[ R_1 + \frac{1}{s C_1} \right] \quad (B.4)$$

$$V_r(s) = \frac{V_{k1}(s)}{1 + \left[ s C_0 + \frac{1}{R_0} \right] \left[ R_1 + \frac{1}{s C_1} \right]}$$

---

After some simplifications, the following expression can be deduced as:

$$F(s) = \frac{V_r(s)}{V_{kl}(s)} = \frac{N_{1,1}s + N_0}{D_2s^2 + D_1s^1 + D_0s^0} \quad (\text{B.5})$$

where,

$$\begin{aligned} D_2 &= \tau_0 \tau_1; & D_1 &= \tau_0 + \tau_1 + \tau_{01}; & D_0 &= 1 \\ \tau_0 &= R_0 C_0; & \tau_1 &= R_1 C_1; & \tau_{01} &= R_0 C_1 \\ N_{1,1} &= \tau_{01}; & N_0 &= 0 \end{aligned}$$

Equation (B.5) can be generalised as:

$$F(s) = k \frac{s}{(s + p_1)(s + p_2)} \quad (\text{B.6})$$

By taking the inverse Laplace transform ( $\mathfrak{I}^{-1}$ ) of equation (B.6), the recovery voltage  $V_r(T_c, t)$  can be obtained in the time domain. For a given charging period ( $T_c$ ), the maximum value of this voltage can be written as:

$$\begin{aligned} V_{r\max}(T_c) &= \mathfrak{I}^{-1}[F(s)] V_{Cl}(T_c) = \hat{A}_1(T_p) V_{Cl}(T_c) \\ &= \hat{A}_1(T_p) V_0 \left[ 1 - \exp\left(-\frac{T_c}{\tau_1}\right) \right] \exp\left(-\frac{T_d}{\tau_1}\right) \end{aligned} \quad (\text{B.7})$$

where,

$$\hat{A}_1(T_p) = k [A_{1,1} \exp(T_p p_1) + A_{1,2} \exp(T_p p_2)]$$

$$\text{and } k = \frac{N_{1,1}}{D_2}$$



---

# References

- [1] R. E. James and Q. Su, *Condition assessment of high voltage insulation in power system equipment*, IET, vol. 53, 2008.
- [2] W. Hauschild, "Critical review of voltages applied for quality-acceptance and diagnostic field tests on high-voltage and extra-high-voltage cable systems," *IEEE Electr. Insul. Mag.*, vol. 29, no. 2, pp. 16–25, 2013.
- [3] M. Zhang *et al.*, "Measurement of dielectric response of transformer moisture content," *IET Sci. Meas. Technol.*, vol. 12, no. 5, pp. 594–602, 2018.
- [4] S. Hvidsten, B. Holmgren, L. Adeen, and J. Wetterstrom, "Condition assessment of 12- and 24-kV XLPE cables installed during the 80s. Results from a joint Norwegian/Swedish research project," *IEEE Electr. Insul. Mag.*, vol. 21, no. 6, pp. 17–23, 2005.
- [5] J. Perkel, Y. Del Valle, R. N. Hampton, J. C. Hernandez-mejia, and J. Densley, "Interpretation of dielectric loss data on service aged polyethylene based power cable systems using VLF test methods," *IEEE Trans. Dielectr. Electr. Insul.*, vol. 20, no. 5, pp. 1699–1711, 2013.
- [6] U. M. Rao, Y. N. Kumar, and R. K. Jarial, "Understanding the ageing behaviour of transformer oil–paper insulation with ester and mixed dielectric fluids," *IET Sci. Meas. Technol.*, vol. 12, no. 7, pp. 851–857, 2018.
- [7] S. Rengarajan, M. D. Agrawal, and R. S. Nema, "Behavior of high voltage machine insulation system in the presence of thermal and electrical stresses," *IEEE Trans. Electr. Insul.*, vol. 20, no. 1, pp. 104–110, 1985.
- [8] J. Kuffel and P. Kuffel, *High voltage engineering fundamentals*, Elsevier, 2000.
- [9] G. C. Montanari and A. Cavallini, "Partial discharge diagnostics: from apparatus monitoring to smart grid assessment," *IEEE Electrical Insulation Magazine*, 2013.
- [10] W. Hauschild and E. Lemke, *High-voltage test and measuring techniques*, Springer, 2014.
- [11] J. C. Fothergill, S. J. Dodd, L. A. Dissado, T. Liu, and U. H. Nilsson, "The measurement of very low conductivity and dielectric loss in XLPE cables: a possible method to detect degradation due to thermal aging," *IEEE Trans. Dielectr. Electr. Insul.*, vol. 18, no. 5, pp. 1544–1553, 2011.
- [12] S. Morsalin, A. Sahoo, B. T. Phung, "Diagnostic testing of power cable insulation for reliable smart grid operation", *37th IEEE Electrical Insulation Conference (EIC)*, Calgary, AB, Canada, June 2019, pp. 509-512.
- [13] H. Mitsui, K. Yoshida, Y. Inoue, and K. Kawahara, "Mechanical degradation of high voltage rotating machine insulation," *IEEE Trans. Electr. Insul.*, vol.16, no. 4, pp. 351–359, 1981.
- [14] L. A. Dissado and J. C. Fothergill, *Electrical degradation and breakdown in polymers*, IET, 1992.
- [15] "Partial Discharge Academy." [Online]. Available: <https://www.eatechnology.com/news/partial-discharge-academy/>. [Accessed: 26-Apr-2019].
- [16] S. S. Refaat and M. A. Shams, "A review of partial discharge detection, diagnosis techniques in high voltage power cables," *12th IEEE International Conference on Compatibility, Power Electronics and Power Engineering (CPE-POWERENG 2018)*,

- 
- 2018, pp. 1–5.
- [17] M. Wang, A. J. Vandermaar, and K. D. Srivastava, “Review of condition assessment of power transformers in service,” *IEEE Electr. Insul. Mag.*, vol. 18, no. 6, pp. 12–25, 2002.
  - [18] M. Farahani, H. Borsi, and E. Gockenbach, “Dielectric response studies on insulating system of high voltage rotating machines,” *IEEE Trans. Dielectr. Electr. Insul.*, vol. 13, no. 2, pp. 383–393, 2006.
  - [19] S. Chatterjee, A. K. Pradhan, S. Dalai, B. Chatterjee, and S. Chakravorti, “Reducing frequency domain spectroscopy measurement time for condition monitoring of transformer oil-paper insulation using non-sinusoidal excitations,” *IET Sci. Meas. Technol.*, vol. 11, no. 2, pp. 204–212, 2017.
  - [20] X. Yang, S. Nielsen, and G. Ledwich, “Investigations of dielectric monitoring on an energised transformer oil–paper insulation system,” *IET Sci. Meas. Technol.*, vol. 9, no. 1, pp. 102–112, 2015.
  - [21] K. Kimura, “Progress of insulation ageing and diagnostics of high voltage rotating machine windings in Japan,” *IEEE Electr. Insul. Mag.*, vol. 9, no. 3, pp. 13–20, 1993.
  - [22] N. Lahoud, J. Faucher, D. Malec, and P. Maussion, “Electrical aging of the insulation of low-voltage machines: model definition and test with the design of experiments,” *IEEE Trans. Ind. Electron.*, vol. 60, no. 9, pp. 4147–4155, 2013.
  - [23] A. B. D. Mishra, N. Haque and S. Chakravorti, “Effect of charge accumulated at oil–paper interface on parameters considered for power transformer insulation diagnosis,” *IET Sci. Meas. Technol.*, vol. 12, no. 7, p. 937, 2018.
  - [24] M. T. Peschel, “Needed changes in medium voltage cable testing. Were you in on it? Welcome to the world of VLF.,” *IEEE International Symposium on Electrical Insulation*, 2010, pp. 1–5.
  - [25] D. Zhang *et al.*, “Study on FDS characteristics of oil-immersed paper insulation bushing under non-uniform moisture content,” *IET Sci. Meas. Technol.*, vol. 12, no. 5, pp. 691–697, 2018.
  - [26] Ing Erling Ildstad, “The power of electrical energy,” 2014.
  - [27] W. Deng, Z. Zheng, L. Ruan, Y. Shen, Q. Xie, and H. Wang, “Power apparatus insulation diagnosis through partial discharge in a smarter grid,” *IEEE International Symposium on Electrical Insulation*, 2010, pp. 1–4.
  - [28] M. Abou-Dakka, A. Bulinski, and S. S. Bamji, “On-site diagnostic technique for smart maintenance of power cables,” *IEEE Power and Energy Society General Meeting*, 2011, pp. 1–5.
  - [29] “IEEE guide for field testing and evaluation of the insulation of shielded power cable systems rated 5 kv and above,” *IEEE Std.*, pp. 1–159, 2012.
  - [30] G. S. Eager, B. Fryszczyn, C. Katz, H. A. Elbadaly, and A. R. Jean, “Effect of DC testing water tree deteriorated cable and a preliminary evaluation of VLF as alternate,” *IEEE Trans. Power Deliv.*, vol. 7, no. 3, pp. 1582–1591, 1992.
  - [31] V. Krotov and A. Cavallini, “Comparison of PD patterns at power and very low frequency: Is diagnostic possible?,” in *2013 IEEE International Conference on Solid Dielectrics (ICSD)*, 2013, pp. 109–112.
  - [32] D. Fynes-Clinton and C. Nyamupangedengu, “Partial discharge characterisation of cross-linked polyethylene medium voltage power cable termination defects at very low frequency (0.1 Hz) and power frequency test voltages,” *IEEE Electr. Insul. Mag.*, vol. 32, no. 4, pp. 15–23, 2016.
-

- 
- 
- [33] A. Cavallini and G. C. Montanari, "Effect of supply voltage frequency on testing of insulation system," *IEEE Trans. Dielectr. Electr. Insul.*, vol. 13, no. 1, pp. 111–121, 2006.
- [34] C. Nyamupangedengu and I. R. Jandrell, "Influence of supply voltage frequency and magnitude on PD pulse parameters," *IEEE Trans. Dielectr. Electr. Insul.*, vol. 15, no. 6, pp. 1590–1600, 2008.
- [35] B. Oyegoke, P. Hyvonen, M. Aro, N. Gao, and M. Danikas, "Selectivity of damped AC (DAC) and VLF voltages in after-laying tests of extruded mv cable systems," *IEEE Trans. Dielectr. Electr. Insul.*, vol. 10, no. 5, pp. 874–882, 2003.
- [36] E. Gulski, J. J. Smit, P. N. Seitz, J. C. Smit, and M. Turner, "On-site PD diagnostics of power cables using oscillating wave test system," *11th International Symposium on High Voltage Engineering*, 1999, vol. 5, pp. 112–115.
- [37] E. Gockenbach and W. Hauschild, "The selection of the frequency range for high-voltage on-site testing of extruded insulation cable systems," *IEEE Electr. Insul. Mag.*, vol. 16, no. 6, pp. 11–16, 2000.
- [38] S. Morsalin and B. T. Phung, "A comparative study of dielectric dissipation factor measurement under very low and power frequencies," *3rd International Conference on Condition Assessment Techniques in Electrical Systems (CATCON)*, 2017, pp. 10–14.
- [39] L. Yang, J. Chen, J. Gao, H. Zheng, and Y. Li, "Accelerating frequency domain dielectric spectroscopy measurements on insulation of transformers through system identification," *IET Sci. Meas. Technol.*, vol. 12, no. 2, pp. 247–254, 2018.
- [40] W. S. Zaengl, "Applications of dielectric spectroscopy in time and frequency domain for HV power equipment," *IEEE Electr. Insul. Mag.*, vol. 19, no. 6, pp. 9–22, 2003.
- [41] "Partial Discharge Measurements," IEC 60270 Std., pp. 5–49, 2013.
- [42] R. Bodega, P. H. F. Morshuis, M. Lazzaroni, and F. J. Wester, "PD recurrence in cavities at different energizing methods," *IEEE Trans. Instrum. Meas.*, vol. 53, no. 2, pp. 251–258, 2004.
- [43] F. J. Wester, E. Guilski, and J. J. Smit, "Detection of partial discharges at different AC voltage stresses in power cables," *IEEE Electr. Insul. Mag.*, vol. 23, no. 4, pp. 28–43, 2007.
- [44] H. Illias, G. Chen, and P. L. Lewin, "Partial discharge behavior within a spherical cavity in a solid dielectric material as a function of frequency and amplitude of the applied voltage," *IEEE Trans. Dielectr. Electr. Insul.*, vol. 18, no. 2, pp. 432–443, 2011.
- [45] C. Forssen and H. Edin, "Partial discharges in a cavity at variable applied frequency part 2: measurements and Modelling," *IEEE Trans. Dielectr. Electr. Insul.*, vol. 15, no. 6, pp. 1610–1616, 2008.
- [46] H. V. P. Nguyen and B. T. Phung, "Void discharge behaviours as a function of cavity size and voltage waveform under very low-frequency excitation," *High Volt.*, vol. 3, no. 2, pp. 96–102, 2018.
- [47] H. V. P. Nguyen, B. T. Phung, and T. Blackburn, "Effects of ambient conditions on partial discharges at very low frequency (VLF) sinusoidal voltage excitation," in *2015 IEEE Electrical Insulation Conference (EIC)*, 2015, pp. 266–269.
- [48] H. V. P. Nguyen, B. T. Phung, and T. Blackburn, "Effect of temperatures on very low frequency partial discharge diagnostics," *11th International Conference on the Properties and Applications of Dielectric Materials (ICPADM)*, 2015, pp. 272–275.
- [49] L. Chmura, H. Jin, P. Cichecki, J. J. Smit, E. Gulski, and F. D. Vries, "Use of dissipation

- 
- 
- factor for life consumption assessment and future life modelling of oil-filled high-voltage power cables,” *IEEE Electr. Insul. Mag.*, vol. 28, no. 1, pp. 27–37, 2012.
- [50] A. K. Pradhan, S. Chatterjee, A. Banik, S. Dalai, and B. Chatterjee, “Condition assessment of outdoor porcelain insulator based on dielectric dissipation factor evaluated from non-linear equivalent circuit,” *IET Sci. Meas. Technol.*, vol. 10, no. 8, pp. 866–873, 2016.
  - [51] W. S. Zaengl, “Dielectric spectroscopy in time and frequency domain for HV power equipment. I. Theoretical considerations,” *IEEE Electr. Insul. Mag.*, vol. 19, no. 5, pp. 5–19, 2003.
  - [52] A. A. S. Akmal, H. Borsi, E. Gockenbach, V. Wasserberg, and H. Mohseni, “Dielectric behavior of insulating liquids at very low frequency,” *IEEE Trans. Dielectr. Electr. Insul.*, vol. 13, no. 3, pp. 532–538, 2006.
  - [53] M. Dong *et al.*, “Explanation and analysis of oil-paper insulation based on frequency-domain dielectric spectroscopy,” *IEEE Trans. Dielectr. Electr. Insul.*, vol. 22, no. 5, pp. 2684–2693, 2015.
  - [54] G. Ye, H. Li, F. Lin, J. Tong, X. Wu, and Z. Huang, “Condition assessment of XLPE insulated cables based on polarization/depolarization current method,” *IEEE Trans. Dielectr. Electr. Insul.*, vol. 23, no. 2, pp. 721–729, 2016.
  - [55] “IEEE guide for field testing of shielded power cable systems using very low frequency (VLF) (less than 1 Hz), IEEE 400.2 Std (Readline)., pp. 1–60, 2011.
  - [56] G. G. Raju, *Dielectrics in electric fields*, CRC press, 2016.
  - [57] T. Shahsavarian and S. M. Shahrtash, “Modelling of aged cavities for partial discharge in power cable insulation,” *IET Sci. Meas. Technol.*, vol. 9, no. 6, pp. 661–670, 2015.
  - [58] C. L. Wadhwa, *High voltage engineering*, New Age International, 2007.
  - [59] X. Feng, Q. Xiong, A. Gattozzi, G. C. Montanari, P. Seri, and R. Hebner, “Cable commissioning and diagnostic tests: The effect of voltage supply frequency on partial discharge behavior,” *12th International Conference on the Properties and Applications of Dielectric Materials (ICPADM)*, 2018, pp. 373–376.
  - [60] T. Tanaka, “Internal Partial Discharge and Material Degradation,” *IEEE Trans. Electr. Insul.*, vol. 21, no. 6, pp. 899–905, 1986.
  - [61] L. Wang, A. Cavallini, G. C. Montanari, and L. Testa, “Evolution of PD patterns in polyethylene insulation cavities under AC voltage,” *IEEE Trans. Dielectr. Electr. Insul.*, vol. 19, no. 2, pp. 533–542, 2012.
  - [62] C. Forssen and H. Edin, “Partial discharges in a cavity at variable applied frequency part 1: measurements,” *IEEE Trans. Dielectr. Electr. Insul.*, vol. 15, no. 6, pp. 1601–1609, 2008.
  - [63] H. V. P. Nguyen, B. T. Phung, and S. Morsalin, “Modelling partial discharges in an insulation material at very low frequency,” *International Conference on High Voltage Engineering and Power Systems (ICHVEPS)*, 2017, pp. 1–5.
  - [64] S. n. Al-Refaie and H. S. B. Elayyan, “Modelling and simulation of KNBO<sub>3</sub> ceramics dispersion,” *IET Sci. Meas. Technol.*, vol. 1, no. 3, pp. 133–137, 2007.
  - [65] G. Liang, Y. Jing, Z. Li, X. Liu, and L. Ma, “Modelling of frequency characteristics of the oil-paper compound insulation based on the fractional calculus,” *IET Sci. Meas. Technol.*, vol. 11, no. 5, pp. 646–654, 2017.
  - [66] T. K. Saha, P. Purkait, and F. Muller, “Deriving an equivalent circuit of transformers insulation for understanding the dielectric response measurements,” *IEEE Trans. Power*
-

- 
- 
- Deliv.*, vol. 20, no. 1, pp. 149–157, 2005.
- [67] X. Zhang and E. Gockenbach, “Asset-management of transformers based on condition monitoring and standard diagnosis,” *IEEE Electr. Insul. Mag.*, vol. 24, no. 4, pp. 26–40, 2008.
- [68] “IEEE guide for field testing of shielded power cable systems using very low frequency (VLF) (less than 1 Hz),” *IEEE Std 400.2*, pp. 1–60, 2013.
- [69] “*Standard for electrical safety in the workplace*”, NFPA, 2004.
- [70] “IEEE recommended practices for safety in high-voltage and high-power testing,” *ANSI/IEEE Std. 510*, pp. 1–19, 1983.
- [71] H. M. Ryan, *High voltage engineering and testing*, IET , Vol. 32. 2001.
- [72] M. Abdel-Salam, *Highvoltage engineering: theory and practice, revised and expanded*, CRC Press, 2000.
- [73] P. Cichecki *et al.*, “Statistical approach in power cables diagnostic data analysis,” *IEEE Trans. Dielectr. Electr. Insul.*, vol. 15, no. 6, 2008.
- [74] C. L. Fletcher *et al.*, “First practical utility implementations of monitored withstand diagnostics in the USA,” in *International conference on insulated power cables JICABLE11, Versailles France*, 2011.
- [75] R. Houtepen, L. Chmura, J. J. Smit, B. Quak, P. P. Seitz, and E. Gulski, “Estimation of dielectric loss using damped AC voltages,” *IEEE Electr. Insul. Mag.*, vol. 27, no. 3, 2011.
- [76] A. Davies, *Handbook of condition monitoring: techniques and methodology*, Springer Science & Business Media, 2012.
- [77] H. A. Illias, M. A. Tunio, A. H. A. Bakar, H. Mokhlis, and G. Chen, “Partial discharge behaviours within a void-dielectric system under square waveform applied voltage stress,” *IET Sci. Meas. Technol.*, vol. 8, no. 2, pp. 81–88, 2014.
- [78] T. Takahashi, T. Takahashi, and T. Okamoto, “Insulation diagnosis for XLPE cables using damping oscillating high voltage,” *Annual Report Conference on Electrical Insulation and Dielectric Phenomena (CEIDP)*, 2008, pp. 471–474.
- [79] M. S. Mashikian and A. Szarkowski, “Medium voltage cable defects revealed by off-line partial discharge testing at power frequency,” *IEEE Electr. Insul. Mag.*, vol. 22, no. 4, pp. 24–32, 2006.
- [80] M. A. Dakka, A. Bulinski, and S. Bamji, “Correlation between DC Polarization and failure characteristics of XLPE and EPR aged with ac voltage in a wet environment,” *IEEE Trans. Dielectr. Electr. Insul.*, vol. 12, no. 4, pp. 700–708, 2005.
- [81] J. C. Hernandez-mejia, R. Harley, N. Hampton, and R. Hartlein, “Characterisation of ageing for MV power cables using low frequency Tan $\delta$  diagnostic measurements,” *IEEE Trans. Dielectr. Electr. Insul.*, vol. 16, no. 3, pp. 862–870, 2009.
- [82] S. Hvidsten and E. Ildstad, “Criteria for diagnostic evaluation of water treed XLPE cables,” *7th International Conference on Solid Dielectrics*, 2001, pp. 385–389.
- [83] S. Morsalin and B. T. Phung, “Comparative phase-resolved analysis of AC corona discharges at very low (0.1 Hz) and power frequencies,” *International Conference on High Voltage Engineering and Power System (ICHVEPS)*, 2017, pp. 1–5.
- [84] H. T. Putter, D. Gotz, F. Petzold, and H. Oetjen, “The evolution of VLF testing technologies over the past two decades,” *IEEE Power Engineering. Society Conference on Transmission and Distribution*, pp. 5–8, 2012.
- [85] Z. Hou, H. Li, S. Chen, B. Li, Y. Lu, and S. Ji, “Development of a novel 20 kV 0.1 Hz



- 
- 
- very low frequency cosine-rectangular voltage generator for multi-functional insulation testing of MV power cables,” *IET Gener. Transm. Distrib.*, vol. 12, no. 1, pp. 1–8, 2017.
- [86] A. J. Dekker, *Electrical engineering materials*, Prentice Hall, 1959.
- [87] J.-S. Chang, A. J. Kelly, and J. M. Crowley, *Handbook of electrostatic processes*. CRC Press, 1995.
- [88] D. Mishra, A. Baral, and S. Chakravorti, “Compensating the effect of residual dipole energy on dielectric response for effective diagnosis of power transformer insulation,” *IET Sci. Meas. Technol.*, vol. 12, no. 3, pp. 314–322, 2018.
- [89] H. C. Verma, A. Baral, A. K. Pradhan, and S. Chakravorti, “Condition assessment of various regions within non-uniformly aged cellulosic insulation of power transformer using modified Debye model,” *IET Sci. Meas. Technol.*, vol. 11, no. 7, pp. 939–947, 2017.
- [90] C. J. F. Böttcher, O. C. van Belle, P. Bordewijk, and A. Rip, *Theory of electric polarization*, Elsevier Science Ltd, vol. 2, 1978.
- [91] H. Fröhlich, *Theory of dielectrics*, Springer, 1949.
- [92] I. Bunget and M. Popescu, *Physics of solid dielectrics*, Elsevier Science Ltd, vol. 19, 1984.
- [93] K. S. Cole and R. H. Cole, “Dispersion and absorption in dielectrics I. Alternating current characteristics,” *J. Chem. Phys.*, vol. 9, no. 4, pp. 341–351, 1941.
- [94] S. Ochiai, M. Ito, T. Mizutani, and M. Ieda, “Interface traps and swelling of polypropylene films immersed in silicone oils,” *IEEE Trans. Electr. Insul.*, no. 3, pp. 575–580, 1985.
- [95] G. M. Tsangaris, G. C. Psarras, and N. Kouloumbi, “Electric modulus and interfacial polarization in composite polymeric systems,” *J. Mater. Sci.*, vol. 33, no. 8, pp. 2027–2037, 1998.
- [96] D. Vanderbilt and R. D. King-Smith, “Electric polarization as a bulk quantity and its relation to surface charge,” *Phys. Rev. B*, vol. 48, no. 7, p. 4442, 1993.
- [97] G. Williams, “Molecular aspects of multiple dielectric relaxation processes in solid polymers,” in *Electric Phenomena in Polymer Science*, Springer, 1979, pp. 59–92.
- [98] F. Bruni, G. Consolini, and G. Careri, “Temperature dependence of dielectric relaxation in H<sub>2</sub>O and D<sub>2</sub>O ice. A dissipative quantum tunneling approach,” *J. Chem. Phys.*, vol. 99, no. 1, pp. 538–547, 1993.
- [99] N. R. Tu and K. C. Kao, “High-field electrical conduction in polyimide films,” *J. Appl. Phys.*, vol. 85, no. 10, pp. 7267–7275, 1999.
- [100] S. Wróbel *et al.*, “Dielectric relaxation spectroscopy,” Springer *Relaxation Phenomena*, 2003, pp. 13–88.
- [101] E. Neagu, P. Pissis, L. Apekis, and J. L. G. Ribelles, “Dielectric relaxation spectroscopy of polyethylene terephthalate (PET) films,” *J. Phys. D: Appl. Phys.*, vol. 30, no. 11, p. 1551, 1997.
- [102] J. R. Macdonald and E. Barsoukov, “Impedance spectroscopy: theory, experiment, and applications,” *History of Electrostatics*, vol. 1, no. 8, 2005.
- [103] M. Jaya, T. Leibfried, and M. Koch, “Information within the dielectric response of power transformers for wide frequency ranges,” *IEEE International Symposium on Electrical Insulation (ISEI)*, 2010, pp. 1–5.
- [104] D. Linhjell, L. Lundgaard, and U. Gafvert, “Dielectric response of mineral oil
-

- 
- 
- impregnated cellulose and the impact of aging,” *IEEE Trans. Dielectr. Electr. Insul.*, vol. 14, no. 1, 2007.
- [105] *Non-destructive water-tree detection in XLPE cable insulation*, CIGRE Brochure 493, April 2012.
- [106] J. P. Van Bolhuis, E. Gulski, and J. J. Smit, “Monitoring and diagnostic of transformer solid insulation,” *IEEE Trans. Power Deliv.*, vol. 17, no. 2, pp. 528–536, 2002.
- [107] D. Wajcer, N. Sommer, and N. Semel, “Apparatus for and method of cable diagnostics utilizing time domain reflectometry,” Google Patents, 17-Jul-2007.
- [108] R. Nikjoo, N. Taylor, and H. Edin, “Dielectric response measurement by impulse stimulus on AC: Measurement considerations, and laboratory testing on a bushing,” *IEEE Trans. Dielectr. Electr. Insul.*, vol. 24, no. 1, pp. 511–518, 2017.
- [109] A. Pradhan, C. Koley, B. Chatterjee, and S. Chakravorti, “Non-linear Modelling of oil-paper insulation for condition assessment using non-sinusoidal excitation,” *IEEE Trans. Dielectr. Electr. Insul.*, vol. 22, no. 4, pp. 2165–2175, 2015.
- [110] S. Sarkar, T. Sharma, A. Baral, B. Chatterjee, D. Dey, and S. Chakravorti, “An expert system approach for transformer insulation diagnosis combining conventional diagnostic tests and PDC, RVM data,” *IEEE Trans. Dielectr. Electr. Insul.*, vol. 21, no. 2, pp. 882–891, 2014.
- [111] C. Hill, T. R. Watts, and G. A. Burr, “Portable schering bridge for field tests,” *Electr. Eng.*, vol. 53, no. 4, pp. 618–622, 1934.
- [112] S. C. Bera and S. Chattopadhyay, “A modified Schering bridge for measurement of the dielectric parameters of a material and the capacitance of a capacitive transducer,” *Measurement*, vol. 33, no. 1, pp. 3–7, 2003.
- [113] R. L. Nelson, “Bridge measurement of very low dielectric loss at low temperatures,” *Electr. Eng. Proc. Inst.*, vol. 121, no. 7, pp. 764–770, 1974.
- [114] A. Cichy, “Non-bridge circuit with double quasi-balancing for measurement of dielectric loss factor,” *IET Sci. Meas. Technol.*, vol. 7, no. 5, pp. 274–279, 2013.
- [115] C. Y. Qiang, “The study on the problem of measuring dielectric loss for large capacitance electric apparatus with Schering bridge and shunt,” *3rd International Conference on Properties and Applications of Dielectric Materials (ICPADM)*, 1991, pp. 1196–1199.
- [116] Peter Werelius, “Development and application of high voltage dielectric spectroscopy for diagnosis of medium voltage XLPE cables,” *PhD dissertation*, Dept. of Electr. Eng., Royal Institute of Technology (KTH) Stockholm, Sweden 2001.
- [117] G. Zhu and J. Wang, “Measurement of  $\tan\delta$  of single-phase electrical apparatus with capacitive insulation under operating voltage,” *2<sup>nd</sup> International Conference on Properties and Applications of Dielectric Materials (ICPADM)*, 1988, pp. 701–703.
- [118] E. Wasilenko and M. Olesz, “On-site loss tangent measurements of high voltage insulation,” *6<sup>th</sup> International Conference on Dielectric Materials, Measurements and Applications*, 1992, pp. 170–173.
- [119] R. Calvert, “The transformer ratio-arm bridge,” *Wayne Kerr Monogram*, vol. 1, pp. 7–8, 1968.
- [120] N. L. Kusters and O. Petersons, “A transformer-ratio-arm bridge for high-voltage capacitance measurements,” *Trans. Am. Inst. Electr. Eng. Part I Commun. Electron.*, vol. 82, no. 5, pp. 606–611, 1963.
- [121] H. A. M. Clark and P. B. Vanderlyn, “Double-ratio ac bridges with inductively-coupled

- 
- ratio arms,” *Radio Commun. Eng.*, vol. 96, no. 41, pp. 189–202, 1949.
- [122] O. Petersons, “A transformer-ratio-arm bridge for measuring large capacitors above 100 volts,” *IEEE Trans. Power Appar. Syst.*, no. 5, pp. 1354–1361, 1968.
- [123] W. H. P. Leslie, “Choosing transformer ratio-arm bridges,” *Electron. Commun. Eng.*, vol. 108, no. 41, pp. 539–545, 1961.
- [124] P. Wang, M. R. Raghuveer, W. McDermid, and J. C. Bromley, “A digital technique for the on-line measurement of dissipation factor and capacitance,” *IEEE Trans. Dielectr. Electr. Insul.*, vol. 8, no. 2, pp. 228–232, 2001.
- [125] S. Morsalin and B. T. Phung, “Modeling of dielectric dissipation factor measurement for XLPE cable based on Davidson-Cole model,” *IEEE Trans. Dielectr. Electr. Insul.*, vol. 26, no. 3, pp. 1018–1026, June 2019.
- [126] A. K. Jonscher, “Dielectric relaxation in solids,” *J. Phys. D. Appl. Phys.*, vol. 32, no. 14, p. R57, 1999.
- [127] J. G. Kirkwood, “On the theory of dielectric polarization,” *J. Chem. Phys.*, vol. 4, no. 9, pp. 592–601, 1936.
- [128] P. Q. Mantas, “Dielectric response of materials: extension to the Debye model,” *J. Eur. Ceram. Soc.*, vol. 19, no. 12, pp. 2079–2086, 1999.
- [129] S. Morsalin and B. T. Phung, “Modelling of dielectric dissipation factor measurement from very low to power frequency,” *2nd International Conference on Dielectrics (ICD)*, 2018, pp. 1–4.
- [130] H. G. David, S. D. Hamann, and J. F. Pearse, “The dielectric constant of ethylene at high pressures,” *J. Chem. Phys.*, vol. 19, no. 12, pp. 1491–1495, 1951.
- [131] M. Zahn, Y. Ohki, D. B. Fenneman, R. J. Gripshover, and V. H. Gehman, “Dielectric properties of water and water/ethylene glycol mixtures for use in pulsed power system design,” *Proc. IEEE*, vol. 74, no. 9, pp. 1182–1221, 1986.
- [132] M. Davies, N. Hill, W. E. Vaughan, and A. H. Price, *Dielectric properties and molecular behaviour*, Macgraw-Hill, 1969.
- [133] “Cable testing and diagnostics.” [Online]. Available: <https://www.baur.eu/products/cable-testing-and-diagnostics/vlf-testing-and-diagnostic>. [Accessed: 22-Apr-2018].
- [134] “Tan Delta.” [Online]. Available: <http://power.sebakmt.com/bg/products/power-networks/diagnosis/dielectric-diagnosis/tan-delta.html>. [Accessed: 26-Apr-2018].
- [135] “VAX/230/214 High Voltage Amplifier.” [Online]. Available: [http://www.intyler-fimaco.com/VAX-230-214\\_DS\\_en\\_V01.pdf](http://www.intyler-fimaco.com/VAX-230-214_DS_en_V01.pdf). [Accessed: 26-Apr-2018].
- [136] “Tettex Products.” [Online]. Available: [http://www.maceysselectrical.com.au/tettex\\_product\\_index.htm](http://www.maceysselectrical.com.au/tettex_product_index.htm). [Accessed: 26-Apr-2018].
- [137] “Tan Delta Cable Diagnostics.” [Online]. Available: <https://hvdiagnostics.com/products/td>. [Accessed: 26-Apr-2018].
- [138] “Dirana.” [Online]. Available: <https://www.omicronenergy.com/en/products/dirana/>. [Accessed: 26-Apr-2018].
- [139] “Dissipation/power factor measurement.” [Online]. Available: <https://www.omicronenergy.com/en/applications/power-transformer-testing/diagnosis-dissipationpower-factor-measurement-tan-delta-on-power-transformers/>. [Accessed: 26-Apr-2018].
- [140] K. Wu, T. Okamoto, and Y. Suzuoki, “Effects of discharge area and surface conductivity on partial discharge behavior in voids under square voltages,” *IEEE Trans. Dielectr. Electr. Insul.*, vol. 14, no. 2, pp. 461–470, 2007.
-



- 
- 
- [141] X. Wang, N. Taylor, and H. Edin, "Enhanced distinction of surface and cavity discharges by trapezoid-based arbitrary voltage waveforms," *IEEE Trans. Dielectr. Electr. Insul.*, vol. 23, no. 1, pp. 435–443, 2016.
- [142] A. N. Esfahani, S. Shahabi, G. Stone, and B. Kordi, "Investigation of corona partial discharge characteristics under variable frequency and air pressure," *IEEE Electrical Insulation Conference (EIC)*, 2018, pp. 31–34.
- [143] L. Niemeyer, "A generalised approach to partial discharge modelling," *IEEE Trans. Dielectr. Electr. Insul.*, vol. 2, no. 4, pp. 510–528, 1995.
- [144] S. A. Boggs, "Partial discharge. III. Cavity-induced PD in solid dielectrics," *IEEE Electr. Insul. Mag.*, vol. 6, no. 6, pp. 11–16, 1990.
- [145] I. W. McAllister, "Electric field theory and the fallacy of void capacitance," *IEEE Trans. Electr. Insul.*, vol. 26, no. 3, pp. 458–459, 1991.
- [146] D. P. Agoris and N. D. Hatzargyriou, "Approach to partial discharge development in closely coupled cavities embedded in solid dielectrics by the lumped capacitance model," *IET Sci. Meas. Technol.*, vol. 140, no. 2, pp. 131–134, 1993.
- [147] A. Alsheikhly, H. Guzman, and H.-. Kranz, "A new diagnostic tool through computer simulation calculation using expanded partial discharge equivalent circuit," *4th International Conference on Conduction and Breakdown in Solid Dielectrics*, 1992, pp. 176–180.
- [148] E. Lemke, "A critical review of partial-discharge models," *IEEE Electr. Insul. Mag.*, vol. 28, no. 6, pp. 11–16, 2012.
- [149] E. Gulski and F. H. Kreuger, "Computer-aided recognition of discharge sources," *IEEE Trans. Electr. Insul.*, vol. 27, no. 1, pp. 82–92, 1992.
- [150] Z. Achillides, G. E. Georgiou, and E. Kyriakides, "Partial discharges and associated transients: the induced charge concept versus capacitive Modelling," *IEEE Trans. Dielectr. Electr. Insul.*, vol. 15, no. 6, pp. 1507–1516, 2008.
- [151] A. Pedersen, G. C. Crichton, and I. W. McAllister, "The theory and measurement of partial discharge transients," *IEEE Trans. Electr. Insul.*, vol. 26, no. 3, pp. 487–497, 1991.
- [152] M. G. Danikas, I. W. McAllister, G. C. Crichton, and A. Pedersen, "Discussion: partial discharges in ellipsoidal and spheroidal voids," *IEEE Trans. Electr. Insul.*, vol. 26, no. 3, pp. 537–539, 1991.
- [153] A. Pedersen, G. C. Crichton, and I. W. McAllister, "The functional relation between partial discharges and induced charge," *IEEE Trans. Dielectr. Electr. Insul.*, vol. 2, no. 4, pp. 535–543, 1995.
- [154] G. C. Crichton, P. W. Karlsson, and A. Pedersen, "Partial discharges in ellipsoidal and spheroidal voids," *IEEE Trans. Electr. Insul.*, vol. 24, no. 2, pp. 335–342, 1989.
- [155] Z. Achillides, M. G. Danikas, and E. Kyriakides, "Partial discharge modelling and induced charge concept: Comments and criticism of pedersen's model and associated measured transients," *IEEE Trans. Dielectr. Electr. Insul.*, vol. 24, no. 2, pp. 1118–1122, 2017.
- [156] F. Gutfleisch and L. Niemeyer, "Measurement and simulation of PD in epoxy voids," *IEEE Trans. Dielectr. Electr. Insul.*, vol. 2, no. 5, pp. 729–743, 1995.
- [157] R. Schifani, R. Candela, and P. Romano, "On PD mechanisms at high temperature in voids included in an epoxy resin," *IEEE Trans. Dielectr. Electr. Insul.*, vol. 8, no. 4, pp. 589–597, 2001.
- 
-

- 
- 
- [158] I. W. McAllister, "Partial discharges in spheroidal voids: Void orientation," *IEEE Trans. Dielectr. Electr. Insul.*, vol. 4, no. 4, pp. 456–461, 1997.
  - [159] C. Forssen and H. Edin, "Modelling partial discharges in a cavity at different applied frequencies," *International Conference on Electrical Insulation and Dielectric Phenomena*, 2007, pp. 132–135.
  - [160] H. A. Illias, G. Chen, and P. L. Lewin, "Partial discharge measurements for spherical cavities within solid dielectric materials under different stress and cavity conditions," *IEEE Conference on Electrical Insulation and Dielectric Phenomena*, 2009, pp. 388–391.
  - [161] H. A. Illias, G. Chen, and P. L. Lewin, "Comparison of partial discharge measurement and simulation results for spherical cavities within solid dielectric materials as a function of frequency using Finite Element Analysis method," *IEEE International Symposium on Electrical Insulation*, 2010, pp. 1–5.
  - [162] H. A. Illias *et al.*, "Modelling of partial discharge pulses in high voltage cable insulation using finite element analysis software," *IEEE Electrical Insulation Conference (EIC)*, 2013, pp. 52–56.
  - [163] H. A. Illias, G. Chen, and P. L. Lewin, "Modelling of cycle to cycle behaviour for partial discharge events within a spherical cavity in a solid dielectric material by using Finite Element Analysis," *10th IEEE International Conference on Solid Dielectrics*, 2010, pp. 1–4.
  - [164] H. A. Illias, G. Chen, and P. L. Lewin, "Modelling of temporal temperature and pressure change due to partial discharge events within a spherical cavity in a solid dielectric material using finite element analysis," *International Conference on High Voltage Engineering and Application*, 2010, pp. 501–504.
  - [165] H. A. Illias, M. A. Tunio, H. Mokhlis, G. Chen, and A. H. A. Bakar, "Experiment and Modelling of void discharges within dielectric insulation material under impulse voltage," *IEEE Trans. Dielectr. Electr. Insul.*, vol. 22, no. 4, pp. 2252–2260, 2015.
  - [166] H. Illias, G. Chen, and P. L. Lewin, "Modelling of partial discharge activity in spherical cavities within a dielectric material," *IEEE Electr. Insul. Mag.*, vol. 27, no. 1, pp. 38–45, 2011.
  - [167] H. A. Illias, M. A. Tunio, A. H. A. Bakar, H. Mokhlis, and G. Chen, "Partial discharge phenomena within an artificial void in cable insulation geometry: experimental validation and simulation," *IEEE Trans. Dielectr. Electr. Insul.*, vol. 23, no. 1, pp. 451–459, 2016.
  - [168] S. Z. Dabbak, H. A. Illias, and B. C. Ang, "Effect of surface discharges on different polymer dielectric materials under high field stress," *IEEE Trans. Dielectr. Electr. Insul.*, vol. 24, no. 6, pp. 3758–3765, 2017.
  - [169] J. Kindersberger and C. Lederle, "Surface charge decay on insulators in air and sulfurhexafluorid - part I: simulation," *IEEE Trans. Dielectr. Electr. Insul.*, vol. 15, no. 4, pp. 941–948, 2008.
  - [170] P. Dordizadeh, K. Adamiak, and G. S. P. Castle, "Numerical investigation of the formation of Trichel pulses in a needle-plane geometry," *J. Phys. D. Appl. Phys.*, vol. 48, no. 41, p. 415203, 2015.
  - [171] C. Lazarou, T. Belmonte, A. S. Chipper, and G. E. Georghiou, "Numerical modelling of the effect of dry air traces in a helium parallel plate dielectric barrier discharge," *Plasma Sources Sci. Technol.*, vol. 25, no. 5, p. 55023, 2016.
  - [172] Y. V. Serdyuk and S. M. Gubanski, "Computer modelling of interaction of gas discharge
-

- 
- 
- plasma with solid dielectric barriers,” *IEEE Trans. Dielectr. Electr. Insul.*, vol. 12, no. 4, pp. 725–735, 2005.
- [173] L. Testa, S. Serra, and G. C. Montanari, “Advanced modelling of electron avalanche process in polymeric dielectric voids: Simulations and experimental validation,” *J. Appl. Phys.*, vol. 108, no. 3, p. 34110, 2010.
  - [174] D. Braun, V. Gibalov, and G. Pietsch, “Two-dimensional modelling of the dielectric barrier discharge in air,” *Plasma Sources Sci. Technol.*, vol. 1, no. 3, p. 166, 1992.
  - [175] M. Mondal and G. B. Kumbhar, “Detection, measurement, and classification of partial discharge in a power transformer: Methods, trends, and future research,” *IETE Tech. Rev.*, vol. 35, no. 5, pp. 483–493, 2018.
  - [176] M. Hikita, S. Okabe, H. Murase, and H. Okubo, “Cross-equipment evaluation of partial discharge measurement and diagnosis techniques in electric power apparatus for transmission and distribution,” *IEEE Trans. Dielectr. Electr. Insul.*, vol. 15, no. 2, pp. 505–518, 2008.
  - [177] R. J. Van Brunt and E. W. Cernyar, “Stochastic analysis of AC-generated partial-discharge pulses from a Monte-Carlo simulation,” *International Conference on Electrical Insulation and Dielectric Phenomena*, 1992, pp. 427–434.
  - [178] R. Bartnikas, “Partial discharges. Their mechanism, detection and measurement,” *IEEE Trans. Dielectr. Electr. Insul.*, vol. 9, no. 5, pp. 763–808, 2002.
  - [179] Y. Nyanteh, L. Graber, C. Edrington, S. Srivastava, and D. Cartes, “Overview of simulation models for partial discharge and electrical treeing to determine feasibility for estimation of remaining life of machine insulation systems,” *Electrical Insulation Conference (EIC)*, 2011, pp. 327–332.
  - [180] G. C. Stone, H. G. Sedding, N. Fujimoto, and J. M. Braun, “Practical implementation of ultrawideband partial discharge detectors,” *IEEE Trans. Electr. Insul.*, vol. 27, no. 1, pp. 70–81, 1992.
  - [181] G. H. Vaillancourt, R. Malewski, and D. Train, “Comparison of three techniques of partial discharge measurements in power transformers,” *IEEE Power Eng. Rev.*, vol. PER-5, no. 4, pp. 46–47, 1985.
  - [182] L. E. Lundgaard, “Partial discharge: Acoustic partial discharge detection-practical application,” *IEEE Electr. Insul. Mag.*, vol. 8, no. 5, pp. 34–43, 1992.
  - [183] J. Rubio-Serrano, J. Posada, I. Bua, and J. A. García-Souto, “Comparison of processing techniques for optimizing the diagnosis of solid insulation based on acoustic emissions from partial discharges,” *IEEE International Conference on Solid Dielectrics (ICSD)*, 2013, pp. 129–132.
  - [184] L. E. Lundgaard, “Partial discharge XIII: Acoustic partial discharge detection-fundamental considerations,” *IEEE Electr. Insul. Mag.*, vol. 8, no. 4, pp. 25–31, 1992.
  - [185] T. Boczar, “Identification of a specific type of PD from acoustic emission frequency spectra,” *IEEE Trans. Dielectr. Electr. Insul.*, vol. 8, no. 4, pp. 598–606, 2001.
  - [186] S. Coenen, S. Tenbohlen, S. M. Markalous, and T. Strehl, “Sensitivity of UHF PD measurements in power transformers,” *IEEE Trans. Dielectr. Electr. Insul.*, vol. 15, no. 6, pp. 1553–1558, 2008.
  - [187] S. Meijer, P. D. Agoris, P. P. Seitz, and T. J. W. H. Hermans, “Condition assessment of power cable accessories using advanced VHF/UHF PD detection,” *IEEE International Symposium on Electrical Insulation*, 2006, pp. 482–485.
  - [188] M. D. Judd, O. Farish, and B. F. Hampton, “The excitation of UHF signals by partial
-

- 
- 
- discharges in GIS,” *IEEE Trans. Dielectr. Electr. Insul.*, vol. 3, no. 2, pp. 213–228, 1996.
- [189] J. Li, T. Jiang, C. Cheng, and C. Wang, “Hilbert fractal antenna for UHF detection of partial discharges in transformers,” *IEEE Trans. Dielectr. Electr. Insul.*, vol. 20, no. 6, pp. 2017–2025, 2013.
- [190] R. Schwarz and M. Muhr, “Modern technologies in optical partial discharge detection,” *International Conference on Electrical Insulation and Dielectric Phenomena*, 2007, pp. 163–166.
- [191] Y. Ming and S. Birlasekaran, “Characterisation of partial discharge signals using wavelet and statistical techniques,” *IEEE International Symposium on Electrical Insulation*, 2002, pp. 9–13.
- [192] L. Hao and P. L. Lewin, “Partial discharge source discrimination using a support vector machine,” *IEEE Trans. Dielectr. Electr. Insul.*, vol. 17, no. 1, pp. 189–197, 2010.
- [193] A. R. Mor, L. C. C. Heredia, and F. A. Muñoz, “New clustering techniques based on current peak value, charge and energy calculations for separation of partial discharge sources,” *IEEE Trans. Dielectr. Electr. Insul.*, vol. 24, no. 1, pp. 340–348, 2017.
- [194] A. Cavallini, G. C. Montanari, F. Puletti, and A. Contin, “A new methodology for the identification of PD in electrical apparatus: properties and applications,” *IEEE Trans. Dielectr. Electr. Insul.*, vol. 12, no. 2, pp. 203–215, 2005.
- [195] L. Niemeyer, L. Pietronero, and H. J. Wiesmann, “Fractal dimension of dielectric breakdown,” *Phys. Rev. Lett.*, vol. 52, no. 12, p. 1033, 1984.
- [196] Y. Lim, J. Lee, W. Kang, and J. Koo, “Chaotic analysis of partial discharge (CAPD) as a novel approach to investigate insulation degradation caused by the various defects,” *IEEE International Symposium on Industrial Electronics*, 2001, vol. 1, pp. 413–416.
- [197] H. Ma, J. C. Chan, T. K. Saha, and C. Ekanayake, “Pattern recognition techniques and their applications for automatic classification of artificial partial discharge sources,” *IEEE Trans. Dielectr. Electr. Insul.*, vol. 20, no. 2, pp. 468–478, 2013.
- [198] S. B. Sert and Ö. Kalenderli, “Determination of source voltage from audible corona noise by neural networks,” *IEEE Trans. Dielectr. Electr. Insul.*, vol. 16, no. 1, pp. 224–231, 2009.
- [199] R. Aldrian, G. C. Montanari, A. Cavallini, and Suwarno, “Statistical analysis for internal and surface discharges identification in XLPE insulation under AC voltages,” *International Conference on High Voltage Engineering and Power Systems (ICHVEPS)*, 2017, pp. 188–192.
- [200] H. A. Illias, G. Chen, and P. L. Lewin, “Partial discharge behaviour within two spherical cavities in a dielectric material,” *International Conference on Electrical Insulation and Dielectric Phenomena*, 2011, pp. 456–459.
- [201] E. M. El-Refaie, M. Besheir, M. K. A. Elrahman, and R. Saad, “Partial Discharge measurement for medium voltage cables using different voltage wave forms,” *International Symposium on Electrical Insulating Materials*, 2014, pp. 315–318.
- [202] C. H. Zhang and J. M. K. MacAlpine, “A phase-related investigation of AC corona in air,” *IEEE Trans. Dielectr. Electr. Insul.*, vol. 10, no. 2, pp. 312–319, 2003.
- [203] H. Illias, T. S. Yuan, A. H. A. Bakar, H. Mokhlis, G. Chen, and P. L. Lewin, “Partial discharge patterns in high voltage insulation,” *IEEE International Conference on Power and Energy (PECon)*, 2012, pp. 750–755.
- [204] A. Contin and S. Pastore, “Classification and separation of partial discharge signals by

- 
- 
- means of their auto-correlation function evaluation,” *IEEE Trans. Dielectr. Electr. Insul.*, vol. 16, no. 6, pp. 1609–1622, 2009.
- [205] A. Contin, A. Cavallini, G. C. Montanari, G. Pasini, and F. Puletti, “Digital detection and fuzzy classification of partial discharge signals,” *IEEE Trans. Dielectr. Electr. Insul.*, vol. 9, no. 3, pp. 335–348, 2002.
- [206] Z. Lv, S. M. Rowland, S. Chen, H. Zheng, and K. Wu, “Modelling of partial discharge characteristics in electrical tree channels: Estimating the PD inception and extinction voltages,” *IEEE Trans. Dielectr. Electr. Insul.*, vol. 25, no. 5, pp. 1999–2010, 2018.
- [207] S. Morsalin, B. T. Phung, and M. G. Danikas, “Influence of partial discharge on dissipation factor measurement at very low frequency,” *International Conference on Condition Monitoring and Diagnosis (CMD)*, 2018, pp. 1–5.
- [208] A. Cavallini, V. Krotov, G. C. Montanari, P. H. F. Morshuis, and L. E. Mariut, “The role of supply frequency in the evaluation of partial discharge inception voltage in XLPE-embedded cavities,” *International Conference on Electrical Insulation and Dielectric Phenomena*, 2012, pp. 487–490.
- [209] R. Miller and I. A. Black, “Partial discharge measurements over the frequency range 0.1 Hz to 50 Hz,” *IEEE Trans. Electr. Insul.*, vol. EI-12, no. 3, pp. 224–233, 1977.
- [210] P. Molinie, “Measuring and modelling transient insulator response to charging: the contribution of surface potential studies,” *IEEE Trans. Dielectr. Electr. Insul.*, vol. 12, no. 5, pp. 939–950, 2005.
- [211] A. Cavallini, F. Ciani, G. Mazzanti, and G. C. Montanari, “First electron availability and partial discharge generation in insulation cavities: effect of light irradiation,” *IEEE Trans. Dielectr. Electr. Insul.*, vol. 12, no. 2, pp. 387–394, 2005.
- [212] S. Morsalin and B. T. Phung, “Corona discharge under non-sinusoidal voltage excitation at very low frequency,” *12th International Conference on the Properties and Applications of Dielectric Materials (ICPADM)*, 2018, pp. 653–656.
- [213] C. Hudon, R. Bartnikas, and M. R. Wertheimer, “Surface conductivity of epoxy specimens subjected to partial discharges,” *IEEE International Symposium on Electrical Insulation*, 1990, pp. 153–155.
- [214] M. Seeger, M. Bujotzek, and L. Niemeyer, “Formative time lag and breakdown in SF<sub>6</sub> at small protrusions,” *17th International Conference on Gas Discharges and Their Applications*, 2008, pp. 317–320.
- [215] P. Mraz, P. Treyer, and U. Hammer, “Evaluation and limitations of corona discharge measurements – An application point of view,” *International Conference on Condition Monitoring and Diagnosis*, pp. 273–276, 2016.
- [216] C. Nyamupangedengu and I. R. Jandrell, “Partial discharge spectral response to variations in the supply voltage frequency,” *IEEE Trans. Dielectr. Electr. Insul.*, vol. 19, no. 2, pp. 521–532, 2012.
- [217] “MPD 600.” [Online]. Available: <https://www.omicronenergy.com/en/products/mpd-600/>. [Accessed: 02-May-2019].
- [218] “Partial Discharge.” [Online]. Available: <https://hvdiagnostics.com/products/pd>. [Accessed: 02-May-2019].
- [219] “Portable PD diagnostics system.” [Online]. Available: <https://www.baur.eu/en/products/cable-testing-and-diagnostics/portable-partial-discharge-diagnostics/pd-tad-62>. [Accessed: 02-May-2019].
- [220] “PDS 62-SIN.” [Online]. Available: <https://megger.com/portable-pd-detection-and->
-



- 
- 
- localisation-system-pds-62-sin-15. [Accessed: 02-May-2019].
- [221] “PD30-E measurement of partial discharges.” [Online]. Available: <https://www.b2hv.com/PD30-E-measurement-of-partial-discharges.html>. [Accessed: 02-May-2019].
  - [222] “ICMsystem.” [Online]. Available: <https://www.pdix.com/products/partial-discharge-measurement-devices/icmsystem.html>. [Accessed: 02-May-2019].
  - [223] J. C. Hernandez-Mejia, R. Harley, N. Hampton, and R. Hartlein, “Characterisation of ageing for MV power cables using low frequency  $\tan \delta$  diagnostic measurements,” *IEEE Trans. Dielectr. Electr. Insul.*, vol. 16, no. 3, 2009.
  - [224] K. Sung-min *et al.*, “The estimation of insulation on MV cables using the VLF  $\tan \delta$  diagnostic measurement,” *IEEE International Conference on Condition Monitoring and Diagnosis*, 2012, pp. 1191–1196.
  - [225] S. Morsalin, T. B. Phung, M. Danikas, and D. Mawad, “Diagnostic challenges in dielectric loss assessment and interpretation: a review,” *IET Sci. Meas. Technol.*, vol. 13, pp. 120–137, 2019.
  - [226] T. K. Saha, “Review of time-domain polarization measurements for assessing insulation condition in aged transformers,” *IEEE Trans. Power Deliv.*, vol. 18, no. 4, pp. 1293–1301, 2003.
  - [227] Y. Liu, Y. Su, L. Wang, and Y. Xiao, “Ageing condition assessment of DC cable XLPE insulation by  $\tan \delta$  measurement at 0.1 Hz voltage,” *IEEE International Conference on Dielectrics (ICD)*, 2016, vol. 2, pp. 776–779.
  - [228] R. Neimanis and R. Eriksson, “Diagnosis of moisture in oil/paper distribution cables-Part I: Estimation of moisture content using frequency-domain spectroscopy,” *IEEE Trans. power Deliv.*, vol. 19, no. 1, pp. 9–14, 2004.
  - [229] K. Thungsook, P. Nimsanong, N. Marukatut, and N. Pattanadech, “Polarization and depolarization current measurement of underground cable with different cable lengths, temperatures and test voltages,” in *2018 Condition Monitoring and Diagnosis (CMD)*, 2018, pp. 1–4.
  - [230] S. Chatterjee, S. Dalai, S. Chakravorti, and B. Chatterjee, “Use of chirp excitations for frequency domain spectroscopy measurement of oil-paper insulation,” *IEEE Trans. Dielectr. Electr. Insul.*, vol. 25, no. 3, pp. 1103–1111, 2018.
  - [231] A. P. De Boer and A. J. Pennings, “Polyethylene networks crosslinked in solution: Preparation, elastic behavior, and oriented crystallization. I. Crosslinking in solution,” *J. Polym. Sci. Polym. Phys. Ed.*, vol. 14, no. 2, pp. 187–210, 1976.
  - [232] S. Morsalin, B. T. Phung, “Dielectric response measurement of service-aged XLPE cable from very low to power frequency range,” *IEEE Electr. Insul. Mag.*, Nov., 2019.[In Press]
  - [233] T. Liu *et al.*, “Dielectric spectroscopy study of thermally-aged extruded model power cables,” *10th IEEE International Conference on Solid Dielectrics*, 2010, pp. 1–4.
  - [234] J. H. Calderwood, “A physical hypothesis for Cole-Davidson behavior,” *IEEE Trans. Dielectr. Electr. Insul.*, vol. 10, no. 6, pp. 1006–1011, 2003.
  - [235] J. Crine, “Rate Theory and Polyethylene Relaxations,” *IEEE Trans. Electr. Insul.*, vol. 22, no. 2, pp. 169–174, 1987.
  - [236] R. H. Boyd, “Relaxation processes in crystalline polymers: molecular interpretation—a review,” *Polymer*, vol. 26, no. 8, pp. 1123–1133, 1985.
  - [237] B. Oyegoke, P. Hyvonen, M. Aro, and N. Gao, “Application of dielectric response
-

- 
- measurement on power cable systems,” *IEEE Trans. Dielectr. Electr. Insul.*, vol. 10, no. 5, pp. 862–873, 2003.
- [238] B. Jonuz, P. H. F. Morshuis, H. J. Van Breen, J. Pellis, and J. J. Smit, “Detection of water trees in medium voltage XLPE cables by return voltage measurements,” *International Conference on Electrical Insulation and Dielectric Phenomena*, 2000, vol. 1, pp. 355–358 vol.1.
- [239] T. K. Saha and Z. T. Yao, “Experience with return voltage measurements for assessing insulation conditions in service aged transformers,” *IEEE Power Engineering Society General Meeting*, 2003, vol. 4, pp. 23-70.
- [240] H. R. M. Dissado L. A, “A cluster approach to the structure of imperfect materials and their relaxation spectroscopy,” *A. Math. Phys. Sci.*, vol. 390, no. 1798, pp. 131 LP – 180, Nov. 1983.
- [241] S. Morsalin and B. T. Phung, "Dielectric response study of service-aged XLPE cable based on polarisation and depolarisation current method," *IEEE Trans. Dielectr. Electr. Insul.*, vol. 27, no. 1, pp. 58-66, Feb. 2020.
- [242] R. D’Agostino, *Goodness-of-fit-techniques*. Routledge, 2017.
- [243] N. Bashir and H. Ahmad, “Diagnosis of XLPE cable using the recovery voltage measurement method,” *5th Student Conference on Research and Development*, 2007, pp. 1–4.
- [244] B. Alijagic-Jonuz, P. H. F. Morshuis, H. J. van Breen, and J. J. Smit, “Detection of water trees in medium voltage cables by RVM, without reference measurements,” *IEEE 7th International Conference on Solid Dielectrics*, 2001, pp. 504–507.
- [245] P. R. S. Jota, S. M. Islam, and F. G. Jota, “Modelling the polarization spectrum in composite oil/paper insulation systems,” *IEEE Trans. Dielectr. Electr. Insul.*, vol. 6, no. 2, pp. 145–151, 1999.
- [246] J. P. van Bolhuis, E. Gulski, J. J. Smit, G. M. Urbani, and H. F. A. Verhaart, “Development of knowledge rules for RVM for interpretation of the condition of transformer insulation,” *IEEE International Symposium on Electrical Insulation*, 2000, pp. 267–270.
- [247] S. Morsalin, B. T. Phung, “Recovery voltage response of XLPE cables based on polarisation and depolarisation current measurements”, *IET Generation, Transmission and Distribution*, vol. 13, no. 24, pp. 5541 –5549, October 2019..
- [248] T. K. Saha and P. Purkait, “Investigation of an expert system for the condition assessment of transformer insulation based on dielectric response measurements,” *IEEE Trans. Power Deliv.*, vol. 19, no. 3, pp. 1127–1134, 2004.
- [249] P. H. F. Morshuis and F. H. Kreuger, “Transition from streamer to Townsend mechanisms in dielectric voids,” *J. Phys. D. Appl. Phys.*, vol. 23, no. 12, p. 1562, 1990.
- [250] S. J. Dodd, J. V Champion, Y. Zhao, A. S. Vaughan, S. J. Sutton, and S. G. Swingle, “Influence of morphology on electrical treeing in polyethylene blends,” *IET- Sci. Meas. Technol.*, vol. 150, no. 2, pp. 58–64, 2003.
- [251] S. Morsalin, B. T. Phung, A. Cavallini, “Measurement and modelling of partial discharge as a function of cavity geometry at very low frequency”, *IEEE Trans. Electr. Insul.*, Feb. 2020. [In Press]
- [252] R. Bartnikas and J. P. Novak, “On the character of different forms of partial discharge and their related terminologies,” *IEEE Trans. Electr. Insul.*, vol. 28, no. 6, pp. 956–968, 1993.
-

- 
- 
- [253] J. Sletbak, "The influence of cavity shape and sample geometry on partial discharge behavior," *IEEE Trans. Dielectr. Electr. Insul.*, vol. 3, no. 1, pp. 126–130, 1996.
- [254] S. Morsalin, B. T. Phung, and M. G. Danikas, "Influence of Cavity Geometry on Partial Discharge Measurement at Very Low Frequency," *37th Electrical Insulation Conference (EIC)*, 2019, pp. 1–4.
- [255] A. Cavallini, G. C. Montanari, and L. E. Mariut, "The influence of test voltage waveforms on partial discharge activity in XLPE," *IEEE International Symposium on Electrical Insulation*, 2012, pp. 554–557.
- [256] M. U. Zuberi, A. Masood, E. Husain, and A. Anwar, "Estimation of partial discharge inception voltages due to voids in solid sheet insulation," *IEEE Electrical Insulation Conference (EIC)*, 2013, pp. 124–128.
- [257] T. Liu, Q. Li, X. Huang, Y. Lu, M. Asif, and Z. Wang, "Partial discharge behavior and ground insulation life expectancy under different voltage frequencies," *IEEE Trans. Dielectr. Electr. Insul.*, vol. 25, no. 2, pp. 603–613, 2018.
- [258] S. Morsalin, B.T. Phung, "Electrical field distribution on the cross-linked polyethylene insulation surface under partial discharge testing", *Journal of Polymer Testing*, vol. 82, pp. 1-8, 2020.
- [259] T. Dao, B. T. Phung, T. Blackburn, and H. V. P. Nguyen, "A comparative study of partial discharges under power and very low frequency voltage excitation," *IEEE Conference on Electrical Insulation and Dielectric Phenomena (CEIDP)*, 2014, pp. 164–167.
- [260] Suwarno and T. Mizutani, "Diagnosis of insulation conditions : Interpretation of partial discharges from  $\phi$ -q-n pattern, pulse-sequence and pulse waveform," *International Conference on Condition Monitoring and Diagnosis*, 2008, pp. 60–63.
- [261] B. Florkowska and P. Zydron, "Analysis of conditions of partial discharges inception and development at non-sinusoidal testing voltages," *IEEE Conference on Electrical Insulation and Dielectric Phenomena*, 2006, pp. 648–651.
- [262] S. Ray, *An introduction to high voltage engineering*. PHI Learning Pvt. Ltd., 2013.
- [263] P. Sattari, G. S. P. Castle, and K. Adamiak, "FEM–FCT-based dynamic simulation of corona discharge in point–plane configuration," *IEEE Trans. Ind. Appl.*, vol. 46, no. 5, pp. 1699–1706, 2010.
- [264] B. Florkowska and R. Wlodek, "Pulse height analysis of partial discharges in air," *IEEE Trans. Electr. Insul.*, vol. 28, no. 6, pp. 932–940, 1993.